

A CONTRIBUTION TO MULTIPATH MODELING AND SIMULATION FOR KINEMATIC TRAJECTORIES

A thesis accepted by the Faculty of Aerospace Engineering and Geodesy of the University of Stuttgart in fulfilment of the requirements for the degree of Doctor of Engineering Sciences
(Dr. -Ing.)

by
Alexandra Avram
born in Fetesti

Main referee: Prof. Dr.-Ing. habil. Volker Schwieger
Co-referee: Univ.-Prof. Mag. Dr. habil. Thomas Pany
Day of the defense: 22.01.2021

Institute of Engineering Geodesy
University of Stuttgart
2021

TABLE OF CONTENTS

ABSTRACT.....	VII
KURZFASSUNG	VIII
1 INTRODUCTION.....	1
1.1 MOTIVATION.....	1
1.2 PREVIOUS RESEARCH.....	3
1.3 STRUCTURE OF THE THESIS.....	4
2 SOME FUNDAMENTS OF STATISTICS AND GLOBAL NAVIGATION SATELLITE SYSTEMS.....	6
2.1 OVERVIEW	6
2.2 STATISTICAL ANALYSIS.....	6
2.2.1 <i>Descriptive data analysis</i>	6
2.2.2 <i>Inferential data analysis</i>	7
2.3 GLOBAL NAVIGATION SATELLITE SYSTEM ARCHITECTURE	10
2.4 MEASUREMENTS AND ERROR BUDGET	12
2.4.1 <i>Pseudorange measurement</i>	12
2.4.2 <i>Carrier phase measurement</i>	12
2.4.3 <i>Error budget</i>	13
2.5 GNSS DATA PROCESSING	17
2.5.1 <i>Combinations of GNSS measurements</i>	17
2.5.2 <i>Cycle-slip detection</i>	20
2.5.3 <i>Receiver noise removal</i>	21
2.6 POSITION ESTIMATION	23

2.6.1	<i>Differential position</i>	23
2.6.2	<i>GNSS/INS integration</i>	25
3	GNSS MULTIPATH	28
3.1	INTRODUCTION	28
3.2	SIGNAL MODEL	29
3.2.1	<i>LOS and multipath components</i>	29
3.3	SIGNAL REFLECTION	30
3.3.1	<i>Fresnel Zone</i>	30
3.3.2	<i>Attenuation factor</i>	32
3.3.3	<i>Specular and diffuse reflection</i>	35
3.4	SIGNAL DIFFRACTION	36
3.5	MULTIPATH MODELING	38
3.5.1	<i>Statistical models</i>	38
3.5.2	<i>Deterministic models</i>	41
3.5.3	<i>Hybrid model</i>	46
3.6	RECEIVER SENSITIVITY TO MULTIPATH	47
3.6.1	<i>Receiver signal tracking</i>	48
3.6.2	<i>Multipath impact on DLL</i>	57
3.6.3	<i>Multipath impact on PLL</i>	59
3.6.4	<i>Multipath impact on SNR</i>	60
4	GNSS PSEUDORANGE MULTIPATH ESTIMATION	62
4.1	CODE MINUS CARRIER	62
4.1.1	<i>CMC estimate</i>	65
4.1.2	<i>Multipath model</i>	66

4.1.3	<i>CMC Limitations</i>	66
4.2	MULTIPATH FROM DOUBLE DIFFERENCES	67
4.2.1	<i>Pseudorange smoothing</i>	68
4.2.2	<i>Geometrical term removal</i>	69
4.2.3	<i>DD multipath estimate</i>	70
4.2.4	<i>Double differences limitations</i>	71
4.3	EXPERIMENTAL VERIFICATION	72
4.3.1	<i>Measurement setup</i>	72
4.3.2	<i>Measurement evaluation</i>	72
5	MULTIPATH SIMULATION	74
5.1	INTRODUCTION	74
5.2	SIMULATIONS SETUP.....	74
5.2.1	<i>Simulation of multipath parameters</i>	75
5.2.2	<i>Receiver type impact on multipath</i>	77
5.3	HiL SIMULATIONS WITH MULTIPATH HYBRID MODEL	80
5.3.1	<i>Simulation environment</i>	80
5.3.2	<i>Simulated multipath parameters</i>	81
5.3.3	<i>Impact on SNR</i>	83
5.3.4	<i>Impact on position</i>	84
5.4	HiL SIMULATIONS WITH MULTIPATH RAY-TRACING ALGORITHMS	85
5.4.1	<i>Simulation environment</i>	85
5.4.2	<i>Simulated multipath parameters</i>	86
5.4.3	<i>Impact on GNSS observables</i>	88
5.4.4	<i>Impact on position</i>	92

5.5	SUMMARY	93
6	MULTIPATH ESTIMATION FROM MEASUREMENT CAMPAIGNS.....	95
6.1	INTRODUCTION	95
6.2	MULTIPATH CHARACTERIZATION FOR DIFFERENT VELOCITIES.....	96
6.2.1	<i>Static site</i>	96
6.2.2	<i>Slow kinematic</i>	98
6.2.3	<i>High kinematic</i>	99
6.2.4	<i>Impact on position</i>	101
6.3	MULTIPATH CHARACTERIZATION FOR DIFFERENT ENVIRONMENTS.....	103
6.3.1	<i>Intercity highway</i>	103
6.3.2	<i>Urban roadway</i>	115
7	CONCLUSIONS AND FURTHER WORK	124
7.1	CONCLUSIONS.....	124
7.2	FURTHER WORK	125
	BIBLIOGRAPHY	128
	APPENDIX.....	136
	APPENDIX A.....	136
	APPENDIX B	141
	APPENDIX C.....	145

Abstract

Over the last years, GNSS technology has been under continuous development and its applications as well. This progress is driven by the emergence of increasingly complex applications. One such trending application for GNSS technology is automated transportation, which expands the boundaries in terms of navigation safety. Since multipath is one of the most challenging errors which affect the position and integrity of a navigation system, research is required in this direction. The multipath topic is complex, since it is dependent on the satellite position in conjunction with the surroundings of the receiving antenna. Therefore, the multipath effects are different for a static user compared to a kinematic one. Environment properties may lead to one or many reflections, diffraction, or non-line-of-sight (NLOS) situations. The characterization of the errors due to multipath in the GNSS observations have been extensively studied since 1972. Nevertheless, most of the focus in this field of study has been towards static applications. This dissertation extends the current multipath research by simulation, characterization, and modeling of multipath errors for kinematic vehicles.

To examine different multipath simulation models for kinematic vehicles, a Hardware-in-the-Loop (HiL) test bench is set up. Deterministic and physical-statistic (i.e. hybrid) multipath simulation models are implemented in the HiL to assess which is adequate for the research scope i.e. multipath for kinematic users. Analysis of the simulations results reveal that the deterministic method is appropriate. Deterministic simulations under same multipath conditions with a static and kinematic vehicle show that the receiver errors due to multipath are larger in the static simulation.

Two multipath estimation algorithms are implemented to characterize the multipath errors on pseudoranges. Based on the estimated multipath, error models are computed. The multipath estimation algorithms are verified by means of cross-correlation with both experimental and simulated data. To examine the kinematics' impact on errors in a multipath environment, experimental data is investigated from a vehicle at various velocities. The computed multipath error models indicate larger errors in the static measurements. For a static GNSS system mounted on the vehicle, the pseudorange error due to multipath is between five and 42 centimeters in an open sky scenario. Kinematics of the vehicle in the same environment reduce the multipath raw error magnitude under the average of the one during the static measurement.

The developed HiL test bench is validated against experimental data in two environments: highway and city. Experimental data from a vehicle on highway shows pseudorange errors due to multipath in the interval from five to 82 centimeters. An error in the interval between eight and 99 centimeters is depicted from simulations in the same environment. A vehicle in the urban environment is prone to larger errors due to multipath. Experimental data indicated errors between 28 and 260 centimeters, while simulations reproduced the error in a range from 32 to 230 centimeters. Since the kinematic deterministic multipath simulations imply large amount of 3D data, the use of synthetic 3D models is proposed. The validation is performed by comparing multipath error models from simulated and acquired GNSS data. The multipath error models are used also to characterize the error magnitude for different vehicle environments. Additionally, both GPS and Galileo signal characteristics with respect to multipath are assessed. Finally, the impact of multipath on coordinate errors is shown for experimental and simulated data. The computed 3D RMSE from highway experimental data is 160 centimeters and from simulated data the value increased to 200 centimeters. Measurement into the city reveal a position 3D RMSE of 900 centimeters, while the simulations in the same environment reproduce 700 centimeters.

Kurzfassung

In den vergangenen Jahren wurden die GNSS Technologie und deren Applikationen stetig weiterentwickelt. Einer dieser Applikationen ist das automatisierte Fahren, welches die Systemgrenzen hinsichtlich des sicheren Navigierens eines Fahrzeuges extrem ausweitet. Da der Mehrwegeeffekt einer der herausforderndsten Fehler ist, welcher die Position und Integrität eines Systems zum automatisierten Steuern eines Fahrzeuges beeinflusst, ist die Forschung in diesem Bereich zwingend notwendig. Der Mehrwegeeffekt ist eine sehr komplexe Thematik, da dieser von der Position des Satelliten und den Einflüssen der Umgebung der Empfangsantenne abhängig ist. Aufgrund dessen sind die Fehler des Mehrwegeeffekts für statische und kinematische Anwendungsfälle unterschiedlich. Die Eigenschaften der Umgebung können zu einer oder mehreren Reflektionen, Diffraktionen oder Nicht-Sichtverbindungs Situationen führen. Die Charakterisierung der Fehler aufgrund von Mehrwegeeffekten in GNSS-Beobachtungen werden seit 1972 umfangreich wissenschaftlich untersucht. Im Zuge dieser Untersuchungen wurde der Fokus bisher auf statische Anwendungsfälle gelegt. Diese Dissertation erweitert die aktuellen Mehrwegeeffekt-Untersuchungen mit Hilfe von Simulationen, Charakterisierungen und dem Erstellen von Modellen des Mehrwegeeffekt-Fehlers für kinematische Anwendungsfälle.

Um die verschiedenen Mehrwegeeffekt Simulationsmodelle für den kinematischen Anwendungsfall zu untersuchen, wurde ein Hardware-in-the-Loop (HiL) Prüfstand aufgebaut. Sowohl deterministische, als auch physikalisch-statistische Simulationsmodelle für Mehrwegeeffekte wurden im HiL Prüfstand erarbeitet und umgesetzt, so dass beurteilt werden konnte, welcher Forschungsansatz für Mehrwegeeffekte im kinematischen Anwendungsfall am geeignetsten ist. Die Analyse der Simulationsergebnisse zeigte, dass die deterministische Methode vielversprechende Ergebnisse erwarten ließ. Deterministische Simulationen unter denselben Mehrwegeeffekt-Bedingungen mit einem statischen und kinematischen Anwendungsfall zeigten, dass der Fehler aufgrund von Mehrwegeeffekten in dem statischen Anwendungsfall größer ist.

Zwei Algorithmen zur Abschätzung von Mehrwegeeffekten wurden implementiert, um den Mehrwegeeffekt-Fehler bei Pseudoentfernungen zu charakterisieren. Basierend auf den abgeschätzten Mehrwegeeffekten wurden Fehlermodelle errechnet. Die Algorithmen zur Abschätzung des Mehrwegeeffekts wurden mit experimentellen und simulierten Daten verifiziert. Um den Einfluss der Kinematik auf den Fehler aufgrund des Mehrwegeeffekts zu untersuchen, wurden experimentelle Daten eines Fahrzeuges unter verschiedenen Geschwindigkeiten geprüft. Das errechnete Mehrwegeeffekt-Fehlermodell zeigte größere Fehler in den statischen Messungen, ebenso wie die deterministischen HiL Simulationen. Für ein statisches GNSS System, welches auf einem Fahrzeugdach montiert wurde, lagen die Fehler der Pseudoentfernung aufgrund des Mehrwegeeffekts zwischen fünf und 42 Zentimetern in einem Szenario ohne Hindernisse. Im kinematischen Anwendungsfall des Fahrzeuges in derselben Umgebung reduzierte sich der Fehler des Mehrwegeeffekts im Rohzustand bereits unter den des Durchschnitts der statischen Messungen.

Der entwickelte HiL Prüfstand wurde mit experimentellen Daten in zwei Umgebungen validiert: Autobahn und Stadt. Für ein Fahrzeug auf der Autobahn zeigen experimentelle Daten einen Mehrwege-Fehler bei Pseudoentfernungen von fünf bis 82 Zentimetern. Ein Fehler im Intervall von acht bis 99 Zentimetern wird durch Simulationen im gleichen Umfeld dargestellt. Ein Fahrzeug in einer urbanen Umgebung ist durch größere Fehler aufgrund des Mehrwegeeffekts gefährdet. Experimentelle Daten zeigen Fehler zwischen 28 bis 260 Zentimetern, welche durch Simulationen

reproduziert werden können; hier liegt der Fehler in einem Bereich von 32 bis 230 Zentimetern. Da die kinematischen deterministischen Mehrwegeeffekt-Simulationen eine große Menge an 3D Daten benötigen, fanden synthetische 3D Modelle Anwendung. Die Validierung wurde durchgeführt, indem die Mehrwege-Fehler des Simulationsmodells mit GNSS Daten verglichen wurden. Die Mehrwege-Fehlermodelle wurden benutzt, um den Fehlerumfang für verschiedene Fahrzeugumgebungen zu charakterisieren. Zusätzlich wurden die Signalcharakteristiken von GPS und Galileo unter Berücksichtigung des Mehrwegeeffekts beurteilt. Schlussendlich wurde die Auswirkung des Mehrwegeeffektes auf die Koordinaten, sowohl für experimentelle, als auch simulierte Daten dargestellt. Der berechnete quadratischen Mittelwert der Fehler aus den experimentellen Daten der Autobahnfahrt liegt bei 160 Zentimetern, bei den simulierten Daten steigt der Wert auf 200 Zentimeter. Die Messungen in der Stadt zeigen einen quadratischen Mittelwert der Fehler von 900 Zentimetern, während sich durch Simulationen in der gleichen Umgebung 700 Zentimeter reproduzieren ließen.

1 Introduction

1.1 Motivation

The Global Navigation Satellite System (GNSS) represents the worldwide used positioning and navigation systems. Since 1995, when the U.S. Global Positioning System (GPS) became operational, numerous applications on water, ground and air made use of this technology. However, the need for increased positioning accuracy leads to continuous research and progress. The emerge of additional GNSS systems (GALILEO, GLONASS, BeiDou) as well as receiving antennas and receivers developed the GNSS industry and increased the number of use cases. Nowadays, one important use case of GNSS technology is vehicle automated driving.

Figure 1-1 shows the roadmap of the automated driving (AD) functions, in the chronological order of their development. These functions are split into levels of automation, which are highlighted by the three lanes. Starting in 2010, the first steps towards AD constitute level 1 of automation, also called assisted driving. This is shown on the left lane of Figure 1-1, together with functions from this category. These are meant as a support during driving or parking. Partial and conditional automation belong to driving functions of level 2 and 3. These are shown in the middle lane of the Figure 1-1. An important feature introduced by this category is that the pilot system is capable to fully control the vehicle for limited periods in some restricted situations. However, the permanent driver supervision is required. At last, the levels 4 and 5 include the high and full automation, represented on the right lane of Figure 1-1. The highest levels of automation imply that the driver is not required. The pilot system is able to perform lateral and longitudinal driving for all situations, given a defined use case.



Figure 1-1: Roadmap of highly AD functions. The left lane shows the starting point of the development, while the middle lane shows the planned accomplishment of partially AD. The right lane shows the highly AD timeline (Robert Bosch GmbH, 2019)

To accomplish assisted and some functions of the partially AD, surrounding sensors were sufficient. Since the development start of the highly AD, a complementary system for the absolute vehicle localization is required. This leads to the use of GNSS for the following AD steps. At the time of writing, the automated driving is one of the latest trends where GNSS positioning is necessary. Users' positioning via affordable GNSS receivers has been integrated on the consumer market into smartphones or portable navigation devices since 1999 (van Diggelen, 2009). Due to safety, integrity and precision necessity, new GNSS equipment which is feasible for vehicles needs to be developed. Numerous challenges have been faced during the development of partially automated driving over the

last years. Besides the legal aspects and traffic safety, the technical aspects represent a challenge. In order to be installed in commercial vehicles, the navigation system for AD should be low-cost. In the same time, precision, redundancy and robustness must be ensured.

The challenge to meet the mentioned AD requirements is represented by the GNSS errors. GNSS measurements are affected by errors introduced by the satellite clocks, orbits, atmosphere (ionosphere, troposphere), multipath and receiver noise. Except for the last two error types, the satellite and the atmospheric errors are correlated for different users. Thus, they can be mitigated by using e.g. correction data services. The errors induced by multipath and noise are user dependent errors, which are not correlated and cannot be easily removed. The receiver noise is typical for each receiver and can be characterized, thus the main remaining error source is multipath. Due to the challenging properties together with its numerous dependencies, multipath errors dominate the total error budget in precise applications. GNSS multipath error is known in literature as a challenging topic and significant scientific work has been dedicated to understand its aspects related to various applications. Since in the AD context, a new setup and use case are available, further understanding about multipath needs to be gained.

Multipath error is introduced by the environment obstructions as natural topography, buildings, degrading the position accuracy. Since the line-of-sight (LOS) reception is required for high precision applications, the multipath error needs to be modeled for mitigation purpose. Satellite signals can be degraded through reflection, diffraction, obstruction or a combination of these phenomena. The situation becomes more challenging for a kinematic scenario, as the surrounding changes constantly. Previous research related to multipath is focused on static users due to the nature of former GNSS applications. As multipath is strictly dependent on the environment, the knowledge gained in the past cannot be applied for the current purpose of AD. Therefore, this work focuses on gaining knowledge regarding multipath behavior in kinematic situations. The scenarios where the error is examined are highway and urban. This choice is justified by the next AD milestones: highway and urban pilot.

The highest automation levels imply self-driving vehicles in highway and city environments. For both scenarios multipath is a dominant source of error that will impact the system performance. Thus, additional studies are needed to gain knowledge of the typical multipath for the mentioned situations. Although research regarding urban multipath effects has been made, this refers to a static use case and cannot be generalized. Referring to the highway environment that includes high kinematics, no multipath examination has been performed until the time of writing.

Besides the environment, the GNSS equipment also plays a role in the multipath characteristics. The effect of the multipath has been investigated previously and several mitigation techniques have been proposed for different applications. The different approaches took into account the type of the antenna used and their locations. For geodetic applications, choke-ring antennas or ground planes have been proposed for multipath rejection. Additionally, the antenna could be mounted in a high and obstruction-free area, to reach the maximum operational range. However, for the AD purpose, the previous solutions are not feasible. The setup for this new application implies that the receiving antenna is mounted on the metallic rooftop. This is an aspect which is taken into account within this work. The presented investigations regarding multipath are based on simulations and recorded measurements from an antenna installed on a vehicle. Therefore, the multipath results are representative for the AD use case.

Given the new GNSS application for the autonomous driving scope, the work within this thesis is dedicated to multipath simulation, modeling and characterization for kinematic vehicles in various environments. The multipath error is dependent on the signal properties and its modulation. With the increasing number of satellite available, the European navigation system, Galileo, becomes an enabler for use of GNSS in autonomous driving. The Galileo signals have different modulation and structure compared with the ones of GPS and thus the multipath error is expected to be different. Meanwhile, GPS remains the oldest and most used navigation system and any GNSS receiver is able to process its signals. Due to the relevance of both satellite systems for autonomous driving, the multipath characterization in this work will focus on the signals broadcast by the GPS satellites on L1 C/A code and L2C frequencies and the European navigation system Galileo on E1 OS and E5b frequencies.

1.2 Previous research

The effect of multipath errors have been recognized and investigated since early 1970s (Hangerman, 1973). Understanding of this GNSS error source has been built over the last decades from numerous publications that tackle multipath from different point of view. Nevertheless, in geodesy books like Seeber (2003), Hofmann-Wellenhof et al. (2007) multipath is presented on an abstract level. An exception is Parkinson et al. (1996), where multipath effects are detailed in a separate chapter by Michael S. Braasch. Progress related to multipath is documented in several dissertations: Braasch (1992), Winkel (2000), Ray (2000), Hannah (2001), Bilich (2006), Lehner (2007), Weiss (2007), Irsigler (2008).

Multipath error is strongly related to the environment and the satellite – receiver geometry. Thus, to mitigate the effects of this error, the multipath environment needs to be characterized. This approach has been explored in Braasch (1992), where multipath is characterized for aircrafts. It is shown that the resulted pseudorange errors are a function of the reflection's signal strength, phase shift and delay. In Hannah (2001), multipath propagation is simulated for a static receiver. Simple, yet effective ray models are implemented to demonstrate the effects due to multipath on the signal's amplitude, phase and delay. Similar, multipath is modeled for an urban environment in Lehner (2007). Extensive measurements are processed to characterize the multipath error in urban and sub-urban environment. Such an approach has the advantage of being precise, but it is site specific and time consuming. In Bilich (2006), the multipath effects on the GNSS measurements are explained and shown for geodetic GPS installations and receivers. Multipath is modeled from signal-to-noise measurements and the limitations of the proposed method are shown. Since pseudorange measurements are affected with errors in meter range due to multipath, in Weiss (2007) these are characterized for various environments and applications: land, marine and aerial. The input for land multipath characterization is represented by static measurements. All the previous studies related to multipath are useful to understand the theoretical background of multipath and its numerous dependencies. However, no in depth characterization of the multipath error for kinematic measurements has been done. The nature of the multipath is different from the other scenarios and thus further research is needed.

As previously mentioned, the multipath error is dependent on the environment. In order to estimate the multipath error for the investigated environment, several modeling techniques can be used. The most popular approaches are deterministic and statistic. Deterministic methods are based on ray-tracing algorithms. Through geometrical optics (GO) and physical optics (PO), site-specific multipath parameters are computed. The use of this method requires a three-dimensional model as input and has the limitation of being site specific. Nevertheless, this is the most accurate method of computing

multipath parameters (Avram et al. 2018). Statistical models are extensively used to model multipath as well. The Rician and Rayleigh models characterize the signal in situations when LOS is either present or absent. Statistical models like State Markov, Suzuki and Loo became the most used models (Fontán & Espiñeira, 2008). The statistical approach is used for urban multipath modeling in the DLR's land mobile multipath propagation (Lehner, 2007). Further, a consolidated model where the land mobile multipath is modeled by Markov or semi-Markov chains is presented in (Prieto-Cerdeira et al. 2010). Since both modeling methods have advantages and drawbacks, the question to be answered within this work is which approach is more adequate for vehicle multipath simulation. Consequently, statistic and deterministic multipath simulation techniques are implemented and analyzed within this work.

The multipath error depends on the characteristics of the receiving antenna. Research dedicated to antennas and their capabilities to reject or minimize the multipath effects has been previously investigated. Popular approaches like usage of antenna arrays, gain and phase patterns for different polarizations prove to be efficient in the multipath error reduction. Nevertheless, the effect of multipath is not completely removed. Depending on the GNSS application, different antennas are appropriate. For example, choke ring antennas are extensively used for reference station applications (Smyrnaiois et al. 2018). Due to their construction, they reject the reflections arriving from negative elevation angles. Nevertheless, they still cannot mitigate the multipath components arriving from positive elevation angles. Antenna type and placement is an important factor in the multipath characterization. Since the antenna is responsible to capture the signals which are later processed by the receiver, its phase and gain patterns as well as the surrounding environment contribute to the multipath magnitude. For the AD purpose, each vehicle must be equipped with a GNSS antenna. The metallic surface of the vehicle favors strong multipath reflections. Consequently, investigations regarding multipath are made within this work to assess the contribution of the antenna montage on the vehicle.

Prior research demonstrates that one technique to mitigate the multipath error relies on the receiver software. The core of receiver technologies is represented by the narrow-correlator which was developed by NovAtel (van Dierendonck, 1992). It was shown that by reducing the chip spacing from 1 to 0.1 the performance in terms of multipath of a C/A code is almost as good as of a P-code receiver. Later on, the method was further improved. This led to tracking algorithms like MEDLL (Townsend et al. 1995) or Teager-Kaiser-Operator-Based MEDLL (Hu, 2013). Studies on different receivers demonstrated the relevance of its algorithms in multipath processing. As the GNSS receiver is an important factor in the multipath impact chain, a part of this work focuses on the receiver investigation. The discriminator function and multipath error magnitude of the used receiver are studied by means of simulation. This study provides an understanding of the receiver sensitivity to different multipath delays as well as different dynamics.

1.3 Structure of the thesis

This dissertation consists of seven chapters and it is structured as follows. Chapter 1 highlights the research motivation. Additionally, a preview over the existing state of the art technology and methods regarding multipath is provided. Theoretical aspects regarding multipath are presented later in Chapter 3 as well.

Chapter 2 gives a short overview of GNSS, describing the general theoretical aspects from literature that are relevant for this research. It starts with some theoretical background related to statistical analysis, it continues with the operational concept of GNSS and it ends with the position estimation. This chapter briefly covers the entire chain, from the signal transmission until the position computation.

Chapter 3 describes the theoretical aspects of GNSS multipath, which represents the core of this dissertation. In the first part, the signal and propagation characteristics related to multipath are presented. Next, multipath propagation modeling techniques are described. The last part of the chapter covers the details regarding a receiver architecture as well as the tracking loops. The description focuses on the elements that are relevant for multipath processing.

Chapter 4 comprises the two implemented algorithms for multipath estimation. Details regarding the processing steps are presented and intermediate results are shown. The algorithms are validated through cross-correlation of the computed multipath series. Discussions related to their advantages and limitations regarding static and kinematic multipath estimation concludes this chapter.

Chapter 5 consists of simulation test bench and multipath simulations at different car velocities through two approaches: physical-statistical and deterministic. These two methods are presented into two sub-chapters, for clarity. The simulated multipath is characterized by statistical means and the estimated error due to multipath after the receiver processing is quantified by pseudorange and position errors.

Chapter 6 contains both measurement campaigns and simulations. The focus is split into two: multipath estimation for a vehicle at different velocities, and thereafter different environments. The velocities are further categorized into static, slow kinematic and fast kinematic. As for the environment, this is classified into highway and urban roadways. At last, multipath impact on position is investigated for specific traffic situations and finally for the entire specific environment.

Chapter 7 summarizes the research within the dissertation. It reveals shortly the conclusions that are reached during the work. The limitations of the research are identified and recommendations for further work are presented.

2 Some Fundamentals of Statistics and Global Navigation Satellite Systems

2.1 Overview

In this chapter, some theoretical background related to statistical analysis and Global Navigation Satellite Systems (GNSS) functionality and operation is given. The statistical part is related to methods that are implemented and used in this work. The GNSS section focuses on GPS and Galileo navigation systems, since this work refers to their signals. In the next sections, the operational system and error sources which affect the GNSS measurements are listed and described. Then, the GNSS data processing and position estimation algorithms that are relevant for this research are presented.

2.2 Statistical Analysis

Statistics consists of various mathematical methods for analysis, characterization, and presentation of data. These methods are split into two categories: descriptive and inferential. Descriptive statistics define properties of data by making use of central tendency (e.g. mean, median, mode) and dispersion (e.g. standard deviation, variance). Through inferential statistics it is possible to examine relationships between data within a sample and make predictions of how it relates to a larger dataset. Probability distributions, correlation testing and regression methods are part of the inferential statistics. In the next sections, statistical methods that are relevant for this work are detailed.

2.2.1 Descriptive data analysis

2.2.1.1 Arithmetical mean and standard deviation

Considering a vector of measurements \mathbf{L} , where:

$$\mathbf{L} = (l_1, l_2, l_3, \dots, l_n), \quad (2-1)$$

the expected value and the theoretical standard deviation are unknown. Instead, the arithmetical mean \bar{l} and the empirical standard deviation s can be computed as follows:

$$\bar{l} = \frac{1}{n} \cdot \sum_{j=1}^n l_j, \quad (2-2)$$

where n is the number of elements of the measurement vector and variance σ^2 is given by:

$$\sigma^2 = \frac{\sum_{i=1}^n (\bar{l} - l_i)^2}{n - 1}, \quad (2-3)$$

$$\sigma = +\sqrt{\sigma^2}. \quad (2-4)$$

2.2.2 Inferential data analysis

2.2.2.1 Statistical distributions

In probability theory and statistics, there are several probability functions which provide the occurrence likelihood for different outcomes of an event. Probability distributions can be divided into two categories: discrete and continuous. The discrete probability functions, also known as probability mass functions can be applied for events where the outcome is discrete. On the other hand, a continuous probability function is adequate for events where the output takes values in a continuous range.

Normal distribution

The normal distribution is a very popular continuous probability function. Also known as Gaussian distribution, it is dependent on two parameters: expected value and standard deviation of a measurement vector i.e. $l \sim N(\mu, \sigma)$. The probability density function (PDF) of a normal distribution is given by the equation:

$$f(x; \mu, \sigma^2) = \frac{1}{\sqrt{2\pi\sigma^2}} \exp\left(-\frac{(x - \mu)^2}{2\sigma^2}\right), \quad (2-5)$$

where:

x a continuous variable in the interval $-\infty < x < \infty$,

μ expected value of the distribution,

σ^2 the variance of the distribution.

Figure 2-1 illustrates the normal distribution that is defined by Equation (2-5) for different combinations of parameters.

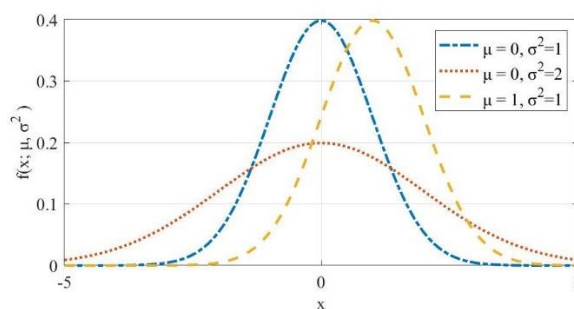


Figure 2-1: The Gaussian probability density for various defining parameters

Log-normal distribution

In statistics, a log-normal distribution is a continuous probability distribution of a random variable whose logarithm is normally distributed. If a continuous variable y has the expected value μ and variance σ^2 , then $x = e^y$ follows a log-normal distribution which is mathematically defined as:

$$f(x; \mu, \sigma^2) = \frac{1}{\sqrt{2\pi\sigma^2}} \cdot \frac{1}{x} \cdot \exp\left(\frac{-(\log x - \mu)^2}{2\sigma^2}\right). \quad (2-6)$$

The expected value and the variance values are given by (Cowan, 1998):

$$E(x) = \exp\left(\mu + \frac{1}{2}\sigma^2\right), \quad (2-7)$$

$$V(x) = \exp(2\mu + \sigma^2) \cdot [\exp(\sigma^2) - 1]. \quad (2-8)$$

It is to be noticed that the parameters μ and σ from Equation (2-6) do not correspond to the same parameters in the normal distributions, but to $E(x)$ and $V(x)$ from Equations (2-7) and (2-8). Figure 2-2 reveals the plots of the log-normal distribution, for several combinations of μ and σ , according to the definition from Equation (2-6).

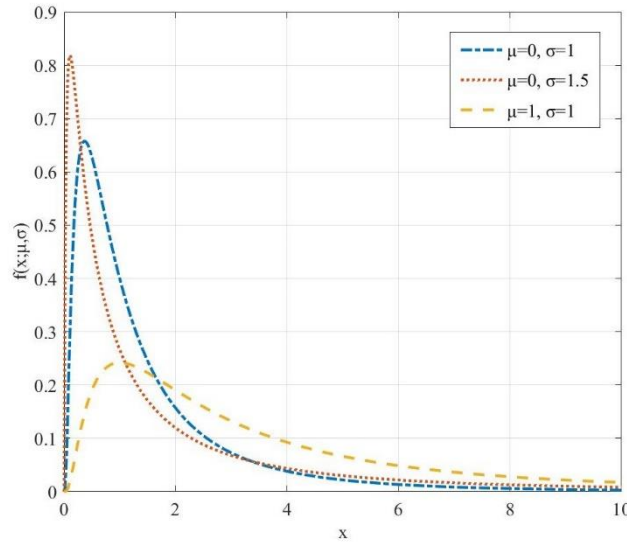


Figure 2-2: The log-normal probability density for several defining parameters

2.2.2.2 Covariance and cross-correlation

The covariance function shows the dependency between two different processes $X(t)$ and $Y(t)$. If the realization of the two processes are represented by the time series $x(t)$ and $y(t)$, then the covariance between them is given by the following formula (Zhang, 2016):

$$\hat{C}_{XY}(k) = \frac{1}{n-k-1} \sum_{i=1}^{n-k} (x_i - \mu_x)(y_{i+k} - \mu_y), \quad (2-9)$$

where:

- k index of the cross-correlation function,
- n length of the measurement vector,
- μ_x expected value of the realization $x(t)$,
- μ_y expected value of the realization $y(t)$.

In order to measure the similarity between the two realizations, the cross-correlation function can be used. The empirical cross-correlation $\widehat{\mathbf{R}}_{XY}(k)$ can be computed with the following equation:

$$\widehat{\mathbf{R}}_{XY}(k) = \frac{\widehat{\mathbf{C}}_{XY}(k)}{\sqrt{\widehat{\mathbf{C}}_{XX}(0) \cdot \widehat{\mathbf{C}}_{YY}(0)}} = \frac{\widehat{\mathbf{C}}_{XY}(k)}{\sigma_x \cdot \sigma_y}. \quad (2-10)$$

The empirical cross-correlation takes values in the interval $[-1, 1]$. As it is a measure of similarity, this function indicates if the two realizations are similar over the time series. The higher the similarity between the realizations over time, the closer to 1 is the $\widehat{\mathbf{R}}_{XY}$ value. The value 0 indicates no correlation and -1 indicates inverse correlation.

2.2.2.3 Least square regression

An observation model, where the observations are linearly related to the unknowns is given by the formula (Niemeier, 2008):

$$\mathbf{l} + \mathbf{v} = \mathbf{A} \cdot \mathbf{x}, \quad (2-11)$$

where:

- \mathbf{l} vector of measurements/observations,
- \mathbf{C}_l covariance matrix of measurements/observations,
- \mathbf{A} design matrix,
- \mathbf{P} weight matrix,
- \mathbf{x} vector of unknowns,
- \mathbf{v} vector of inconsistencies.

Considering the following forms of the covariance matrix and vector of inconsistencies:

$$\mathbf{P} = \frac{1}{\sigma_0^2} \cdot \mathbf{C}_l^{-1}, \quad (2-12)$$

$$\mathbf{v} = \mathbf{A} \cdot \mathbf{x} - \mathbf{l}, \quad (2-13)$$

the least square estimate is given by the formulation:

$$\mathbf{v}^T \cdot \mathbf{P} \cdot \mathbf{v} \rightarrow \min. \quad (2-14)$$

In order to obtain the minimum in Equation (2-14), leads to:

$$(\mathbf{x}^T \cdot \mathbf{A}^T - \mathbf{l}^T) \cdot \mathbf{P} \cdot (\mathbf{A} \cdot \mathbf{x} - \mathbf{l}) = \mathbf{0}, \quad (2-15)$$

$$(\mathbf{A}^T \cdot \mathbf{P} \cdot \mathbf{A}) \cdot \mathbf{x} = \mathbf{A}^T \cdot \mathbf{P} \cdot \mathbf{l}. \quad (2-16)$$

By multiplying the left side of Equation (2-16) with the term $(\mathbf{A}^T \cdot \mathbf{A})^{-1}$, the vector of unknowns can be determined:

$$\mathbf{x} = (\mathbf{A}^T \cdot \mathbf{P} \cdot \mathbf{A})^{-1} \cdot \mathbf{A}^T \cdot \mathbf{P} \cdot \mathbf{l}. \quad (2-17)$$

2.3 Global Navigation Satellite System architecture

Global Navigation Satellite Systems consists of three segments: the space segment, control segment, and user segment. The space segment consists of the operational satellites as well as the transmitted signals. The control segment is responsible for the supervision, performs satellite tracking and generates clock and orbit corrections. The user segment includes the whole spectrum of GNSS receivers that use the navigation systems for different applications (Parkinson et al. 1996).

Space segment

To provide continuous position globally, satellite constellations are developed in such a way that at least four satellites are visible anywhere. Each navigation satellite provides a platform for atomic clocks, radio transceivers and computer equipment for the system operation. The radio transmitted signals allow the receiver to compute the range and the satellite broadcast message enables the user to compute the orbital position at each epoch (Hofmann-Wellenhof et al. 2007). Ranging signals contain a code known as pseudorandom noise (PRN) as well. The PRN consists of chip units whose frequency varies for different satellite systems. The space segment is represented by the satellites also known as space vehicles i.e. SVs of a navigation system, which provide time and ranging measurement to the users. The measurements are transmitted via different signal frequencies, which are encoded with unique PRN-codes. Due to its functional concept, GNSS is a passive system whose signals can be used by an unlimited number of users in the user segment. Initially developed in 1973, the NAVSTAR Global Positioning System (GPS) represents the first navigation system in the world. It was directed by the US Department of Defense (DoD) and was later released for civilian use as well (Hofmann-Wellenhof et al. 2007). At the moment of writing, the GPS space segment consists of 31 operational satellites, placed on six orbits. Due to their configuration, they repeat an identical track over a place each sidereal day (23h 56m). Each satellite transmits data on three carrier frequencies: L1 (1575.42 MHz), L2 (1227.60 MHz) and L5 (1176.45 MHz).

Since the satellite position and navigation are essential for the European infrastructure, in 1994 the European Council had the initiative of developing an augmentation system of the existing navigation systems. As next, in 1999 the European Space Agency (ESA) was involved in designing a new satellite navigation system for Europe, Galileo. Although fully compatible with GPS, Galileo was designed as an open, independent and global system. Once fully developed, the European global navigation system, Galileo will include 30 Medium Earth Orbit (MEO) satellites. At the time of writing, the system consists of 22 usable satellites, which broadcast signals on three frequencies: E1 (1575.42 MHz), E5 (1191.795 MHz) and E6 (1278.75 MHz). Galileo satellites are placed on three equally spaced orbital planes (Galileo System Status, 2021).

Control segment

The ground or control segment is responsible for steering the navigation system. Besides satellite tracking, maintenance, prediction and adjustment of the clock and orbital parameters, the control segment is in charge of protecting the services against unauthorized usage (Hofmann-Wellenhof et al. 2007). The control segment updates the clock, ephemeris, and almanac in the navigation message at least one time per day. If improved accuracy is required, more frequent updates can be scheduled. Since the ephemeris parameters are an accurate fit to the SVs orbits, they are valid for 4 hours. Almanac data represents a reduced subset of an ephemeris file, as it contains 7 from the 15 ephemeris

orbital parameters. Another function of the control segment is to collect the pseudorange and carrier phase measurements from remote monitoring stations in order to determine clock and orbit corrections. To accomplish this, this segment consists of three components: master control stations, monitor stations and ground antennas (Kaplan & Hegarty, 2006).

Since 1985, the Operational Control Segment (OCS) for GPS is functional. It includes five monitoring stations and four ground antenna upload stations. The sites are spread worldwide to have a significant separation in latitude and longitude. For Galileo, the Control Centres (GCC) are located in Oberpfaffenhofen (Germany) and Fucino (Italy). Additionally, the infrastructure is complemented by European GNSS Service Centre (GSC), Geodetic Reference Service Provider (GRSP), Time Service Provider (TSP), Galileo Security Monitoring Centre (GSMC), Galileo Data Service Provider (SGDSP) and Galileo Reference Centre (GRC) (Galileo System Status, 2021).

User segment

All military and civilian applications that imply the use of GNSS signals form the user segment. The equipment which processes the L-band signals and determines the user position, velocity, time (PVT) solution is generically called the GNSS receiver set. This comprises the following elements: antenna and receiver. Satellite signals are received via a right-hand circularly polarized (RHCP) antenna, which usually has a coverage gain pattern. The antenna transfers the GNSS signals to the receiver which is responsible for processing and computing PVT. Therefore, the estimated position is the electrical phase center of the antenna. The physical and electrical center of the antenna might vary. Calibration is necessary for high-accuracy applications. A detailed description of how the receiver is operating and processing the GNSS signals is provided in section 3.6.

Besides providing PVT, there are numerous other applications for GNSS. Aircraft, marine and land mobile navigation, kinematic surveys, ionosphere measurements are just a few applications whose functionality is based on satellite signals. The unidirectional communication between satellites and receivers enables the utilization of an unlimited number of users.

2.4 Measurements and error budget

This chapter describes the GNSS measurements that are used within this work together with the errors which affects them. Although the multipath error for pseudorange (i.e. code) measurements is of interest for this dissertation, the theoretical background which is required for its computation is introduced as well. This is the basis for the algorithms presented later in chapter GNSS pseudorange multipath estimation 4.

2.4.1 Pseudorange measurement

Also known as GNSS observable, a pseudorange is derived from the traveling time of the signal which is transmitted from the phase center of the satellite antenna to the phase center of the receiving antenna. Thus, the pseudorange is the geometrical distance between the satellite and receiver. Unlike the terrestrial distance measurements, the satellite distance measurements involve two clocks: receiver and satellite clock. As these induce errors, satellite distance measurements are referred in the literature as pseudoranges. These are provided by receivers in two forms: code measurements and carrier phase measurements. Unlike the carrier phase measurements, the code measurements are computed through the receiver code correlation with the incoming signal PRN. Taking into consideration the clock errors and the transmission medium, the mathematical model of the pseudorange measurements is defined as follows (Hwang et al. 1999):

$$\rho_i = r + c(dt_u - dt^s) + T + I_i + MP_{\rho,i} + \varepsilon_{\rho,i}, \quad (2-18)$$

where:

r	true range,
c	speed of light,
dt_u	the receiver clock bias,
dt^s	satellite clock bias,
T	troposphere delay,
I_i	ionosphere delay,
$MP_{\rho,i}$	the multipath error on frequency i for code (ρ_i),
$\varepsilon_{\rho,i}$	receiver code tracking noise.

It is known from the literature that the derived pseudoranges from code measurements can be approximately 1% of a chip length precise. Thus, a civil C/A code which is 300 meters long yields a precision of 3 meters and assuming a precise P-code, the precision is 0.3 meters. However, the precision of the pseudorange measurements depends on the receiver correlation techniques as well.

2.4.2 Carrier phase measurement

The carrier phase observations represent a measure of signal phase at the reception time, relative to the signal phase at the transmission time. These are derived from a phase comparison between the Doppler-shifted received carrier signal and the receiver reference frequency. In literature, a complete carrier wave is called a cycle and its measure varies as a function of the signal frequency. The unknown integer number of cycles is called ambiguity. Although ambiguous, carrier phase measurements are more accurate compared to the code measurements due to a higher frequency (Xu,

2016). Similar to the code measurements, the carrier phase observables are affected by the atmosphere and the clock measurements as well. Considering this, the fundamental carrier phase observation equation is (Hwang et al. 1999):

$$\phi_i = r + c(dt_u - dt^s) + T - I_i + N_i\lambda_i + MP_{\phi,i} + \varepsilon_{\phi,i}, \quad (2-19)$$

where:

- λ_i the wavelength of the frequency i ,
- N_i ambiguity term,
- $MP_{\phi,i}$ carrier multipath error,
- $\varepsilon_{\phi,i}$ receiver carrier tracking noise.

As the carrier phase observable determines the phase within one signal wavelength, the main difficulty related to the carrier phase determination is the computation of the cycle ambiguity. It is to be noticed that the ambiguity changes when the receiver suffers a signal loss of lock, producing jumps or measurement discontinuities.

2.4.3 Error budget

To obtain an error-free GNSS measurement, the satellite and receiver clock should be perfectly synchronized, the satellite orbits have to be ideal and the transmitted signal would propagate to the receiver through the vacuum at the speed of light. Nevertheless, in reality, the Earth rotation, relativistic effects, atmosphere effects, receiver clock, orbit errors and receiver instrumental errors contribute to the measurement's error budget. These errors can be categorized into satellite related errors, signal propagation errors and receiver errors. Finally, the total error propagation is affected by the geometrical arrangements of the satellites. Table 2-1 reveals typical values of the errors GNSS observables, measured with a dual-frequency receiver according to Hegarty (2013).

Table 2-1: GPS error budget for civilian use dual-frequency receivers without Selective Availability (SA). The first four errors are related to the satellite and signal transmission, while the last four depend on the receiver

Error Source	Error Budget [m]	Remarks
Satellite		
Ephemeris	0.8	Broadcast ephemeris residual error
Clock	1	Error due to clock drifts
Signal propagation		
Ionosphere	~0.0	Depends on satellite position and solar activity
Troposphere	0.2	Depends on humidity and temperature
Code multipath	0.3	Varies with code frequency, signal modulation, environment
Carrier multipath	0.05	Varies with carrier frequency, signal modulation, environment
Receiver		
Receiver code noise	0.3-3	Depends on dynamic stress and receiver
Antenna phase center	0.001-0.01	Depends on the calibration process

2.4.3.1 Satellite related errors

Ephemeris error

Ephemeris errors occur due to the orbit irregularity. Even if the satellites travel in very precise orbits, there is a set of disturbances which must be accounted for: non-sphericity of the Earth and its non-homogeneous mass distribution, the gravitational effect of other celestial bodies and the solar radiation pressure (Subirana et al. 2013). Due to these phenomena, the satellite position in the orbit is different to the one sent in the ephemeris. The GNSS ground control system is responsible for the detection and correction of these disturbances. The International GNSS Service (IGS) operates a network of ground stations, which is able to provide broadcast GNSS ephemerides with an accuracy of 0.1 m according to IGS (2020).

Clock error

The time scale of the GPS system is GPS time and the satellite clocks tag the signals in this time frame. Since a synchronization error of $1 \mu\text{s}$ between the GPS time and the satellite clocks leads to an error of 300 meters, the SVs are equipped with atomic clocks. Rubidium and cesium clock oscillators have short-term stability of 10^{-10} and long-term stability of 10^{-13} (Seeber, 2003). Nevertheless, small drifts exist and they lead to inaccurate determination of the user position. Additionally, errors occur due to a lack of synchronization between the GPS time system and the time when the satellite broadcasts signals. Clock errors are determined and sent to the satellite by the ground control stations. Within the downlink data, satellites provide their clock offsets as coefficients of a polynomial to the user (Li et al. 2018). IGS provides real-time satellite clock solutions with an accuracy of 5 ns according to IGS (2020).

2.4.3.2 Signal propagation errors

Ionosphere delay

The ionosphere is a part of the atmosphere that is extended between 50 km and 1000 km. As it is mentioned by Logan (2013), the ionosphere affects a GNSS signal in two ways: through the variation in the refraction index because of the electrons content and scintillation. Due to its content of electrons, the ionosphere affects the range and the range-rate of the GNSS signals through signal bending, carrier phase advance or distortion (Klobuchar, 1996). Scintillation refers to irregularities in the ionosphere content. This causes short-term signal fading that results in positioning errors. However, this phenomenon occurs especially in low latitude areas.

Troposphere delay

The troposphere is the lowest layer of the atmosphere, from the sea level up to 18 km. As opposed to the ionosphere, the troposphere is the non-ionized part of the atmosphere and consists of dry gases and water vapor (Hobiger & Jakowski, 2017). Its effect is known as tropospheric delay and the impact on the GNSS observables is shown in Equation (2-18) and Equation (2-19). Since the troposphere is a nondispersive medium for frequencies up to 15 GHz, it has the same impact on the carrier and code measurements (Kaplan & Hegarty, 2006). This implies that it cannot be determined from dual-band measurements.

The troposphere comprises a wet and a dry component. The wet one is difficult to model due to the fact that it depends on the water vapor distribution in the atmosphere. Nevertheless, the wet component represents only 10% of the total tropospheric refraction. To model the dry component, existing models can be employed. The total delay due to troposphere is proportional to the elevation angle. Hopfield developed a model to determine the troposphere error by considering the hydrostatic and the wet delay. Saastamoinen developed an accurate model to compute the hydrostatic delay. In the case that the user does not have enough data to apply the mentioned models, MOPS Hydrostatic Delay Model (1998) tropospheric algorithm can be utilized (Schüler, 2000). This algorithm makes predictions regarding the troposphere delay by using standard data that is dependent on the latitude of the user.

Multipath error

Multipath error occurs when a satellite signal arrives at the receiver not only via the line of sight (LOS) signal, but also through other paths due to reflection and diffraction. The multipath components are delayed and phase shifted with respect to the LOS signal. Depending on the relative delay and phase shift, constructive or destructive interference appears. The interference of multipath signals and LOS signal affects the GNSS carrier, code measurements and the signal to noise ratio. Multipath errors are challenging due to the number of factors that influence them. Since multipath is determined by the satellite – user geometry and the surrounding environment, it is a local error. In time domain, the error is not constant, but shows a sinusoidal pattern for a stationary receiver. The pattern is determined by the satellite movement above the antenna horizon. Multipath error depends on the satellite signal structure and frequency of the carrier. Additionally, the receiver which processes the multipath signals also has a contribution to the resulting error on the GNSS measurements. As this error represents the core of this work, the influence of multipath on GNSS signals is discussed in detail in Chapter 3.

2.4.3.3 Receiver related errors

Antenna error

Pseudorange measurements might be biased due to the receiving antenna as well. Accurate knowledge regarding the antenna phase center and phase center variations is required to obtain accurate GNSS measurements. Based on the frequency of the received signal, azimuth and elevation of the transmitting satellite, the antenna phase center varies in position. Therefore, antenna calibration is necessary to determine the phase center corrections for a given antenna model. The Right Hand Circularly Polarized (RHCP) Left Hand Circularly Polarized (LHCP) antenna gain patterns play an important role in the attenuation of the multipath signals that are transmitted to the receiver.

Receiver noise

Receiver noise is an error similar to white noise and can be removed with a low-pass filter. It arises from the high-frequency thermal noise and the dynamic stress of the tracking loops. Additionally, it contains the noise induced by the receiving antenna, cables and amplifiers. Both GNSS observables are biased by receiver noise at different magnitudes, frequency-dependent (Subirana et al. 2013). According to Karaim et al. (2018), the modern receivers have a carrier phase error of 0.1-1% of a cycle and a pseudorange error in range of centimeters.

2.4.3.4 Satellite geometry

The accuracy of a GNSS position is influenced by two factors: the accuracy of the measurements and the geometric distribution of the satellites. If σ_r denotes the accuracy of the pseudorange observation, the connection to the positioning standard deviation σ_p and satellite geometry i.e. dilution of precision (DOP) is given by the equation (Seeber, 2003):

$$\sigma_p = DOP \cdot \sigma_r. \quad (2-20)$$

DOP values for a location can vary considerably during a day. However, since GPS comprises 31 fully operational satellites, the DOP variations are less critical. The launch of other navigation systems like Galileo contributed to even better DOP values due to the satellite redundancy. Nevertheless, the critical situations can occur in urban environments, where the buildings' height and narrow streets yield to signal blockage of the satellites of low elevation. Due to this phenomenon, the DOP values and implicitly the accuracy can be degraded.

2.4.3.5 Positioning errors

Accuracy and precision are mostly used to describe the position in satellite geodesy. Nevertheless, the terms are distinct in meaning. Accuracy measures the closeness degree of the measured value with respect to the true value. Precision indicates the closeness of the measurements to their mean value. An accuracy measure that is often used in satellite geodesy is the standard deviation (σ) or root mean square error (*RMSE*). The *RMSE* represents the squared differences between acquired coordinates and true coordinates. Assuming ΔE_i , ΔN_i and ΔH_i the errors in the east, north and vertical components in the epoch i , the 3-D *RMSE* is defined as (Subirana et al. 2011):

$$3D \text{ RMSE} = \sqrt{\frac{1}{n} \sum_{i=1}^n (\Delta E_i^2 + \Delta N_i^2 + \Delta H_i^2)}. \quad (2-21)$$

2.5 GNSS data processing

As mentioned previously in section 2.4, the GNSS measurements contain several errors on code and carrier observables. To assess the error which is caused by the occurrence of multipath, the other errors on the measurements should be estimated and removed. For this, several algorithms can be used. In the next sections, the relevant methods that are used within this work to isolate the errors affecting GNSS measurements are shown.

2.5.1 Combinations of GNSS measurements

2.5.1.1 Code minus carrier

Multipath errors on code measurements can be determined by the combination of code and carrier measurements on the same frequency. Considering the mathematical definition of the GNSS observables in equations (2-18) and (2-19), the multipath error on code measurements can be computed by means of code-minus-carrier (CMC) combination as follows:

$$\rho_i - \phi_i = 2I_i + N_i\lambda_i + MP_{\rho,i} + MP_{\phi,i} + \varepsilon_{\rho,i}. \quad (2-22)$$

Through this combination the clock errors, tropospheric delay and ephemeris error are removed. Equation (2-22) expresses the CMC observable with the remaining errors: the ionosphere, ambiguity, code and carrier phase multipath, and receiver noise. The ionosphere delay can be removed by making use of dual-frequency measurements. The procedure is known as geometry-free combination and it is shown in the following section. Ambiguities from carrier phase observables are constant for each satellite, as long as no cycle slips occur. Therefore, they can be removed by averaging, if the cycle-slip occurrence is known. For this, a detector of cycle-slips can be used. The CMC approach neglects the multipath which affects the carrier phase measurements. This is because of the magnitude of carrier multipath errors, compared with the code multipath errors. Multipath influence on carrier measurements may reach a maximum of a quarter of wavelength i.e. 4.75 cm for L1. The multipath magnitude on code measurements can reach up to the signal code length i.e. 293 m for C/A code (Yedukondalu et al. 2011). However, the amount of multipath error on pseudorange is dependent also on the receiver technology as shown later in chapter 3.6. Assuming that the mentioned errors are determined and removed, the CMC estimate consists only of multipath error on pseudorange and receiver noise. This can be expressed as follows:

$$\rho_i - \phi_i - (2I_i + N_i\lambda_i) = MP_{\rho,i} + \varepsilon_{\rho,i}. \quad (2-23)$$

2.5.1.2 Geometry-free combination

According to Sanz Subirana et al. (2011) the geometry-free combination cancels up the first-order ionosphere effect. This means that 99.9% of the ionospheric delay is removed from the GNSS measurements. As indicated in Equation (2-18) and Equation (2-19), the error due to ionosphere depends on the signal frequency i . This property allows GNSS users who use more than one frequency to correct the ionosphere error, as follows (Subirana et al. 2013):

$$I_i = \frac{f_j^2}{f_i^2 - f_j^2} (\phi_i - \phi_j) - \frac{f_j^2}{f_i^2 - f_j^2} (N_i \lambda_i - N_j \lambda_j), \quad (2-24)$$

where:

- f_i, f_j the two frequencies of the GNSS signal,
- ϕ_i, ϕ_j carrier phase measurements,
- λ_i, λ_j wavelength,
- N_i the ambiguity on frequency i .

For the case of GNSS single frequency users, the ionosphere delay error can be approximated by the Klobuchar model expressed in Equation (2-25). By using the coefficients within the satellite broadcast navigation message, the ionosphere error can be determined (Hofmann-Wellenhof et al. 2007):

$$I_i = A_1 + A_2 \cdot \cos \frac{2\pi(t-A_3)}{A_4}, \quad (2-25)$$

where $A_1 = 5 \text{ ns}$ and $A_3 = 14^h$ local time. The values for A_2 and A_4 are computed with the coefficients from the navigation message as follows (Hofmann-Wellenhof et al. 2007):

$$\begin{aligned} A_2 &= \alpha_1 + \alpha_2 \varphi_{IP}^m + \alpha_3 \varphi_{IP}^{m^2} + \alpha_4 \varphi_{IP}^{m^3}, \\ A_4 &= \beta_1 + \beta_2 \varphi_{IP}^m + \beta_3 \varphi_{IP}^{m^2} + \beta_4 \varphi_{IP}^{m^3}. \end{aligned} \quad (2-26)$$

Another possibility to correct for the ionosphere delay is provided by the TEC (Total Electron Content) maps. Globally, TEC models are derived from the International GNSS Service. TEC maps are available every 24 hours, at a sample interval of 2 hours per 5° latitude x 5° longitude grids (IGS, 2020).

2.5.1.3 Single and double combinations

Widely used for relative positioning, linear combinations of GNSS observables requires simultaneous measurements at both a reference and a remote station. This means, that the measurements from the two stations must be synchronized. Assuming two satellites i.e. PRN A and PRN B and two close-by receivers i.e. Q and R as illustrated in Figure 2-3, single and double differences can be built for phase and code measurements.

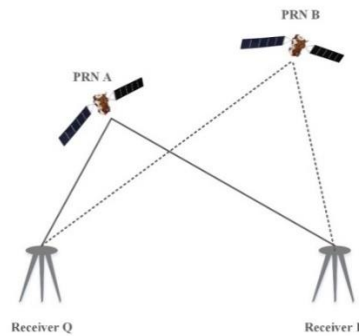


Figure 2-3: Between receiver differential technique

The differentiation can be performed between receiver, between satellite and between time (Logsdon, 1992). One of the reasons why this method is popular is that it eliminates the correlated errors. By forming single differences between observables, the satellite clock error is eliminated. Since the baseline between receivers is typically short, the atmospheric and orbital (i.e. ephemeris) errors are similar. Thus, these can be also reduced. Nevertheless, it must be noticed that the larger the baseline between the receivers is, the less correlated the common errors become.

The double differences cancel the satellite and receiver clock errors. However, the ambiguities of the carrier phase measurements and the multipath errors are not eliminated. Thus, double differences can be used for the determination of the multipath magnitude if the ambiguities are removed. Restricting to the literature regarding multipath estimation, the presence of multipath has been identified in 1988 by double differenced phase observations in Georgiadou & Kleusberg (1988).

Single differences

GNSS pseudorange and carrier phase measurements mathematical formulations are presented in section 2.4. Considering the equations and the notations in Figure 2-3, the single difference (SD) for pseudorange and carrier measurements are formed with the observables from one satellite and two receivers:

$$SD\rho_{QR}^A = \rho_Q^A - \rho_R^A = r_{QR}^A + c \cdot (dt_Q - dt_R) + (MP_{\rho,Q}^A - MP_{\rho,R}^A) + \varepsilon_{\rho,QR}, \quad (2-27)$$

$$SD\phi_{QR}^A = \phi_Q^A - \phi_R^A = r_{QR}^A + c \cdot (dt_Q - dt_R) + \lambda_i(N_Q^A - N_R^A) + (MP_{\phi,Q}^A - MP_{\phi,R}^A) + \varepsilon_{\phi,QR}. \quad (2-28)$$

where:

ρ_Q^A	pseudorange from satellite A to receiver Q ,
ρ_R^A	pseudorange from satellite A to receiver R ,
r_{QR}^A	difference of geometric ranges,
c	speed of light,
$dt_{Q,R}$	clock corrections of receiver Q , respectively R ,
$MP_{\rho,Q,R}$	pseudorange multipath at receiver Q , respectively R ,
$\varepsilon_{\rho,QR}$	cumulative code error corresponding to receiver Q and R noise,
ϕ_Q^A	carrier phase measurement from satellite A to receiver Q ,
ϕ_R^A	carrier phase measurement from satellite A to receiver R ,
$N_{Q,R}$	ambiguity integer number of receiver Q , respectively R ,
$MP_{\phi,Q,R}$	carrier phase multipath at receiver Q , respectively R ,
λ_i	the wavelength of the GNSS signal frequency,
$\varepsilon_{\phi,QR}$	cumulative carrier phase error corresponding to receiver Q and R noise.

It is to be noticed that the differences expressed by Equations (2-27) and (2-28) do not contain the ionosphere and troposphere delay terms. Because of the proximity of the two receivers, these terms are considered almost identical and are reduced.

Double differences

By performing between satellite difference and between receiver differences, the double differences (DD) are formed. This removes the receiver clock bias from the SD. Neglecting the receiver noise, the DD may be formed for both pseudorange and carrier phase observations as follows:

$$DD\rho_{QR}^{AB} = SD\rho_{QR}^A - SD\rho_{QR}^B = (r_{QR}^A - r_{QR}^B) + (MP_{\rho,Q}^A - MP_{\rho,R}^A) - (MP_{\rho,Q}^B - MP_{\rho,R}^B), \quad (2-29)$$

$$DD\phi_{QR}^{AB} = SD\phi_{QR}^A - SD\phi_{QR}^B = (r_{QR}^A - r_{QR}^B) + (MP_{\phi,Q}^A - MP_{\phi,R}^A) - (MP_{\phi,Q}^B - MP_{\phi,R}^B) + \lambda_i \cdot (\Delta N_{QR}^A - \Delta N_{QR}^B). \quad (2-30)$$

The terms in the first pair of brackets in Equations (2-29) and (2-30) represents the geometry term corresponding to the differenced unit baseline to different satellites. The next two pairs of brackets contain the multipath for the two satellites *A* and *B* from the two receivers *Q* and *R*. Equation (2-29) contains the multipath on code measurements and Equation (2-30) the carrier multipath. It is noticed that DD on carrier phase measurements contains the ambiguity differences as well. This can be removed through averaging. Within the continuous pass of the two satellites with no cycle slip events, the last term of Equation (2-30) is a constant number.

To pursue only the multipath effect in DD, the term $r_{QR}^A - r_{QR}^B$ must be removed. Each SD includes the term r_{QR}^i , which is the projection of the relative position vector onto the LOS vector to each satellite *i*. In the case of a DD, the differentiation of the projection results in a geometry term that includes the difference between unit vectors to different satellites for all possible combinations. To determine this variable and subtract it from the DD, the least square regression is employed.

The goal of the polynomial analysis is to model the trend of each geometrical term by means of the lowest possible degree. The regression model is given by (Brandt, 1999):

$$p(x) = \beta_0 + \beta_1 \cdot x_i + \beta_2 \cdot x_i^2 + \dots + \beta_m \cdot x_i^m + \varepsilon, \quad (2-31)$$

where:

- β_i polynomial coefficients,
- x time variable,
- ε a random error of the polynomial fitting.

By solving Equation (2-31), a unique least square solution is obtained, which is a set of values to compute the best fit for the DD geometrical term.

2.5.2 Cycle-slip detection

As previously mentioned in 2.5.1.1, receiver losses of lock cause discontinuities in the carrier phase measurements. This is known in the literature as cycle-slip. When this occurs, the integer ambiguity in the carrier measurement of a satellite changes. In order to remove the ambiguity from the CMC estimate, average is performed over segments where no cycle-slip occurred. To have the information about cycle-slip occurrence, a cycle-slip detector has to be implemented. Different methods can be implemented for cycle-slip detection, according to the application type and available data. Within this

work, due to the availability of dual-frequency measurements, the detector is based on carrier phase data from two frequencies. This has the advantage of eliminating the clock and geometry errors. The first step to detect the cycle-slips is computing the differences of consecutive samples as follows (Subirana et al. 2013):

$$\Delta\phi_{ij}(k) = \phi_i(k) - \phi_j(k), \quad (2-32)$$

where i, j are two frequencies of a GNSS signal and k represents an epoch. As the second step, the second order polynomials are further computed for each satellite carrier measurements. The computed polynomial is compared to the observed value $\Delta\phi_{ij}(k)$ for each epoch k . If discrepancies larger than a threshold appear, then a cycle-slip is declared. The threshold can be computed by using the following equations (Subirana et al. 2013):

$$thr = a_0 - a_1 \cdot e^{\frac{\Delta t}{T_0}}, \quad (2-33)$$

$$a_0 = \frac{\lambda_j - \lambda_i}{2}, \quad (2-34)$$

$$a_1 = a_0 / 2, \quad (2-35)$$

where Δt refers to the measurement sampling rate and T_0 is the length of the segment which the threshold is applied to.

Based on the differences presented algorithm, cycle-slips are detected. However, it should be noticed that jumps in the carrier phase measurements can occur also due to signal instabilities. Therefore, the method can lead to false detections.

2.5.3 Receiver noise removal

Pseudorange smoothing

The receiver processes the incoming GNSS signals by means of two tracking loops called delay-locked-loop (DLL) and phase-locked-loop (PLL). The output of these loops consists of the pseudoranges and carrier phase measurements. The process is described in more detail in chapter 3.6. The noise within the tracking loops is inversely proportional to the frequency of the processed input. The code frequency for C/A code (1.023 MHz) is smaller compared to the carrier phase frequency (1575.42 MHz for GPS L1). Consequently, the code measurements are noisier than the carrier measurements. The noisy code measurements can be smoothed with the precise carrier measurements by employing a low pass-filter, namely the Hatch filter. Such a filter can be implemented as follows (Circiu et al. 2015):

$$\hat{\rho}(w) = \frac{w-1}{w} \cdot (\hat{\rho}(w-1) + \Delta\Phi_w) + \frac{1}{w} \cdot \rho_w, \quad (2-36)$$

where:

$\hat{\rho}$ smoothed pseudorange,
 w smooth window width,
 $\Delta\Phi_w$ carrier phase change within the smoothing window,
 ρ_w raw pseudorange value.

The Hatch filter is a smoothing technique that makes use of the variation of the carrier phase. The choice of the smoothing window size has been extensively investigated. It was found in Byungwoon et al. (2017) that the filter residual error for smoothed pseudoranges is the smallest for a 100 second window width. As described by Equation (2-36), the filter is recursive and uses the previous measurement to estimate the current one. Although the Hatch Filter reduces the noise on the pseudorange, it amplifies the ionosphere error which is present in the code measurement. Therefore, it is recommended that the smoothing process is employed either after removing the error produced by the ionosphere or using a divergence-free Hatch filter (Pathak et al. 2013).

2.6 Position estimation

2.6.1 Differential position

The error sources in a GNSS standard positioning system are related to the following: the satellite because of clock and ephemeris error, the atmosphere via ionosphere and troposphere errors and finally the user through multipath, receiver clock error and noise. The errors related to satellite are spatially correlated and vary slowly in time. In 1980, the technique called differential GPS (DGPS) was developed in order to remove the spatially correlated errors. Besides improving the accuracy, DGPS has a positive impact on integrity, as it reduces the probability that a GNSS user suffers from an undetected system fault (Parkinson et al. 1996). Nowadays, the generic name DGNSS might be used instead of DGPS since further navigation systems are utilized by the algorithm to compute the position.

The DGNSS algorithm principle is based on the mathematical formulation presented in section 2.5.1.3. Assuming that one of the two receivers is a base station and the other one is the rover, the differential equations from GNSS observations are built. To generate corrections by using the precise measurements of the base station, the following procedures may be used (Seeber, 2003):

- a) Corrections in the position domain: the position of the reference station which is derived from GNSS observations is compared with a previously known position. The position corrections are sent to correct the rover position;
- b) Corrections in the measurement domain: The pseudoranges observed from the base stations are compared with the pseudoranges computed from the known base station coordinates and satellite position. The differences are transmitted to the rover station;
- c) Corrections in the space domain: observations from several reference stations are used to estimate a vector of errors in the area.

The DGNSS based on corrections in the measurement domain can be further classified with respect to the observations which are used as follows: ordinary DGNSS, carrier smoothed DGNSS and precise DGNSS. Ordinary DGNSS is based on pseudorange measurements. The accuracy which can be reached for this algorithm varies between 1 and 3 meters, depending on the closeness to the base station. The second approach, namely carrier smoothed DGNSS applies smoothing of the pseudoranges at the rover station. This approach leads to accuracies under 0.5 meters. Lastly, the precise DGNSS is using the carrier phase corrections from the reference station to solve the ambiguities.

According to Hofmann-Wellenhof et al. (2007), Sennott & Pietraszewski (1987), Lachapelle, et al. (1989), the multipath errors of the rover stations do not cancel out by using differential positioning algorithms. Thus, to assess the impact of multipath biased pseudoranges on the position, the DGNSS based on code observations is employed in post-processing in Chapter 6.

2.6.1.1 Code-based DGNSS

The basic equations for ordinary DGNSS according to Seeber (2003) are detailed below. By taking into account the mathematical formulation of the GNSS observables, the pseudoranges from the reference i.e. R and the rover station i.e. P can be written as:

$$\rho_p = R_r + c(dt_p - dt^s) + T_p + I_p + MP_{\rho,p} + \varepsilon_{\rho,p}, \quad (2-37)$$

$$\rho_r = R_r + c(dt_r - dt^s) + T_r + I_r + \varepsilon_{\rho,r}. \quad (2-38)$$

It is to be noticed that the reference station is considered to experience no multipath biases in Equation (2-38) for simplicity. The reason for this assumption is due to the fact that the reference stations are positioned in high, open-sky environments and the GNSS antennas are rejecting multipath. The geometric range (R_r) is given by:

$$R_r = |x_s - x_r|. \quad (2-39)$$

Where R_r is computed based on the known satellite position derived from ephemeris and the known position of the reference station. The differential correction (DC) which is computed is given by:

$$DC = R_r - \rho_r = -c \cdot (dt_r - dt^s) - T_r - I_r - \varepsilon_{\rho,r}. \quad (2-40)$$

At the rover station, the corrections are applied as follows:

$$\widehat{\rho}_p = \rho_p + DC = R_p + c \cdot (dt_p - dt_r) + (T_p - T_r) + (I_p - I_r) + (\varepsilon_{\rho,p} - \varepsilon_{\rho,r}) + MP_{\rho,u}. \quad (2-41)$$

Assuming no latency, the satellite clock error is identical and it cancels out. The differences in ionosphere and troposphere biases are negligible for separation up to a few kilometers between rover and reference stations. As the separation increases, the errors decorrelate. Since corrections according to (2-41) are applied to pseudoranges at the rover stations with a separation of fewer than 5 kilometers, the position is affected only by the multipath at the rover.

2.6.1.2 Carrier phase-based DGNSS

Also known as Real Time Kinematic (RTK) if the corrections latency is near to zero, this processing algorithm is well-known due to its accuracy. RTK can deliver real-time centimeter accuracy over short separation between the reference station and rover and millimeter accuracy in post-processing (Kaplan & Hegarty, 2006). Since the carrier phase measurements are only a fractional part of the carrier cycle, the difficulty in this algorithm consists of finding the ambiguity. The algorithm implies the following features:

- a) Transmission of GNSS observation from the reference station to the rover in real-time;
- b) Resolution of ambiguities;
- c) Real-time baseline vector determination.

Two important factors that determine the quality of the algorithm are the transmission data type and the time to fix the ambiguities. With dual-frequency receivers, for example, the ambiguity fixing requires less time than for single-frequency receivers.

Similar to the code-based DGNSS, corrections are computed for the rover. In this case, these are carrier phase corrections. According to Seeber (2003), the carrier phase correction (CPC) at the reference stations is given by:

$$CPC_r = \phi_r - \left(\frac{R_r}{N_r \cdot \lambda}\right), \quad (2-42)$$

where:

- ϕ_r raw phase measured at the base station;
- R_r the geometric range at the base station;
- N_r the ambiguity at the base station;
- λ the wavelength of the GNSS carrier signal.

The corrected phase at the rover station is given by the equation:

$$\widehat{\phi}_p = \phi_p + CPC_r. \quad (2-43)$$

2.6.2 GNSS/INS integration

The term INS is an acronym for Inertial Navigation System. The integration of GNSS and INS is often used as the two systems operate complementarily. The GNSS solution corrects the INS drifts, whereas the INS is smoothing the GNSS solution, rejects outliers and bridges outages. The navigation solution resulted from such a system is complete and continuous (Groves, 2013). The basic principle of an integration algorithm is based on the fusion between the GNSS navigation solution with the INS output. The final navigation solution is usually given by a Kalman filter. By having this architecture, the INS is able to bridge the GNSS outages. There are different methods to integrate the measurements from the two systems. Depending on the input that is used e.g. raw measurements or navigation solution and the mathematical algorithm, there are three types of coupling: loose, tight and deep. The loose and tight integration algorithms are presented in the next sections, as these are relevant for this work.

2.6.2.1 Loosely coupled

The GNSS and INS systems are working independently in a loosely coupled (LC) integration architecture. This is visible in Figure 2-4 as well, where three main blocks can be distinguished. From top to bottom, the first block represents the GNSS receiver processing, the second one shows the INS processing and the latter one symbolizes the integration software. Both GNSS Receiver and INS blocks feed their outputs to the integration software, which provides an integrated solution. Figure 2-4 reveals sub-variants of the LC architecture, depending on the equipment which is used. For example, the system can be designed to have an open or closed-loop configuration. The dashed line in Figure 2-4 which connects the navigation and filtering algorithm to the INS pre-processing is absent for the case of an open-loop configuration. This feedback is required if the inertial sensors' quality is poor due to high drifts. Otherwise, the closed-loop configuration is employed and the feedback to the INS processing not performed (Avram et al. 2018b).

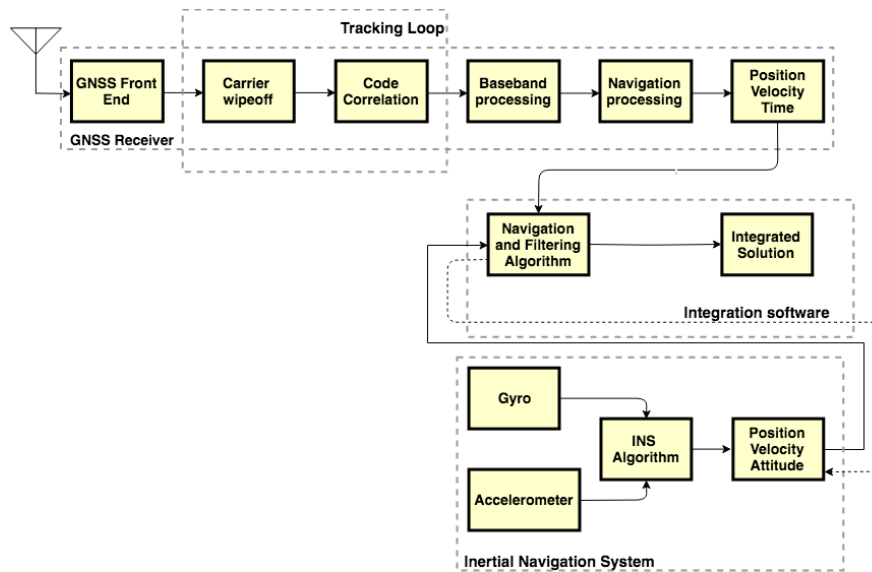


Figure 2-4: Schematic architecture of a GNSS/INS LC integration (Avram et al. 2018b)

The filtering algorithm in an LC integration is generally a Kalman filter implementation. A generic Kalman filter model can be written as in Gianluca et al. (2017):

When using the LC integration for real-time positioning, there are several limitations. One important aspect is that neither the GNSS nor the INS solution is improved. Due to the fact that the navigation solutions are initially computed separately and afterward fused, the position can be affected in two ways. In the case that the INS sensor is drifting, its measurement weight becomes smaller within the filter until only GNSS is used. Thus, the integrated solution coincides with the GNSS solution. On the other hand, if less than four satellites are in view no solution is available despite from the INS system. An alternative to overcome these limitations is the tightly coupled integration.

2.6.2.2 Tightly coupled

Generally, a tightly coupled (TC) implementation has an overall better performance compared to the previous one. The reason is that the two systems are not working independently to provide a solution, but they are fused at a higher level and aid each other in challenging situations. Figure 2-5 illustrates the basic architecture of a TC system. For such a system, the integration is achieved by means of a Kalman filter (KF) and it occurs at the raw measurement level. This means that raw pseudoranges, pseudorange rates, acceleration and gyro measurements are fused to obtain the integrated navigation solution. Consequently, a system that benefits from a TC integration is more robust and provides better accuracy. The better accuracy is the result of a smaller temporal correlation in a KF, as in a PVT solution. The increased robustness is owed to the fact that an integrated solution can be provided even if less than four satellites are in view (Gleason & Gebre-Egziabher 2009). However, due to the drifts of the INS sensors, it is not feasible to output an accurate position for long time periods without GNSS aid. The role of the GNSS measurements is to correct the INS drifts. The time interval where the integrated solution is accurate without GNSS observations depends on the implemented KF, the quality of the INS sensors and the TC variant that is implemented.

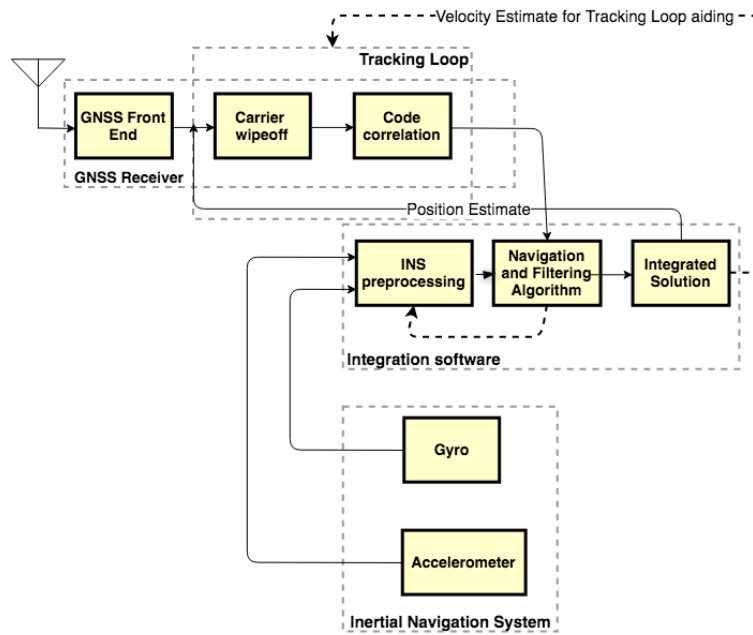


Figure 2-5: Scheme of a generic GNSS/INS tightly coupled integration (Avram et al. 2018b)

Similar to the LC architecture, the TC architecture comprises three sub-variants as well. The basic one implies no velocity estimates for tracking loop aiding and feedback to the INS pre-processing. These are marked with a dashed line in Figure 2-5. Another sub-variant implies feeding information about the previously computed integrated velocity and/or position to the GNSS tracking loops. This increases the accuracy of the computed GNSS observations and decreases the acquisition/re-acquisition time of satellites.

3 GNSS multipath

3.1 Introduction

The term GNSS multipath describes the arrival of a GNSS signal to a receiving antenna through one or many paths besides the direct signal. This impairment occurs when an electromagnetic wave encounters obstacles on its way, producing reflection, diffraction or scattering of the line-of-sight (LOS) signal (Saunders & Aragon-Zavala, 2007). Among the other errors which affect the GNSS measurements, multipath remains one of the most challenging errors in the budget due to its randomness. Within this chapter, the complete chain which is affected by GNSS multipath signals is described and the multipath influences are explained. Additionally, methods for multipath modeling are presented.

Since reflected signals travel a longer way to the receiving antenna, they are delayed with respect to the LOS signal. One of the multipath describing characteristics is a relative time delay. Further multipath characteristics are amplitude and phase. The amplitude of a multipath signal is dependent on the electromagnetic characteristics of the reflecting or diffracting surface. The signal phase is proportional to the additional travelled path and the reflector's electrical properties, and the phase variation over time depends on satellite-user dynamics. When the multipath signal arrives in phase (0° phase shift) with the direct signal, this results in a positive interference. The opposite occurs when the multipath signal arrives out of phase (180° phase shift) with respect to the direct signal. This is known as negative interference. Due to the changing phase of the multipath signal relative to the direct signal within positive and negative interference, the multipath for a static receiver has a periodic pattern, which resembles a sine wave (Irsigler, 2008).

A multipath environment is shown in Figure 3-1. Depending on the surrounding environment, reflector's geometry and reflection properties, a GNSS signal can be reflected from the ground or lateral directions. Another phenomenon which occurs is signal diffraction due to edges of reflectors. These phenomena are described in the next sections. Another aspect which determines the impact of the multipath signals is whether they reach the GNSS receiver together with the LOS or not. Within this work, both situations are modeled: combination of LOS with reflected signal and non-line-of-sight (NLOS).

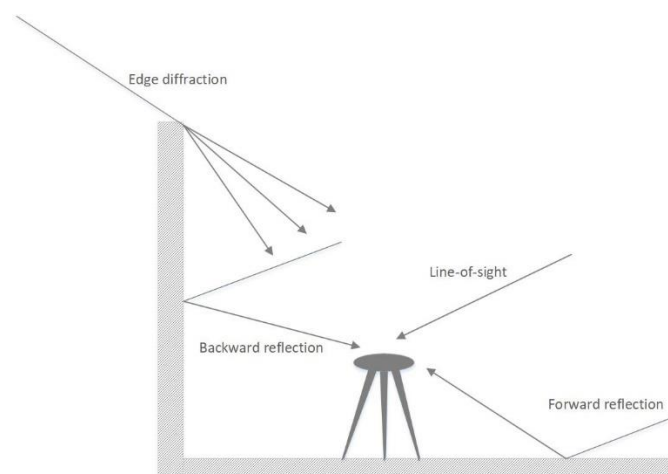


Figure 3-1: Line-of-sight signal and multipath effect due to diffraction, forward and backward reflection cf. Hannah (2003)

3.2 Signal model

Each GNSS system sends navigation signals to the Earth. These are allocated differently to frequency bands; all of them being spread between 1 and 2 GHz. GNSS signals overlap in the frequency domain when the carrier frequency is the same, as shown in Figure 3-2 in the case of GPS L1 and Galileo E1. Additionally, this indicates that the central frequencies of GPS L2 and Galileo E5a/E5b lay in the lower L-Band, whereas GPS L1 and GAL E1 are located in the upper L-Band.



Figure 3-2: GPS L1/L2 and Galileo E1/E5a/E5b frequency bands (Sanz Subirana et al. 2011)

GNSS signals overlap in the time domain as well. This means that signals from satellites are sent simultaneously to the user segment. However, each satellite signal is unique due to the pseudorandom number (PRN). To distinguish signals from each other, a GNSS receiver makes use of the signal's individual properties through correlation. The operating mode of the GNSS navigation systems is known in literature as Code Division Multiple Access (CDMA) (Ondrej et al. 2017).

The method which is used to modulate the code information on the carrier of the signal impacts the multipath sensitivity of a GNSS signal. The carrier and code frequencies also have an impact. GPS L1 signals for example are modulated with the C/A code through the binary phase shift key (BPSK) modulation. Galileo E1 signal modulation is CBOC (Composite Binary Offset Carrier) and originates from MBOC (Multiplexed BOC) (Avila-Rodriguez et al. 2008). Galileo signals are more resistant against multipath signals than GPS, due to the larger bandwidth together with the modulation scheme (Sleewaegen & De Wilde, 2008).

3.2.1 LOS and multipath components

Regardless of the satellite navigation system and considering the LOS component only, a GNSS signal at an intermediate frequency can be mathematically modeled as follows (Misra & Enge, 2006):

$$s_{LOS}(t) = A_D G_d(t) D(t - \tau_0) \rho(t - \tau_0) \cos [2\pi(f_{IF} + f_D)t + \phi_{LOS}(t)], \quad (3-1)$$

where A_D is the signal amplitude, G_d is the antenna gain applied to the signal, D stands for the navigation data bits, ρ is the ranging code, f_{IF} is the intermediate frequency, f_D is the Doppler frequency and ϕ_{LOS} is the carrier phase of the LOS signal. The signal time of emission is t and the time of arrival at the user is τ_0 . When the navigation signal arrives at a GNSS receiver, it is down-converted to the baseband by mixing it with an internally generated replica and a Doppler frequency estimate. Assuming that the receiver front-bandwidth preserves the entire signal spectrum, the Doppler frequency estimate error is negligible over the integration time, and that the navigation message is decoded, the resulting signal is (Weiss, 2007):

$$s_{LOS}(t) = A_D G_d(t) \rho(t - \tau_0) \cos [\phi_{LOS}(t)]. \quad (3-2)$$

Equation (3-2) expresses the LOS signal as a function of amplitude, antenna gain, ranging code and carrier phase. In the presence of a multipath signal, considering an ideal antenna pattern, the equation (3-2) will become:

$$s(t) = A_D \rho(t - \tau_0) \cos [\phi_{LOS}(t)] + A_D \sum_{i=1}^n \alpha_i \rho(t - \tau_i) \cos [\phi_{LOS}(t) + \phi_i]. \quad (3-3)$$

In equation (3-3) the first term represents the direct signal component and the second term the multipath component, where:

- $s(t)$ the composite signal that reaches the receiving antenna,
- α_i multipath attenuation with respect to the direct signal (A_0), $\alpha_i = \frac{A_i}{A_0}$,
- τ_i arrival time of the i multipath signal, $\tau_i > \tau_0$,
- ϕ_i multipath phase shift relative to the direct signal.

The parameters presented in Equation (3-3) together with the receiver type determine the size of the error determined by multipath. This is detailed in Section 3.6 together with the receiver architecture.

3.3 Signal reflection

To understand the multipath phenomenon, it is necessary to understand the determining factors and influences. In the case of a satellite system, because of the large distance between the transmitter and the receiver antenna, multipath effects occur in the vicinity of the user (Saunders & Aragon-Zavala, 1999). For the computation purpose of the minimum reflector size that produces multipath around the receiving antenna, the Fresnel zone concept can be employed (Zhang, 2016). The amplitude of the multipath signal, as well as its impact on the composite signal, can be mathematically determined by reflection coefficients of the reflector's material. Depending on the physical nature of the reflector, the electromagnetic waves can be affected by different types of reflection or diffractions. All these aspects are discussed in the next section.

3.3.1 Fresnel Zone

The areas which contribute to the signal reflection are known in literature as Fresnel zones. Assuming that the Earth's surface is a plane, the concept of Fresnel zones is presented in Figure 3-3. The Fresnel zones are defined by the intersection between the plane where the receiving antenna is located and the satellite-antenna link.

According to Rappaport (2002), the first Fresnel ellipsoid plays the most important role, because this is where most of the signal passes through. In the case that it is partially occupied by a reflector which is larger than the signal wavelength, multipath effects are expected. If the reflector is bigger than the first Fresnel zone, the signal is completely blocked. Therefore, the first Fresnel zone (f1 in Figure 3-3) should be free of obstructions.

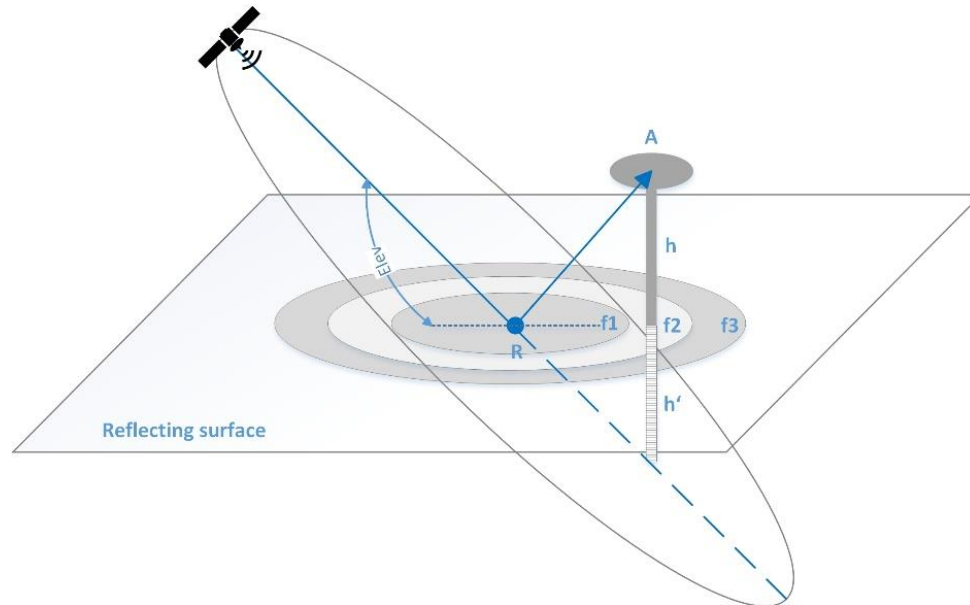


Figure 3-3: Fresnel zones (f) of a GNSS signal for a static user A. R stands for the reflection point (Zimmermann et al. 2018)

According to Eissfeller (1997), the semi-major and semi-minor axis of the first Fresnel zone can be expressed as a function of the signal wavelength and the satellite elevation angle as follows:

$$a_{f1} = \sqrt{\frac{n\lambda h}{\sin E}} \quad \text{and} \quad b_{f1} = \sqrt{\frac{n\lambda h}{\sin^3 E}}, \quad (3-4)$$

where:

- a_{f1} the semi-major axis of the first Fresnel zone,
- b_{f1} the semi-minor axis of the first Fresnel zone,
- h height of the receiving antenna,
- n number of Fresnel zone,
- λ the wavelength of the GNSS signal,
- E satellite elevation angle.

Equation (3-4) is valid for a planar reflector. Figure 3-4 shows the size of the first Fresnel zone for GPS L1/Galileo E1 frequency of 1575.42 MHz, 1227.6 MHz equivalent to GPS L2 and 1207.140 MHz for Galileo E5b frequency. Different antenna heights were used over the elevation interval from 10° to 90°.

As the elevation angle increases, the first Fresnel zone area decreases. Consequently, the multipath phenomenon is more likely to appear at lower than at higher satellite elevations. Moreover, for elevation angles larger than 60° the size of the Fresnel zone hardly changes ($< 1 \text{ m}^2$), regardless of the signal frequency. The satellite signal also plays a role. According to Figure 3-4, for the same antenna height, the E5b frequency is more susceptible to multipath effects than the L2 frequency and L1/E1 frequency. Therefore, for the same satellite position with respect to the receiver, the signal will be affected differently at different frequencies.

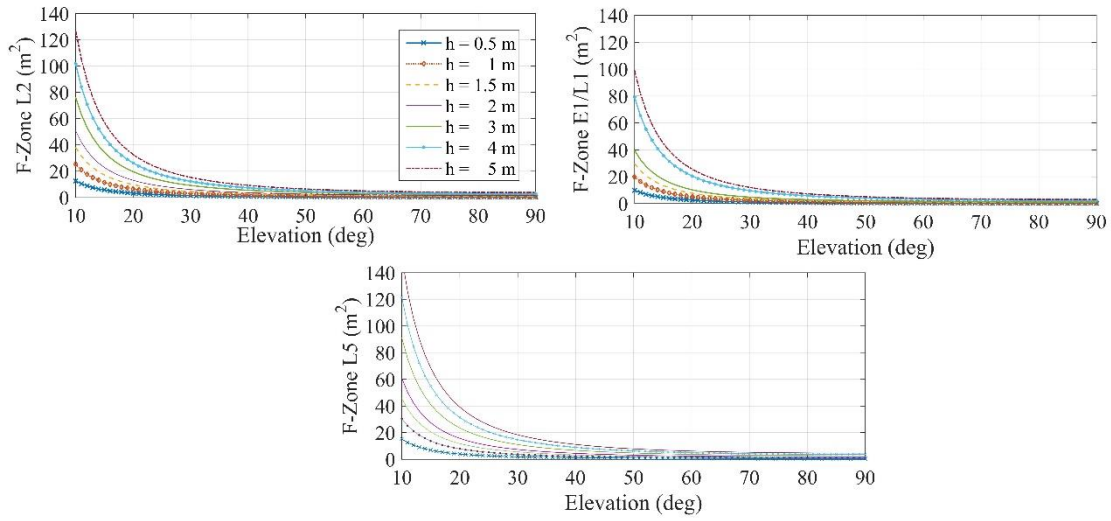


Figure 3-4: First Fresnel zone areas for L1/E1, L2 and E5b frequencies for different antenna heights

3.3.2 Attenuation factor

As previously mentioned multipath signals appear due to reflection, diffraction or diffuse scattering. Depending on the reflector properties that produces the multipath, the attenuation of the signal can be determined. Assuming a LOS and multipath reflection, the composite signal $s(t)$ that arrives at the GNSS receiver has an amplitude that contains following parameters:

$$A_c = A_D \cdot \sqrt{1 + 2 \cdot \alpha_i \cdot \cos \Delta\phi_M + \alpha_i^2}, \quad (3-5)$$

where:

- A_c amplitude of the composite signal $s(t)$,
- A_D amplitude of the direct signal,
- α multipath attenuation with respect to the direct signal,
- $\Delta\phi_M$ multipath phase shift relative to the direct signal.

Equation (3-6) shows the dependency between the resulting amplitude of the GNSS signal which is affected by a multipath and the attenuation factor due to multipath. Nevertheless, the attenuation factor depends on the surface of the reflector and indicates how strong the multipath signals are affecting the composite signal. According to Rodgers (1992), the signal attenuation α due to multipath can be mathematically modeled as:

$$\alpha = \eta_F \cdot \eta_R \cdot \eta_D \cdot \eta_A, \quad (3-6)$$

where:

- η_F free space loss,
- η_R signal attenuation due to reflection,
- η_D signal depolarization,
- η_A signal attenuation due to the antenna pattern.

The terms η_F and η_A are negligible, as $\eta_F = 0.999$ for path delays up to 450 m and $\eta_A = 1$ for the omnidirectional antenna is considered within this work. The variables η_R and η_D can be computed considering the signal polarization properties and refer to the left and right polarization of the signal. The navigation satellite systems use signals that are right-hand-circular polarized (RHCP) (Stutzman, 1993). The RHCP is the particular case of the elliptical polarization, i.e. the electromagnetic wave is composed of two linearly components: the horizontal component and the vertical component. The reflection coefficient η_R for the horizontal component Γ_H and for the vertical component Γ_v can be expressed as a function of the elevation angle (Hannah, 2003) as shown in Equation (3-7). The sum of the horizontal and vertical components determines the total reflection coefficient η_R .

$$\Gamma_H = \frac{\sin E - \sqrt{\varepsilon - \cos^2 E}}{\sin E + \sqrt{\varepsilon - \cos^2 E}}, \quad \Gamma_v = \frac{\varepsilon \cdot \sin E - \sqrt{\varepsilon - \cos^2 E}}{\varepsilon \cdot \sin E + \sqrt{\varepsilon - \cos^2 E}}, \quad (3-7)$$

with:

$$\varepsilon = \frac{\varepsilon_R + j60\lambda\sigma}{\mu_R}, \quad (3-8)$$

where:

- E elevation angle of the incoming signal (deg),
- ε_R dielectric constant,
- λ the wavelength of the signal (m),
- σ conductivity in the reflective medium (S/m),
- μ_R relative permittivity (F/m),
- ε complex relative permittivity.

The polarization of the signal can be expressed by means of the two linear components Γ_H and Γ_v . The signal components are represented by: a co-polarized (Γ_o) and a cross-polarized (Γ_x) component, as follows (Aloi & van Graas, 1999):

$$\Gamma_o = \frac{\Gamma_h + \Gamma_v}{2}, \quad \Gamma_x = \frac{\Gamma_h - \Gamma_v}{2}. \quad (3-9)$$

Nevertheless, due to signal reflections the signal circular polarization is modified. This is known as depolarization η_D and it is determined by the ratio between the two linear components Γ_h and Γ_x . Depending on their values, following cases are defined:

- a. Elliptically polarized if $\Gamma_h \neq \Gamma_v$;
- b. Circularly polarized if $\Gamma_h = \Gamma_v$;
- c. Linearly polarized if $\Gamma_v = 0$ or $\Gamma_h = 0$.

Assuming that a GNSS signal encounters a concrete reflection surface, the values of the reflection coefficients are computed within the elevation interval from 0° to 90° , for both the circular and linear coefficients. These are plotted in Figure 3-5. The constants which are used for concrete are $\varepsilon_R = 3$, $\sigma = 2 \cdot 10^{-5}$ S/m, and $\lambda = 0.19$ m, corresponding to a concrete reflector and L1/E1 signal according to ITU (2015). Nevertheless, for the L2 and L5 frequency, the values remain identical for the

reflection coefficient, as the wavelength difference to L1/E1 (i.e. 0.05 m and 0.09 m) does not impact the polarization.

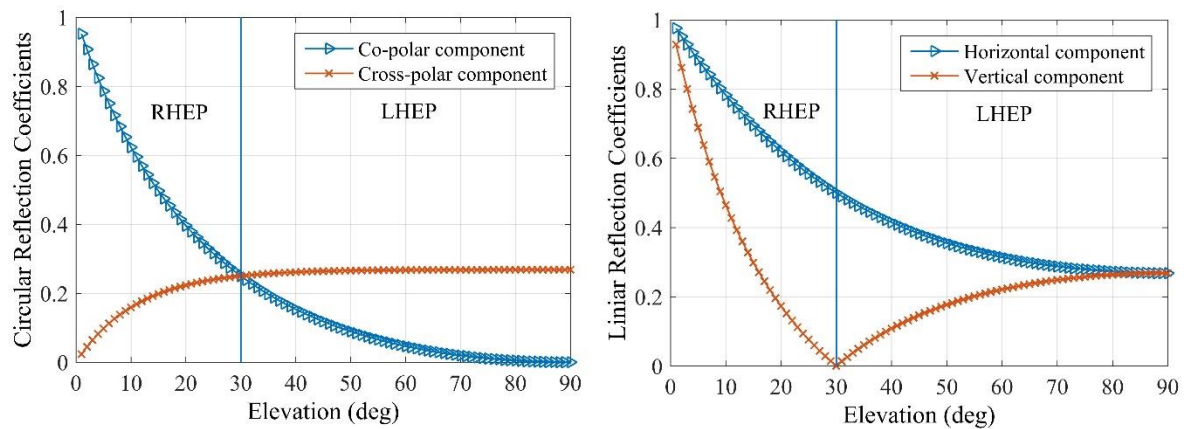


Figure 3-5: Circular (Γ_o, Γ_v) and linear reflection coefficients (Γ_h, Γ_v) for a GNSS signal within the elevation angle interval $[0^\circ, -90^\circ]$. The reflection coefficient values correspond to incoming signals that encounters a concrete reflector

At the elevation $E = 0^\circ$, the signal is RHCP, as the satellite is transmitting them. For the angles below 30° , the signal is right-hand elliptically polarized (RHEP). This can be seen in both plots of Figure 3-5, by the different magnitudes of the two components. At 30° , the polarization of the signal is changing. This is also known in literature as the Brewster angle. From 30° , the signal is left-hand elliptically polarized (LHEP) until 90° elevation, where it becomes left-hand circularly polarized (LHCP). Figure 3-6 shows the attenuation α of a GNSS signal if it receives one multipath reflection. The signal attenuation (α) over the elevation angle is computed considering the material reflection coefficients presented in Figure 3-5 on the logarithmic scale. It is to be mentioned that the attenuation values differ for other material of the reflector i.e. metal, glass, water according to the corresponding permittivity (μ_R) and dielectric constant (ϵ_R). The constant values for other materials can be extracted from tables as in ITU (2015).

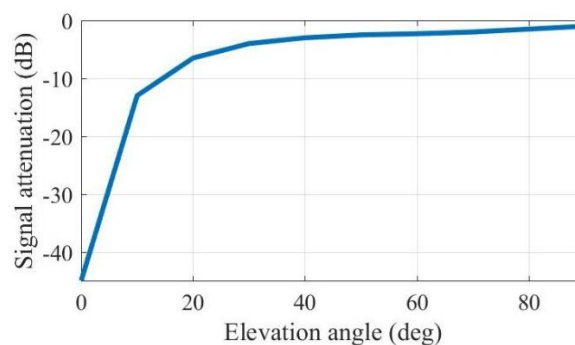


Figure 3-6: Signal attenuation (α) due to a multipath reflection over the elevation angle cf. Hannah (2003). The reflecting surface is concrete.

3.3.3 Specular and diffuse reflection

The reflection coefficients presented in the previous section are valid for the case of specular reflection. In reality, there is also the possibility that the reflector's surface is not smooth. As a consequence, the signal has diffuse components after the reflection. In Figure 3-7 it is illustrated how in the case of specular reflection, the incident angle of the signal (Ψ) is equal to the angle of the signal after the reflection. Oppositely, in the case of diffuse multipath, the incoming angle differs from the angle after the reflection.

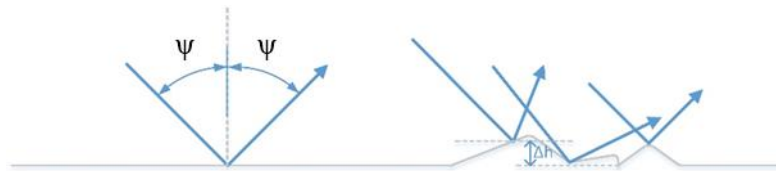


Figure 3-7: Illustration of specular reflection (left) and diffuse reflection (right) according to Zhang (2016)

In the case of diffuse reflection, the signal power is scattered in different directions. Additionally, the reflected signals have different phase shifts. For the purpose of determining if a surface produces diffuse or specular reflection, the Rayleigh criterion can be used (Kerr, 1964):

$$\Delta H \geq \frac{\lambda}{8 \sin \psi}. \quad (3-10)$$

The term ΔH in Equation (3-10) represents the height difference between two reflection points and it is used as a measure to establish whether the reflecting medium is producing a specular or diffuse reflection. This criterion is also depending on the signal wavelength (λ) and the incident angle of the incoming ray (Ψ). Figure 3-8 is the interpretation of the Rayleigh criterion for the three carrier frequencies corresponding to GPS L1 and L2, Galileo E1 and E5b. The plot indicates the little difference between the carrier frequencies and that for elevation angles bigger than 50° , reflectors that have irregularities bigger than 2 cm cause diffuse reflection.

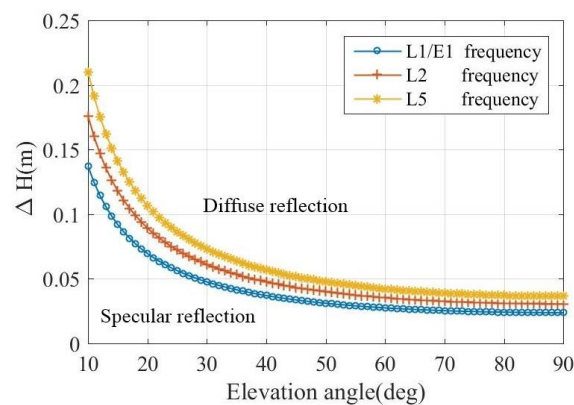


Figure 3-8: Influence of the reflector irregularities on the signal reflection type. L1/E1 and L2 carrier frequencies are considered along with the elevation interval from 0° to 90°

In the case of diffuse reflection occurrence, the reflection coefficients in Equation (3-9) must be modified by applying a magnitude reduction factor. The reflection coefficient for diffuse reflection can be computed as a function of the reflection coefficient for specular reflection Γ and the reduction factor ρ_s by using the formula (Hannah, 2003):

$$\Gamma_s = \rho_s \cdot \Gamma_0. \quad (3-11)$$

The magnitude reduction factor ρ_s is a function of the carrier phase difference ($\Delta\Phi_H$) between two reflecting signals coming from different levels. These are mathematically modeled as:

$$\rho_s = \exp\left(\frac{1}{2}\Delta\Phi_H\right), \quad (3-12)$$

$$\Delta\Phi_H = \frac{4\pi \cdot \Delta H}{\lambda} \cdot \sin \psi. \quad (3-13)$$

3.4 Signal diffraction

Prior research generally confirms that multipath is primarily produced as an effect of specular reflection. There is one more signal propagation effect that can affect the GNSS signal and produce secondary multipath effects: signal diffraction. This occurs when the LOS signal is obstructed by reflectors and a fraction of the bent signal still reaches the GNSS receiver. This is illustrated in Figure 3-9. There are two possibilities of receiving a diffracted signal: with and without the LOS component. The region where only the diffracted signal is present is known as shadow region. If a receiver is positioned in this area, the signal attenuation is pronounced since a part from the signal is blocked by the obstacle.

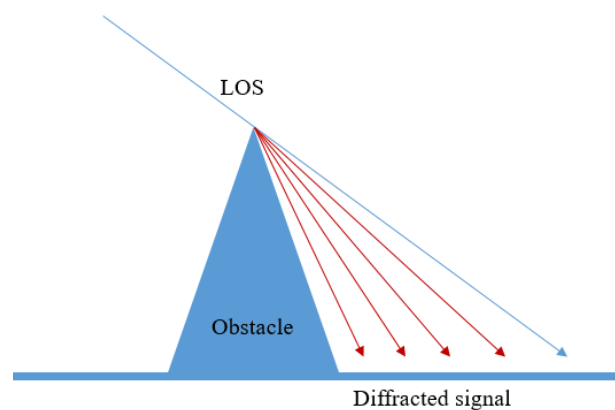


Figure 3-9: Diffraction of a GNSS signal

It is expected that the signal stops being tracked by the receiver when facing an obstacle. In reality, the LOS signal can pass despite the presence of an obstacle, as long as it is not bigger than the first Fresnel zone (see section 3.3.1). Previous studies have considered the knife-edge diffraction problem to compute the power loss of the signal strength. This approach is adopted also into this work. The formula to derive the signal strength attenuation due to diffraction is a function of the antenna and

obstruction height, distance of the antenna from obstruction and angle of incoming GNSS signal. If β is the angle between the LOS and diffracted signal, this can be computed as (ITU, 2019):

$$\beta = \tan^{-1}\left(\frac{h_a}{d_a}\right) - E, \quad (3-14)$$

where:

- h_a height difference between the receiving antenna and the obstruction,
- d_a horizontal distance to the obstruction,
- E Elevation angle of the incoming GNSS signal.

The Fresnel diffraction parameter, which determines the signal strength attenuation, can be written as:

$$v = \left(\sqrt{h_a^2 + d_a^2} \cdot \sin \beta\right) \cdot \sqrt{\frac{2}{\lambda \cdot \sqrt{h_a^2 + d_a^2}}}. \quad (3-15)$$

To determine the signal attenuation on the logarithmic scale, the following equation should be applied:

$$\alpha = 6.4 + 20 \cdot \log\left(\sqrt{v^2 + 1} + v\right). \quad (3-16)$$

Assuming that h_a and d_a from Equation (3-14) have both the value of 2 meters, the signal attenuation is computed and plotted below in Figure 3-10. The attenuation values on the decibel scale are plotted for a range of possible elevation angles of the incoming signal. The value 0 dB represents no attenuation and the value -60 dB indicates a weak signal. Most of the commercial receivers are able to track signals which are above 30 dB-Hz. It is visible from the plot below that from 45°, the signal does not experience attenuation anymore. This is known in literature as signal being in the clear.

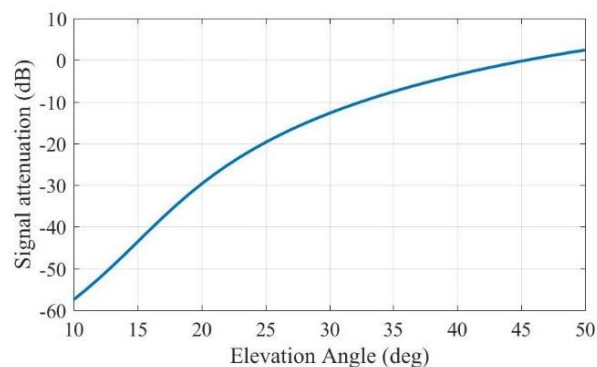


Figure 3-10: Signal attenuation (α) due to diffraction over signal elevation angle

3.5 Multipath modeling

Despite the efforts that have been done by researchers to model the multipath, several aspects regarding this topic are still open (Smyrnaioi et al. 2018). The reflections number, the satellite-receiver geometry, the multipath parameters changing nature at each epoch together with the antenna and the receiver architecture make the multipath challenging and difficult to model. Prior research has thoroughly investigated different multipath aspects, focused on different applications. By modeling the propagation of multipath signals, an assessment regarding the delay and magnitude of the multiple reflections is done. This approach is developed and used in Hannah (2001), Fontán & Espiñeira (2008) and Lehner (2007) for instance. Although the modeling techniques are different, the common objective is to determine the multipath behavior for different scenarios. Another approach used in literature is the modeling through geometrical optics (GO), that is ray-tracing. Whilst this approach is computationally expensive, it provides accurate results if the environment is known (Panicciari et al. 2017). Multipath can also be statistically modeled by the well-known Rician and Rayleigh models. Several derived models, based on measurement campaigns have been presented in Lehner (2007), Goldhirsh & Vogel (1998), Weiss (2007).

Due to the complexity of the topic, the multipath modeling topic is split into three sections within this work. For clarity, this structure is presented in Figure 3-11. The first two blocks are detailed within this chapter, whereas the last one is presented in Chapter 4. Following the phenomenon chronology, the first part examines several multipath propagation modeling approaches. Modeling the multipath propagation serves to obtain a relationship between signal reflections and carrier frequency, environment and user-satellite relative speed (Gallager, 2006). It is of high importance to reproduce multipath through propagation modeling for simulations both in software and hardware and eventually for system testing (Villaceros, 2011). According to Schnell & Fiebig (2002), the propagation models can be divided into three categories: statistical, deterministic and physical-statistical models. The multipath modeling section is followed by the multipath influence on the receiver. As numerous receiver signal processing techniques influence the incoming multipath signal and process it differently, there is a need for understanding the process. Ultimately, the focus lies on the multipath error, which affects the GNSS observables that are output of the GNSS receiver.

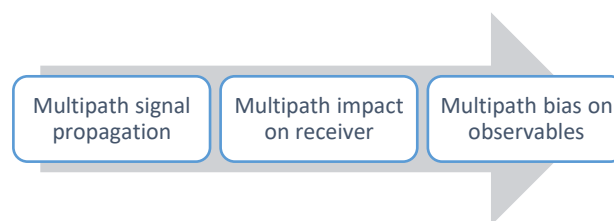


Figure 3-11: Multipath impact chain. The first two topics are detailed within Chapter 3.5 and 3.6, whereas the last one is detailed within Chapter 4

3.5.1 Statistical models

As previously mentioned, the signal propagation changes according to the environment. Therefore, statistical models have been developed to demonstrate the propagation features for a different area of interest. Some examples can be found in Fontán et al. (2001), Mella (2007) and Joseph & Braasch

(2000). Widely accepted, signal propagation channels are often categorized into narrowband and wideband. Narrowband propagation channels are used in applications where the signal bandwidth is smaller than the coherence bandwidth of the multipath fading (Proakis, 2001). Narrowband models include Rayleigh and Rice models, which are typically used for modeling land-mobile satellite channels (Lutz et al. 1991). Wideband models are used in situations when the time difference between the LOS component and the multipath reflections exceeds the signal bandwidth. This means, that the multipath delays are solvable within the signal bandwidth and the propagation channel is modeled as a tapped delay line, with time-varying coefficients (Rice et al. 2004).

Within this work, both methods are implemented to simulate multipath in static and kinematic situations. Depending on which kind of multipath signals are produced due to the environment, different modes can be used. Rice model is used for modeling a situation when both multipath and the LOS signal are present, while Rayleigh is modeling the signal characteristics when multipath is present, but the LOS is blocked i.e. non-line-of-sight (NLOS) situation.

3.5.1.1 Rice Model

Rice equation can be used to model the signal amplitude in a situation when the received signal consists of LOS and an unknown number of multipath components. Assuming that the signal strength of the multipath components are equal, the amplitude of the composite signal is described by a statistical distribution. The probability distribution function (PDF) is described by Rice fading model, as follows (Fontán & Espiñeira, 2008):

$$p_{Rice}(A_c) = \begin{cases} \frac{A_c}{\alpha^2} \exp\left(-\frac{A_c^2 + A_D^2}{2\alpha^2}\right) I_0\left(\frac{A_c A_D}{\alpha^2}\right); & A_D > 0 \text{ and } A_c \geq 0 \\ 0 & ; A_c < 0 \end{cases} \quad (3-17)$$

where:

- A_c amplitude of the composite signal,
- α multipath attenuation relative to LOS signal,
- A_D amplitude of the LOS signal,
- I_0 modified Bessel function of order zero.

Equation (3-17) reveals that the Rice distribution depends on two parameters: the direct signal amplitude and the multipath attenuation relative to LOS. Considering a multipath signal that has a constant amplitude ($\alpha = 1$) and that the amplitude of the LOS component is varying, the Rice PDF variations are plotted in Figure 3-12. This plot outlines the evolution of the Rice distribution from the situation when the LOS component is blocked and for a range of increasing values. It can be noticed that as the LOS power increases with respect to the multipath power, the distribution tends towards a Gaussian one. In literature, the Rice k-factor is often used. This represents the carrier-to-multipath ratio and is defined as:

$$k = \frac{A_D^2}{\alpha^2}; K(dB) = 10 \log k. \quad (3-18)$$

The k -factor is important, as it determines the distribution function, therefore the attenuation that the signal will experience. If $k = 0$, then the Rician distribution becomes the Rayleigh distribution. Figure 3-12 illustrates the PDF of the Rice fading model expressed by the Rice k -factor.

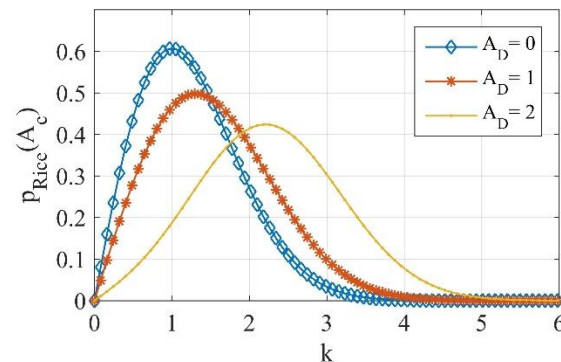


Figure 3-12: Rician cumulative distribution function (CDF) for various amplitude values

3.5.1.2 Rayleigh distribution

In a worst-case scenario, the direct link between the satellite and the user is blocked and only the multipath contributions are received. This is a typical non-line-of-sight situation (NLOS). Assuming that the multipath signals are uncorrelated, normally distributed, of equal amplitude and zero-mean distributed, their distribution can be modeled by the Rayleigh model. This distribution is known in literature as a chi distribution (χ^2) with two degrees of freedom (Fontán & Espiñeira, 2008). The sum of two quadrature Gaussian noise signals follows a Rayleigh distribution (Rappaport, 2002). The Rayleigh model is known as the special case of the Ricean function without the LOS signal and can be mathematically modeled as (Ma et al. 2001):

$$p_{\text{Rayleigh}}(A_c) = \begin{cases} \frac{A_c}{\alpha^2} \exp\left(-\frac{A_c^2}{2\alpha^2}\right); & 0 \leq A_c \leq \infty \\ 0 & ; A_c < 0 \end{cases} \quad (3-19)$$

In Equation (3-19), the term α plays the role of the scale parameter of the distribution. Assuming that the multipath signal strength increases, Figure 3-13 shows the spread of the Rayleigh function. This indicates that the more powerful the multipath component is, the wider is the resulting amplitude spread.

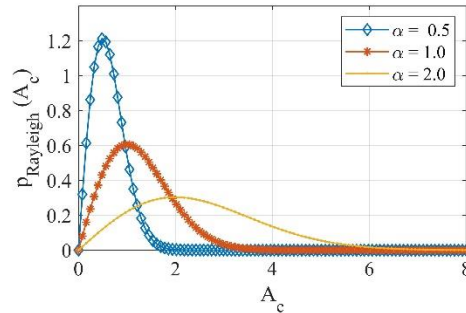


Figure 3-13: Rayleigh distribution function for various multipath amplitudes

3.5.2 Deterministic models

In the case of deterministic modeling of the propagation channel, input knowledge about the environment is required. To make accurate assumptions, information about the geometrical and electrical properties of the environment have to be known. However, this is computationally expensive and environment simplifications are often made, at the cost of results accuracy. The output is specific to particular locations, in contrast to the statistical models where it is rather an average characterizing value. There are two categories of deterministic models: exact and asymptotic (Villacieros, 2011). The asymptotic methods are used to model the satellite receiver link and are therefore the focus in this work.

Asymptotic models include physical optics (PO), geometrical optics (GO), geometrical theory of diffraction (GTD) and uniform theory of diffraction (UTD). PO methods are used to analyze large scattering surfaces by performing a high-frequency approximation. The GO is a ray-based method, which considers the existence of LOS, reflected and refracted waves. GTD is an extension of the GO method proposed by Keller (1962), which additionally postulates the existence of diffracted rays. Although is more accurate than GO, the GTD approach has the drawback of failing in the shadowing boundary, since it is purely based on ray optical theory. Nevertheless, by using the UTD method, the shadowing problem is solved. The UTD, also named the 'uniform version of GTD' uses the local nature of the ray diffraction to determine diffraction coefficients (Chen et al. 2009). Within the next sections, three multipath modeling deterministic models, which are relevant for this work are detailed. They are presented in the order of their complexity, starting with the most basic one.

3.5.2.1 Ground reflection

In a satellite navigation system, a single and direct link between the satellite and the user, as expressed by Equation (3-2) is seldom the only propagation path. Ground multipath originates from a reflection off the ground, with a relative delay and a phase shift with respect to the LOS signal. The relative phase of the reflected signal varies differently if the user moves (Schneckenburger et al. 2017). Figure 3-14 illustrates the ground reflection multipath, where A is the receiving antenna, h is its height, d represents the horizontal distance from antenna to the reflecting point and E is the satellite elevation angle. According to Irsigler (2008), for this kind of multipath, the following rules apply:

- a) As a consequence of the reflection law, the angle of incidence equals the angle of reflection;
- b) As a result of the satellite movement, the distance d changes and can be expressed as a function of the satellite elevation (E), as expressed in Equation (3-20).

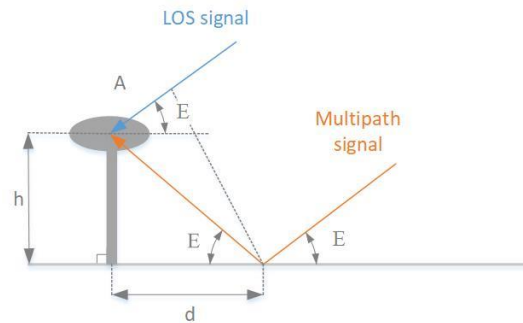


Figure 3-14: Ground reflection geometry

$$d = \frac{h}{\tan E(t)}. \quad (3-20)$$

The significance of term d consists in the fact that it influences the frequency of multipath variations. These are directly proportional to the distance from the antenna to the reflector as it was shown in Irsigler (2008). This implies that the multipath variations are a function of the satellite elevation. An additional influence on multipath behavior is the user state: static or dynamic. Prior research confirms that theoretically, the maximum multipath fading frequency of a static user reaches the value of 0.5 Hz. However, depending on the geometry, for a user velocity of 15 m/s the fading frequency can reach 180 Hz according to van Nee (1992).

Based on the assumptions above, the additional path traveled by the multipath ray, due to the time delay (τ_i in Equation (3-3)) with respect to LOS and the relative phase delay (Φ_i in Equation (3-3)) can be computed as follows (Zhang, 2016):

$$\Delta\rho_i(t) = 2h \sin E(t), \quad (3-21)$$

$$\Delta\phi_i(t) = \frac{2\pi}{\lambda} \cdot \Delta\rho_i(t) = \frac{4\pi h \sin E(t)}{\lambda}, \quad (3-22)$$

where:

- $\Delta\rho_i$ reflection additional path with respect to LOS (m); $\Delta\rho_i = \rho_i - \rho_{LOS} = c \cdot \tau_i$,
- h height of the receiving antenna (m),
- E elevation of the satellite (deg),
- $\Delta\phi_i$ the phase shift of the reflected signal with respect to LOS signal (deg),
- λ the wavelength of the signal (m).

Equation (3-21) shows that the additional path travelled by a multipath reflection is a function of the satellite elevation angle and the antenna height. Assuming different heights of the receiving antenna, the left plot in Figure 3-15 reveals the increasing pattern of the path delay as a function of the satellite elevation angle. Regardless of the chosen wavelengths, the pattern of the graph remains the same. Consequently, it is visible from Figure 3-15 that the error trend is the same. This shows that multipath reflections influence with different delays, but with the same pattern.

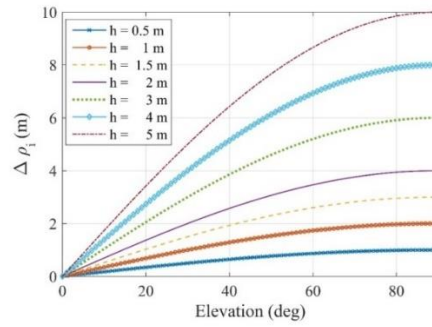


Figure 3-15: Ground reflection additional path relative to LOS

3.5.2.2 Arbitrary reflection

Besides reflections from the ground, incoming signals might be reflected from obstructions in the vicinity of the antenna. This situation is illustrated in Figure 3-16. Assuming that the receiving antenna is the center of the local coordinate system, the errors induced by the reflected signal are a function of the satellite position (Irsigler, 2008). Considering Figure 3-16, the components of the multipath additional paths are shown by l_1 and l_2 , the elevation of the satellite is represented by E and the horizontal distance to the reflecting point by d_H .

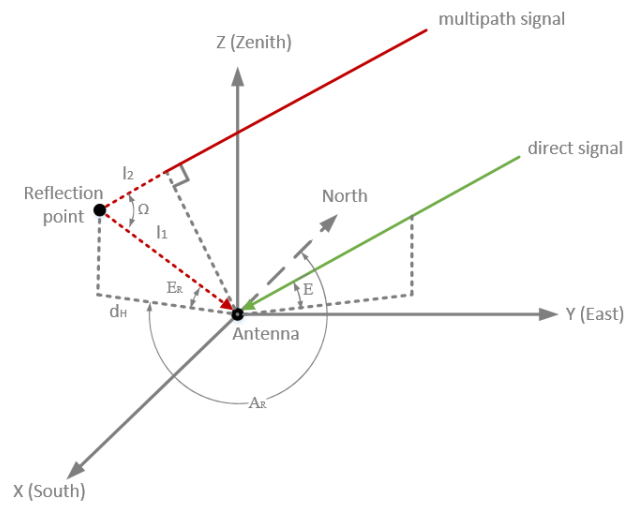


Figure 3-16: Geometric conditions for a signal reflection from an arbitrary reflection point cf. Zhang (2016)

Considering the geometrical arrangement illustrated in Figure 3-16, the delay due to multipath consists of two segments l_1 and l_2 . If l_1 represents the distance to the reflecting point, the extra path travelled by a reflected signal can be expressed as:

$$\Delta\rho(t) = l_1 + l_2 \cdot \cos \Omega, \quad (3-23)$$

$$l_2 = l_1 \cdot \cos \Omega. \quad (3-24)$$

The angle Ω can be computed as the dot product between the vector determined by the direction of the incoming signal and the vector determined by the reflected signal direction. In this way, the phase shift of the reflected signal can be mathematically modeled as follows (Zhang, 2016):

$$\Delta\phi(t) = \frac{2\pi}{\lambda} \cdot l_1(t) \cdot (1 - \cos E(t) \cdot \cos E_R(t) \cdot \cos(A(t) - A_r(t)) - \sin E(t) \cdot \sin E_R(t)), \quad (3-25)$$

where:

- λ wavelength of the GNSS signal (m),
- E elevation of the satellite (deg),
- A azimuth of the satellite (deg),
- E_R elevation of the reflected signal (deg),
- A_r azimuth of the reflected signal (deg),
- l_1 distance from the antenna to the reflection point (m).

3.5.2.3 Ray-tracing

Ray-tracing techniques are known in literature to realistically model multipath, considering all the complex changes of the GNSS signals in both time and frequency domain. Compared to the previously presented deterministic models, ray-tracing has the advantage of being very precise within the simulation environment (Schmitz et al. 2009). Nevertheless, accuracy is obtained at the cost of long computational time. Prior studies investigate methods to reduce it and maintain precision. Most of the deterministic algorithms that predict the signal strength, phase and delay, are based on the computation of the wave's reflection, diffraction and scattering. In 1980, successful computation based on Geometrical Optics (GO) algorithms was presented in Whitted (1980). Later, in Ikegami et al. (1991) the ray-tracing algorithms for signal loss due to multipath propagation are extended for urban areas. Within this work, the theoretical predictions show a good agreement with the measured values. Further improvements on ray-tracing methods through Geometrical Theory of Diffraction (GTD) and Uniform Theory of Diffraction (UTD) are presented in Schaubach et al. (1992), Seong-Cheol et al. (1999), Schmitz (2012) and von Hünerbein & Moura (2014). The GO ray-tracing algorithms are based on Fermat's principle. The mathematical formulation can be found in Farkas & Kály-Kullai (2007). The basic postulates of GO are according to Jenn (2000):

- a) the waves are transverse electromagnetic modes (TEM),
- b) rays travel in straight lines in a homogenous medium,
- c) polarization is constant along a ray in an isotropic medium,
- d) power in a 'bundle of rays' is conserved,
- e) reflection and refraction obey Fermat's principle,
- f) the reflected field is related to the reflection point field through the reflection coefficient described in Chapter 3.3.2.

Since this principle postulates only the existence of direct and reflected rays, an enhancement has been achieved by adding the Geometrical Theory of Diffraction, i.e. signal propagating in the geometrical shadow regions of an obstacle. According to this model, edges form the strongest fields, while corners develop discontinuities. Assuming a random point P , where a signal reflection occurs,

the total field of the signal at Q , $\vec{E}_T(Q)$ can be decomposed into GO and GTD components, as follows (Pathak et al. 2013):

$$\vec{E}_T(Q) = \vec{E}_r(Q) + \vec{E}_d(Q), \quad (3-26)$$

where:

$\vec{E}_r(Q)$ field of the signal due to reflection at reflection point Q ,

$\vec{E}_d(Q)$ field of the signal due to diffraction at reflection point Q .

The field of a direct signal, also known as ray, has the following expression:

$$\vec{E}_i(P) = \vec{E}_i(O) \cdot \sqrt{\frac{\rho_1^i \cdot \rho_2^i}{(\rho_1^i + s^i) \cdot (\rho_2^i + s^i)}} \cdot e^{j\lambda s^i}, \quad (3-27)$$

where:

$\vec{E}_i(O)$ incident field of the signal at the transmitting point,

ρ_j^i principal radius of curvature of the signal's wave front,

s^i length of the direct signal from transmitter to receiving antenna,

λ wavelength of the signal.

Assuming that the signal is reflected by a surface in the point Q , the reflected field $\vec{E}_r(Q)$ can be computed with the equation:

$$\vec{E}_r(Q) = \vec{E}_i(Q) \cdot \bar{\Gamma} \sqrt{\frac{\rho_1^r \cdot \rho_2^r}{(\rho_1^r + s^r) \cdot (\rho_2^r + s^r)}} \cdot e^{j\lambda s^r}, \quad (3-28)$$

where:

$\vec{E}_i(Q)$ incident field of the signal at the reflecting point,

$\bar{\Gamma}$ the reflection coefficient of the surface,

s^i length of the reflected signal from reflection point Q to receiving antenna.

The reflection coefficients for the vertical and horizontal components of the signal are computed based on the theory presented in 3.3.2.

In order to model the diffraction, both regions presented in 3.4 must be taken into consideration: the shadowed and LOS areas. The UTD has the following expression to compute the diffracted field $\vec{E}_d(P)$:

$$\vec{E}_d(P) = \vec{E}_i(Q_E) \cdot \bar{D}_E \sqrt{\frac{\rho_d}{s^d \cdot (\rho_d + s^d)}} \cdot e^{j\lambda s^d}, \quad (3-29)$$

where:

$\vec{E}_i(Q_E)$	incident field of the signal at the diffraction point,
$\overline{D_E}$	the diffraction coefficient of the edge,
ρ_d	wave front radius of the signal's diffracted components,
s^d	signal length from the diffraction edge to the receiving antenna.

The practical implementation of the GO and UTD algorithms imply computational speed. An approach which is nowadays used to decrease the computational load is shown in Figure 3-17. The 3D environment can be simplified by considering the surfaces as 2D triangular grids. According to the receiving antenna position in the 3D model and the position of the satellites, the fields of the signals are computed when intersecting with the surfaces delimited by orange lines. The figure illustrates a screenshot taken from a ray-tracing software, namely Sim3D (Spirent Communications, 2019).

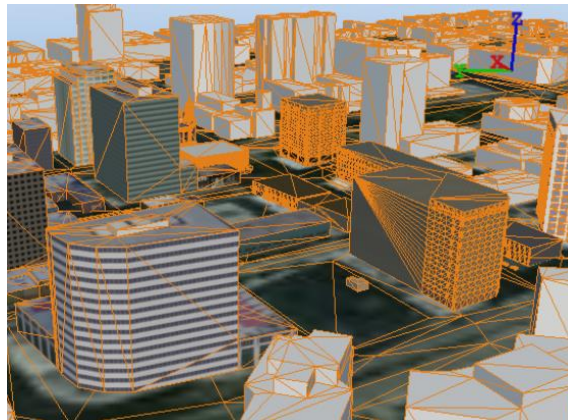


Figure 3-17: 3D model with obstacles modeled as polygons for ray-tracing computation

3.5.3 Hybrid model

As already mentioned, there are either statistical or deterministic methods to model the propagation of multipath signals. However, according to the state of the art, no model can deal with errors due to multipath regardless of the environment. The statistical models are based on statistical distributions from measured data. These are straightforward to use, but not precise. Deterministic models, on the other hand, are precise, yet requiring computational power and environment input data for ray-tracing algorithms (Avram et al. 2018). To lower the computational requirements of a deterministic model and to improve the accuracy of a statistic one, the physical-statistical (i.e. hybrid) approach can be used. Several models of this kind were proposed in Tzaras et al. (1998), Oestges et al. (1999) and Oestges & Vanhoenacker-Janvier (2001), considering different input parameters. A random environment where this model can be applied is presented in Figure 3-18. Considering the illustrated geometry, the hybrid model is implemented within this work, by applying the following steps:

- a) Considering the size of the buildings, the relative position of the receiving antenna and the satellite position, the following can be established by means of ray-tracing computation: the receiving antenna receives either the direct signal, the direct signal and multipath reflections or no direct signal and multipath directions;
- b) According to the computation in the previous step, multipath components can be modeled by the statistical methods presented in 3.5.1.

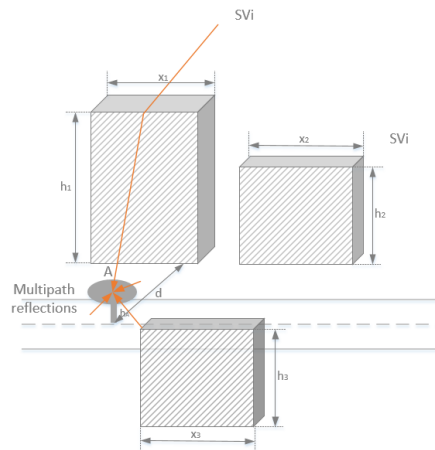


Figure 3-18: Example of environment for multipath computation with the hybrid model

The satellite SV_i in Figure 3-18 experiences multipath from the facades of the buildings around the antenna. Assuming that the buildings have the same surfaces, therefore same reflection coefficients, the signal attenuation due to reflections is equal. Consequently, the multipath for this specific satellite can be modeled by Rayleigh, as expressed by equation (3-19) if the direct signal is blocked. If the LOS signal is present, then the signal multipath amplitude can be modeled by the Rician model.

3.6 Receiver sensitivity to multipath

Receivers provide position, velocity and time information, based on incoming GNSS signals and they represent the user segment. The components of a generic receiver consist of a radio frequency (RF) component, digital signal processing and navigation data processing (Weiss, 2007), as illustrated in Figure 3-19. The RF component receives the GNSS spread spectrum signals employing right hand circularly polarized (RHCP) antennas because the GNSS signals are RHCP as well (Ray, 2000). In the case of an active antenna, the additional use of a Low Noise Amplifier (LNA) is required. This has the role of reducing the noise from the RF down-conversion and compensates for the cable loss (van Dierendonck, 1996). After the down-conversion and sampling of the signal, this goes further into the next block. At this point, the GNSS signal consists of a mixture of all the visible satellites.

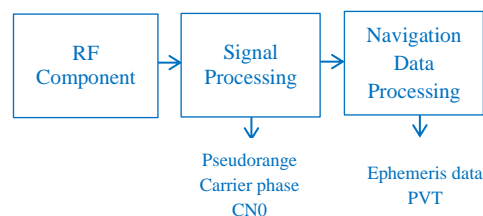


Figure 3-19: Architecture of a generic GNSS receiver

The digital signal processing block represents the core of a GNSS receiver. It performs several functions in real-time, using the input signal from the first block in Figure 3-19. Signal tracking loops are incorporated in the signal processing block, which provides the pseudorange and carrier phase measurements. To achieve this, the signal must be correlated and tracked. The hardware responsible for this function is called a channel (Principe & Bacci, 2011). A modern receiver contains many

channels that can be operated in parallel, independent on each other. Each channel contains code and carrier tracking loops together with their hardware and software. Pseudoranges and carrier phase measurements are the outcome of the Delay Lock Loop (DLL), respectively Phase Lock Loop (PLL). The navigation data processing block has the function of data extraction and position, velocity, time (PVT) computation.

3.6.1 Receiver signal tracking

After obtaining the coarse code delay and carrier Doppler in the acquisition phase, the next step is the signal tracking. Within this process, the fine estimates of signal parameters are obtained. These are obtained by means of the receiver code and phase tracking loops. The Delay-Locked Loop (DLL) and Phase-Locked Loop (PLL) block diagrams with descriptions can be found in the literature: Spilker (1980) and Dafesh et al. (1998). For the further understanding of the receiver mechanisms, a simplified scheme of the tracking loop is presented in Figure 3-20. Each receiver channel has a tracking loop that works independently. According to Weiss (2007), depending on their code discriminator type, the code tracking loops can be split into coherent DLL and non-coherent DLL. Considering the phase tracking, the most popular is the Costas tracking loop.

Figure 3-20 illustrates the signal processing required to obtain the pseudoranges and carrier phase measurements. The first step after the A/D conversion of the GNSS signal at an intermediate frequency is multiplication. The receiver's Numerically Controlled Oscillator (NCO) generates in-phase (I signal samples), which are 0° phase shifted and quadra-phase (Q signal samples), which are 90° phase shifted. To match the incoming phase of the signal, the NCO is permanently adjusted in real-time. The I and Q samples are mixed with the incoming signal to produce the I and Q channels. The next step is the correlation. Most of the receivers generate three signal replicas at constant chip offset resulting in early (E), prompt (P) and late (L) copies of the signal. These are correlated with the incoming signal on both I and Q channels.

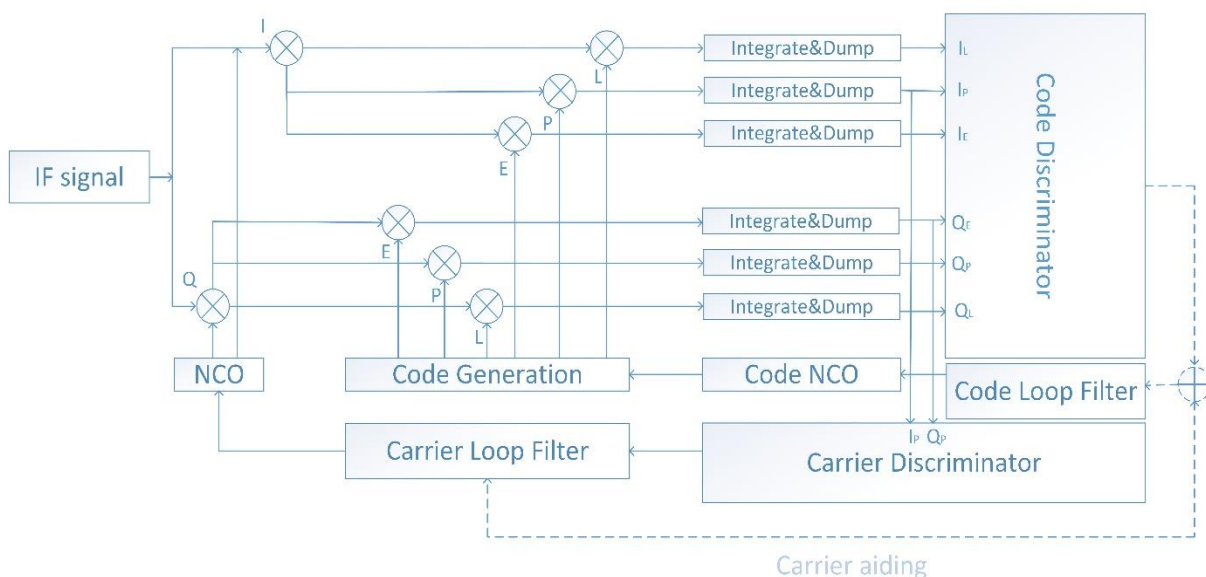


Figure 3-20: Receiver tracking loops architecture after Pany (2010)

The result of the accumulation during the integration time leads to the values: I_E , I_P , I_L , Q_E , Q_P , and Q_P . These are used by the code and phase discriminators to compute the signal error and then fed into the loop filters. After being filtered, the result is communicated through a transfer function to the NCO, to adjust itself to maintain track of the signal (Pany, 2010).

3.6.1.1 Tracking loops

Depending on the signal parameter that is being tracked, the loops are split into: code, phase, and frequency. Considering the purpose of this work, the first two type of loops are presented further. The code loop i.e. DLL is tracking the code phase τ , while the phase loop i.e. PLL is tracking the signal carrier phase ϕ . Assuming a linear model of the tracking loop, the output of $\delta\theta$ can be expressed as (Teunissen & Montenbruck et al. 2017):

$$\delta\theta = \theta(s) - \hat{\theta}(s), \quad (3-30)$$

where:

- $\delta\theta$ linear equivalent of discriminator output also known as signal tracking error,
- $\theta(s)$ input for the tracking loop,
- $\hat{\theta}(s)$ output from the NCO.

The term computed in Equation (3-30) can express either the code or the carrier tracking error estimate, depending on the tracking loop type. As seen Figure 3-20, the output of both loops represents the input for their filter. The loop filter transfer function is defined as:

$$F(s) = \frac{\theta(s)}{\delta\theta(s)}, \quad (3-31)$$

where:

- $\theta(s)$ Laplace transform of the input $\theta(s)$,
- $\delta\theta(s)$ Laplace transform of output $\delta\theta$.

The loop filters estimation is processed further by the NCO. Assuming unity gain for the NCO and considering that $H(s)$ stands for the overall tracking loop transfer function, its mathematical representation is:

$$H(s) = \frac{\hat{\theta}(s)}{\theta(s)} = \frac{N(s) \cdot F(s)}{1 + N(s) \cdot F(s)} = \frac{F(s)}{s + F(s)}, \quad (3-32)$$

where:

- $\hat{\theta}(s)$ NCO integrator output,
- $N(s)$ NCO transfer function; $N(s) = 1/s$.

Considering that $H_e(s)$ is the transfer function error and $\varepsilon(s)$ its error function, the steady state error $\varepsilon(s = 0)$ can be computed by applying the Laplace transform. The mathematical formulation of the three tracking loop parameters can be expressed as follows:

$$H_e(s) = 1 - H(s), \quad (3-33)$$

$$\varepsilon(s) = H_e(s) \cdot U(s), \quad (3-34)$$

$$\varepsilon(s = 0) = \frac{d^n G}{\omega_0^n}, \quad (3-35)$$

where:

- $U(s)$ the input signal,
- n filter loop order,
- $\frac{d^n G}{dt^n}$ maximum line of sight dynamics,
- ω_0 loop filter natural radian angular frequency.

Since the steady state error depends on the loop filter order, the type of the tracking loop error depends of the loop filter order. The types of loop filter are discussed in more detail in 3.6.1.4.

3.6.1.2 Correlators

The integration between the incoming signal and the receiver generated replica is done within the correlation process. The integration time can vary depending on the hardware and software resources of the receiver. The accumulation of many integration values for various consecutive signal samples results in an increase of integration time even in the presence of limited hardware resources. Long integration time determine an increased bandwidth of the pre-detection process. On the one hand, this leads to increased sensitivity in tracking a signal which is weak or interfered. On the other hand, the robustness of tracking a signal in dynamic conditions is decreased for long integration time.

The position of the correlators with respect to the signal true values in the code and phase domain are shifted with an amount noted with $\delta\tau$ and δf_d . The values that the correlators are shifted with vary between 0.1 and 1 chip. Considering I the in-phase component of a processed signal and Q the quadrature component, the correlators B can be modeled as a function of the signal parameters (Teunissen & Montenbruck et al. 2017):

$$B = h(D, d, A, \delta\tau, \delta f_d, \delta\phi) + \eta, \quad (3-36)$$

$$\text{with } h = \begin{bmatrix} A \cdot D \cdot R \cdot \left(\delta\tau \pm \frac{d}{2} \cdot \text{sinc}(\delta f_d \cdot T) \cdot \cos\delta\phi \right) \\ A \cdot D \cdot R \cdot \left(\delta\tau \pm \frac{d}{2} \cdot \text{sinc}(\delta f_d \cdot T) \cdot \sin\delta\phi \right) \\ A \cdot D \cdot R \cdot \delta\tau \cdot \text{sinc}(\delta f_d \cdot T) \cdot \cos\delta\phi \\ A \cdot D \cdot R \cdot \delta\tau \cdot \text{sinc}(\delta f_d \cdot T) \cdot \sin\delta\phi \end{bmatrix}, \quad (3-37)$$

where:

B	early, late and prompt correlators, $B = [I_E, Q_E, I_L, Q_L, I_P, Q_P]$,
D	navigation data,
d	correlator spacing,
A	signal amplitude,
$\delta\tau, \delta f_d, \delta\phi$	shifted code, Doppler and carrier frequencies,
T	integration time,
η	correlator noise, $\eta = [I_E, Q_E, I_L, Q_L, I_P, Q_P]$.

Depending on the signal modulation and receiver architecture, an additional number of correlators can be used and the correlator offset can vary. In Figure 3-21 various correlation phases are shown. In (a) and (b) the early correlation at 1/2 and 1/4 chip offset is shown, whereas in (b) and (c) the same distancing is illustrated but the late receiver generated replicas.

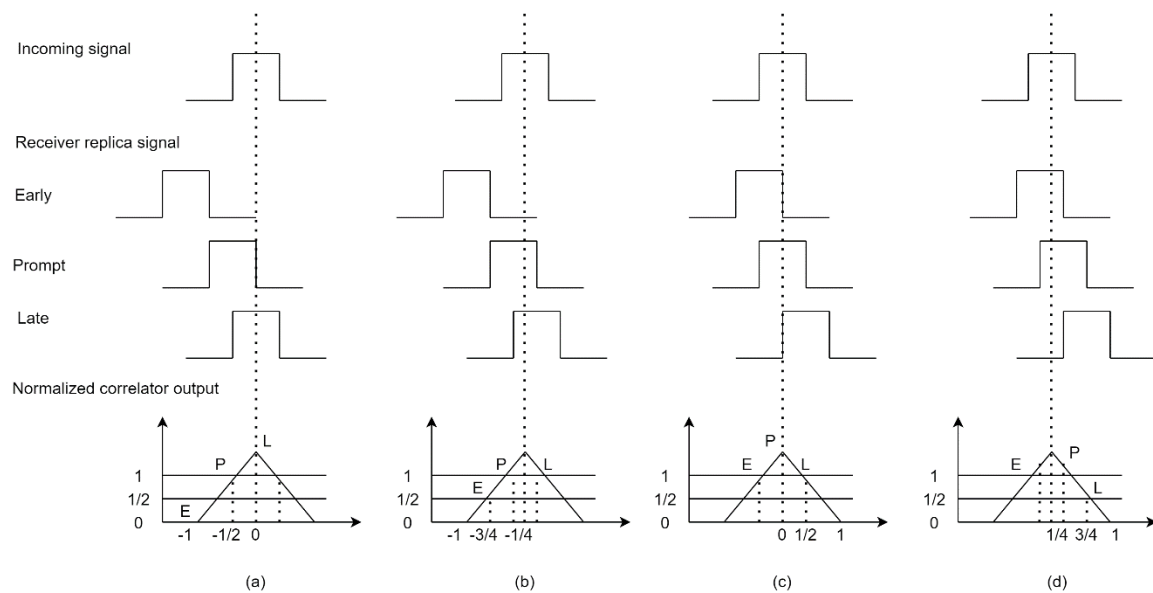


Figure 3-21: Code correlation with different correlator distancing after Kaplan & Hegarty (2006)

The output of the correlators computed as shown in Equation (3-36) represents the input for the next processing step – discriminator.

3.6.1.3 Discriminators

The role of the discriminators is to determine the error for the signal code and carrier phase from the early, prompt and late I and Q correlators output. The output of the discriminator is known in literature as the S-curve and it represents the amount of error in the receiver generated replica with respect to the incoming signal. Discriminator types determine the kind of tracking loop (i.e. PLL, DLL) and the characteristics of the receiver (i.e. robustness to dynamics/multipath, amplitude sensitivity, etc.).

PLL

The PLL is the phase tracking loop of a receiver. PLL can be split into two categories: pure PLL and Costas PLL. The main difference between the two types is that the pure PLL is sensitive to the navigation bits from the modulated signal, while the Costas PLL is insensitive. Another advantage of the Costas PLL is that it is accurate, but it has the drawback of being sensitive to dynamic stress. The mathematical formulation of two PLL discriminators are described as (Kaplan & Hegarty, 2006):

$$\delta\phi = \tan^{-1} \frac{Q}{I}, \quad (3-38)$$

$$\sin \delta\phi = \frac{Q}{A \cdot \sqrt{I^2 + Q^2}}. \quad (3-39)$$

The discriminator in Equation (3-39) is known as the four-quadrant arctangent. It is optimal for both high and low SNR (signal to noise ratio) but it implies computational burden. The second discriminator presented in (3-39) is computationally not expensive, but still provides the advantages of the four-quadrant arctangent. Two common Costas discriminators are expressed as follows (Kaplan & Hegarty, 2006):

$$\sin 2\delta\phi = Q \times I, \quad (3-40)$$

$$\sin \delta\phi = Q \times \text{sign}(I). \quad (3-41)$$

Equation (3-40) represents the classic Costas discriminator. It has the characteristics of being near optimal at low SNR at the cost of moderate computational burden. The discriminator in Equation (3-41) is the Costas discriminator with the least computational burden and the slope is proportional to the signal amplitude.

DLL

The delay-locked loop (DLL) is the tracking loop which estimates the code error ($\delta\tau$) between the incoming signal and receiver replica. The basic functionality resembles the PLL, except that the DLL has a triangular shape of the correlation function which has no different peak when no code errors exist. There are two important characteristics of a receiver: the code loop thermal noise and the maximum LOS dynamics. These are determined by the predetection integrators, discriminator of the code tracking loop and the code loop filter. The most common code tracking loop discriminator is known as normalized early-power minus late-power and can be expressed as (Teunissen & Montenbruck et al. 2017):

$$\delta\tau = \frac{I_E^2 + Q_E^2 - I_L^2 - Q_L^2}{I_P^2 + Q_P^2}. \quad (3-42)$$

The discriminator expressed in Equation (3-42) is first-order linearly proportional with the code tracking error. Considering the correlator distancing shown in Figure 3-21, the discriminator output is illustrated below in Figure 3-22. The discriminator output is also known as the S-Curve and it indicates the errors of the generated replica alignment. If the incoming signal is perfectly aligned with the generated replica, the output error is zero as also shown in the figure below.

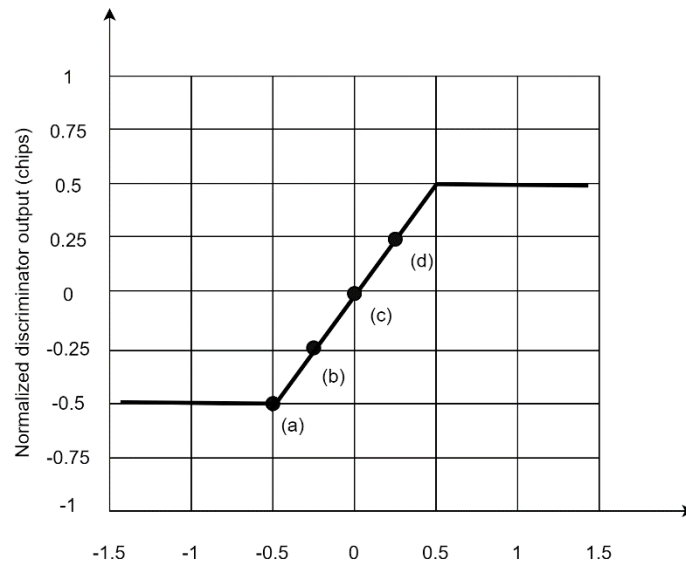


Figure 3-22: Code discriminator with respect to receiver generated replica at different offsets after Kaplan & Hegarty (2006)

Further discriminators which are used for receiver architectures are presented below (Kaplan & Hegarty, 2006):

$$\delta\tau = \frac{1}{2} \cdot [(I_E - I_L) \cdot I_P + (Q_E - Q_L) \cdot Q_P], \quad (3-43)$$

$$\delta\tau = \frac{1}{2} \cdot (I_E - I_L). \quad (3-44)$$

Equation (3-43) represents the quasi-coherent dot product discriminator. It is characterized by the employment of all three correlators and a low computational burden. Considering a 1-chip $E - L$ correlator spacing and no noise, this discriminator outputs the true error of the code misalignment. The discriminator expressed in Equation (3-44) is a coherent dot product. This has also the advantage of low computational burden and accurate output, but it can be used only when the carrier phase of the signal is in lock.

Both discriminators (PLL and DLL) output is provided further to the numerically controlled oscillator (NCO) which controls the carrier and code generators. However, the discriminator output contains noise that needs to be suppressed before the feedback is sent to the NCO. Therefore, the next step is that the discriminators output is provided to the loop filters.

3.6.1.4 Loop filters

The scope of loop filters is to minimize the noise from the discriminators output. In this way, the feedback to the NCO is more accurate and the receiver tracking error is minimized. The choice of filter order and noise bandwidth determines the filter's response to signal dynamics. Assuming that x is the state vector and y is the output, the implementation of a loop filter in a receiver is given by the following equations (Teunissen & Montenbruck et al. 2017):

$$x_{k+1} = \mathbf{F} \cdot x_k + \mathbf{L} \cdot \delta\phi_k, \quad (3-45)$$

$$y_k = \mathbf{C} \cdot x_k + \mathbf{D} \cdot \delta\phi_k, \quad (3-46)$$

where:

F	transition matrix,
L	gain filter matrix,
$\delta\phi$	discriminator output (either code or phase),
C, D	matrices to obtain the system output from the system state and input.

Depending of the receiver type, loop filters can have different orders. Their details are presented in Table 3-1. To be noticed that the filter natural radian frequency ω_0 is computed based on the value of the filter noise bandwidth which is selected when the design of the receiver is defined. The choice of the filter order is made relating to the application. For example, if a receiver is exposed to high accelerations, the third order loop can be an option. The minimization of the jerk stress succeeds by choosing a wider noise bandwidth B_n . However, it should be considered that regardless the design of the receiver, the loop filter becomes unstable when the product $B_n \cdot T$ is not below unity as shown in (Kaplan & Hegarty, 2006).

Table 3-1: Loop filter characteristics after (Teunissen & Montenbruck et al. 2017)

	First order	Second order	Third order
Loop filter transfer function	$F(s) = \omega_0$	$F(s) = \frac{a_2 \cdot \omega_0 \cdot s + \omega_0^2}{s}$	$F(s) = \frac{b_3 \cdot \omega_0 \cdot s^2 + a_3 \cdot \omega_0^2 + \omega_0^3}{s}$
$F(s)$ implementation		$x = [\dot{\theta}]$ $F = [1]$ $L = [T \cdot \omega_0^2]$ $C = [1]$ $D = [a_2 \cdot \omega_0]$	$x = [\dot{\theta} \ \ddot{\theta}]^T$ $F = \begin{bmatrix} 1 & T \\ 0 & 1 \end{bmatrix}$ $L = [T \cdot a_3 \cdot \omega_0^2 \quad T \cdot \omega_0^3]^T$ $C = [1 \quad 0]$ $D = [b_3 \cdot \omega_0]$
Loop noise bandwidth	$B_n = \frac{\omega_0}{4}$	$B_n = \frac{\omega_0}{1.89}$	$B_n = \frac{\omega_0}{1.2}$
Filter coefficients	1	$a_2 = \sqrt{2}$	$a_3 = 1.1, \quad a_2 = 2.4$
Steady-state error	$\frac{dR/dt}{\omega_0}$	$\frac{d^2R/dt^2}{\omega_0^2}$	$\frac{d^3R/dt^3}{\omega_0^3}$
Loop filter characteristics	Sensitive to velocity stress	Sensitive to acceleration stress	Sensitive to jerk stress

3.6.1.5 Tracking loop measurement errors

Thermal noise

The PLL thermal noise is considered the main error source in the phase tracking loop since the other errors are often negligible. The same is valid for a DLL tracking loop, as in the absence of multipath, thermal noise is also a dominant error source. Considering an arctangent PLL and a noncoherent DLL discriminator, the mathematical expression for the thermal noise is as follows (Kaplan & Hegarty, 2006):

$$\sigma_{PLLt} = \frac{\lambda_{f_1}}{2\pi} \cdot \sqrt{\frac{B_n}{C/N_0} \cdot \left(1 + \frac{1}{2 \cdot T \cdot C/N_0}\right)}, \quad (3-47)$$

$$\sigma_{PLLt} = \frac{1}{T_c} \cdot \sqrt{\frac{B_n \cdot \int_{-B_{fe}/2}^{B_{fe}/2} S_s(f) \sin^2(\pi \cdot f \cdot D \cdot T_c) df}{(2\pi)^2 \cdot \frac{C}{N_0} \cdot \left(\int_{-B_{fe}/2}^{B_{fe}/2} S_s(f) \sin^2(\pi \cdot f \cdot D \cdot T_c) df\right)^2}}. \quad (3-48)$$

$$\sqrt{1 + \frac{B_n \cdot \int_{-B_{fe}/2}^{B_{fe}/2} S_s(f) \cos^2(\pi \cdot f \cdot D \cdot T_c) df}{T \cdot C/N_0 \cdot \left(\int_{-B_{fe}/2}^{B_{fe}/2} S_s(f) \cos^2(\pi \cdot f \cdot D \cdot T_c) df\right)^2}}$$

where:

λ_{f_1}	wavelength of the signal frequency f_1 ,
C/N_0	carrier-to-noise ratio,
$S_s(f)$	power spectral density of the signal normalized over infinite bandwidth,
B_{fe}	double-sided receiver front-end bandwidth,
T_c	chip period, $T_c = 1/R_c$, where R_c is the chipping rate,
D	refers to correlator spacing of the receiver.

It is visible from Equation (3-7) that the carrier thermal noise standard deviation is dependent on the carrier-to-noise ratio C/N_0 , the noise bandwidth B_n and the integration time T . The C/N_0 is an important performance measurement for GNSS receivers since the stronger the recovered signal is, the noise amount decreases. This leads also to a decrease of the thermal noise error. Another method to decrease σ_{PLLt} is to decrease the noise bandwidth. Lastly, the decrease of the integration time reduces the squaring, and this also leads to a decrease of σ_{PLLt} . However, this comes at the cost of receiver incapability to accommodate higher signal dynamics.

The thermal noise error of a DLL is affected by various parameters as shown in Equation (3-48). The power spectral density is the Fourier transform of the second derivative of the correlation function expressed in 3.6.1.2 as shown in Teunissen & Montenbruck et al. (2017). Although GPS signals which have a BPSK modulation occupy the same bandwidth as BOC modulated signals, the latter have a higher power at the spectrum edge. For this reason, the correlation peaks are sharper for BOC

modulated signals compared to BPSK and therefore the tracking accuracy is increased. This leads to less noise when tracking the code in a DLL.

Transient errors

An additional type of error that influences both kind of loops is the transient error (p_T). This error reveals the inability of the loop to accommodate to the user dynamics. The mathematical formulation for a transient error corresponding to a first order DLL is a function of the loop bandwidth (B_{DLL}) and the user range jump (Teunissen & Montenbruck et al. 2017):

$$p_T = e^{-4B_{DLL}t}, \quad (3-49)$$

Transient errors for both PLL and DLL are dependent on the user motion, therefore they are time correlated and independent on the measurement rate. These are present for all orders of loop filter and the design of the receiver is a trade-off between thermal noise and transient errors as stated in Teunissen & Montenbruck et al. (2017).

Carrier cycle slips

After the acquisition of a GNSS satellite, the role of the tracking loops is to keep continuous tracking of the locked signal. However, interruptions in the tracking of the carrier phase may occur. When the tracking errors exceed the receiver tracking threshold, signal loss-of-lock is experienced. This is also known as cycle slip and it is seen as a jump in the integer number of wavelengths of the carrier phase. Figure 3-23 illustrates the tracking loop errors evolution versus the carrier-to-noise ratio. It is visible that the lower the satellite elevation, the higher is the tracking loop error as the C/N_0 decreases. Additionally, for each receiver, there is a region where the C/N_0 tracking threshold is set. In Figure 3-23 is also shown that the receiver dynamics and the tracking loop errors are directly proportional. Therefore, if the C/N_0 threshold or if the loop tracking error are exceeded, cycle slips occur. Considering a dynamic receiver, cycle slips might be experienced due to signal obscuration in the presence of obstacles. When this phenomenon occurs, the cycle slips are either detected and repaired or if not possible, the satellite signal is not tracked unless favorable conditions are present again.

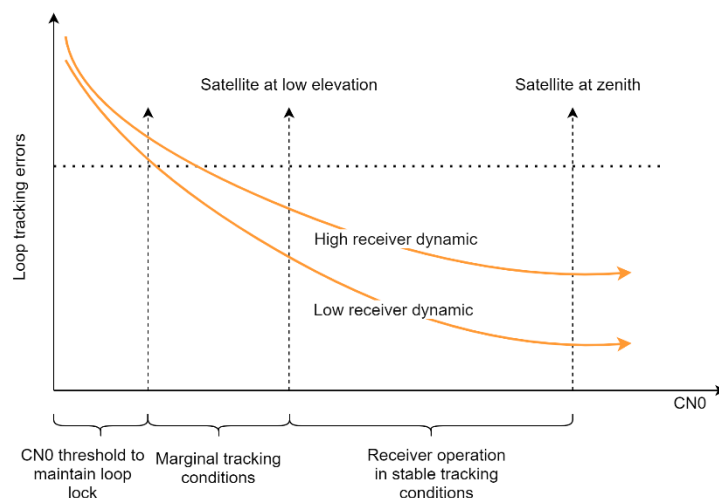


Figure 3-23: Tracking loop error with respect to carrier-to-noise ratio after Teunissen & Montenbruck et al. (2017)

Signal tracking threshold

Assuming multipath free conditions, the main tracking measurement errors are due to the tracking jitter and the dynamic stress. The tracking loops should maintain the lock of the signal if the tracking errors are below thresholds defined by the rule of thumb. The rule of thumb is expressed as (Teunissen & Montenbruck et al. 2017):

$$3\sigma_{XLL} = 3\sigma_{j,XLL} + \varepsilon_{D,XLL} \leq T_{XLL}, \quad (3-50)$$

where:

σ_{XLL}	1-sigma error for a PLL or DLL,
$\sigma_{j,XLL}$	1-sigma phase or code jitter,
$\varepsilon_{D,XLL}$	dynamic stress error for either code or phase,
T_{XLL}	threshold corresponding to the used discriminator.

The threshold which is computed depends on the type of loop. For a DLL in the absence of multipath, the main error source is the thermal noise, whereas for a PLL there are many additional contributions as follows: vibration induced oscillator phase noise, Allan deviation error and reference oscillator acceleration stress error (Kaplan & Hegarty, 2006).

3.6.2 Multipath impact on DLL

The multipath error influences directly the tracking loop performance of the GNSS receivers. Given the prior description of how the DLL and PLL are operated, a description of how the error impacts their functionality is presented. As presented in Section 2.4, Equation (3-3), a signal reflection has three components relative to the LOS i.e. the attenuation α_i , time delay τ_i and phase shift θ_i . Neglecting the receiver channel noise and assuming N multipath reflections, the DLL discriminator function can be written as:

$$S(\tau) = \int_t^{t+T_{avg}} \sum_{i=0}^N \alpha_i(t) \cdot \cos(\theta - \theta_i) \times \left[R \cdot \left(\tau - \tau_i + \frac{D}{2} \right) - R \cdot \left(\tau - \tau_i - \frac{D}{2} \right) \right] dt, \quad (3-51)$$

where:

T_{avg}	integration time over which the correlation outputs are averaged,
$R(\tau)$	the correlation function,
D	receiver correlator spacing.

The errors induced by multipath (α_i , τ_i and θ_i) can be processed in various ways. An illustrative representation according to Chang (2011) regarding the correlation function and the discriminator output is given in Figure 3-24. It is to be noticed that the graphs provide an understanding of the process in an ideal receiver with an infinite front end bandwidth. In reality, the front-end receiver bandwidth is limited consistent with electrical considerations, application accuracy, signal spectrum and bandwidth. The decrease of the bandwidth leads to the correlation peak loss and appearance of

constant parts in the correlation maximum. This hinders the determination of the exact time of arrival of the signal.

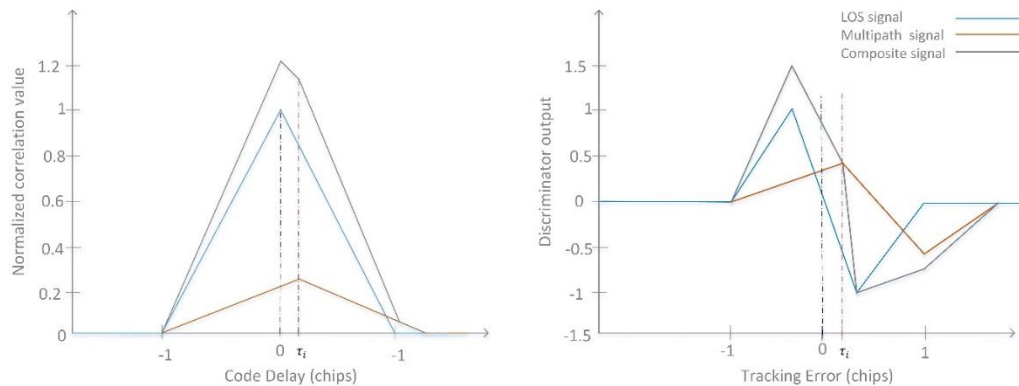


Figure 3-24: Schematic representation of correlation function for a LOS, multipath and composite signal (right) and the equivalent E-L discriminator response after Chang (2011)

The correlation distortion in the presence of a multipath reflection is presented on the left side in Figure 3-24. This is the case of the positive interference, i.e. the multipath signal reaches the receiving antenna in-phase with the LOS signal. It is assumed that the multipath amplitude attenuation relative to the direct signal α_i represents 0.3 from the LOS signal. It is visible how the time delay τ_i distorts the composite signal correlation peak. This precedes the distortions of the discriminator output, visible on the right side in Figure 3-24. The S-Curve of the discriminator output represents the sum of integrations over an integration period. For a LOS signal, the S-Curve is symmetric around the zero value as shown in Figure 3-22. When a multipath signal is added to the LOS, the S-Curve is distorted in the same way as the correlation, with a value, which corresponds to the time delay τ_i as seen on the right side of Figure 3-24. However, the way how τ_i is processed depends on the discriminator function. Thus, a multipath delay results in different tracking errors and implicitly pseudorange errors, depending on the kind of receiver is used. The schematic representation in Figure 3-24 shows the coherent discrimination, i.e. early minus late from 3.6.1.3.

The amount of error which is produced by multipath signals is known in literature as multipath envelope. By simulating a GNSS receiver and the signal structure that is being processed, the multipath envelope can be determined. Figure 3-25 shows an illustrative example of the multipath error envelopes for different signal modulations considering a narrow correlator ($d = 0.1$). The BPSK(1) signal is representative for a GPS C/A signal, the BPSK(10) shows a similar modulation to Galileo E5b and CBOC(6,1,1/11) stands for a signal of Galileo E1.

In Figure 3-25 it is visible how the pseudorange error due to multipath is influenced by the modulation type of the signal. The lines above the zero value represent the maximum errors and the ones below represent the minimum errors for different multipath delays. Maximum pseudorange errors in multipath conditions occur when the LOS signal and the multipath reflection reach the receiver in-phase (i.e. relative phase of multipath signal is zero). Minimum pseudorange errors take place when the multipath reflection arrives out-of-phase at the receiver. This means, that the relative phase of multipath is 180° . In reality, the multipath phase with respect to LOS oscillates constantly, therefore pseudorange errors are visible between the maximum and minimum curves. By comparing

the three signal structures, it is visible that GPS C/A has the least resistance to multipath. Both signal structures for Galileo are better with multipath but the E5b outperforms the first frequency considering all the range of multipath delay. Nevertheless, Figure 3-25 also reveals that for Galileo signals, the multipath error envelopes overlap for multipath reflections with delay up to 40 meters, therefore the errors on pseudorange are similar.

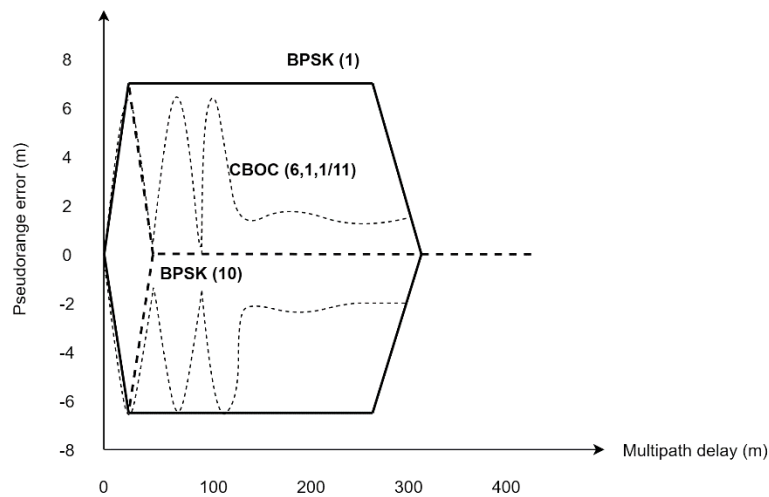


Figure 3-25: Multipath error envelopes for pseudorange assuming a narrow-correlator for BPSK(1), BPSK(10) and CBOC(6,1,1/11) after Teunissen & Montenbruck et al. (2017)

3.6.3 Multipath impact on PLL

The carrier phase measurements are also affected by the correlation distortions due to multipath. However, these are affected in a different way, compared to pseudoranges, as shown in section 3.3 and illustrated in Figure 3-26. Figure 3-26 describes the carrier phase measurement error, as a function of time delay τ_i , induced by multipath with an amplitude $A_i = 0.5$, for a narrow correlator spacing i.e. 0.1 chips. The error envelope corresponds to a tan PLL discriminator described in Equation (3-38).

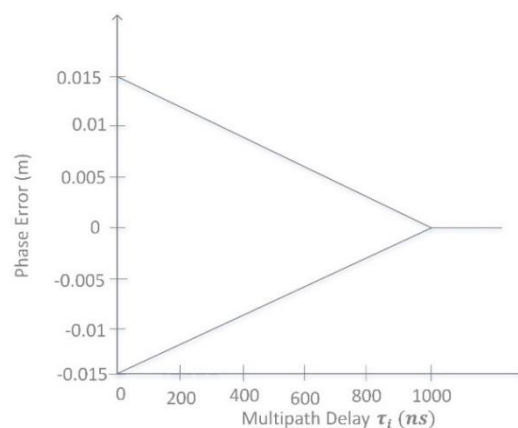


Figure 3-26: Phase error envelope due to multipath delay τ_i for a PLL discriminator and a correlator offset of 0.1 chip after Irsigler (2008)

Interestingly, the multipath carrier error has an inversely proportional behavior compared to the pseudorange (i.e. code) multipath error. This means that for short delay multipath, the error of the carrier phase is at its maximum and continues decreasing until it reaches zero when the code delay is bigger than 293 meters, i.e. $1 \mu\text{s}$ time delay. The mathematical expression of the carrier phase measurement error (ϕ_C) is given by (Teunissen & Montenbruck et al. 2017):

$$\phi_C = atg \left[\int_t^{t+T_{avg}} \sum_{i=0}^N \alpha_i \cdot e^{-j\phi_i} \cdot R(\tau - \tau_i) dt \right]. \quad (3-52)$$

Contrary to the pseudorange multipath error which can reach several meters, the maximum multipath error for the phase measurements reaches only the centimeter level. This is the case, because of the high frequency of the carrier, i.e. 1575.42 MHz for GPS L1/Galileo E1. As the multipath error occurs within a period, the error interval for the code is from 0 – 293 meters for C/A and E1 open service (OS) codes, while for the carrier phase it is 0 – 0.19 meters. However, according to Leick (2004) in the worst-case scenario, the resulting carrier phase multipath error is $\pi/2$ radian or one-quarter of the wavelength, i.e. 0.045 meters.

3.6.4 Multipath impact on SNR

In addition to pseudorange and carrier phase measurements, multipath affects also the GNSS signal's SNR. By definition, a high SNR indicates a strong signal, while a low SNR indicates that the signal is close to the noise floor and is not easily tracked by the receiver (Bilich, 2006).

As previously mentioned in Section 3.6.3, the carrier phase is also not changed by the navigation bits, due to the signal encoding techniques. Therefore, the SNR indicates the power of the signal, independently of the code and data bits. If multipath occurs, the reflected signals add constructively and destructively to the direct signal and this affects the amplitude of the composite signal and implicitly the SNR. The explanation of this dependency, with respect to the I and Q signal components presented previously is outlined in Figure 3-27. Generally, in a receiver, the SNR is dependent of the amplitude of the composite signal (A_C) as follows (Irsigler, 2008):

$$SNR = \frac{A_C^2}{2}, \quad (3-53)$$

$$A_C = I_P + Q_P. \quad (3-54)$$

where:

- I_P in-phase component from output of receiver correlation with the prompt signal replica,
- Q_P quadrature component from output of receiver correlation with the prompt signal replica.

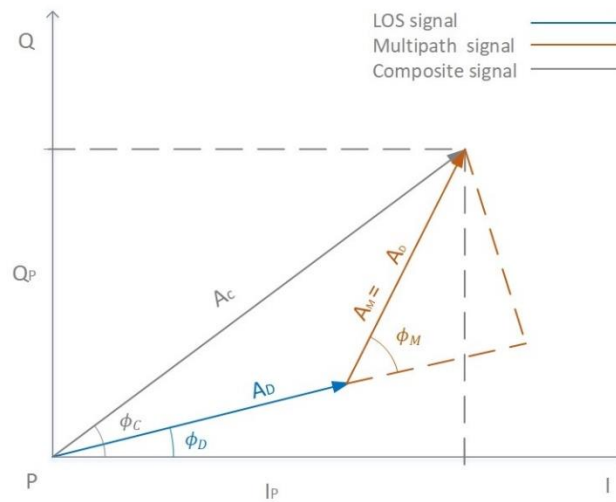


Figure 3-27: Diagram illustrating the impact of one multipath reflection on A_C after Bilich & Larson (2007)

Figure 3-27 shows the connection between the I and Q components of the signal and the amplitude of the composite signal, which arrives at the receiver. Assuming a tracking loop which is tracking the signal under multipath conditions, the multipath amplitude is A_M , the composite signal amplitude is A_C , the LOS signal amplitude is A_D and the terms ϕ_M , ϕ_C and ϕ_D represent their phases. Since the A_C represents the amplitude of composite signal, it can be modeled as (Bilich, 2006):

$$A_C = \sqrt{A_D^2 + A_M^2 + 2 \cdot A_D \cdot A_M \cdot \cos \phi_M} \quad (3-55)$$

Equation (3-55) indicates that changes in the A_C show the presence of reflected signals. Thus, according to Equations (3-54) and (3-55), depending on the multipath phase and amplitude, the SNR of the composite signal can oscillate. This implies that in the presence of LOS only, the SNR value has a constant behavior, assuming an ideal antenna pattern, and ignoring the satellite elevation and azimuth contribution.

4 GNSS pseudorange multipath estimation

This chapter presents two algorithms for pseudorange multipath estimation and their experimental verification. The first implemented algorithm is code minus carrier. An overall architecture and intermediate steps towards the estimated multipath are detailed. Since this approach indicated limitations for kinematic measurements, a second algorithm based on double differences is implemented. An overview, as well as the algorithm's steps for multipath estimation through double differences are detailed in the subsequent section. Lastly, two data sets of GNSS measurements are used to verify the estimated multipath through the implemented algorithms. Both data sets are GNSS measurements acquired from a fixed antenna, from two consecutive days and under multipath conditions. The difference between the data sets is the following: one of them is acquired from real GNSS signals and the second one are simulated signals. Multipath is influenced by geometry and the GPS constellation period is one sidereal day (Hofmann-Wellenhof et al. 2007). Therefore, the multipath error for GPS satellites is approximately repetitive. To verify the results provided by the implemented algorithms, cross-correlations between GPS satellites' multipath from consecutive days are computed.

4.1 Code minus carrier

It is challenging to isolate multipath contribution from the total error present on pseudorange measurements. One popular technique is the code minus carrier (CMC) differentiation. This has been studied since 1996 (Parkinson et al. 1996). Although this method eliminates the common errors between pseudorange and carrier measurements, the ionosphere error is doubled and ambiguities are present. Depending on the available data, several approaches solve these issues. Therefore, there are various methods to isolate multipath using code minus carrier differentiation. Within this work, the ionosphere error is removed by making use of the available dual-frequency measurements. Further, the ambiguities are removed by averaging, after a cycle-slip detector is applied. It is to be mentioned that when the cycle-slips are detected, but they are not repaired. The epoch where cycle-slips occur is considered within the further computation by splitting the measurements into segments where no cycle-slips happen.

Figure 4-1 shows the flowchart of the implemented algorithm, by means of code minus carrier differentiation. The succession of the illustrated steps leads to the computation of multipath error on pseudoranges. As a first step, the RINEX observation files provided by the receiver are parsed and stored in matrices. Then, the data is analyzed to look for data gaps in the measurements. If gaps are present, segments of continuous measurements are created. The next step is to identify the cycle slips. In the presence of cycle slips, the number of ambiguities change. For a successful ambiguities removal through average, the measurements are split into segments when cycle slips occur. The ionosphere error on the investigated frequency is determined from dual-frequency measurements. When the ionosphere and ambiguities are removed, the remaining error is multipath. As a final step, the multipath data is categorized, according to the satellite elevation and statistics are computed to determine a multipath empirical model.

The following sections detail each processing step of the measurements and exemplify intermediate results before isolating the multipath error.

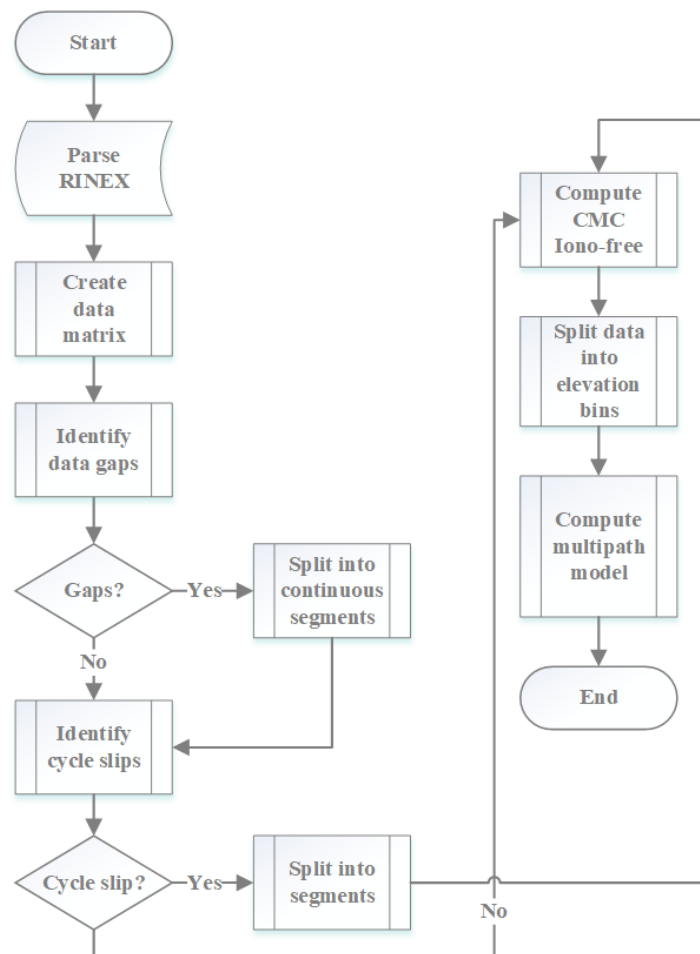


Figure 4-1: Implemented CMC algorithm flowchart

Measurement parsing

The GNSS data is recorded by most commercial receivers in RINEX observation and navigation files. In order to process them, the files are parsed and organized in matrices. An example of how the data is organized for GPS L1/L2 is presented in Table 4-1. The input needed for the CMC algorithm is the following: GPS time of week (TOW), satellite system, PRN number, frequency, pseudorange (C), carrier phase measurements (P) and PRN elevation (E).

Table 4-1: Parsing data header for GPS L1/L2

TOW (s)	GPS	PRN	C1 (m)	C2 (m)	P1 (m)	P2 (m)	E (deg)
---------	-----	-----	--------	--------	--------	--------	---------

Ionosphere delay

The error induced by the ionosphere is computed from dual-frequency carrier phase measurements. In the case of a single frequency receiver, the ionosphere error can be computed using measurements from a nearby receiver. According to Parkinson et al. (1996), the ionosphere delay differs up to 1 m per 100 km receiver separation.

The effect of the ionosphere delay on the CMC observables is illustrated on the left side of Figure 4-2. Table 4-2 summarizes the satellite change in position during the observation time. It can be noticed that the downward trend due to the ionosphere delay is inversely proportional to the SV elevation angle. The left side of Figure 4-2 reveals the CMC of SV3 and SV8, which contains the ionosphere error twice. On the right side, the same quantity with the ionosphere delay removed is plotted. The subtraction of the bias due to ionosphere is accomplished by means of the theory presented in section 2.4. The data used for the plots is experimental and was acquired on November 21, 2018.

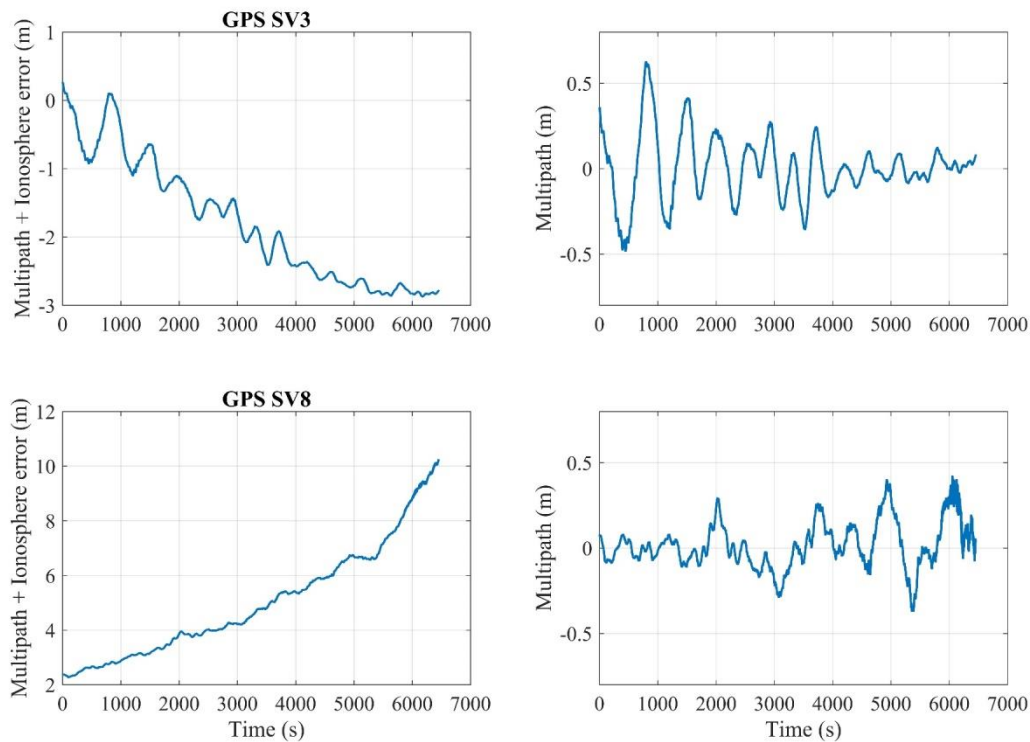


Figure 4-2: CMC differentiation before and after removing the ionosphere error for GPS SV 3 and 8 using acquired data from November 21, 2018

Table 4-2: Corresponding satellite elevation and azimuth angles

PRN	Elevation start	Elevation end	Azimuth start	Azimuth end
3	25,7°	65,7°	232,3°	264,4°
8	42,3°	6,4°	176,2°	174,4°

Carrier Phase Cycle-Slip Detection

Receiver loss of lock cause discontinuities in the carrier phase measurements, which determine the change of wavelength integer number, i.e. N_i in Equation (2-19). To detect cycle-slips, different methods can be implemented, according to the application type and available data. For dual-

frequency signals, the geometry-free combination can be used. This has the advantage of eliminating the non-dispersive effects in the signal, clock error and geometry error.

Nevertheless, it must be taken into notice that the results are influenced by a reduced signal to noise ratio, signal instabilities, and scintillation. After detecting the cycle-slips and splitting the data accordingly, the ambiguity ($N_i\lambda_i$) becomes a constant over a continuous pass of the satellite. Thus, this influence can be removed by averaging and subtraction from measurements. Within this work the cycle slips are not repaired, but just detected and the ambiguity is computed again. The cycle-slip algorithm for the purpose of this work is implemented by the mean of the theory presented in section 2.5.2.

4.1.1 CMC estimate

After applying the previous presented steps, the multipath error present on a pseudorange can be determined. Nevertheless, the estimate contains two additional noise terms, which are one order of magnitude smaller. The remaining errors that cannot be separated from pseudorange multipath are carrier phase multipath and receiver noise. However, the carrier multipath has a maximum value of a quarter of the signal wavelength (Ahmed, 2002) and the receiver noise for carrier measurements is in the order of millimeter. Therefore, these are not affecting the results as found in Weiss (2007).

To show the estimated pseudorange multipath by applying the CMC algorithm, a simulation with the GSS7000 GNSS signal generator is performed. Ground multipath is applied to the GPS L1 SV7 and Galileo E1 SV21. The GNSS antenna is simulated to be static and its height is set to 2 meters above the ground. The simulated multipath signal is half as strong as the LOS signal. The RINEX data is recorded using a GNSS receiver and post-processing using the presented algorithm is employed. Figure 4-3 shows the resulted multipath error magnitude. By applying the CMC algorithm, the sinusoidal pattern typical for a multipath error is revealed. This is typical for a static GNSS antenna, as found in literature (Irsigler, 2008). It can be noticed that the multipath errors differ, although the same multipath is simulated in both cases. This is owed to the different signals that the two navigation systems have and to the position evolution of the satellites during the simulation time.

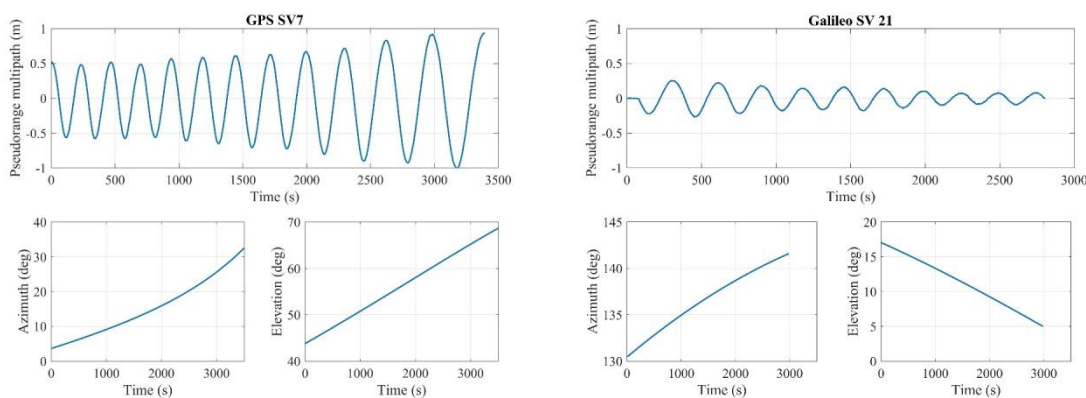


Figure 4-3: Code-minus carrier multipath error on simulated pseudorange observations for GPS L1 SV7 and Galileo E1 SV21

4.1.2 Multipath model

Since the multipath environment in the simulation models is dependent on the satellite position, the evaluation of the receiver output is done with respect to satellite elevation. The elevation range is from zero to 90 degrees (i.e. zenith). This interval is split into nine intervals, each interval bin containing 10° , as shown in Table 4-3.

Table 4-3: Definition of interval bins used for evaluation of the multipath errors

Elevation bin	1	2	3	4	5	6	7	8	9
Elevation interval	$0^\circ-10^\circ$	$11^\circ-20^\circ$	$21^\circ-30^\circ$	$31^\circ-40^\circ$	$41^\circ-50^\circ$	$51^\circ-60^\circ$	$61^\circ-70^\circ$	$71^\circ-80^\circ$	$81^\circ-90^\circ$

4.1.3 CMC Limitations

The major limitation of this approach is the dependency on carrier phase measurements for the following reason: cycle slips. In challenging environments, the receiver may lose the signal lock several times during a measurement. This leads to cycle slips and implicitly, the change of the ambiguity integer number N_i . By using the CMC algorithm, there is the need to restart the time-averaging process given the event of a cycle slip, to perform correctly the multipath estimation. Using a receiver pre-defined model or a reference receiver is not possible, since the ambiguity number differs from receiver to receiver.

Another aspect to consider is the need for dual-frequency measurements, in order to be able to determine the ionosphere delay. However, a single-frequency receiver can also be used, if a close-by receiver is measuring in parallel. Another alternative is the derivation of ionosphere delay from TEC (Total Electron Measurements) maps. Nevertheless, depending on the applied method, the ionosphere computation has different precision (dos Santos Prol et al. 2017).

To verify if the implementation provides correct multipath estimates, the algorithm is tested by means of cross-correlation with real and simulated measurements. The procedure and results are presented in Section 4.3.

4.2 Multipath from double differences

Kinematic measurements of GNSS observables include frequent measurement data gaps and cycle slips, especially for satellites which are not situated in zenith. Considering this and the limitations that are found regarding the CMC algorithm, a second method to determine the multipath error is implemented. Considering the availability of reference data, a feasible alternative to compute the multipath error is represented by the linear combinations.

Widely used for relative position computation, the double differences between a rover and a master station and between pairs of satellites can be successfully used for multipath modeling as well. The benefit of this method consists of the fact that almost all the correlated errors are removed in the process of differencing (Hofmann-Wellenhof et al. 2007), besides multipath. A schematic representation of the implemented algorithm that is used for code and phase multipath determination is shown in Figure 4-4.

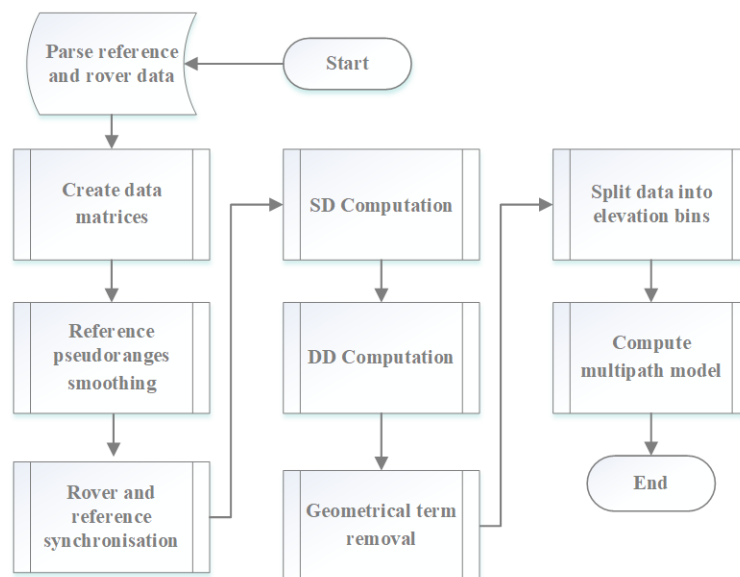


Figure 4-4: Scheme for multipath estimation from linear differentiation

Compared to the CMC algorithm, this approach does not require double-frequency measurements, but a reference station near the receiver. This is necessary to remove the ionosphere and troposphere delay through receiver single differencing. The ionosphere is the bias that has a larger spatial decorrelation than the troposphere. According to Konno (2007) the ionosphere is typically varying at the level of 1 to 4 mm/km. Although the carrier phase is considered as reference, compared with the noisy pseudorange, it is affected by multipath too. Prior research substantiates the belief that the multipath carrier error magnitude is 1% of the code error. A benefit of this method is that it offers the possibility to investigate the carrier phase multipath errors assuming that the cycle slips are detected. Although this is beyond the scope of this work, knowledge about carrier multipath is essential for high-precision applications that rely on phase observations. Thus, the modeling of the error is essential for the latter mitigation purpose.

The first steps are similar to the CMC algorithm, as they consist of data parsing. Nonetheless, in this case, the data originates from two sources: rover and reference receiver. The reference data is

provided by means of a Cloud-Based Positioning Network (i.e. AXIO-NET). Before computing linear combinations, the reference pseudoranges are smoothed and then synchronized with the rover data. After the double difference computation, the geometrical term is removed and the multipath data is split according to satellite's elevation.

In the next sections, the steps to determine the multipath error on pseudorange, by means of linear combinations of GNSS observations are detailed and intermediate results are shown. Finally, the implemented algorithm is verified in section 4.3 by means of cross-correlation to confirm that the computed multipath estimates are correct.

4.2.1 Pseudorange smoothing

The carrier measurements are more accurate than the code measurements, due to the higher transmission frequency. To eliminate the code jitter that induces noise on pseudoranges, because of internal receiver algorithm, the carrier measurements are used. This procedure is known in literature as carrier smoothing of code pseudoranges or pseudorange smoothing. The approach that was implemented to make pseudorange smoothing for reference data is the Hatch filter.

The algorithm was firstly introduced by Hatch, therefore it is known in literature as Hatch-Filter (Zhang & Huang, 2014). The performance of the Hatch-Filter is determined by the smoothing window width k . If the value of k is a constant during the smoothing process, the filter becomes unstable, due to the ionosphere error opposite sign in the pseudorange and carrier phase equations. To avoid this, a possibility is to use the ionosphere-free combination of the code and carrier. By using ionosphere-free observations as input in the Hatch-Filter, the filter remains stable with a constant window.

A description of the theoretical aspects of the Hatch filter is presented in section 2.5.3. The results after implementing and applying the smoothing algorithm are plotted in Figure 4-5. The upper plot reveals the ionosphere delay variation on L1 measurements for 2h30' observation time. The plot below indicated the unbiased measurements and the corresponding smoothed pseudoranges are plotted.

The window widths are 50-seconds and 100-seconds in the shown example. The choice of the window width has an impact on the accuracy of the smoothed pseudorange. As noticed in the below plot of Figure 4-5, the two lines are not perfectly overlapping. Therefore, different choices of the window width result in different approximations of the pseudorange. Another aspect to be taken into consideration is the measurement frequency. Although the Hatch-Filter is used with the same window width, the results are different for various measurement frequencies. Within this work, the 1 Hz interval is used. According to Zhang & Huang (2014), the best pseudorange accuracy for this measurement frequency is given when the smoothing window is 100-seconds. Hence, to get the best results, the pseudorange smoothing is performed using 100-seconds constant on ionosphere free observations.

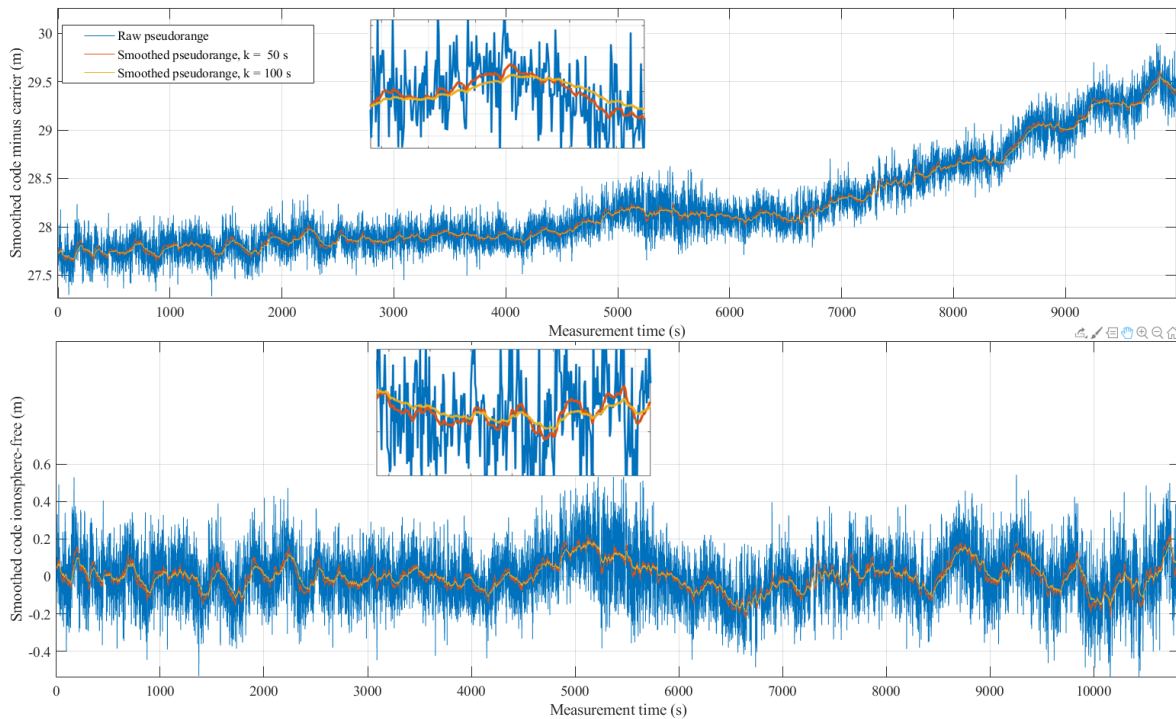


Figure 4-5: Smoothing of the code noise with the Hatch filter by using different window widths. The upper plot shows the filter output with measurements containing ionosphere error. The plot below represents the same output without ionosphere error

4.2.2 Geometrical term removal

The theoretical aspects regarding linear combinations to determine the multipath error from GNSS observations are shown in 2.5.1.3. The correlated errors, such as the satellite clock bias, ionosphere and troposphere delays are eliminated through single differences. Double differences (DD) additionally remove the receiver clock error. In the case when the baseline is different from zero, meaning that the signal is not coming to the two receivers through the same GNSS antenna, an additional geometrical term has to be eliminated. Figure 4-6 illustrates an example of a DD, computed using experimental data before the geometrical term is removed. The red lines indicate the fitted unique least square solution, which is computed as the best fit for the DD series.

The regression line represents a second-order polynomial, which fits the data trend. The correctness of the fit is tested by applying the χ^2 -test on the regression errors ε . The 95% confidence bounds are plotted in Figure 4-6. These show the relevance of the applied method. The narrower is the confidence interval, the more precise is the estimate.

It is to be noticed that the trend plotted in Figure 4-6 is common to all DD, although the regression coefficients differ. This is the case, because the geometrical term that is being modeled contains the Earth rotation, with respect to the satellite movement within the measurement time. In the case of kinematic measurements, the geometrical term also contains the contribution of the rover movement (Hofmann-Wellenhof et al. 2007).

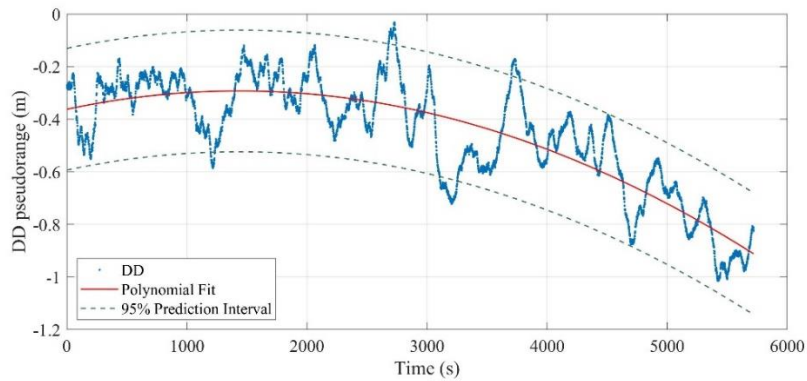


Figure 4-6: Double differenced pseudoranges with polynomial regression and 95% confidence bounds

4.2.3 DD multipath estimate

The last step of the multipath computation by means of linear combinations is the removal of the computed polynomial for each satellite pair. To check the application on simulated data, a one-hour multipath simulation is performed, by the mean of the GSS7000 signal generator. The modeled multipath is a ground reflection for an antenna situated 2 meters above the ground. The simulated multipath amplitude is three times smaller as the amplitude of LOS. In order to apply the presented algorithm to determine multipath, a second simulation has to be made. The simulation is error-free and replaces the virtual reference stations (VRS) data, which is available for the measurement campaigns. After recording the RINEX observations for both simulations, the multipath is computed by means of linear combinations for carrier and phase observations. Although the carrier phase multipath is not the purpose of investigation within this work, it is computed and plotted for two reasons. The first one is to confirm the theoretical relation of the phase multipath with the code multipath and the second reason is to show the relevance of the algorithm for eventual further carrier multipath investigations.

Figure 4-7 reveals the multipath resulted from simulations for GPS 7. The plotted multipath error magnitude are the output of the proposed algorithm. It is obvious from the plots that there is a strong correlation between the code and carrier multipath. Nevertheless, the carrier multipath error represents 1% from the code multipath, which is according to the findings in the Section 3.6.2.

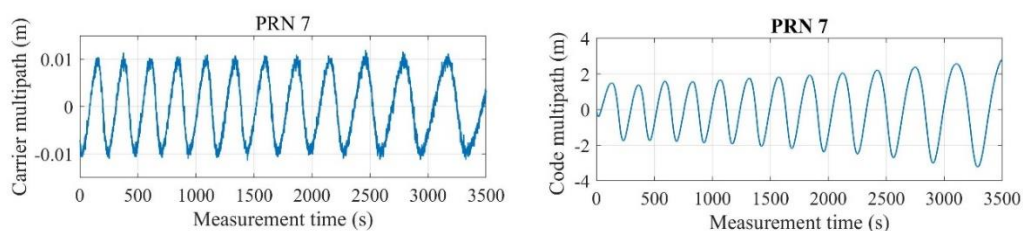


Figure 4-7: Code and carrier phase multipath obtained from simulations. The multipath is computed from the GNSS observations through the proposed algorithm with linear combinations

4.2.4 Double differences limitations

Since the double differences make use of pseudorange measurements, the results are not influenced by the cycle-slips which affect the carrier phase measurements used in the CMC method. Therefore, this is the main advantage of using the DD method over CMC. Nevertheless, there are some limitations when applying DD method as well.

Assuming that multipath-free observations are available from reference data, the multipath at the rover receiver is computed by means of double differences. This implies the use of two satellite pairs: one pair from the rover and one from the reference. Consequently, one satellite from the rover observations situated in zenith is used to determine the multipath for the second satellite in the pair. The choice of a satellite in the zenith is based on the assumption that it contains no multipath, due to the convenient position in the sky plot. However, this premise relies on previous research and implies that the satellites situated in zenith are multipath-free.

4.3 Experimental verification

The multipath estimation through the two implemented algorithms is verified by considering the geometrical aspect of the error. According to Hofmann-Wellenhof et al. (2007), multipath is related to geometry. GPS satellites have an orbital period of half sidereal day, i.e. 11 hours 58 minutes and 2 seconds. This means that the multipath error repeats itself for measurements acquired from a fixed antenna each consecutive day, with a time lag of 4 minutes and 4 seconds (Spilker, 1980). This is the case if the user is stationary and the environment remains unchanged, so that the multipath error changes only due to satellite motion.

In order to verify the implemented CMC and DD algorithms, GPS data was gathered. The measurements are acquired from both simulated and real GNSS signals in two consecutive days. The setup that is used, the evaluation of the acquired data and the results are presented in the following sections.

4.3.1 Measurement setup

The GPS data used for verification originates from two sources: the GSS7000 GNSS signal generator and a fixed roof top antenna. The setup is detailed in Figure 4-8. The simulations are performed for two consecutive days: 7.02.2020 and 8.02.2020, at the same hour: 8 a.m. For four GPS SVs (i.e. 2, 5, 12, 20), multipath is simulated by means of the reflection multipath model presented in section 3.5.2.1. Thus, the NovAtel receiver processes the generated multipath for the four GPS satellites. The receiver output with the GPS measurements under multipath conditions is stored.

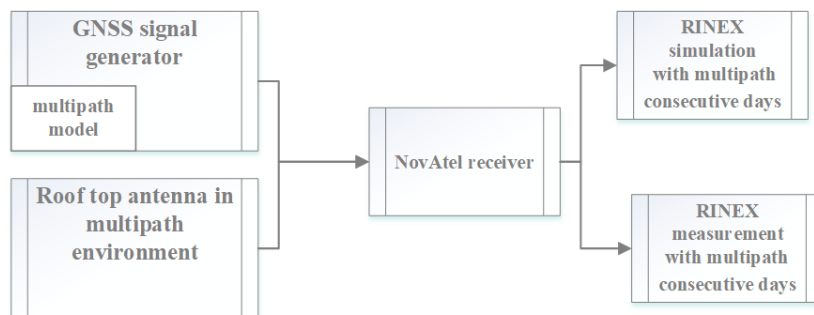


Figure 4-8: Setup for measurement of simulated and real GPS signals for the verification purpose

Similar, two measurements of real GPS signals are performed on 29.01.2020 and 30.01.2020 at 17:30. The fixed antenna on the rooftop that has a tall building in the vicinity represents the adequate multipath environment to investigate the error's repetitive behavior. As known from literature, the ionosphere impact on the GNSS signals is stronger during the day, due to the solar radiation. Consequently, the measurements are acquired after sunset, in order to minimize the effect of the ionosphere on the observables.

4.3.2 Measurement evaluation

The data that was acquired with the previously described setup represents the input for the verification of the two multipath estimation algorithms. As indicated in Figure 4-9, the RINEX files from measurement and simulation serve as input for the CMC algorithm. The multipath error for GPS

satellites is computed for all four data sets. Then, cross-correlation is calculated between the estimated multipath, in the consecutive days for both simulation and measurement.

The RINEX files, together with reference data are required to estimate the multipath error, with the DD algorithm for the same four data sets: simulated and measured in two consecutive days. The error is estimated for the same GPS satellites and cross-correlations are computed, to verify the multipath results that are provided by the second algorithm.

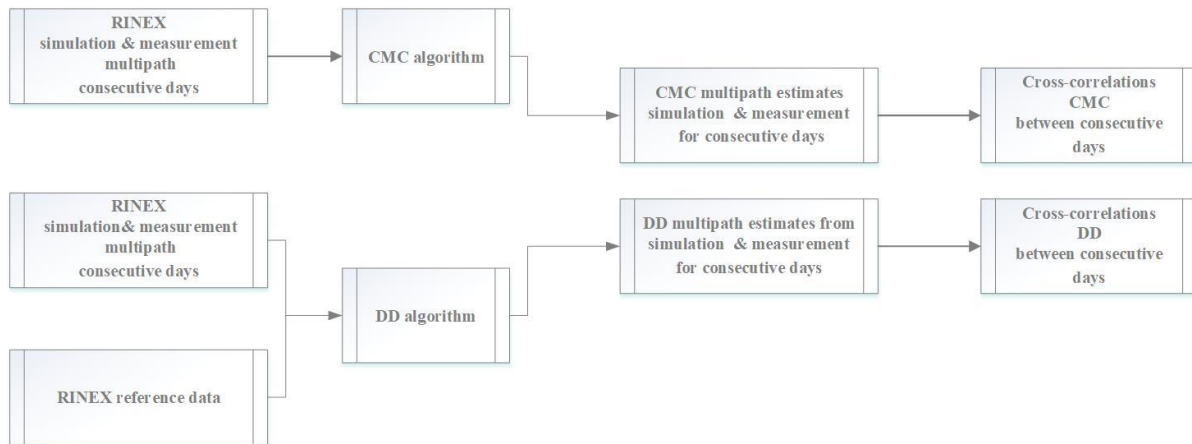


Figure 4-9: Evaluation scheme of the measured GPS data

Table 4-4 below shows the results of the cross-correlations, after the evaluation is done. The correlation lag at 244 seconds indicate that the computed errors have the period found in literature for multipath. For the measured GPS 12, the time lag indicates 245 seconds. This is acceptable according to Zhang (2016), due to the small clock periodic errors of satellites. The cross-correlations magnitude is different for the investigated satellites due to the different geometry conditions and other errors influences, besides multipath. The limitations of the methods which lead to different correlation values have been presented in 4.1.3 and 4.2.4.

Table 4-4: Cross-correlation results for estimated multipath from consecutive days

	Simulated GPS signals with multipath			Measured GPS signals with multipath		
	SVID	Cross-correlation coefficient	Cross-correlation lag	SVID	Cross-correlation coefficient	Cross-correlation lag
CMC	2	0.796	244	14	0.879	245
	5	0.828	244	29	0.702	244
	12	0.826	244	32	0.864	244
	20	0.829	244			
DD	2	0.782	244	14	0.651	245
	5	0.826	244	29	0.621	244
	12	0.823	244	32	0.735	244
	20	0.821	244			

5 Multipath simulation

5.1 Introduction

The interest in the multipath behavior in kinematic situations urges from the current technology trend: automated driving. Due to the lack of multipath investigations in this scenario, the simulations in this chapter focus on this use case, as well as establishing to which extent the user velocity has an influence. The advantage of the simulations is that one can set-up situations which in reality are hard or impossible to recreate. For instance, the simulations are designed to keep the same geometric arrangement, while the user's velocity is varied to assess its impact. Additionally, static simulations are carried out to analyze the discrepancies to the kinematic use case. Based on these assumptions, investigations regarding two different multipath models, velocity impact and multipath magnitude on GPS L1 and L2, Galileo E1 and E5b are accomplished.

In order to make a realistic quantitative assessment of multipath, the receiver architecture, signal type, user kinematics and multipath environments have to be considered. Considering these, in this chapter multipath simulations in Hardware-in-the-Loop (HiL) are implemented, carried out and evaluated. The background of the multipath models which are implemented in the HiL simulations are introduced in section 3.5. The chapter is split as follows: simulations setup, HiL simulations with the hybrid multipath model, HiL simulations with the deterministic multipath model and a summary section. First, the simulations' implementation and steps are detailed for both investigated multipath models. Then, the used hardware is described and the receiver sensitivity to multipath is analyzed. After performing the simulations for static and kinematic use cases, the generated multipath parameters with each method and the corresponding receiver errors are evaluated. Multipath estimates from the receiver observations are computed, based on the algorithm implemented and validated in Chapter 4. Finally, the summary section reviews the simulation results from the employed models and it concludes which is more adequate for the kinematic use case.

5.2 Simulations setup

Over the past decades, researchers have made progress in simulating multipath. As a first step, multipath simulations by means of software have been developed based on the corresponding mathematical models. Some examples of successful implementations regarding GNSS multipath can be found in Hannah (2001), Winkel (2000), Lau (2005) and Weiss (2007). Due to the multipath changing nature and complexity, it is unfeasible to use the same model for different applications. Moreover, the hardware (i.e. GNSS antenna, receiver) has multipath mitigation techniques. Thus, in order to have knowledge of the multipath magnitude and behavior, investigations are required for new use cases and/or hardware.

Within this work, both software and hardware multipath simulations are performed for dual-frequency constellation: GPS and Galileo. The frequencies which are simulated are L1/E1, L2C and E5b for the reasons mentioned in section 1.1. By means of simulation, information regarding the impact due to multipath on the complete satellite-receiver chain can be gained. Figure 5-1 indicates the software (SW) simulation. This is the first step in the simulation setup. The output consists of multipath parameters i.e. attenuation, phase and code shift for each simulated satellite per frequency. These are sent to the signal generator GSS7000. Following, the signal generator produces GNSS signals by means of hardware (HW) and sends them to the receiver. It is to be mentioned that the simulated

receiving antenna is isotropic. This implies that the gain zero is applied for all frequencies. The simulation chain presented Figure 5-1 is also known in literature as Hardware-in-the-loop (HiL) simulation.

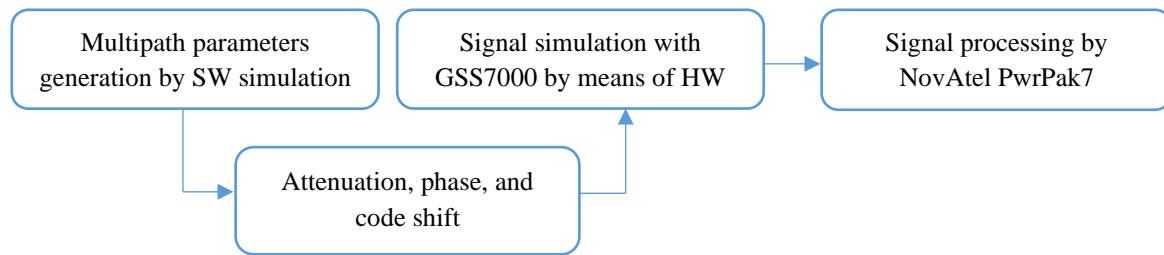


Figure 5-1: Equipment and setup of the satellite-receiver simulation chain. Software simulation output is being used to generate multipath signals with the hardware of GSS7000. The signal processing is performed by NovAtel receiver

5.2.1 Simulation of multipath parameters

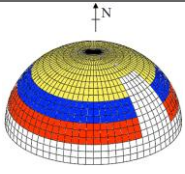
The multipath parameters can be computed with software simulation by using the models presented in section 3.5. From the introduced models, the most representative ones are chosen for the simulations in this chapter. These are the hybrid model and the ray-tracing model. Within the hybrid model, the multipath parameters are computed based on the statistical approach, considering the geometry of environment. The ray-tracing method computes the multipath parameters only based on the geometry of the environment. This means, that the output is deterministic and representative to the 3D environment which is simulated. Although both multipath modeling models are known in literature, these have been extensively used for static applications. Thus, their implementation and simulation in a HiL setup are necessary to investigate their capabilities to reproduce the GNSS multipath parameters, also in kinematic situations.

5.2.1.1 Multipath parameters with hybrid model

The statistical models that are used to model multipath assume that the path between the satellite and receiver is a sum of the direct signal and reflections that can be statistically modeled, as shown in Chapter 3.5.1. It is assumed that the multipath components are not resolvable in the time domain, therefore phase shifts and attenuation of the signal occur, but no time delay is experienced by the receiver. Making additional presumptions on the surrounding environment, by connecting the arriving signal type (i.e. no/direct signal, direct signal and multipath reflection, multipath reflection) with the angle of arrival as in the deterministic models presented in Chapter 3.5.2, leads to the hybrid model. The theoretical background of the hybrid model has been detailed in Chapter 3.5.3. This simulation model is implemented by making use of the SimGEN software from Spirent®.

In order to perform multipath simulations by means of hybrid multipath model, the first step is to define four potential signal categories. Table 5-1 summarizes the meaning of the categories and a possible distribution, as a function of satellite elevation. In the last column, the visualization of the environment definition is added for clarity.

Table 5-1: Hybrid model environment definition

Label	Significance	Elevation (°)	
Category A	Obscuration	0-25	
Category B	NLOS and multipath	26-35	
Category C	LOS and multipath	36-70	
Category D	LOS	71-90	

The grid is defined by the azimuth and elevation angle of arrival of the direct signal. This can be modified according to the geometry of the environment. For example, for an open-sky environment, the LOS category can occupy a larger elevation interval. According to the labeled category defined by the environment, multipath is modeled by statistical means. That is, for LOS and multipath i.e. Category C, the Rice Model presented in Section 3.5.1.1 is employed. As for the NLOS and multipath i.e. Category D, this is modeled by Rayleigh, as shown in 3.5.1.2. In the obscuration situation, the satellite signals are not simulated.

In order to make a more realistic simulation, the hybrid model can be parameterized, by using values from look-up tables (LUT). These contain parameters which have been derived from measurement campaigns in different environments. The parameters which were used for the simulation with the hybrid model within this work are detailed later in section 5.3.15.2.1.1. The ease of environment definition and shorter computation times represent the advantage of this approach. Nevertheless, the main limitation consists of the inflexibility to change the environment during a dynamic simulation.

5.2.1.2 Multipath parameters with ray-tracing model

Ray-tracing simulations produce multipath components which are resolvable in the time-domain, thus a significant temporal dispersion is observed. The second method to simulate multipath within this work is based on the ray-tracing algorithms implemented in the software Sim3D[®]. By using such a tool, the propagation of the signal from satellite transmission until reception is deterministically modeled. The ray-tracing algorithm computes the multipath parameters based on three inputs: satellite constellation, 3D data and user position. The satellite constellation is defined by ephemeris files. As for the 3D data, this consists of the 3D model of the environment. A 3D model is developed for the purpose of deterministic simulations. Besides this, the dielectric properties of the objects present in the 3D model are considered. Material properties are required to compute the reflection coefficient's impact, due to the interaction of objects with the electromagnetic waves. The theoretical background for these dependencies is discussed in section 3.5.2.3. Finally, yet importantly, the user position is required. Depending on the simulation type, this can be either static or dynamic, i.e. a trajectory is defined. With this input, the ray-tracing algorithm computes multipath parameters by means of uniform theory of diffraction (UTD) and geometrical optics (GO), as previously detailed in section 3.5.2.3.

Refracted and diffracted GNSS signals, which are the result of the interference with the objects modeled in a 3D scene, are shown in Figure 5-2. The white rays represent the LOS, the red ones are reflections, and the blue ones indicate diffraction. The multipath parameters are computed and sent with a sampling rate of 10 Hz for each satellite, frequency, and route point. To integrate the multipath simulation in the HiL, the information (phase shift, code delay and power loss) is sent to the GSS7000 by a specific protocol.

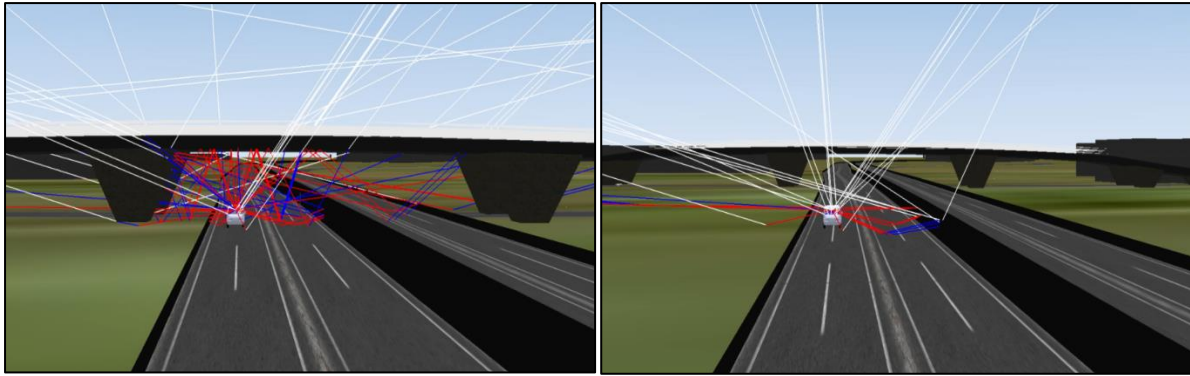


Figure 5-2: Screenshot of ray-tracing simulation with Sim3D using a street model and a dynamic vehicle

5.2.2 Receiver type impact on multipath

Since GNSS is a ranging and positioning system, it is imperative that the reception from the satellites is the LOS only. However, multipath is always present to some degree in reality and this is critical for the accuracy of the position, velocity and time (PVT) results. This issue has been known since the beginning of the GPS use. Therefore, the receiver techniques for multipath mitigation started to be developed very early. At the beginning of their development, GPS receivers have used one-chip spacing between the early and late signal replicas and a pre-correlation bandwidth of 2 MHz. Later, research has revealed that using larger bandwidths in combination with closer spacing ($> \frac{1}{2}$ chip) of the early and late reference codes leads to multipath reduction as shown in section 3.6.1. The evolution of receiver tracking loop configurations is presented in Figure 5-3. Region 1 stands for the receiver discriminator configuration beginnings, ascending to Region 4 that is the best in terms of performance. This leads to better positioning results, even in the presence of a multipath.

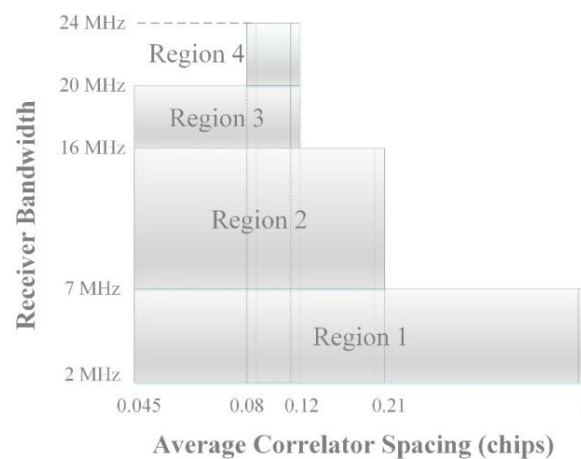


Figure 5-3: Evolution of receiver discriminator tracking configurations after RTCA DO-253C (2008)

Each GNSS receiver nowadays has one of the configurations shown in Figure 5-3. Depending on the bandwidth and correlator spacing capability of a receiver, the multipath signals are differently processed. The bandwidth determines how much information of the signal is processed. Thus, it has an impact on the correlation output described in section 3.6.1. The correlation output is used after integration to compute the discriminator function. This function determines the multipath error, which

represent the contributions $MP_{\rho,i}$ and $MP_{\phi,i}$ to the pseudorange and carrier phase measurement model presented in section 2.4.

Thus, it is essential to understand that a multipath signal, which reaches the receiver, is processed differently by receivers having different configurations. This leads to various pseudorange and carrier phase errors for the same multipath error, when using different receivers. For the multipath investigations within this work, the receiver NovAtel PwrPak7 is used. In order to create an understanding regarding the receiver processing of multipath signals, an analysis is performed. The setup and results of the analysis are presented in the next section.

5.2.2.1 NovAtel PwrPak7 multipath sensitivity

The technical specification of commercial receivers does not offer specific information regarding the multipath mitigation algorithms. Nevertheless, it is known from literature that narrow correlator technology has been developed and used since 1992 by NovAtel Inc. Considering this and in order to understand the PwrPak7 Delay-Lock-Loop (DLL) influence on multipath, a series of simulations are performed. To begin with, investigations regarding the multipath error magnitude of the narrow-correlator have been made. Multipath simulations for different correlator spacing have been published in Chang (2011). These reveal that the receiver with narrow correlator (0.5 chip E-L) is affected by multipath delays from zero up to 350 meters. The value of 350 meters is chosen based on the previous research, which show, that delays with a larger value are successfully decorrelated by the receiver, therefore they produce no errors. Several publications, such as Townsend et al. (1995), Wang (2002), Hu (2013) analyze the receiver error for delays within the mentioned interval. Therefore, simulations are performed with a multipath signal whose delay is within the mentioned interval. Additionally, different velocities are considered for the analysis. In this way, a first understanding is created regarding the receiver's behavior for multipath under kinematic situations. A similar approach for testing a receiver DLL can be found in Weiss (2007).

Four simulations with an increasing multipath delay are completed for different velocities. The settings remain identical during all simulations, except for the multipath. Characteristics of the injected multipath are described by (5-1). The reflected signal's delay increases linearly with time, as follows:

$$mp(t) = a + b(t), \quad (5-1)$$

where $mp(t)$ is the simulated multipath delay as a function of time, a is the initial error and b is the increasing error with the time. The initial error is set to zero and it is going up to 350 m, which is the equivalent of 1.2 C/A code chip. The same multipath error is added to a satellite for simulations in static and kinematic conditions, so that the influence of the kinematic under multipath conditions is analyzed.

Figure 5-4 shows the results of the simulations. The simulated multipath delay is plotted to the corresponding pseudorange error produced by the receiver. The results in Figure 5-4 shows two facts regarding the receiver: (1) the correlators are found to resemble PAC (pulse aperture correlator), according to the analysis in Jones et al. (2004) and (2) multipath magnitude is inversely proportional to the velocity. This means that the receiver copes better with the same multipath error in a slow kinematic case, compared to a static one. This result is justifiable, as low pass filters in the receiver

eliminate the multipath effects produced by the signal dynamics in a kinematic scenario (Winkel, 2000).

For NovAtel PwrPak7, the highlighted blue areas in Figure 5-4 indicate where the correlators are susceptible to multipath errors: 0 - 35 m and 255 - 320 m. However, the maximum resultant receiver error is 0.37 m, which is negligible compared to the injected error. This is the effect of the receiver bandwidth, which allows the correlation function to be sharper, therefore efficient in delay tracking (Avram et al. 2019).

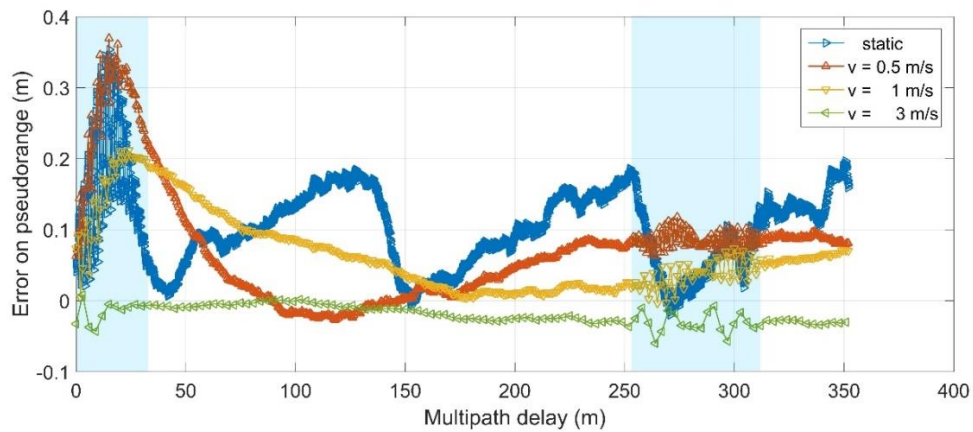


Figure 5-4: Receiver tracking error on pseudorange measurements for a direct signal and one multipath reflection under various kinematics. The multipath signal has a constant power loss of 6 dB relative to LOS and increasing pseudorange error

5.3 HiL simulations with multipath hybrid model

5.3.1 Simulation environment

The first approach to simulate multipath in the HiL setup is by means of the hybrid model. As previously mentioned in section 5.2, this method models the environment using four signal categories. Multipath reflections are not easily predictable, especially for a kinematic user. To assess if this modeling method is adequate to recreate multipath in different kinematic situations, simulations with a user at different velocities are performed.

The first step is to define a scenario for the signal generation. The scenario is defined by: the satellite constellation, the simulated user position, time and duration of the simulation. The GPS and Galileo constellations are defined by using post-processed ephemeris data from November 21, 2018. The signal frequencies to be simulated are L1/E1 and L2, E5b. These are the frequencies of interest within this work. The user's position is defined in WGS84 coordinates by a trajectory which is randomly created, with the length of 20 kilometers. To make an additional analysis between different use cases, two kinds of simulations are performed: static and kinematic. The kinematic simulations are done to distinguish between various commonly used vehicle velocities: 8, 14, 19, 25 and 30 m/s (i.e. approximately 30, 50, 70, 90 and 110 km/h). The starting time of the simulation is the same for all, in order to have the same GNSS constellation.

The second step is to model the environment. For this, the four categories presented in Table 5-1 are defined around the receiving antenna: obscuration, direct signal, direct and multipath signal and multipath signals only. These are delimited by elevation and azimuth arrival angles. Through deterministic modeling these limits are determined according to the reflector's position and size in the surrounding environment. Figure 5-5 shows the environment, which was modeled and used for the simulations.

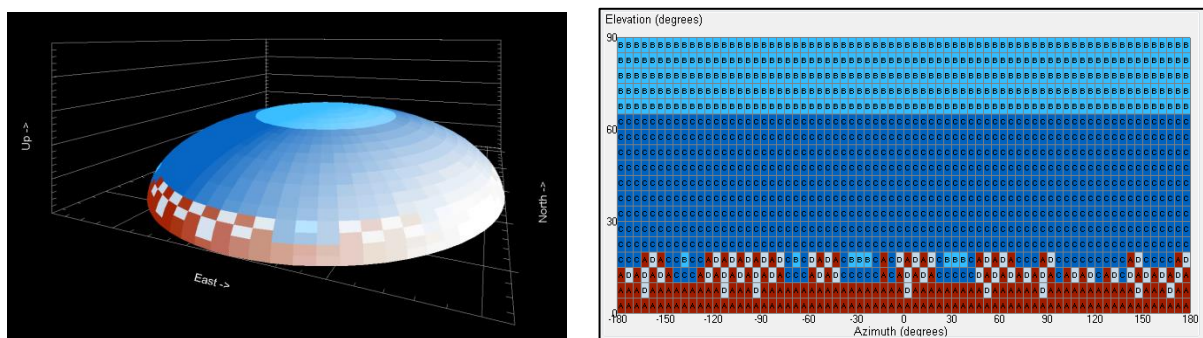


Figure 5-5: 3D and 2D view of the environment for hybrid model simulations. Different colors indicate the four categories determined by the environment geometry.

A limitation of this approach is that the four categories which are defined remain the same during the kinematic simulations. Therefore, the environment around the receiving antenna does not change. The type of multipath which is simulated depends on the signal angle of arrival. This means, that only the satellite motion determines a change in the simulation. For example, if a satellite is not simulated at the beginning because it lays at 5° elevation with respect to the user, this can change when the satellite lays at 10° elevation. The plot on the right in Figure 5-5 shows the categories of signals generated, with respect to the satellite elevation and azimuth. The red areas indicate obscuration, the white ones multipath only, the dark blue show multipath and direct signals, the light blue show only direct

signals. The grid which defines the type of signals that are modeled has a 5° resolution. This means, that the satellite must move more than 5° during a simulation, so that the type of signal for the specific satellite changes from direct signals to direct signals plus multipath, for example. The modeled environment for this set of simulations is an open-sky environment on the highway. The echo sources in these conditions are hills and vegetation. Choosing the highway environment serves to the motivation of this work, that is multipath investigation for the autonomous driving. Additionally, in literature, most of the research related to multipath is done in critical environments as cities. Thus, choosing the highway environment additionally complements the current studies in this domain.

After the categories are determined, the signals are modeled by statistical means. As presented in the theoretical background, the mixture of LOS and multipath signals is modeled by the Rician fading and the NLOS signals by Rayleigh fading. To make the simulation as realistic as possible, the parameters in the mentioned models are provided from look-up tables (LUTs). There are LUTs specific for each environment type, as the parameters are computed after measurement campaign analysis. Table 5-2 shows the LUT values to model the signal attenuation for the Rayleigh and Rice distribution in a highway environment. The values are provided according to the ratio between the composite signal strength and attenuation due to multipath. It is to be noticed that the values used for the physical-statistical simulation are according to the LUT for a highway environment, as indicated in Spirent Communications (2018).

Table 5-2: Rayleigh and Rice modeling of multipath reflections

E ($^\circ$)	0-10	10-20	20-30	40-50	50-60	60-70	70-80	80-90
A_D/α (Rayleigh)	281.5	140599.1	360.6	107497.9	475.4	109776.7	128190.3	122638.5
A_D/α (Rice)	4.9	8.2	42.5	41.5	6.3	43.4	138.2	123.3

5.3.2 Simulated multipath parameters

The objective of this section is to analyze and understand the output of the hybrid multipath simulations with different user velocities. As this approach simulates the signal characteristics in terms of attenuation due to multipath, this means that the power of the transmitted signal is affected. Consequently, the output consists of the attenuation because of multipath. Figure 5-6 reveals the resulted cumulative probability of the signal attenuation during the simulations at the mentioned velocities.

The data resulted from simulations in the environment described in 5.3.1. It is noticed that regardless the user velocity, the signal attenuation follows a similar trend. In 80% of the time, the multipath signals have an attenuation between $-\infty$ and 15 dB. On the presented scale, 0 dB attenuation indicates no attenuation and -50 dB indicates that the signal is weak, under the noise floor. The resulted cumulative probability indicates that the simulated multipath signals have the same attenuation, regardless of the velocity and they are weak with respect to the direct signal.

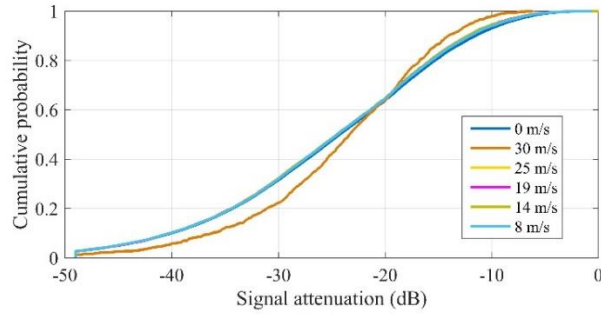


Figure 5-6: Cumulative probability of attenuation due to multipath for static and kinematic simulations at different velocities

The multipath signal fluctuations over a 1200 seconds simulation are plotted in Figure 5-7, together with the average signal attenuation for all six simulations. The scaling of the simulation time over 1200 seconds is done for clarity purposes. The attenuation that occurs in the same environment with static and kinematic users is plotted on the left side in Figure 5-7. A visual inspection indicates a random multipath attenuation spread, which is similar despite the different kinematics. The average attenuation value for all simulation is plotted on the right side of Figure 5-7. This confirms the similarities, by indicating an average multipath attenuation of approximately 10 dB power loss in all cases.

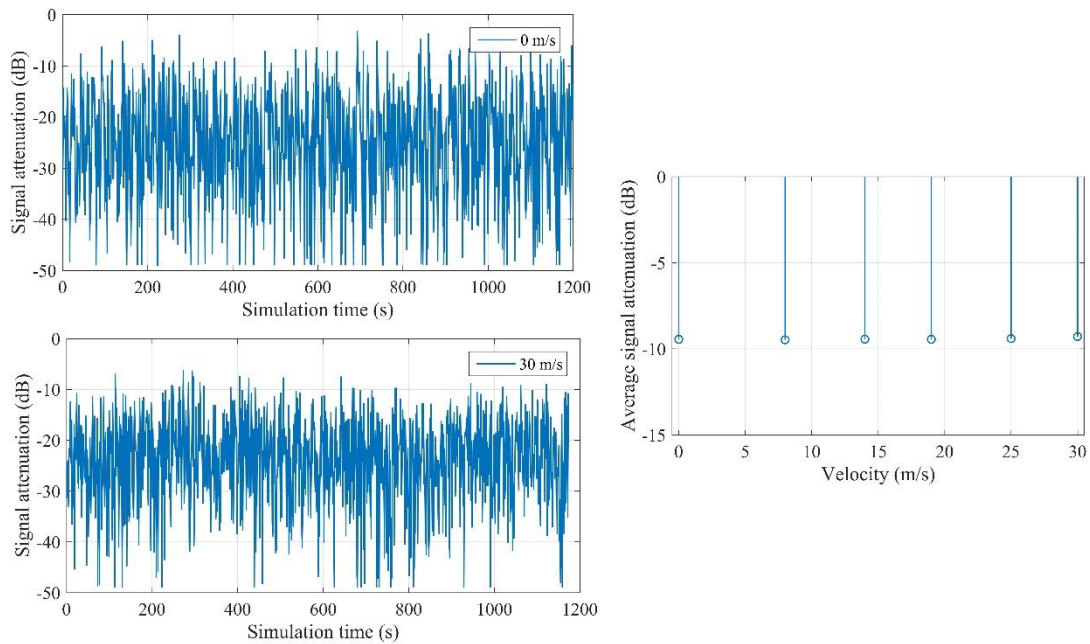


Figure 5-7: Comparison between simulated multipath attenuation at different user velocities

5.3.3 Impact on SNR

Due to the simulation with changing multipath attenuation within the mentioned statistical distributions, the strength of the GNSS signals is affected. Therefore, within this section, the SNR values of the simulated satellites are investigated. As described in the simulation setup, the multipath parameters depend on the satellite position with respect to the user. Therefore, the SNR attenuation is characterized according to the satellite elevation, as described in section 4.1.2. SNR mean values pro elevation bin intervals are computed.

Figure 5-8 describes the average SNR evolution over the satellite elevation for GPS and Galileo, within the simulated scenarios. The results reveal an increase in the SNR with the elevation. This makes sense, since the closer are the satellites to zenith, the less multipath they experience. Thus, this aspect is realistically simulated by the hybrid model. Another result revealed by the simulations is represented by the differences between GPS and Galileo. A zoom into the plots shows a better average SNR for Galileo, which is realistic as well. This is owed to the fact that Galileo satellites benefit from a higher signal power compared to GPS.

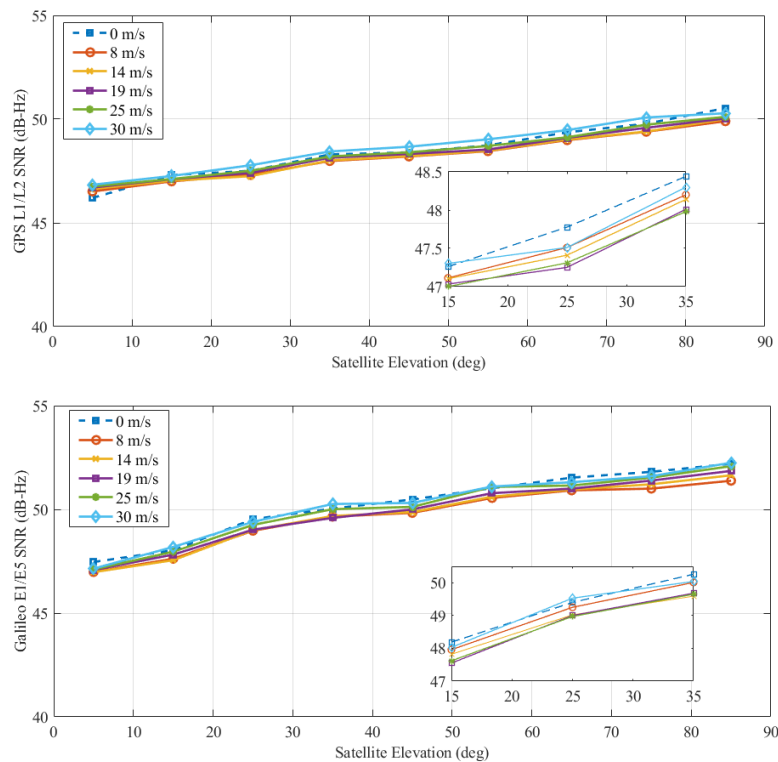


Figure 5-8: Dual-frequency SNR for static and kinematic multipath physical-statistic simulations. Average values pro elevation bins are illustrated separately for GPS and Galileo

Nevertheless, it is difficult to identify a pattern in the SNR by comparing the static and kinematic simulations. They show very close values within 0.5 dB difference. Therefore, no conclusion can be drawn regarding this aspect when simulating multipath by using the hybrid model. This was expected, as the investigation of signal attenuation showed approximately equal values in all situations. A limitation of the carried out simulations is the lack of a real receiving antenna. A GNSS antenna is a component of the signal processing chain and it influences the multipath impact on the receiver. This

is the case because of the presence of the antenna phase and gain pattern. Since during the simulations an isotropic i.e. ideal antenna pattern is used, the resulted SNR values might deviate from the reality.

5.3.4 Impact on position

After analyzing the multipath attenuation and its impact on the SNR, the last investigations are made on the coordinates. For comparison purpose, six multipath free simulations are carried out with the same HiL setup. Having both error-free and multipath measurement output, the absolute 3D root mean square error (RMSE) is computed for each simulation. For this purpose, the method presented in section 2.4.3.5 is used. To analyze the computed errors, these are modeled by statistical distributions corresponding to each performed simulation. The errors for each simulation fitted the lognormal distribution. The left side of Figure 5-9 shows the fitted distribution of the 3D RMSE in the static simulation. On the right side of Figure 5-9, the results for kinematic simulations are plotted. By comparing the two cases, it is noticed that the errors distributions are similar. This means that the simulated multipath with the hybrid model has the same effects on the receiver for all the simulations.

By looking at the fitted lognormal error distributions in Figure 5-9, it can be noticed that the expected value lays around 0.4 meters. The differences between the simulations are in the centimeter range. The variances for the fitted distributions lay in the interval from 25 to 29 centimeters. Comparing distributions plotted in Figure 5-9, it can be concluded that the positioning errors are spread within the same interval for multipath simulations with all velocities. The settings for all simulations are identical except for the velocity and the only simulated error is multipath. Since the error distributions are similar in all cases, this indicates that the simulated multipath remains similar despite the kinematics.

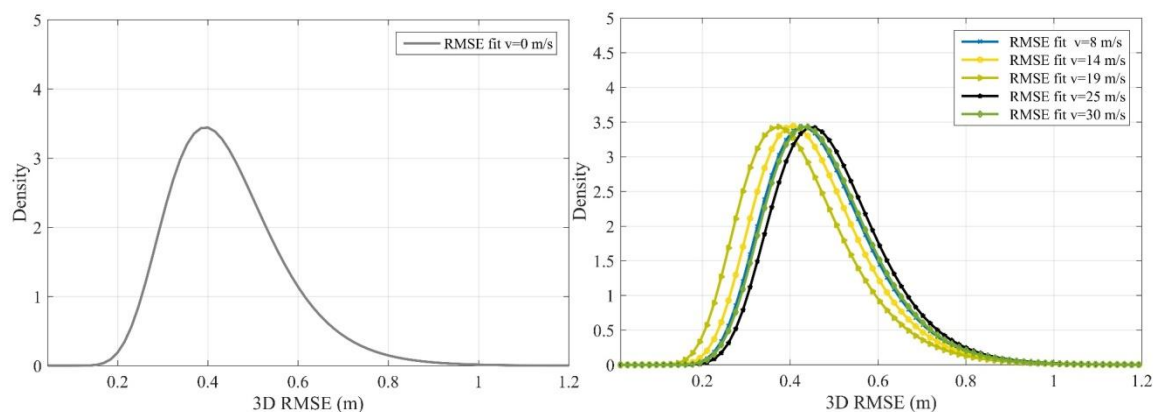


Figure 5-9: Error distributions resulted from simulations with physical-statistical multipath model in static and kinematic situations

The tracking loop filter bandwidth impacts the quality of the measurements, when multipath is present. In kinematic conditions, the bandwidth is expanded, to keep the GNSS phase-locked and to avoid cycle slips (Mao et al. 2004). A wider bandwidth allows more frequencies of the signal to be processed and despite the noise, the correlation with the receiver internal replicas can identify the multipath component in the incoming signal. This can reduce the error due to multipath on the GNSS observation and consequently lead to an enhancement of the position result.

5.4 HiL simulations with multipath ray-tracing algorithms

5.4.1 Simulation environment

In this section, the second multipath modeling technique is investigated. This approach models the multipath in a deterministic way, through ray-tracing. The theoretical background of the method is detailed in section 3.5. By means of these modeling techniques, the multipath components are resolvable and a temporal dispersion is observed. To compare these multipath model capabilities with the previous one, the six HiL simulations are performed again. The only difference is that within these runs, the multipath parameters are determined deterministically. The simulation chain is the one presented in Figure 5-1, where the channel parameters are computed by means of ray-tracing. A screenshot during the simulation is shown in Figure 5-10. The lines represent the incoming GNSS signals and their color varies, depending on the ray nature: LOS, reflection or refraction. A visual inspection reveals that the created environment determines two kinds of reflections/diffraction: short-range and long-range. The short reflections/diffractions are caused by the car structure and the metallic barrier that delimits the road. The source for the long-range multipath is the natural environment (i.e. hills, mountains). Different objects in the created 3D scene are attributed to various materials. The multipath attenuation is computed based on material's reflection coefficients, as shown in section 3.3.

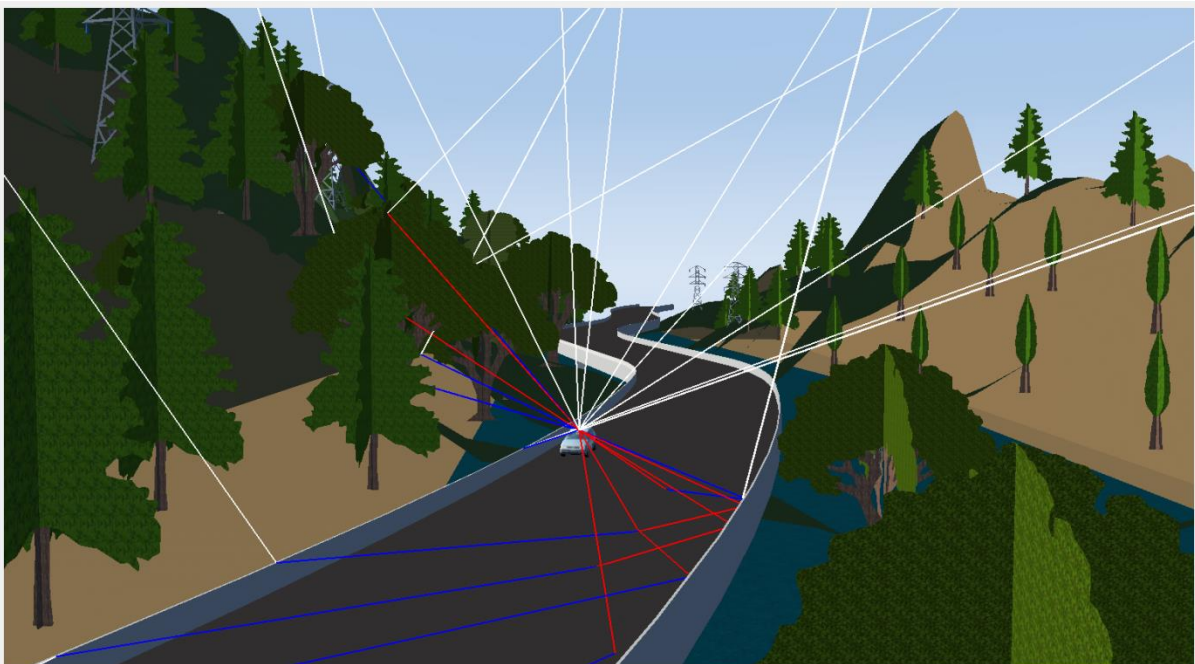


Figure 5-10: Multipath simulation with Sim3D. The environment is represented by the generated 3D model; the white lines show the LOS signal, the red lines stand for reflection and blue lines for diffraction

Similar to the previous scenario, the simulated signals are GPS L1 and L2, Galileo E1 and E5b. To study the multipath impact for a static use case, as well as for different velocities, the developed HiL setup is used to carry out six ray-tracing simulations. All the settings (see Appendix B.2) remain identical during the six simulations, except for the user velocity. The same trajectory is simulated with the following velocities: 8, 14, 19, 25 and 30 m/s (i.e. approximately 30, 50, 70, 90 and 110 km/h). These velocities are chosen, because they represent different street sectors.

Similar to the setup in the previous section, a static simulation is performed, in order to assess the differences compared to the kinematic simulations in the same environment. In all simulations, the strongest two multipath reflections and diffraction are considered. Several simulations revealed that using more than two reflections and diffraction for the simulated environment leads to creating weak GNSS signals, which the receiver is not able to track.

5.4.2 Simulated multipath parameters

This section explores the type of multipath delays that are created in the same environment, but considering different user velocities. The cumulative probabilities of the delays from the deterministic multipath computations, both in static and kinematic simulations are computed. These are shown Figure 5-11. The probability is shown from 0.5 for clarity. The delays due to reflections lay in the range from zero to 400 meters. The plot reveals that the multipath delays which are produced for different velocities follow a similar trend. The probability of having delays up to 50 meters due to multipath is higher as the velocity decreases.

In the case of static simulation, the probability does not follow the pattern of the kinematic user. The different pattern for the static case was expected, as the multipath varies in the static case only due to the satellite movement. Overall, results show that for the performed simulations, the highest density of multipath delays lays within the interval from 0 to 200 meters. Nevertheless, delays up to 400 meters are produced during all simulations.

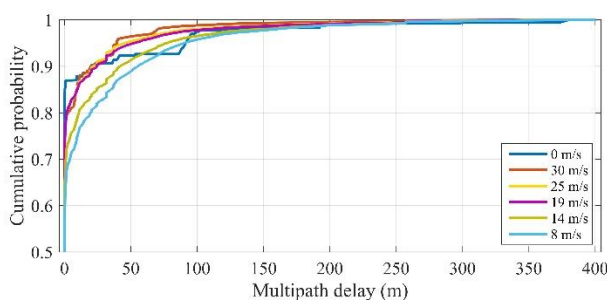


Figure 5-11: Cumulative probabilities of multipath delay for static and kinematic simulations. The multipath delays are computed in the same environment by means of ray-tracing.

To show the main difference between a static and a kinematic multipath channel, the delay spread over simulation time is plotted on the left side of Figure 5-12. During the static simulation, the delays change is determined by the satellite movement only. The upper plot in Figure 5-12 depicts the multipath which is produced in these conditions. It is noticed that the delays have constant behavior during the simulation and they change slowly, according to the satellite movement.

The opposite occurs when the user is moving. As multipath is strongly dependent on the geometry, the delays change fast, according to the surrounding environment. This is shown in the second plot of Figure 5-12. However, the user is static in the first 200 seconds of the simulation, where the delays show a constant value. This is set up intentionally at the beginning of the simulation, so that the signals are tracked by the receiver, before starting the kinematic simulation in multipath conditions. After the 200 seconds, the user starts moving. Fast changing delays occur, as a consequence of the user movement, because the distances to obstacles in the 3D model are changing.

Although the error magnitude resembles the static channel, the behavior is different. Consequently, the receiver perceives the multipath error also in a different way. The average multipath delay produced during the studied velocities is plotted on the right side of Figure 5-12. The trend is decreasing while user-velocity is increasing. This phenomenon occurs due to satellite movement and sampling of the route at different velocities. Assuming the same trajectory and environment, the geometry is favorable to bigger delays, in average, for lower velocities. This is because, within a multipath event for a specific route point, the user spends more time in the unfavorable geometry, due to the low velocity. On the contrary, when the velocity increases, the user spends less time there. This is also visible when comparing the multipath delays in Figure 5-12. For the static case, there is a bundle of delays near 400 meters, which vanish in the kinematic multipath channel.

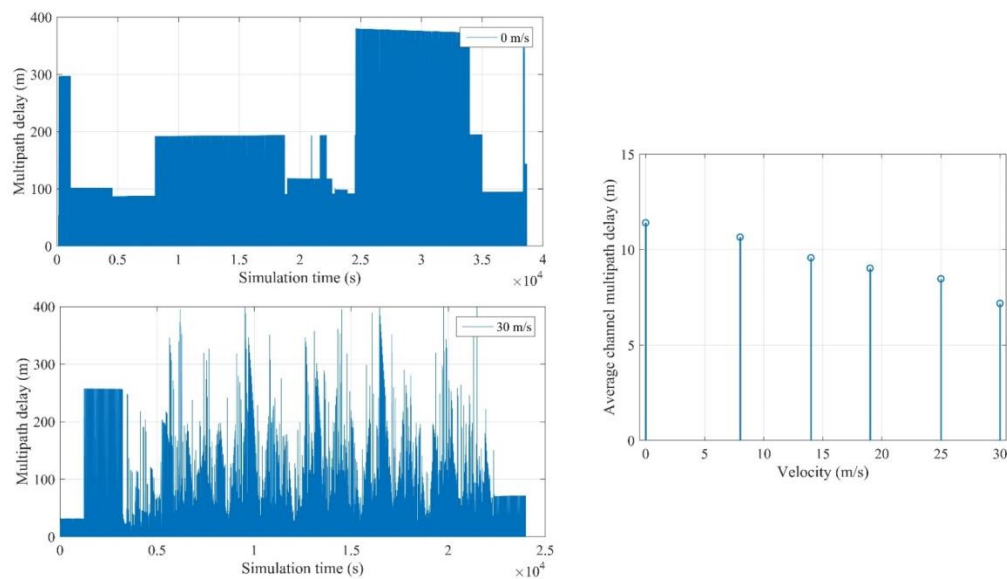


Figure 5-12: Multipath delays for a static and high kinematic user in the same environment

As this multipath model takes into account the reflection coefficients of the multipath sources, the signal attenuation due to reflections is analyzed. Similar to the investigation on the reflections delay, Figure 5-13 shows the power loss behavior and magnitude for a static and high kinematic user. On the right side, the average power loss due to multipath at various velocities is revealed. The plots on the left side are zoomed in, for clarity reasons.

As expected due to the behavior of the delay, the signal attenuation in the static case has a repetitive non-changing pattern. In contrast, in the kinematic simulation, irregularities appear as a consequence of the changing path delays. Regarding the average power loss, significant differences between simulations are present. The computations reveal stronger multipath delays for higher velocities. This trend is decreasing with velocity. Given the dependency between the signal power loss and the travelled path, it was expected that in the case of smaller delays, the power loss is also smaller.

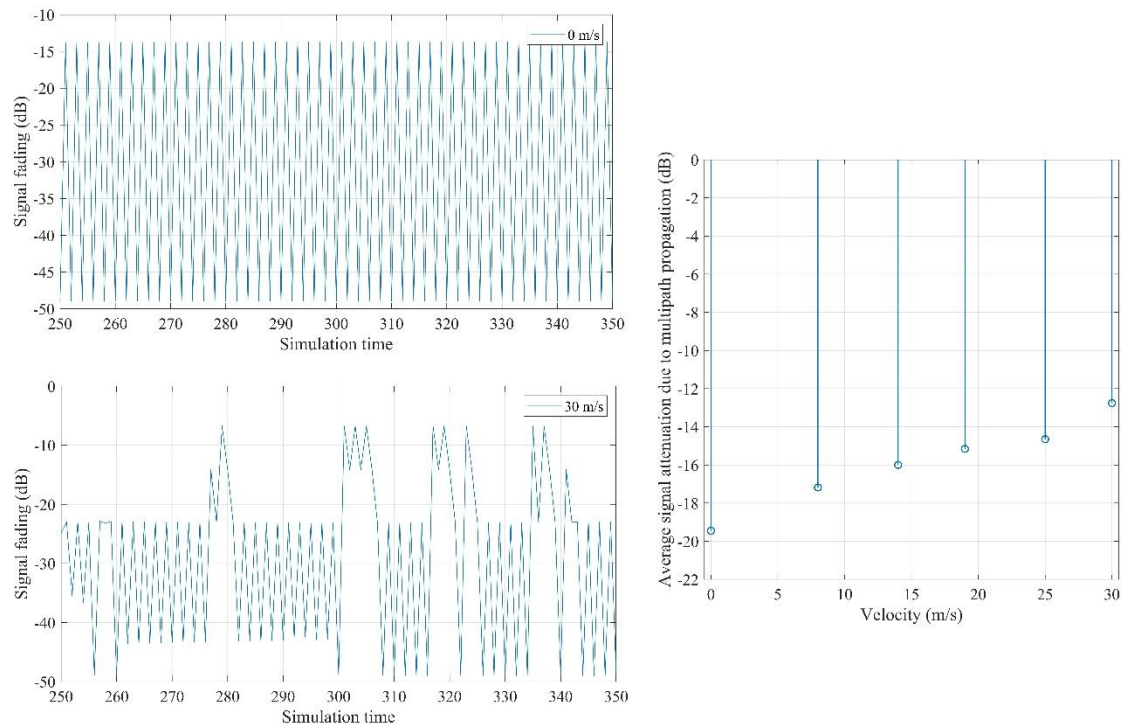


Figure 5-13: Zoom for a short time period into signal attenuation for static and kinematic users. Average power delay per complete duration of simulation is plotted on the right side

5.4.3 Impact on GNSS observables

To determine the multipath behavior and magnitude for the simulations from the receiver point of view, the first step is to convert the NovAtel output data to a RINEX format. Next, the errors on pseudorange due to multipath are computed. This is done for the static simulation with the algorithm presented in section 4.1 and for the kinematic one with the algorithm presented in section 4.2. Then, the mean value of the error pro elevation intervals is computed, as presented in section 4.1.2. This evaluation is performed on both simulated frequencies of GPS and Galileo. Figure 5-14 shows the results for the first frequencies, namely L1 and E1, with respect to the satellite elevation. The result for the different simulated velocities, as well as for the static simulation are overlapped for a better comparison.

It is noticed that the multipath error magnitude is more significant on GPS L1, compared to Galileo E1. For the simulated environment, the differences in terms of multipath between the two frequencies are approximately 10 cm. The better performance of Galileo compared to GPS can be explained by the modulation scheme of the two navigations systems and the signals' bandwidth. Galileo signals have the Binary Offset Carrier (BOC) modulation scheme (CBOC for E1 frequency and AltBOC for E5) and wider signal bandwidth. According to Rodríguez (2014) due to these characteristics, Galileo signals have a lower sensitivity to multipath signals, compared to the Binary Phase Shift Keying (BPSK) modulation scheme of GPS (Ward et al. 2006). The advantage of the BOC over BPSK modulation is that the BOC modulated signals have narrower correlation peaks. These lead to improved signal tracking and consequently to multipath rejection.

Regarding the error evolution, with respect to the elevation bins, the behavior is descending, as expected. The reason is that the satellites at low elevation angles are more likely to suffer reflections and diffractions, compared to the satellites situated in zenith direction. Nevertheless, in the case of GPS, an increase of the multipath bias occurs for the interval $65^\circ - 90^\circ$. A possible source is the car structure, where the antenna is mounted, that produces strong reflections. Moreover, an ideal antenna is used for all simulations. Thus, the gain pattern does not reject the signals coming from lower elevation angles, as in the case of a real antenna. Consequently, the impact is visible on the GPS error magnitude. In the case of Galileo, this is not visible, as the receiver can cope with the short-range reflections, due to the enhanced signal structure.

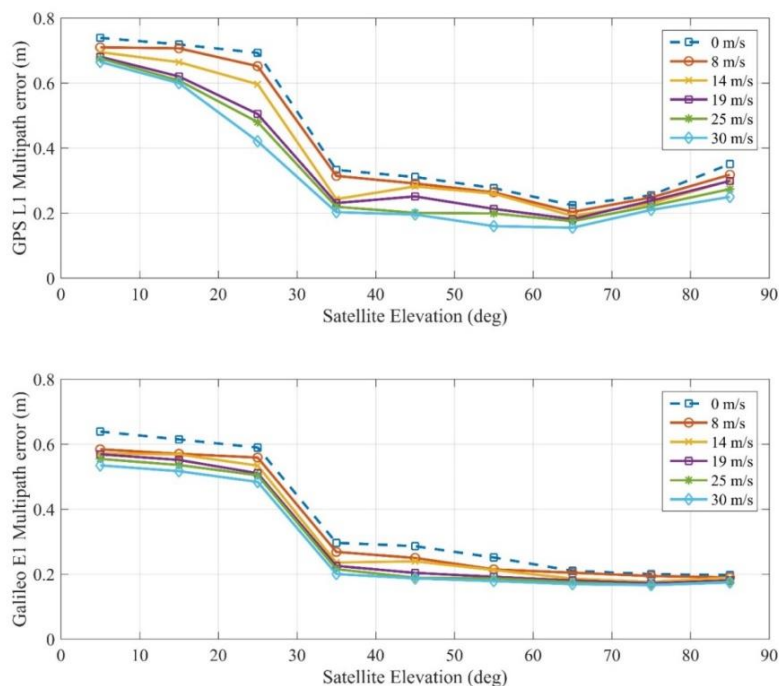


Figure 5-14: GPS L1 and Galileo E1 pseudorange error due to multipath for static and kinematic users. The multipath estimate contains receiver noise

Another interesting aspect is that the multipath distribution over the elevation angles is similar for all simulations. This reveals the environment correlation with the error magnitude. The sudden decrease from 25° to 35° indicates that the multipath occurrence is less likely for satellites situated above 35° in the investigated environment. Another finding based on the performed simulations is that multipath affects the pseudorange observations differently for a static and a kinematic user. The latter one shows a decreased multipath error, due to the receiver architecture and the multipath properties showed in Figure 5-12.

As explained in section 3.1, the multipath propagation for a static receiver results in an error with sinusoidal pattern. The amplitude of the error is determined by the reflector position with respect to the receiving antenna, the reflector material properties and the satellite position. In kinematic situations, multipath error properties change, due to the additional time-varying reflector distance, as

shown in the previous section. Consequently, the sinusoidal frequency vanishes and the multipath error can be described as noise (Beitler et al. 2015). Due to these characteristics, the receiver tracking loop filter presented in section 3.6.1.4 is able to filter multipath out, as shown in Winkel (2000). Simulations to prove this fact for the used receiver are described in section 5.2.2.1.

Carrying out kinematic simulations for the same trajectory and environment at different velocities revealed that in these conditions, the multipath error is inversely proportional to the velocity. This means, that the multipath error decreases as the user accelerates. This is a consequence of the multipath propagation behavior. As shown previously in the analysis of the simulated multipath, due to geometrical aspects, the average multipath delay that is produced decreases with the velocity increase.

Figure 5-15 shows the results for the second pair of frequencies of GPS and Galileo, namely L2 and E5b. This evaluation revealed the same multipath behavior as for the first frequencies. That is, the decreasing trend with respect to the satellite elevations, the improved performance of Galileo over GPS and the improvement in the kinematic case over the static one. However, the overall multipath error is larger on L2 and E5b. The lower performance on L2 can be explained by the signal reference power level (Yedukondalu et al. 2009).

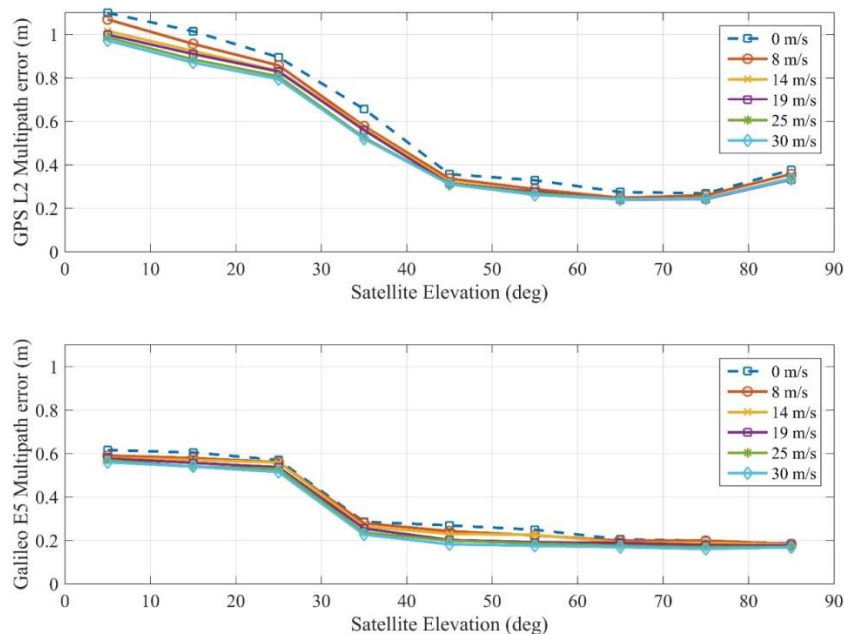


Figure 5-15: GPS L2 and Galileo E5b pseudorange error due to multipath for static and kinematic user. The multipath estimate contains receiver noise

GPS L1 and L2 signals transmitted power levels are -130 dBm and -136 dBm respectively. As a result, the measurements are noisier on L2, compared to the first frequency. Thus, L1 frequency has a better performance than L2. The difference is more significant at the lower elevation angles. As E1 has the power reference -125.5 dBm and E5 -128.5 dBm, the second frequency is noisier for Galileo as well. Nevertheless, the differences of the multipath errors are not visible as for the two frequencies of GPS, but they are rather similar. This is the consequence of the simulation results in 5.4.2 and the short-range multipath error magnitude for the Galileo signal structures.

The presence of multipath affects not only the pseudorange measurements, but also the signal-to-noise ratio. The theoretical connection between multipath and SNR is detailed in section 3.6.4. As the SNR indicates the presence of multipath as well, the values for the investigated scenario with respect to the satellite elevation are plotted in Figure 5-16 for GPS and Galileo.

Comparable performance can be depicted by comparing GPS with Galileo. Direct proportional growth of the SNR values with respect to the elevation is revealed. This shows an agreement with the findings related to the pseudorange multipath error. The lower elevations are more biased; therefore, in this range the SNR is lower. In terms of user velocity, the same trend is followed. To distinguish between static and kinematic users, the SNR is higher, although the code is mostly affected according to the previous findings. Nevertheless, the SNR of the signal is not related to the multipath only, but also to the receiver's internal architecture.

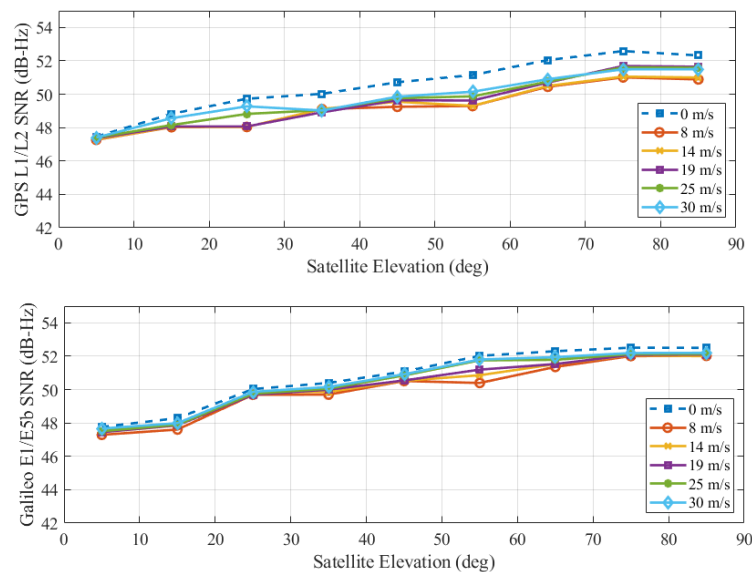


Figure 5-16: Dual-frequency SNR (signal-to-noise ratio) average pro elevation for the same route simulated at different velocities in multipath conditions

Considering the theoretical aspects with respect to the receiver (see Appendix C) presented in Section 3.6.1, it is to be considered that the signal noise that is entering the receiver is controlled by the tracking loop filter. As described in 3.6.1.4, the receiver noise bandwidth of the tracking loop filter is a trade-off between accuracy and robustness to user dynamics. This is the consequence that for kinematic users the bandwidth must be larger to cope with the signal dynamics. This implies that the signal can be tracked, but has the disadvantage of allowing noise to enter the tracking loops. On the other hand, for a static user, the bandwidth can be limited to a narrow one. Since the GNSS signal in these conditions does not suffer sudden changes, a narrowband bandwidth is sufficient to keep track of the signal in stable conditions. The advantage of a narrower filter bandwidth is that it allows less noise to enter the tracking loops. This has an impact on the resulting SNR. Nevertheless, under dynamics, the receiver would not be able to track the signal by using the same bandwidth. Thus, the noise that is present in the SNR estimate is not only the resultant of the multipath, but also the different tracking loop procedures according the user state.

5.4.4 Impact on position

Further analysis is performed, to study the impact of the computed multipath error magnitudes at the coordinate level. In order to obtain the position deviation due to multipath, six additional multipath free simulations are carried out. Each of these simulations corresponds to the ones that are performed to analyze multipath. This means that the settings remain identical, but this time no multipath is simulated. In this way, the impact on the receiver due to multipath can be computed, by having the multipath-free simulations as a reference.

Two sets of coordinates are available: one set from the six multipath simulations and one set from the multipath-free reference simulations. After synchronizing the position between the multipath and multipath free simulations, the root-mean-squared error (RMSE) is computed as shown in section 2.4.3.5. Therefore, for both static and kinematic simulations, the RMSE is obtained. To better visualize the spread of the error for each use case, the statistical distributions are computed and plotted. Figure 5-17 shows the results for the static case on the left and for the kinematic case on the right. The two situations are plotted separately and scaled differently for clarity. For all simulated velocities, the RMSE errors are characterized by normal distributions.

Considering the static simulation first, it can be noticed that the RMSE spread lays from 1.43 meters to 1.55 meters. Therefore, the positioning error oscillates within a 0.12 meters range. On the other hand, the RMSE results for the kinematic use cases show a significant difference. The positioning error is spread in the interval from 0.5 to 2.5 meters. This means that compared to the static simulation in the same environment, the kinematic position error fluctuates within an interval that increases 16 times.

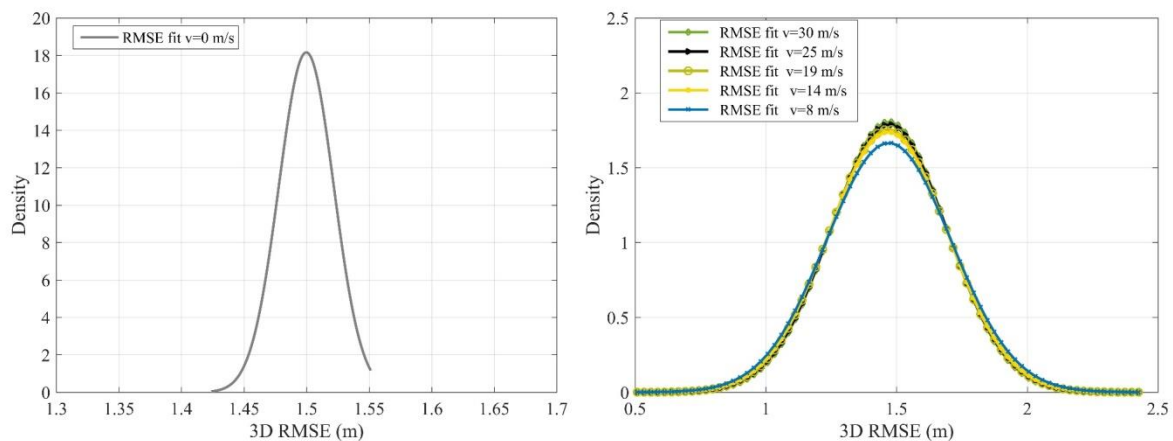


Figure 5-17: 3D RMSE normal distribution fit for the static position (left) and kinematic position at different velocities (right)

The investigations on the position RMSE in kinematic conditions reveal a similar behavior as seen on the right side of Figure 5-17. However, the RMSE distribution for the static simulation shows a different pattern which correlates with the higher positioning errors found for this case. The differences between the static and kinematic RMSE is connected to the different behavior of the multipath delays for a static versus kinematic user .

5.5 Summary

Despite the existent approaches which have been developed to understand multipath, this error is challenging due to its numerous dependencies. Varying aspects like the number of multipath reflections, multipath signal strength, diffraction, scattering or ray geometry make it difficult to obtain a model, which characterizes the multipath propagation in all use cases. The question that arises in this chapter is the following: which multipath propagation model is more adequate to simulate multipath for kinematic users. The problem is tackled by implementing hybrid and deterministic multipath propagation models in a HiL setup. The advantage of this approach is that the computed multipath parameters by this method can be simulated on GNSS signals. Therefore, it is possible to analyze the impact of different multipath reflections on a hardware receiver. In this way, the complete chain from the satellite to the receiver is analyzed.

To find out which of the two multipath models is more adequate for the investigated use case, various simulations are carried out. Within the simulations, multipath parameters are computed with both methods for the same environment and trajectory. Error free simulations are carried out as well, to have a position reference for each multipath simulation. The following aspects are analyzed: the computed multipath parameters by using each method, their impact on GNSS observables and on position. On average, the hybrid model outputs stronger multipath reflections, compared to the deterministic one. Nevertheless, the latter one shows differences between the various user velocities. The impact of the signal attenuation due to multipath is visible in the SNR values that are output of the receiver. The average SNR values pro elevation bins resulted from both multipath models are consistent with the expectations. That is, a lower SNR corresponds to the hybrid model output, where the multipath is stronger. In contrast, an increased average SNR is found for the deterministic channel, where the reflections are less strong, compared to the ones resulted in the first method. Nevertheless, the differences are small, due to the lack of a receiving antenna. The gain pattern, which increases the power of the received signals, according to their angle of arrival and polarization is set to zero during simulations. Consequently, the values obtained from simulations might be different, compared to real measurements in a multipath environment.

The deterministic model outputs, besides signal attenuation, pseudorange delays for each reflected signal. Taking into consideration the behavior of multipath delays for the static and high kinematic simulations, the results obtained from the deterministic model are feasible. The reason is that in the first case, the delays change slowly, as the geometry modifications are determined by the satellite movement. In the kinematic case, the geometry changes fast with the user velocity. This is visible also in the delay variations. The results show that the delays decrease inversely proportional to the velocity. Considering the average power loss for the deterministic simulations, it can be concluded that as the velocity increases, the multipath delays are shorter and stronger. This is feasible, since the power of the received signal depends, among other parameters, on the distance from the transmitter to the receiver.

Investigations on the position estimation in both cases indicate that larger errors are produced by deterministic multipath model. Approximately 1.4 meters deviation from the reference position is found, while for the first method the error lays around 0.4 meters. The larger error is the consequence of the additional produced delays, which lead to errors on the receiver computed pseudoranges. When computing multipath with the deterministic model, errors for the same trajectory can be distinguished between the different user velocities. The 3D RMSE is the worst in the static case, where the largest

delays are also produced. Regarding the kinematic case, the error varies within 0.006 meters and the smallest error is found at the largest velocity. Another finding is that although the largest error is found in the static case, this has the lowest spread i.e. 0.13 meters. During the kinematic simulations, the positioning errors are spread in a wider interval up to 2 meters. The presented analysis in this chapter leads to the following conclusions:

- considering the presented hybrid model, it is difficult to distinguish between the multipath effects for a static and kinematic user. Nevertheless, it is possible that further optimization increases the relevance of this simulation method;
- the deterministic multipath model together with the receiver properties indicate that for the same environment, the multipath delays and positioning error are correlated with the user velocity;
- the 3D position error, produced by the multipath parameters computed with a deterministic model is larger than the one computed with the hybrid model.

Since this work focuses on the kinematic use case in multipath conditions, the deterministic modeling method is considered adequate for further investigations. The reason is that the deterministic approach showed a realistic impact on GNSS observables, as it is correlated with the user velocity.

The following chapter focuses on two multipath dependencies: velocity and environment. Experimental data from measurement campaigns are analyzed and compared against simulated data. Only the deterministic multipath model is employed for simulations in the next sections, since it proved to provide realistic results for kinematic users.

6 Multipath estimation from measurement campaigns

6.1 Introduction

This chapter presents a multipath analysis for GPS and Galileo observations, acquired for various user velocities and different environments. Additionally, a series of deterministic multipath simulations are carried out in similar environments to evaluate the agreement with the experimental data. As mentioned in the previous chapter, deterministic multipath simulations are based on a 3D model of the environment. The second focus in this chapter is to use representative 3D models for the test drive environment and not an exact duplication. There are two reasons for this:

- a) there is the need of a large amount of data to reconstruct 3D environment for a kinematic user;
- b) if the data is available, the resulting 3D model would be excessively large for computation with a deterministic i.e. ray-tracing algorithm for multipath.

The ray-tracing algorithm that is employed for multipath computation has been validated against measurements, in an identical reconstructed 3D environment in Panicciari et al. (2017) and Spirent Communications (2017). The question to be answered in this chapter is how well can the multipath error be reproduced, if instead of identical 3D models, representative 3D models are used.

This chapter is organized into three sections: measurement setup, multipath characterization for various velocities and lastly for various environments. Firstly, the equipment that is used for the data collection is detailed. Next, the multipath is characterized by measurement campaigns at different velocities to validate the simulation results. Finally, multipath is analyzed by means of simulations and measurement campaigns for highway and urban environments.

All the measurement campaigns are carried out using the same setup, so that the multipath estimation results in different situations can be compared to each other. Figure 6-1 shows a scheme of the hardware that was mounted in the car.

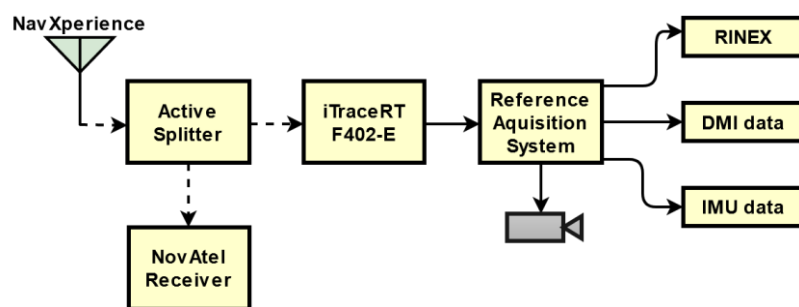


Figure 6-1: Equipment and measurement setup for the measurement campaigns. GNSS signals from NavXperience antenna are directed through a signal splitter to the NovAtel PwrPak7[®] receiver and to the reference system iTraceRT F402-E (Avram et al. 2019b)

The 3G+C maritime NavXperience antenna is a high-precise multi-constellation triple-frequency GNSS antenna and it is mounted on the car rooftop. The dashed lines represent the cables that conduct the signal to the GNSS receiver. A signal splitter is used to direct the signal simultaneously to the NovAtel PwrPak7[®] receiver and to the car reference system. The reference system consists of the

iTraceRT F402, an INS/GNSS deeply coupled inertial navigation system (see Appendix C.2). Due to the algorithm that performs data fusion, the sensor is able to suppress outliers and outputs position even in difficult GNSS environments. The horizontal/vertical position accuracy in the presence of GNSS is 2 centimeters and 5 centimeters, respectively according to iMAR Navigation & Control (2018). Although the reference system outputs a real time positioning solution, it also stores raw data: RINEX, Distance Measurement Increment (DMI) and Inertial Measurement Unit (IMU), for the post-processing purpose. Additionally, a camera provides videos from all the measurement campaigns. Despite the low quality image to avoid a huge amount of data storing, this is very useful for the multipath analysis in different environments presented later in section 6.3. The GNSS observations are stored at 1 Hz rate, during all measurement campaigns for both NovAtel receiver and reference system.

6.2 Multipath characterization for different velocities

Different multipath propagation models are investigated in chapter 5. Besides concluding which is the most appropriate for the kinematic use case, a correlation is found between the velocity and the resulting multipath error on GNSS observables. The motivation for the measurement campaigns at different velocities within this section is to assess the multipath behavior and magnitude for realistic situations. By means of the multipath estimation algorithms from chapter 4, the multipath error can be computed from real measurements in static and kinematic conditions. Discussions regarding static multipath dominated research in this field since 1980, according to Parkinson et al. (1996). It was found that the strongest multipath dependencies are the geometry and the antenna-receiver system. For kinematic applications as AD, the geometry changes constantly, according to the user velocity. Moreover, the setup (i.e. antenna, receiver) is different from other applications that use GNSS data. Therefore, investigations with the new setup are necessary.

6.2.1 Static site

In the previous chapter, simulations in static conditions showed an increased error on pseudorange due to multipath, compared to the kinematic ones. For comparison to the reality, the first measurement is carried out in static conditions. Figure 6-2 shows the area where this measurement campaign is completed. An open-sky area is chosen, so that the multipath sources are restricted to the ground and car reflections. In this way, conclusions can be drawn regarding the multipath error, for a vehicle setup in open-sky conditions.



Figure 6-2: Test vehicle in the open-sky environment during the static measurement campaign. The antenna mounted on the rooftop is visible while the rest of the equipment is installed in the car (Avram et al. 2019)

Besides investigating the error magnitudes for this measurement site, a comparison with a state of the art multipath model is achievable. Furthermore, this enables also the possibility to distinguish between the error characteristics for a static and kinematic vehicle. As multipath is created by any obstacle around the car, the parking lot was closed during the measurements. On November 20, 21 and 22, data is acquired in the presented site at 1 Hz rate, for GPS L1 C/A, L2C and Galileo E1 OS and E5b. In total, 216 satellite hours are stored.

The multipath error on the pseudorange is computed, by means of the algorithm presented in section 4.1, as it is appropriate to determine static multipath, without the need of reference data. After evaluating the recorded frequencies and sorting the results according to the satellite elevation bins, the results are plotted in Figure 6-3. On the left side, the multipath error computed for the pseudorange of GPS satellites is plotted and on the right side, the same for Galileo. The empirical multipath models, which are computed from the experimental data, show a similar behavior for both satellite navigation systems to the validated model presented in Murphy et al. (2005). Nevertheless, differences regarding the error magnitude are present. An agreement with the standard model regarding the error magnitude is found for GPS at elevation angles below 50° . For higher elevation angles, the difference of the error found due to multipath differs with 5 to 7 centimeters. This is likely to be the case because of the open-sky measurement site. In such an environment, it is unlikely that reflections occur for high elevation satellites. Regarding Galileo, the agreement in terms of error magnitude is between 6 and 10 centimeters, over all elevation intervals. However, the model presented in Murphy et al. (2005) does not include evaluation on Galileo signals, since at that time the first Galileo test satellite GIOVE-A was launched. For this reason, the computed error magnitude deviates from the standard elevation model.

Considering the error resulted from the measurement campaign, the absolute mean error is 0.15 meters and the standard deviation 0.11 meters for L1 frequency. Similar, on L2, the mean bias is 0.17 meters and 0.14 meters is the standard deviation. Although the error due to multipath has the same pattern on both L1 and L2 frequencies, the magnitude of the error is larger on L2, as also concluded in Yedukondalu et al. (2009) and Yedukondalu et al. (2013). Additionally, the resulted pattern is in agreement with the pattern from the deterministic multipath simulation in section 5.4. Although the simulated environment is hilly and the resulted multipath error magnitude reach 0.8 meters for L1 and 1 meter for L2, the increased performance of L1 over L2 can be observed. The same is concluded from the static multipath simulations with the deterministic model. Thus, simulating the multipath propagation with the deterministic i.e. ray-tracing model provides results according to real measurements, as also concluded in Weiss (2007).

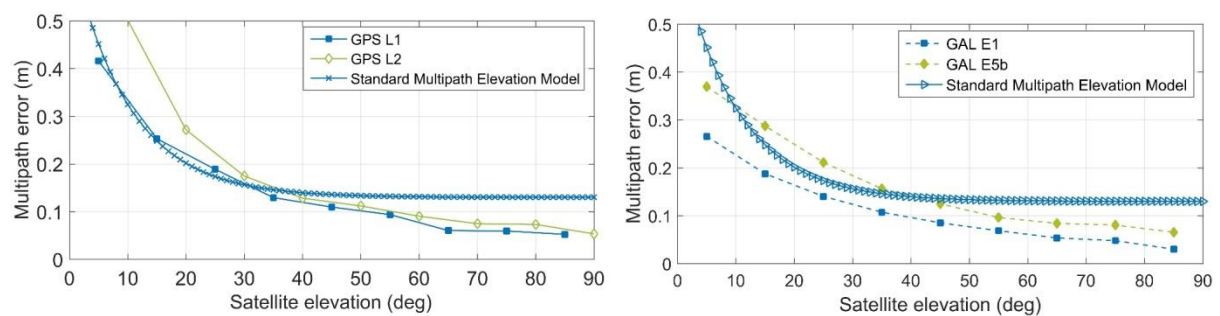


Figure 6-3: Multipath pseudorange error per satellite elevation for GPS L1 C/A and L2C, Galileo E1 OS and E5b frequencies. The multipath estimate contains the receiver noise

Regarding the performance of the two GNSS, results in Figure 6-3 depict a more significant error for GPS pseudoranges. This can be explained by the different signal modulation that GPS and Galileo have. As Galileo is recently built, it has new signals that have the BOC modulation scheme (CBOC for E1 frequency and AltBOC for E5), as documented in Rodríguez (2014). GPS signals have a BPSK modulation scheme, which is more prone to be distorted by multipath as mentioned in section 3.6. The improvement of Galileo signals is especially significant for multipath, according to Ward et al. (2006).

A further point to be considered regarding the computed models is satellite availability. Although the same post-processing method is employed for all recorded observations, the predominant data is from GPS satellites. During the static measurement campaign, from the visible satellites, 33 % are Galileo and 67% are GPS. This means that the results in Figure 6-3 contain more data for GPS elevation model than for Galileo.

6.2.2 Slow kinematic

Unlike the previous case, where the vehicle and surroundings are static, in this measurement campaign the vehicle is moving at slow velocities. The purpose is to gain knowledge regarding the multipath error magnitude and behavior when adding a new variable, namely kinematic. Additionally, this measurement campaign serves as comparison to the simulations at slow kinematics, which are previously presented in section 5. During the data collection, the environment remains static, to avoid the contribution of other aspects besides kinematic to the multipath magnitude.

Additionally, the data is recorded in the same place as previously, to keep the same surroundings as in the static measurement. Due to space restrictions, because the test drive occurred on a parking lot, the duration and velocity are limited to 15 minutes and 6 m/s i.e. 20 km/h. Figure 6-4 reveals the results, after processing the acquired GPS and Galileo observations. The analysis implied challenges due to the limited measurement time and the low SNR on the second frequency. The latter factor leads to data gaps and discontinuities of the cycle integer number. Consequently, only multipath error magnitudes of GPS L1 and Galileo E1 can be computed. The raw multipath values are plotted in Figure 6-4 due to the reduced number of available measurements. However, these offer a preliminary overview of the multipath magnitude for slow kinematic measurements. Similar to the static case, the same inverse proportionality between the error and the elevation angle is found, showing that larger errors occur for lower elevations.

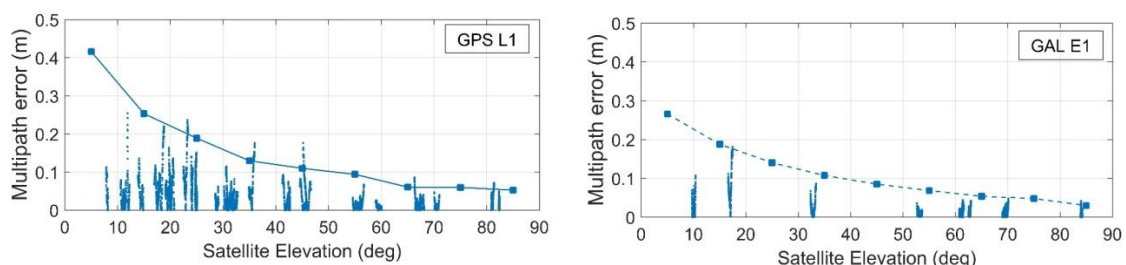


Figure 6-4: Raw multipath errors on pseudorange as a function of SV elevation for L1 C/A and E1 OS frequencies from the slow kinematic measurement campaign. The lines in the plot stand for the mean multipath error on pseudorange during the static data acquisition

Nevertheless, the magnitude of the error is significantly smaller in the slow kinematic user case. Lines in Figure 6-4 show the mean multipath error in the static measurements. These are above the raw multipath errors in the kinematic case. This is due to the changed multipath properties in the kinematic case, compared to the static one. Due to the fast changes of the multipath signal phase, relative to line of sight in kinematic conditions, the sinusoidal pattern that is explained in chapter 3 vanishes, as shown in Beitler et al. (2015). This is replaced by fluctuations, as indicated from the results of the multipath simulations in the static and kinematic conditions shown in section 5.4. For this reason, the receiver perceives multipath reflections as a noise in kinematic conditions and it is able to filter it out, by the tracking loops filters presented in section 3.6.1, Figure 3-20. The filtering capacities of receiver tracking loops are demonstrated in Winkel (2000).

6.2.3 High kinematic

To further understand the multipath error properties for a car setup, an eight-hour-long test drive is analyzed. The GNSS observations within this section are gathered in a highway environment. Similar to the simulations, this measurement campaign is investigating multipath for high velocities (i.e. 30 m/s). Nevertheless, not only the velocity changed compared to the previous measurement campaigns, but also the environment. Besides velocity, a challenging environment has also an impact on the multipath error magnitude. Although often associated with an open-sky environment, the highway comprises challenging situations due to the changing environment, closeness to the reflectors, vegetation, traffic signs and bridges. Figure 6-5 reveals the typical environment during the measurement campaign and highlights the relevance of multipath investigations for this street sector.



Figure 6-5: Typical investigated highway environment. Screenshot from the video recorded during the measurement campaign

The algorithm presented in section 4.1 is applied to the gathered GPS and Galileo measurements as in the static and slow kinematic section. Figure 6-6 illustrates the results for the first frequency of both navigation systems. Since the measurements on the second frequency are noisy in the presented situation, the processing shows difficulties by means the algorithm based on code-minus-carrier. This limitation is detailed in section 4.1.3. Reference measurements are not available in order to estimate the multipath by means of the algorithm presented in section 4.2. Therefore, the evaluation is completed with code-minus-carrier for L1 and E1 only.

A similarity to the prior findings is the decreasing pattern of the error with the elevation increase. Nevertheless, in terms of the multipath, the magnitude is increased with approximately 0.2 meters

compared to the two previous analyzed situations. Galileo reveals a slightly better performance than GPS. This is in agreement with the prior results.

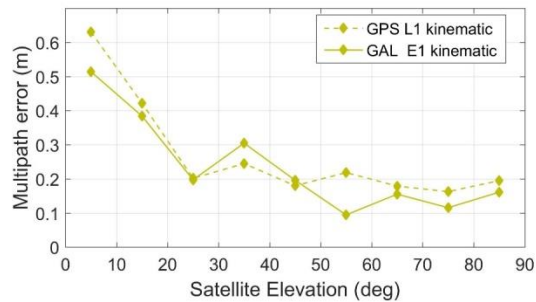


Figure 6-6: Multipath absolute mean error on pseudorange as a function of satellite elevation for measurements recorded during the highway measurement campaign

The error magnitude due to multipath is larger for this measurement campaign compared to the previous ones in open-sky. This confirms that although the highway is considered an open-sky environment, the other traffic participants and vegetation shown in Figure 6-5 do have an impact on the GNSS observables.

Multipath contaminates both pseudorange measurements and SNR values as shown in the theory presented in section 3.6.4. To establish whether this connection can be depicted in the acquired measurements, the mean SNR is computed for the same elevation bins employed for pseudorange multipath. Figure 6-7 provides the results separately for GPS and Galileo from static and fast kinematic data. The correlation between SNR and pseudorange errors due to multipath is confirmed through the plotted average. It is visible that more noise is present in the kinematic data, leading to a lower SNR average for both. The differences between the two user-cases lay between 2-5 dB-Hz, although the satellites situated below 30° are similarly affected. Additionally, the increasing tendency of the SNR average confirms the correlation to the computed multipath errors as well. Small SNR values indicate a noisy signal, whereas the large values indicate the opposite. This means, that the SNR values are inversely proportional to the multipath errors which affect the signals. When comparing the SNR pattern with the computed multipath in Figure 6-3, Figure 6-4 and Figure 6-6 it can be noticed that they are inversely proportional. The same connection between the multipath error on pseudorange and SNR is confirmed by the simulations presented in section 5.3. It is to be mentioned that besides multipath, the antenna pattern influences the SNR values in the Figure 6-7 as well. Lower elevation signals have a decreased gain compared to the ones which arrive from zenith.

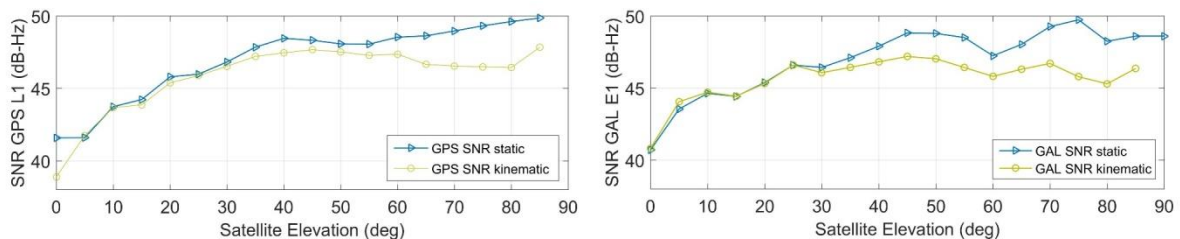


Figure 6-7: Average SNR for GPS L1 and Galileo E1 in static and high kinematic measurement campaign as a function of satellite elevation

6.2.4 Impact on position

To determine the impact of the computed multipath magnitudes at the coordinate level, further analysis is performed. The vehicle position is computed by means of code ranging differential position (DGNSS) using virtual reference stations (VRS) as detailed in section 2.6.1.1. The RINEX files used for post-processing purposes with the mentioned algorithm are the output from NovAtel PwrPak7[®] during the measurement campaigns. According to Hofmann-Wellenhof et al. (2007), Sennott & Pietraszewski (1987), Lachapelle et al. (1989), the multipath errors do not cancel out by using differential positioning algorithms. If the DGNSS algorithm is applied and assuming that the VRS is error-free, multipath is the main error source that affects the computed coordinates.

The data for the reference position during all three measurement campaigns is provided by the GNSS/INS integrated system, iTraceRT 402-E, as described in section 6.1. For evaluation of the errors due to multipath, the difference for each epoch is computed between the reference coordinates and the coordinates obtained from DGNSS. Figure 6-8 reveals the mean values of the estimated position errors. The plot with the error results reveals the same pattern as in the case of pseudorange multipath for the three analyzed user-cases. As shown previously, the error on pseudorange caused by multipath is larger in the static case as in the slow kinematic one. In the same way, the positioning error is larger in the static case than in the kinematic one. The same pattern is found in the simulation results presented in section 5.4.4. The largest positioning error is found in the third measurement campaign, which is in a challenging environment. This is in agreement with the multipath error magnitude found in this environment, which has shown the largest error as well. Nevertheless, it should be considered that the results in Figure 6-8 might have contributions from other errors besides multipath as well.

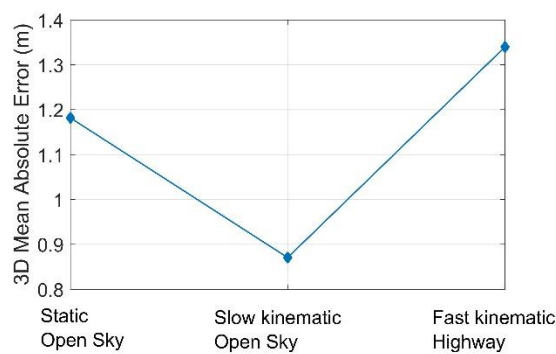


Figure 6-8: Mean absolute 3D RMS error base on code DGNSS during the three measurement campaigns (Avram et al. 2019)

The magnitude of the multipath error on pseudorange observations is a function of receiver tracking loop bandwidths, correlators and discriminators. In the view of gathered data, the highway dataset proved to be the most affected by multipath. The findings in Figure 6-8 related to the position are in agreement, as the largest error is found in the highway measurement campaign. Despite the similarities between the positioning errors and estimated multipath, other elements that impact the coordinate's accuracy have to be considered as well. Table 6-1 summarizes the average position dilution of precision (PDOP), its standard deviation (SD) and the average number of satellites. The average PDOP values indicate excellent satellite geometry in all three situations. On the other hand,

the standard deviation differs for the last user-case. This indicates that the changing environment due to high kinematics on highway produces fluctuations.

Table 6-1: GNSS quality statistics for the three measurement campaigns

	Static	Slow kinematic	Fast kinematic
Avg. PDOP	1,0	1,1	1,5
SD PDOP	0,2	0,2	0,9
Avg. No. Sat	16	16	12

6.3 Multipath characterization for different environments

As shown in the previous sections, the error magnitude is not only influenced by the vehicle velocity but is also strongly dependent on the surroundings. Therefore, measurement campaigns are conducted to gain information about the error. Figure 6-9 shows that even restricting to a use case, the defining features can vary. In order to perform the multipath analysis, this section narrows down to the following environments: intercity highway and urban roads. The two categories are defined according to the distinct multipath sources. As the nearby buildings are typical for an urban area only, the error magnitude and behavior are expected to differ from the other case.

The following sections show experimental and simulated multipath results for the two proposed environments. Due to the previous investigations which show that the deterministic model (i.e. ray-tracing) is adequate for multipath simulations, this approach is further employed. In the literature, ray-tracing techniques to model multipath include a precise 3D reconstruction of the reality. The method used to be feasible due to the nature of multipath simulation, which is for a static receiver. Nevertheless, for a kinematic use case, it is unfeasible to model the entire trajectory of a highway measurement campaign. The high velocity leads to a long trajectory, therefore the complexity and data input of such a 3D model is massive. Moreover, objects in the scene are represented by polygons and more details result in more polygons needed in the 3D model. This leads to a computational burden and slows the ray-tracing simulation or makes it impossible. Considering this, a different approach is proposed for this research: synthetic 3D models. The simulation setup which is employed for each environment is detailed in sections 6.3.1 and 6.3.2. Multipath estimation from simulations is validated against experimental data via statistical comparison regarding the error range, characteristic behavior, distribution, and signal SNR.



Figure 6-9: Different types of highway environments. These represent screenshots from recordings during measurement campaigns

6.3.1 Intercity highway

A highway is characterized by high kinematics, an open-sky area, and wide lanes. Nevertheless, reflection sources like safety fence, traffic participants, traffic signs and vegetation are present as well. To assess the multipath magnitude for this kind of environment, simulations and measurement campaigns are carried out and the results are processed.

Simulation environment

As previously mentioned, the multipath is simulated deterministically, i.e. with ray-tracing algorithms. The test bench remains identical to the setup presented in 5.2. Nevertheless, the 3D model that is used in this section is developed to fit the investigated environment, which is the highway. Figure 6-10 shows the synthetic 3D model which is created for this purpose. On the left side, the

vehicle trajectory used for the 3D model is plotted. The simulated velocity is between 110-130 km/h, representative to the simulated street segment. The 2D geographic coordinates of the trajectory are plotted and the segments which identify the 3D scenarios are marked with different colors. The arrangement is as follows: the first five minutes are static. The initial static, error-free simulation has the scope of having track of signals when starting the multipath simulation. The segment from a_1 to b_1 corresponds to the urban highway. This is represented by buildings, light poles, and fence on both sides of the road. Segments $b_1 - a_2$ and $b_2 - a_1$ represent the open sky highway, where the multipath sources are represented by steel safety fence and traffic signs. Lastly, in the $a_2 - b_2$ part, the vegetation next to the street is simulated by the forest. This approach is practical for a kinematic simulation, as the simulated vehicle is driving in a loop, allowing the data collection for a longer time, in a changing environment without the need for extensive 3D models. The simulation parameters that are employed are the following:

- multipath reflections: the strongest two multipath reflections;
- diffraction;
- simulated frequencies: GPS L1, L2, and Galileo E1 and E5b;
- isotropic antenna, i.e. no gain pattern or signal rejection.

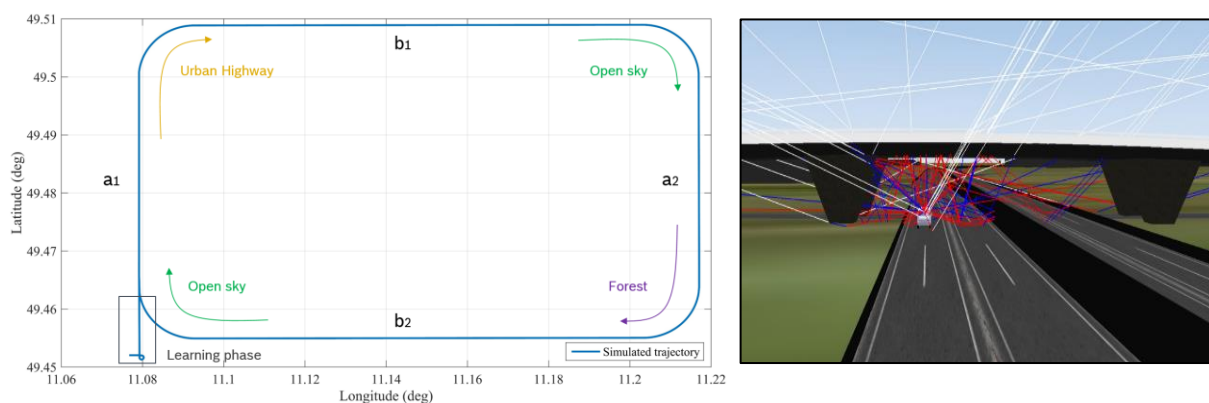


Figure 6-10: Simulated trajectory based on the 3D model. Schematic representation of the 3D model and driving direction

Measurement campaign

Empirical findings provided by simulations are compared against experimental data. For this, two measurement campaigns on the highway are carried out and analyzed. The setup in the vehicle is the same presented in Section 6.2. The data which is recorded with the iTraceRT F402-E is used to compute the reference coordinates of the trajectory. The data recorded by NovAtel is used to compute the errors due to multipath on pseudoranges and coordinates. Additional analysis based on specific situations is performed based on the measurements on the highway A6 in direction Crailsheim due to the highway alignment with respect to the parallel at $9^{\circ}51'$.

The acquired experimental data consists of four hours drive, i.e. approximately 52 satellite hours and 380 kilometers on highway. Figure 6-11 illustrates the trajectory of the vehicle during the measurement campaigns. The starting point is Abstatt and the two destinations are Würzburg and Crailsheim.

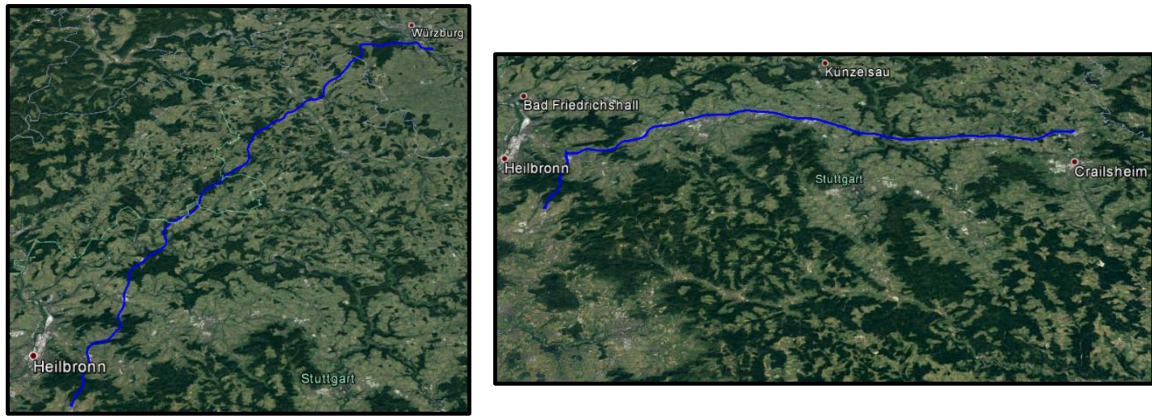


Figure 6-11: Google Earth® screenshots of the trajectory driven during the measurement campaigns. The blue lines represent the reference coordinates of the vehicle trajectory

6.3.1.1 Multipath error magnitude

The errors on pseudorange due to multipath are computed from simulations and experimental data by means of the algorithm presented in section 4.2. In the simulation case, error-free simulations are used as a reference, while for the measurement campaigns, virtual reference stations (VRS) are utilized. Figure 6-12 shows GPS L1 multipath time series from measurement and simulation in the urban highway environment, as well as the SNR estimated by the receiver. The multipath amplitude in the interval from -1 to 1 meter is reproduced by means of simulation, although the time series cannot be compared by timestamp as the ephemeris data and trajectories are different. It can be noticed that in the SNR figure from the measurement campaign the multipath signature is present through oscillations of different frequencies. The different frequencies indicate the presence of multiple reflections of the GNSS signal. The bottom plot in Figure 6-12 below shows that this influence is also present in the SNR from the simulations. The theoretical relationship between multipath and SNR is presented in 3.6.4. It can be noticed that the SNR values during the simulations vary less compared to the measurement campaign. This is the effect of the ideal antenna used during the simulations. An ideal i.e. isotropic antenna is insensitive to multipath and collects all the signals without applying gain or loss.

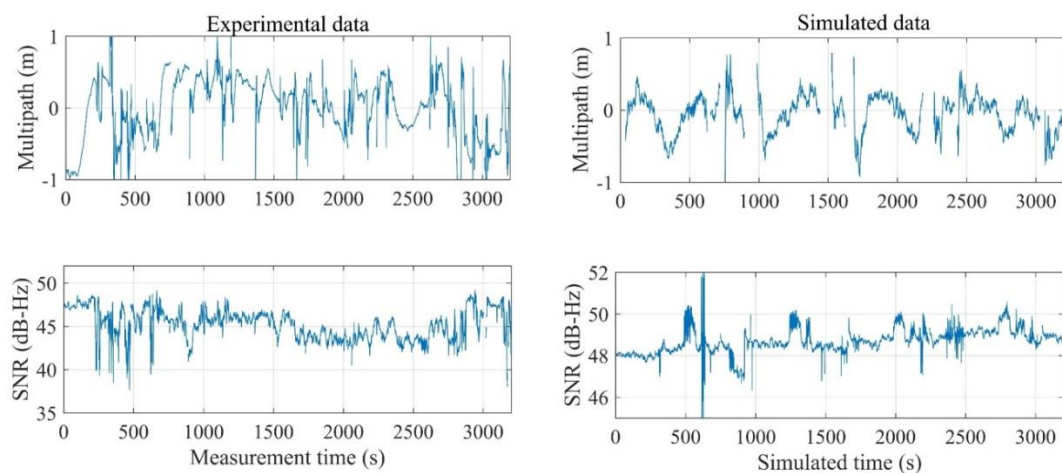


Figure 6-12: Experimental and simulated multipath time series for different GPS L1 satellites in urban highway scenarios. Corresponding signal-to-noise values are plotted below multipath estimates

Multipath depends mainly on the satellite elevation and the vehicle surrounding. As the environment from simulations and measurement campaigns is similar, the comparison is made over the satellite elevation intervals. The evaluation of multipath error is done as presented in section 4.1.2. This procedure is applied for the evaluated frequencies and constellations: GPS L1, L2 and Galileo E1, E5b. Figure 6-13 shows the multipath statistics for GPS and Figure 6-14 for Galileo. Overall, the plots reveal an error increase for the second frequency, as previously found in sections 5.4.3 and 6.2. Comparing the experimental measurements with the simulated data, these agree within 20 centimeters. The plot proves that the simulated multipath produced larger pseudorange errors over all elevation intervals, except for Galileo E5b between 30° and 40°. The reason why the simulation outputs a larger error is that the 3D model objects produce more severe multipath. This is likely to occur in the highway section with buildings besides the street, due to their closeness to the vehicle, due to their density and height, compared to the reality.

Additionally, the GNSS antenna plays an important role, as previously detailed. The analysis showed that in reality, the multipath error does not always decrease when the elevation increases. This applies to both GPS and Galileo. The result ties well in with the previous results presented in section 6.2, where the same conclusions are drawn. GPS spikes in the interval 20°- 30° to 30°- 40° confirm the presence of random reflectors in reality, which is not accounted for in the 3D model. The reflectors which produce this phenomenon can consist of static or dynamic traffic participants. Due to the position and closeness to the GNSS antenna, these produce multipath reflection and diffraction which come from high elevations. Therefore, it is likely that the antenna processes multipath signals taking into account the angle of arrival. Although static reflectors can be modeled in a 3D scene, the traffic is a challenging part, due to the arbitrary presence.

Considering the simulation results for GPS, an error increase due to multipath is noticed for the satellites situated at 80°- 90° elevation compared to the values for the previous interval. Simulation results from section 5.4.3 point out the same pattern. However, the 3D models used in the simulations are different, but the car and antenna models are identical. This leads to the fact that the satellites located at the high elevations are affected by car reflections and not by the ones in the surroundings. Since in the measurement campaigns a real antenna was used and the signals arriving from low elevations are not considered, this increase of the multipath error is not present. The 3D model used for simulations is representative for measurement campaign environment, but is not modeled precisely. As mentioned in 6.1, the scope is to verify the agreement extent between multipath error magnitude from simulations and reality by reconstructing 3D similar environments.

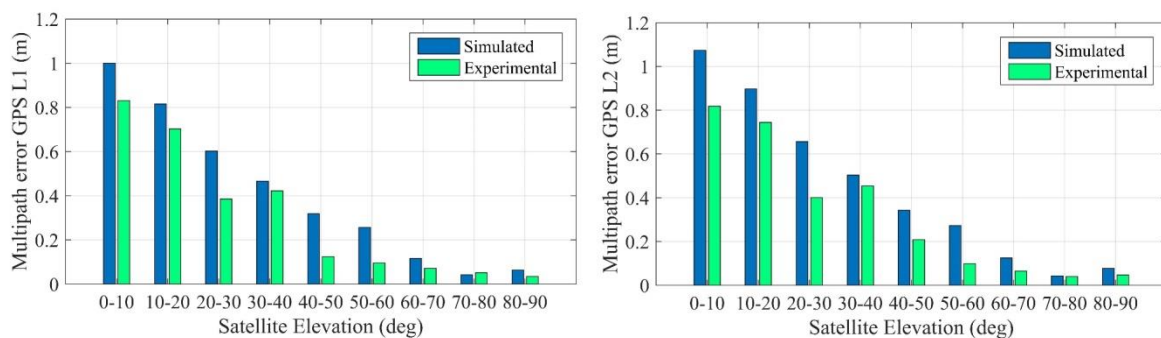


Figure 6-13: Intercity highway empirical model for GPS L1 C/A and L2C frequencies from simulation and experimental data. The multipath estimates contain receiver noise

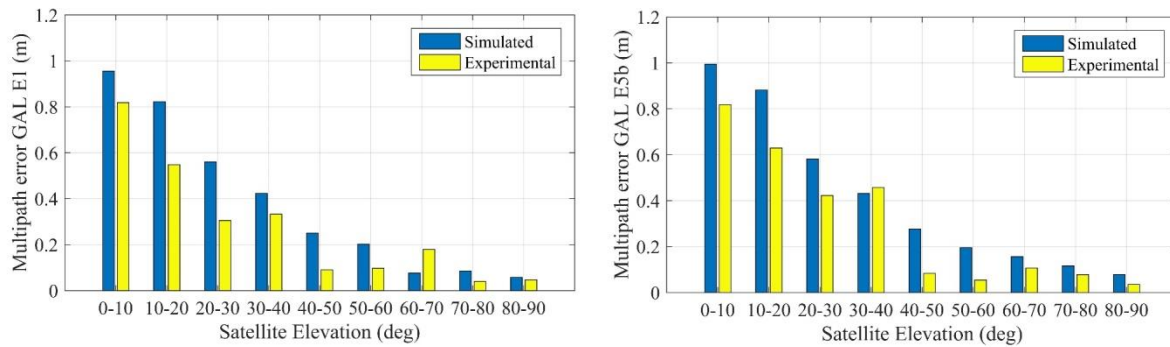


Figure 6-14: Intercity highway empirical model for Galileo E1 OS and E5b frequencies from simulation and experimental data. The multipath estimates contain receiver noise

The errors due to multipath vary within an interval determined by multipath delay, amplitude and number of reflections. In section 5.2.2.1, the errors caused by one multipath reflection in the presence of LOS are shown with respect to the delay of the reflected signal. The produced error varies from zero to 37 centimeters. In Irsigler (2008), the error magnitude for different kind of multipath reflections is computed. It is shown that the error due to multipath can vary from zero to three meters. For the investigated environment within this work, simulations and measurement campaigns with the presented setup indicate that the error due to multipath varies from zero to 1.1 meters. The error distribution over the elevation angles show the same pattern for errors from simulated and acquired data. The pattern is in agreement with the findings from the previous investigations in sections 5.4.3 and 6.2. The simulated multipath errors are consistent with the experimental data results, however some discrepancies are present. These vary from 0.05 to 0.26 meters. The largest discrepancy is found for the satellites at low elevation angles. This is determined by the approximations done in the 3D model and the lack of an antenna pattern in the simulation. In line with previous studies where multipath propagation is modeled, the discrepancies between simulated and experimental errors are of decimeter order. This is also the case in Weiss (2007), where the differences between the errors obtained from ray-tracing simulations and the errors from experimental data are up to 0.8 meters.

Regarding the error magnitude from the simulations within this work, the maximum multipath error for GPS is 1.075 meters and for Galileo 0.994 meters. The minimum errors are 0.058 and 0.043 meters for GPS, respectively Galileo. Regarding the experimental data, the largest error is found to be 0.831 meters for GPS and 0.818 meters for Galileo. Minimum errors for the two investigated navigation systems are almost similar: 0.033 and 0.036 meters.

6.3.1.2 Multipath impact on SNR

To check the SNR figure from simulation and measured data, mean values are computed with respect to the elevation intervals, similar as in the case of multipath error. The purpose of this investigation is to check the similarities and discrepancies of the modeled and measured GPS and Galileo signals, as well as the impact of multipath on the SNR figure. Figure 6-15 illustrates the resulted mean for L1, L2, and E1, E5b frequencies. The mean values from experimental GNSS observations contain peaks, whereas the simulated SNR is characterized by a constant direct proportional increase with the satellite elevation. This discrepancy from the experimental data could be attributed to the random short-term reflectors in traffic that are the consequence of a kinematic user.

The same irregular behavior is found for the pseudorange errors, indicating the connection between the SNR fluctuations and pseudorange multipath. For in-phase multipath signals, the values increase and the out-of-phase multipath signals produce decrease as detailed in 3.1. Therefore, the SNR oscillations are typical for a multipath contaminated signal.

The analysis of the GPS SNR from simulations and experimental data reveals a difference of 11 dB-Hz for L1 and 6 dB-Hz for L2. The discrepancy is smaller for the second frequency because the SNR values are generally decreased compared to L1. Consequently, the signals with an SNR under 25 dB-Hz are not tracked by the receiver anymore. Thus, the L2 average cannot decrease proportionally with the L1 average where the multipath affected signals are still tracked, as the transmitted signal is stronger. Since the discrepancy occurs for the satellites below 40°, there are two possible reasons to explain it. Firstly, the use of an ideal antenna for the simulations and an antenna with gain pattern for measurement is likely to produce the difference at low elevation angles. Secondly, studying the videos from the measurement campaigns revealed the presence of vegetation along the road most of the time. According to the literature, the effect of trees on GNSS signals differs according to the season. Nevertheless, in the presence of leaves, it is expected that the signal power is undermined according to their thickness, size, and form (Wu et al. 2017).

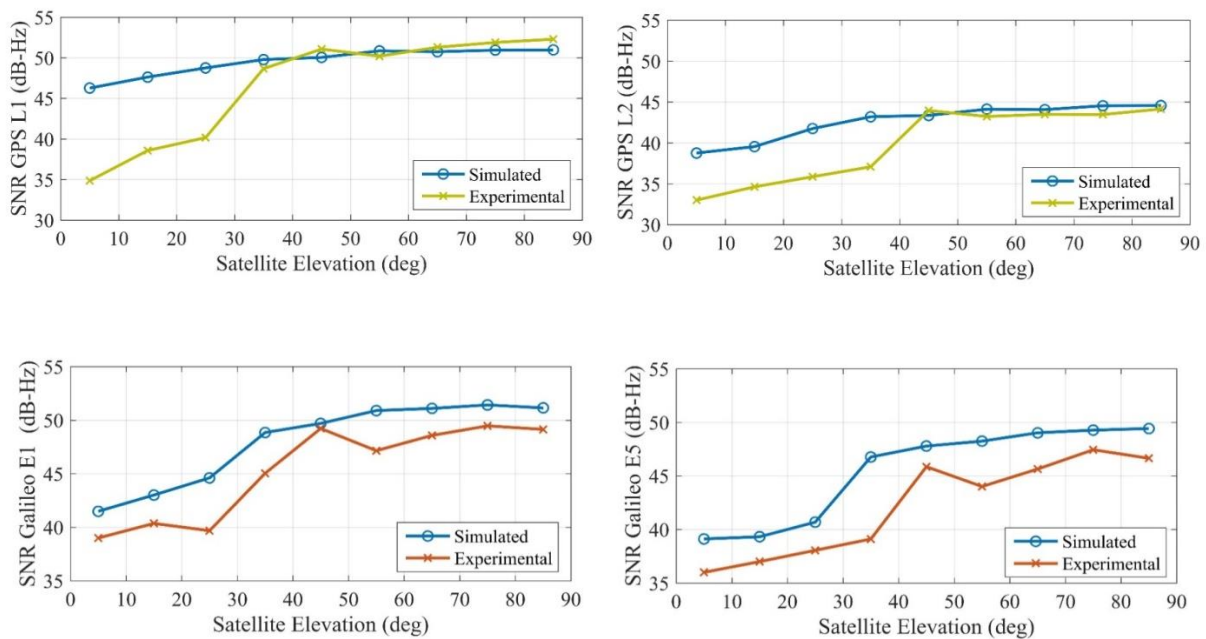


Figure 6-15: Signal-to-noise ratio behavior with respect to satellite elevation for simulated and experimental data in an urban highway environment

The two investigated frequencies of Galileo show the same pattern as in the case of GPS. The linear increase of the SNR with the satellite elevation is justifiable, as the power loss is smaller for satellites situated in zenith. For the most part, the simulated signals are stronger than the ones recorded during the measurement campaign. Nevertheless, SNR bumps are present for both constellations. For the satellites in the first 30° elevation, a larger discrepancy is noticed between the simulation and measurement data. Besides the multipath signals, the discrepancy is also the effect of the missing antenna gain and phase pattern in the simulations. Since a physical antenna has different patterns for each constellation and frequency, the SNR variation for Galileo signals between simulation and experimental data is different from GPS.

6.3.1.3 Multipath impact on position

Depending on the continent and country, a highway can be defined differently. The traffic frequency and location determine if the road can be categorized as arterial or collector (Todorova et al. 2009). The surrounding environment also differs due to natural and artificial features. Different time and weekdays when a vehicle is crossing a highway also influence the obstacles are encountered. All parameters that change the surroundings of a GNSS antenna mounted on a car, change also the multipath which occurs on the highway.

In the next section, the impact of multipath on the vehicle position for specific situations is analyzed. The GNSS position of the vehicle is computed by means of DGNSS based on pseudoranges, as presented in 2.6.1.1. Thus, the errors on pseudoranges due to multipath affect the position results. The DGNSS coordinates are compared against the reference coordinates. The car reference coordinates are provided by iTraceRT F402-E, as presented in 6.1. An analysis based on the videos taken from the measurement campaigns indicates the typical environment for a highway in Germany. The main characteristics are: a high volume of traffic, the presence of large vehicles i.e. trucks on the first lane, and vegetation along the road. Traffic jam situations are frequent. Firstly, these situations are separately analyzed to understand the importance of such events in the highway environment. In the end, an overall characterization of the test drive's position errors is made.

Open sky

Although the highway is considered to be less challenging than other environments due to the good satellite visibility and absence of massive reflectors, the multipath error still occurs. Figure 6-17 illustrates an intercity highway segment from the south of Germany, namely A6. The Google Earth® screenshot reveals that the vehicle heading during the test drive is towards east. The velocity for this section varies between 100 and 130 km/h as shown in Figure 6-16. The number of visible satellites is fluctuating between 12 and 16, as a consequence of the open sky environment. Thus, the DOP values do not influence the GNSS position negatively. The examination of the test drive video unfolds that there are three main factors that might represent multipath sources: the dense vegetation, the metallic safety fence, and the trucks. Additionally, these are present in the opposite driving direction as well. Small cars could also produce signal reflections since they are in the vicinity of the test vehicle where the antenna is mounted. Moreover, their closeness to the receiving antenna and metallic surfaces are likely producing strong multipath signals.

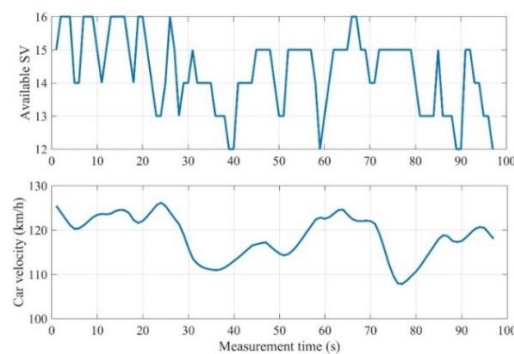


Figure 6-16: Satellite availability and car velocity for the illustrated area



Figure 6-17: Reference (blue) and multipath affected position (red) superimposed over Google Earth®

Figure 6-18 reveals the errors which occur for the selected measurement interval. The height and latitude are mostly affected, both having error magnitudes of 3.4 and 3.3 meters, respectively. The corresponding value for longitude is 1.2 meters. Figure 6-17 shows that the heading of the road is towards east and that the vehicle position error is more pronounced in the north direction. Vegetation, trucks and the safety fence are all situated at the highway margin. Considering these factors, it is likely that the increased error on longitude is the effect of reflections coming from the lateral sides of the road. The dependency between multipath errors and the positioning error on the latitude and longitude components has been shown with simulated data in Mubarak & Dempster (2010).

The positioning error contains peaks at irregular time intervals, which indicate the temporary presence of reflections. Multipath simulations at high velocity that are detailed in section 5.4 reveal that random and short-term multipath is typical for the kinematic multipath occurrence. As the test vehicle constantly overtakes the trucks, it can impact the position randomly for short periods. Overall, the RMS error fluctuates from 1 to 3.2 meters. The average is 1.62 meters with 0.4 meters standard deviation.

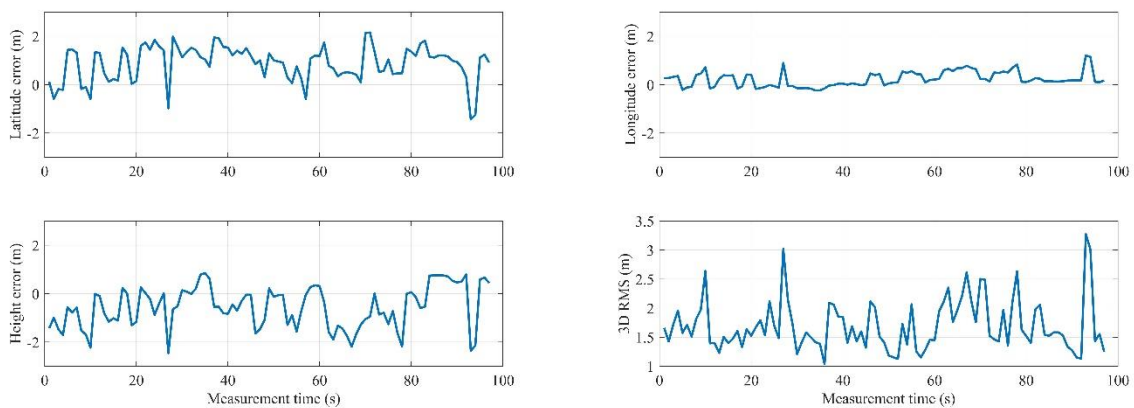


Figure 6-18: Deviation from the car reference position on the 3D geographic coordinates for an open-sky intercity highway segment. The corresponding RMS values are plotted along the measurement time

Highway construction site

This investigation is related to a situation that is often encountered on the highway: the road construction site. The question which addresses is if the narrow lanes and heavy traffic affect the position due to multipath. Analysis of the video and Google Earth® overlapped trajectory shows that the test vehicle trajectory deviates on a narrow lane in the opposite driving direction. Thus, besides the metallic safety fence on the right side, vehicles drive close and in the opposite direction of the test vehicle.

The left side of Figure 6-19 shows a screenshot of the investigated segment. Although the driven trajectory is longer than what is presented by means of Google Earth®, the part is intentionally illustrated to indicate an additional challenging factor that appeared: bridges crossing over the highway. From the plotted satellite availability, it is visible that bridges are crossed three times. The two consecutive peaks arise between 200 and 250 seconds and correspond to the two bridges that are shown in the screenshot on Google Earth®. The velocity for this segment is smaller compared to the previous case. This is typical for the construction road areas, due to the temporary narrow lanes.

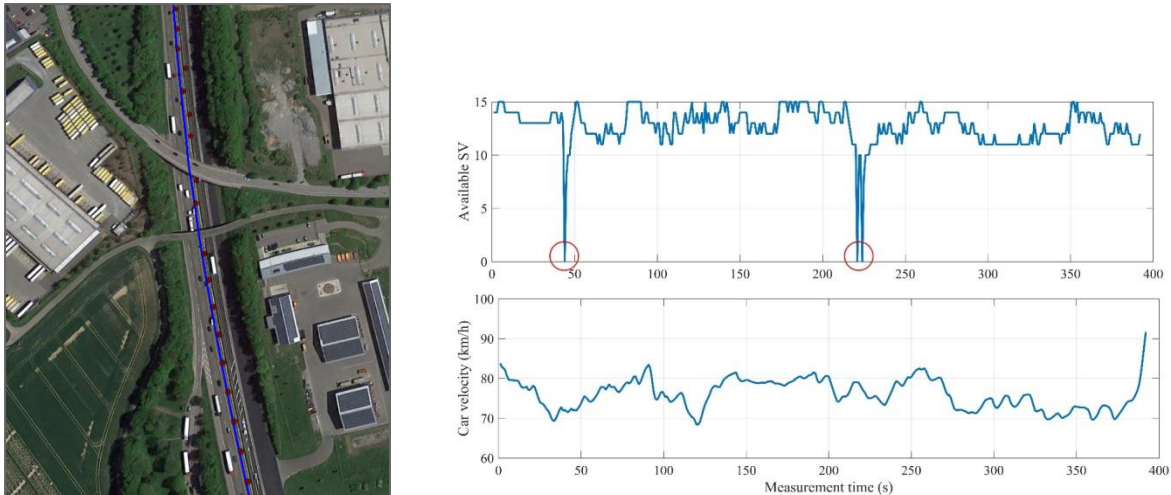


Figure 6-19: Google Earth® screenshot with overlapped car reference position (blue) and multipath biased position (red). Satellite visibility and car velocity for the investigated highway segment are plotted on the right

From Figure 6-20, it is visible how the GNSS position deviates from the reference trajectory in the vicinity of the bridge. The differences over the measurement time are plotted separately in Figure 6-20 together with the corresponding RMS. Significant spikes can be identified in the latitude, longitude, and height. For clarity, these are marked with red circles as well. Judging by the time stamp, these correspond to the three bridges, that can be identified on the satellite visibility plot as well. Although loss of satellite track occurs for 1 second, the gap is filled due to the Kalman Filter which is employed in the DGNSs post-processing.

An additional spike at 170 seconds is present in the latitude plot and it is marked with violet. The spike is present on height and longitude as well. The video during the test drive does not indicate any anomalies besides intense truck traffic on the right lane. As previously mentioned, it was shown in Mubarak & Dempster (2010) that there is a connection between multipath coming from specific satellites and the positioning error. Considering this and the alignment of the highway along the $N 49^{\circ}10'30''$ as shown in Figure 6-17 it is concluded that the increased deviation in latitude is owed to lateral reflections from trucks and vegetation. Figure 6-20 reveals that the errors are overall more significant than in the previous case i.e. in open sky. The differences from the previously investigated segment are lane width, closeness to the opposite traffic and decreased velocity. Further research could verify with simulations and measurements if this specific scenario is likely to produce more signal reflections which leads to an overall error growth. The average value of the 3D RMS is 2.7 meters with 2 meters standard deviation.

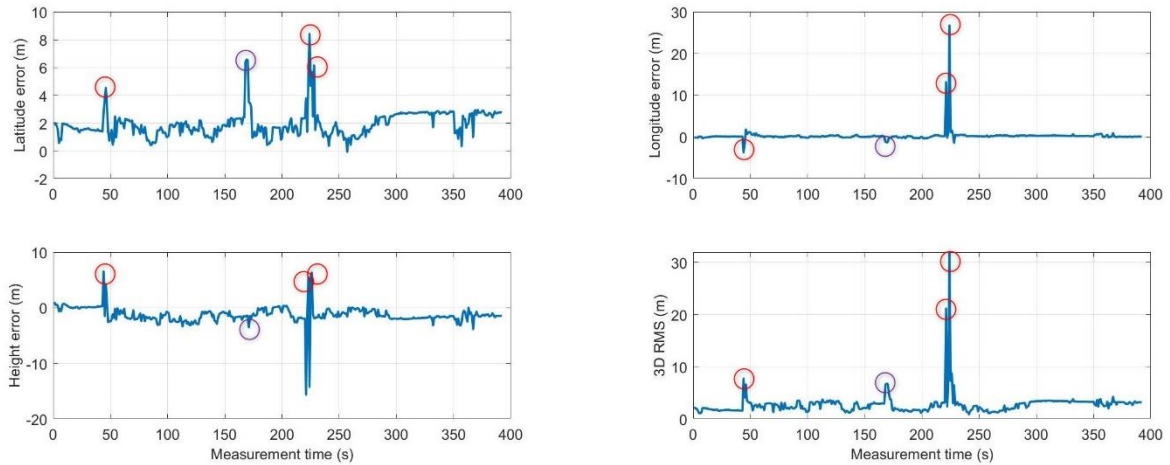


Figure 6-20: Position deviation of geographic coordinates due to multipath and obscuration. The corresponding RMS error over the time series is plotted on the right

Traffic congestion

Another frequently encountered situation on the highway is a traffic jam. In such circumstances, the environment is susceptible to multipath due to the closely static and kinematic traffic participants. Additionally, as shown in sections 5.4.4 in 6.2, the car is likely to experience increased pseudorange errors for smaller velocities due to multipath and receiver properties. Figure 6-21 illustrates the connection between two highways, where the traffic congestion occurs. The Google Earth[®] screenshot shows that the car heading is north-east, thus the multipath reflections should affect both with an equal magnitude both latitude and longitude.

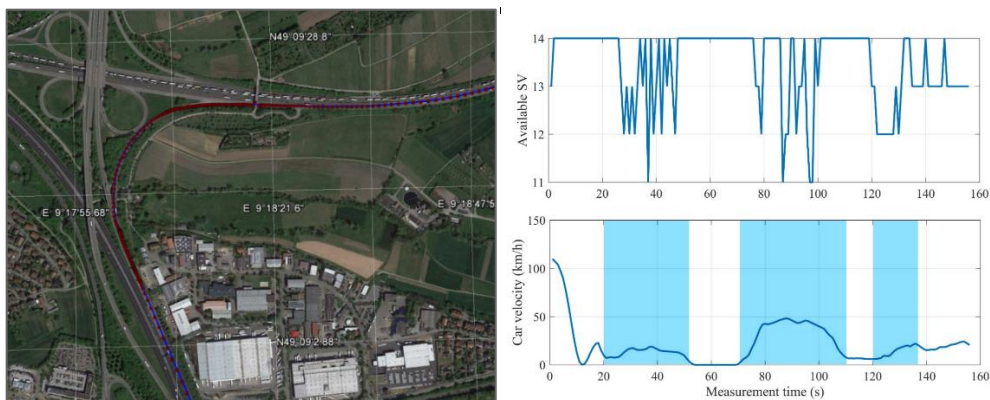


Figure 6-21: Google Earth[®] screenshot with overlapped car reference position i.e. blue and multipath biased position i.e. red for traffic congestion. Satellite availability and vehicle velocity are plotted on the right

The number of available satellites is between 11 and 14, leading to good DOP values, due to the open sky conditions in the highway environment. The velocity plot indicates that the vehicle decelerates suddenly due to the traffic jam. The video taken during the test drive reveals the following events: the vehicle decelerates and advances slowly when encountering the traffic jam. Next, in the area between 70 and 110 seconds, the vehicle is overtaking the trucks, which are static on the right lane. In the end, two lanes merge and the test vehicle continue driving behind a truck. The three events are important to understand the multipath sources that cause position degradation. Figure 6-22 indicates peaks in the

position that match the described events. In the velocity and RMS error plots, these are marked with blue. The latitude and longitude errors are affected equally due to the driving direction, as expected. The error that occurs from second 120 to 135 is prominent on longitude. This is likely to be the effect of driving directly behind the truck and receiving frontal signal reflections, leading to a bias oriented towards east/west. The RMS error for the traffic congestion segment reaches 6.6 meters. In the open sky segment, the RMS error reached 3.2 meters. Considering the related events, the position deviations as well as the vehicle heading, it can be concluded that the increase of RMS error for the traffic congestion segment is due to multipath occurrence.

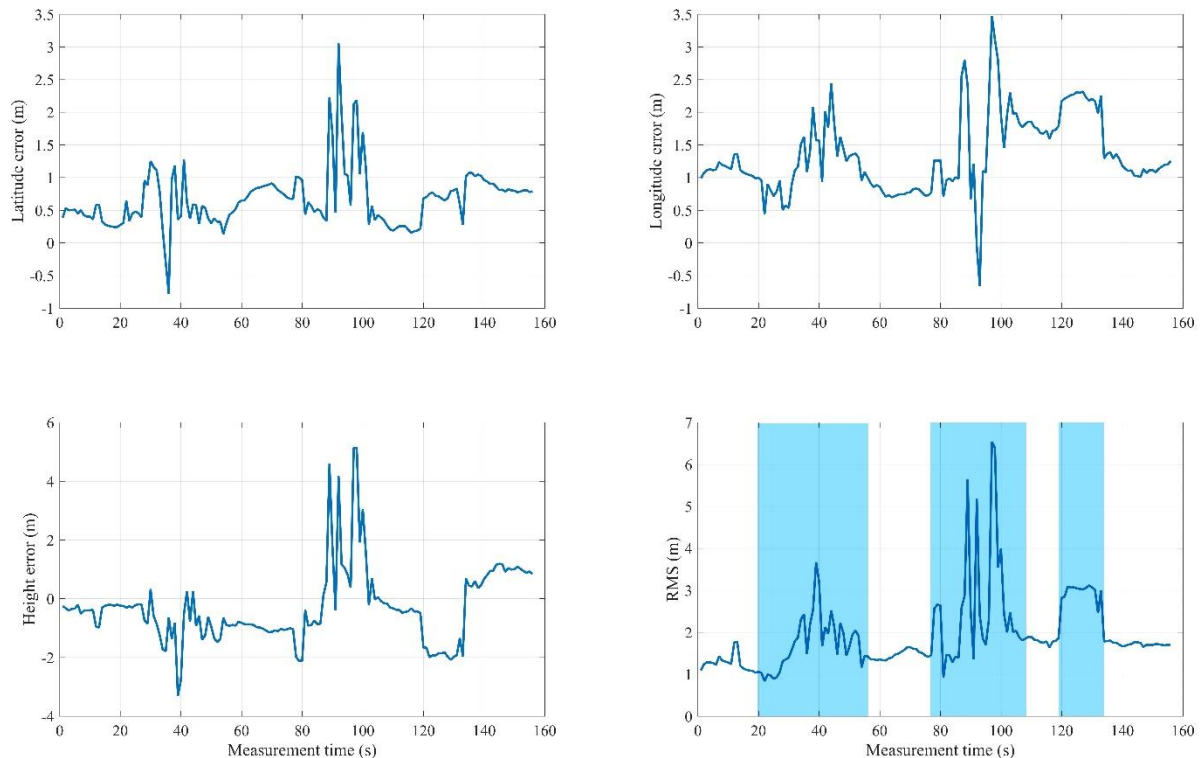


Figure 6-22: Position deviation of geographic coordinates due to multipath in highway traffic congestion

Overall error for a highway environment

After the analysis for short time intervals during the measurement campaign, an overall average for the position deviation is computed. The position error is computed with respect to the reference position for both simulated and experimental data. Reference position for simulations stems from error-free simulations and for experimental data from the iTraceRT 402-E, a GNSS/INS integrated system. The same receiver, namely NovAtel PwrPak7[®] is employed for simulations and data collection to establish the impact of multipath on the pseudorange error. For a better assessment, the position is determined in post-processing by means of DGNSS, based on pseudorange measurements. Therefore, the estimated multipath errors on pseudorange influence the position accuracy.

Figure 6-23 indicates an overall increased position error from simulations, compared to the acquired data. This is likely to be caused by increased multipath errors present in simulations. The results are in line with the analysis from section 6.3.1.1, where is shown that the simulation produces a more challenging multipath environment than the one that occurs in reality. Regarding the error

individually, the best agreement between simulation and experimental data is found for the height. This is the most affected component, as the GNSS satellites are above the terrestrial receiver. The latitude and longitude discrepancies between simulation and measured data are approximately 0.4 meters. The error is more significant for the latitude than for longitude. The impact of multipath on the latitude and longitude coordinates is dependent on the reflections angle of arrival and the vehicle heading, as shown in the previous detailed analysis. Overall, the estimated RMSE error for simulations is 1.9 meters and for the measured data 1.6 meters.

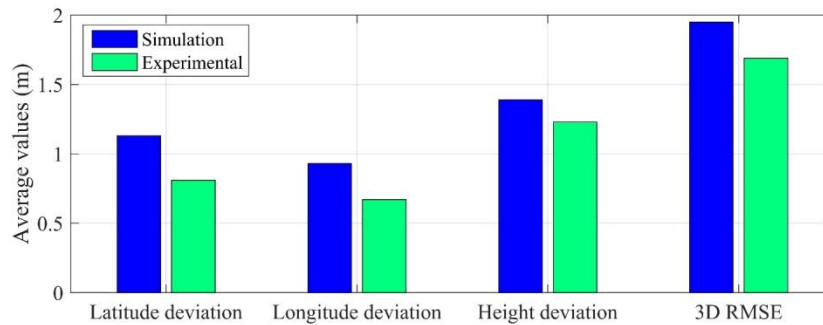


Figure 6-23: Mean absolute position deviation of geographic coordinates and the corresponding 3D root-mean-square error for the measurement campaigns and simulations in a highway environment

6.3.2 Urban roadway

Urban roadway represents a more challenging GNSS environment. Due to the constructions in the city areas, the errors caused by multipath are likely to be more severe. Thus, collection of kinematic experimental data and simulations are required to gain awareness of the generated bias.

By having the same measurement setup presented in section 6.1, the video timestamp is used to determine the car surroundings. Raw GNSS dual-frequency data for GPS and Galileo at 1 Hz is recorded during measurement campaigns in Stuttgart and Frankfurt. For the HiL multipath simulation the same receiver is employed, as in the measurement campaigns. In total, two hours of kinematic measurements in urban environments that are typical to south Germany are recorded and the same amount is simulated by means of ray-tracing. A 3D model of an urban environment is implemented and used for the multipath simulations scope. The trajectory of the vehicle is generated based on the created 3D model and the velocities are set between 30-50 km/h. The left side of Figure 6-24 reveals part of the test drive trajectory plotted over Google Earth[®]. The right side illustrates the urban 3D scenario. In Figure 6-24 the vehicle trajectories are outlined with yellow for both cases.



Figure 6-24: Google Earth[®] screenshot showing part of the investigated data and 3D model used for urban simulation. The yellow lines represent the vehicle driven/simulated trajectory

6.3.2.1 Multipath error magnitude

In total, two hours of experimental data in an urban environment is acquired. For consistency, the simulation has the same duration. Nevertheless, more relevant is the recorded number of satellite hours. For the urban scenario, an average of nine satellites (GPS and Galileo) is in view. Thus, approximately 18 satellite hours are analyzed from experimental data. The same amount of data is simulated to compare the multipath properties with the acquired data.

Figure 6-25 illustrates the computed multipath series for the recorded data during the measurement campaign and simulation. Since the vehicle trajectories for the two cases are not identical and the 3D model is representative but not identical, it is not expected that the multipath series matches along with the time series, but with the magnitude. This is successfully reproduced, as the plots indicate that the multipath error is varying in both cases from -2 to 2 meters. Compared to the highway error, the error is double for urban roadway surrounding. The experimental multipath time series indicates the presence of multiple frequencies, which is also visible in the corresponding SNR series. Although the

simulation reproduces the multipath behavior and magnitude, less variations are present on the GNSS observables. There are two possible reasons for that. Firstly, the simulation is limited by the number of physical channels of the GNSS signal generator. For this reason, two reflections pro satellite are considered. It is likely that in a real urban environment, more than two reflections occur. The second reason might be that the synthetic 3D model does not include all the details of reality. For instance, the buildings are modeled as blocks. Thus, the absence of sharp roofs or windows might negatively affect the simulation results. Nonetheless, the magnitude of the multipath is captured and the SNR indicates the bias on pseudorange due to reflections as well.

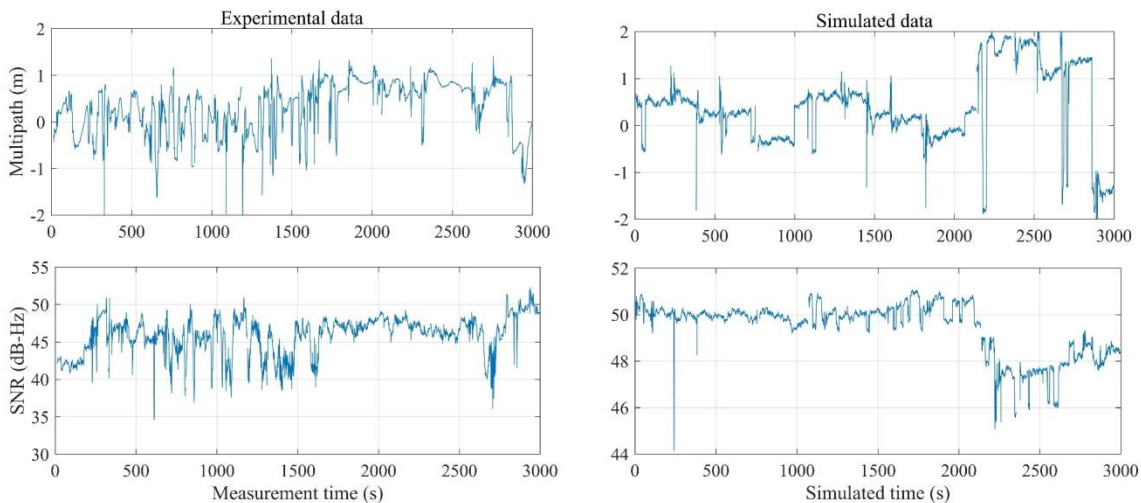


Figure 6-25: GPS L1 multipath error for different constellations from simulation and experimental data. The corresponding SNR is plotted under the errors on pseudorange

Both recorded and simulated data are analyzed separately, by employing the same approach as for the data presented in section 6.3.1. Similar to the highway simulations, the 3D model is synthetic. This means that the main characteristics of the environment are captured, but they are not modeled in detail. Kinematic simulations require massive amounts of data and a 3D model identical to the vehicle surroundings. This is not feasible due to the changing elements in the environment. Figure 6-26 reveals the results after the data processing for GPS L1, L2 and Galileo E1, E5b. Comparing the simulation to the acquired data, it is visible that the simulation mostly undermined the error due to multipath. The reason for this can be due to the reduced number of multipath reflections which can be simulated, as previously explained. If many reflections occur, this leads to a longer time delay, therefore an increased pseudorange bias. Another reason for the discrepancies might be because the 3D model is an approximation of reality.

The spread of the standard deviation over the elevation bins is not proportional to the elevation increase, as in a static case. The simulation reveals this trend which was also found in the experimental data. This result highlights the random multipath occurrence in kinematic situations, due to variation of reflectors dimensions and location with respect to the vehicle. However, the GPS maximum average error due to multipath is 2.6 meters for acquired data and 2.2 meters for simulated. The minimum average error is 0.2 meters and it occurs as expected for the satellites in zenith. Although the magnitude of the error has the tendency of decreasing as the elevation angle increases, oscillations occur between 40° and 70° . This phenomenon can be explained by the presence of buildings, which produce signal echoes even for higher elevations. In regions where buildings are

surrounding the vehicle, it is likely that the lower elevation satellites are obscured. Therefore, the average for lower elevation angle data remains constant, due to absence of GNSS observations. Meanwhile, the higher elevation angle satellites average error increases, because of LOS with multipath or NLOS reception.

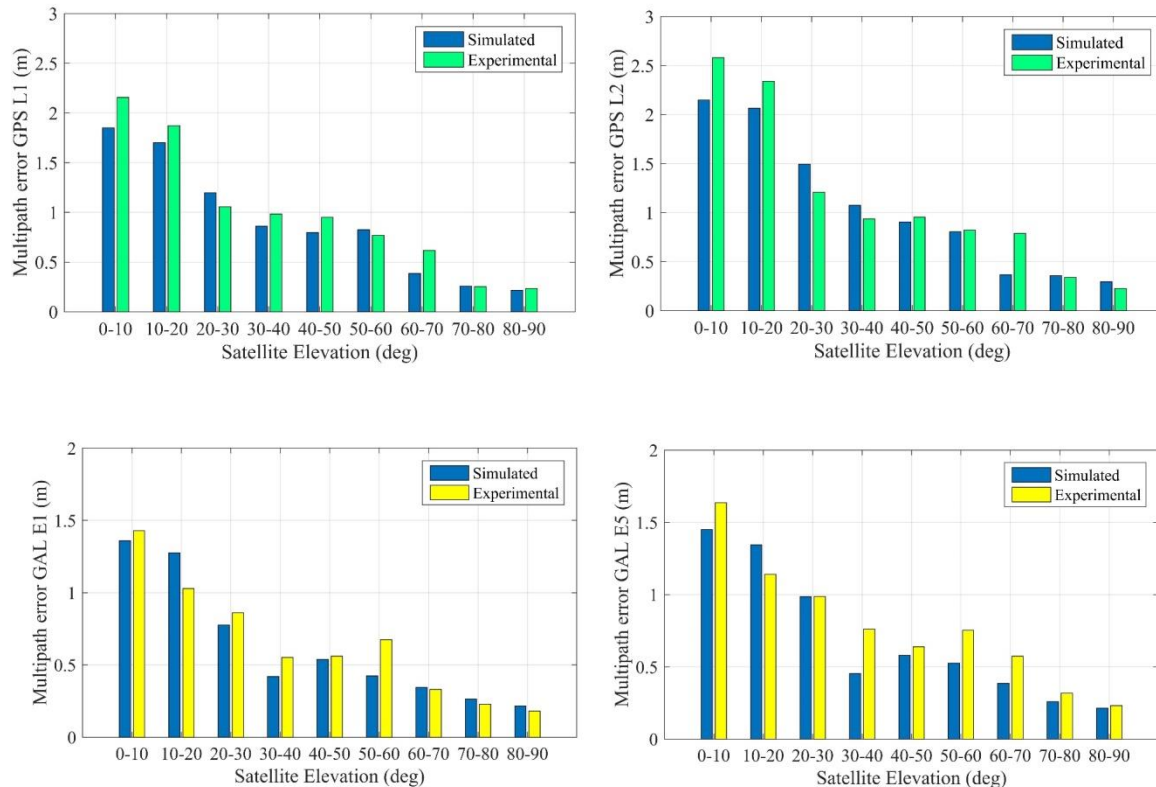


Figure 6-26: Mean multipath error on pseudorange as function of satellite elevation for experimental and simulated data for GPS L1 C/A, L2C and Galileo E1 OS, E5b. The plotted estimates contain receiver noise

The plots in Figure 6-26 indicate that the pseudorange errors due to multipath on Galileo have a similar distribution over the elevation angles, but a decreased value compared to GPS. This result is in accordance with the highway dataset investigation. Nevertheless, the multipath error magnitude increases for the urban roadway due to the presence of buildings close to the vehicle. Similar to the GPS case, the Galileo experimental data shows increased multipath bias compared to the simulation. Nevertheless, it was expected that both navigations systems are affected consistently during the simulation. The maximum measured average multipath for Galileo is 1.6 meters and simulated 1.4 meters. Simulation and acquired data show similar results for the satellites close to zenith, which is 0.18 meters.

6.3.2.2 Multipath impact on SNR

Since the multipath signature can be found on the SNR of the GNSS signals as well, the average SNR values of the recorded and simulated observations are computed. It is to be mentioned that this quantity is affected besides multipath, by the GNSS antenna pattern, receiver signal processing and the transmitted power of the signal from the satellites. Figure 6-27 illustrates the average values computed from the simulated and acquired data in urban environment. The mean values for both investigated navigation systems vary between 30 and 50 dB-Hz and increase with the elevation angle.

It is known from literature that the SNR increases with the satellite elevation. The reason for this phenomenon is that the power of the electromagnetic wave attenuates in the atmosphere since the path is longer for lower situated satellites. However, fluctuations due to multipath reflections contribute to the SNR value oscillations. The peaks present in the mean values presented below can be explained by the positive and negative interference.

Moreover, the satellite obscuration has a similar impact as in the case of the multipath errors on pseudorange, as previously detailed. For the investigated data, the SNR shape is similar for the two frequencies but the overall values are decreased for the second one. This is reasonable, because the multipath reflections affect similarly a satellite on both frequencies. However, the second frequency is transmitted with lower power than the first one and this is reflected in the SNR as well. The discrepancies between the simulated and acquired GNSS signals SNR is due to the same factors which explain the pseudoranges error differences. An additional important factor is the GNSS antenna as detailed in section 6.3.1.2. Since the antenna influences are not simulated, this induces discrepancies with respect to the measured data where a physical antenna collected the GNSS signals. By comparing the results from Figure 6-27 with the SNR recorded on highway, it can be noticed that values for the highway are larger. This is the consequence because less multipath is experienced in the highway environment. This is also an indicator that the multipath affects SNR values, as shown theoretically in section 3.6.

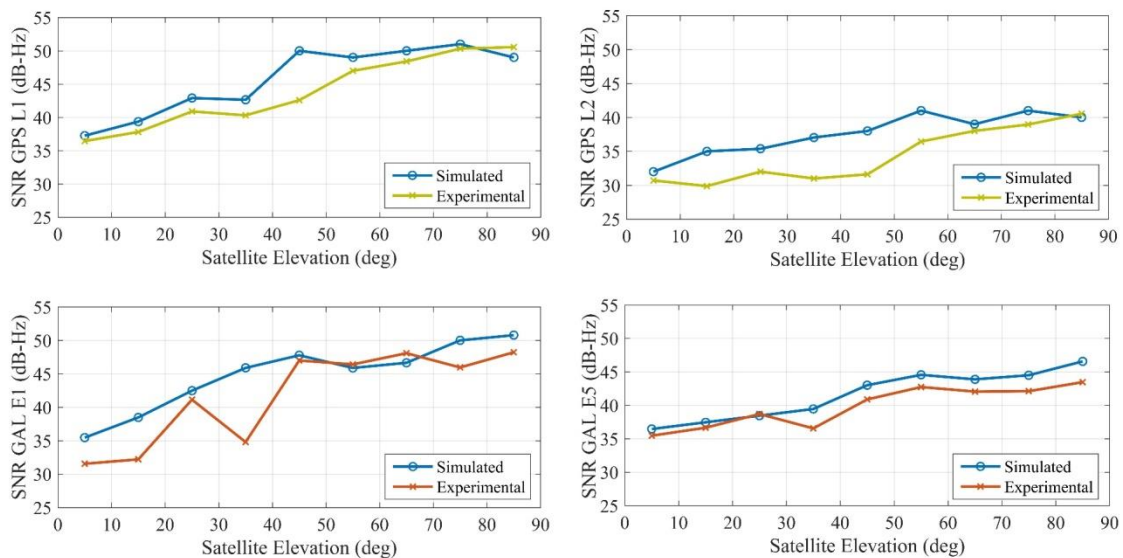


Figure 6-27: SNR mean values related to the satellite elevation angle. The simulated and experimental averages are plotted for GPS L1, L2 and Galileo E1 and E5b. Simulated data lacks antenna pattern

6.3.2.3 Multipath impact on position

To investigate the impact of multipath on position, further analysis is accomplished. To understand the critical situations for an urban roadway, a few representative situations are considered: high buildings, stand still at red light and open sky. The reference coordinates of the car are computed by using the same approach as in section 6.3.1.3. These are compared with the GNSS position obtained by means of DGNSS based on pseudorange. A comparison against the reference coordinates is also performed in the case of simulations. The reference coordinates in this case are obtained from multipath-free simulations.

The next section is organized as follows. Firstly, the analysis of representative situations in an urban highway is shown. The position deviation is locally plotted. Then, the RMS errors for the experimental and simulated data in urban environment are computed. This shows if the errors in the multipath simulation can reproduce the errors produced during data acquisition in the investigated environment.

Buildings

The biggest challenge related to multipath in the urban environment is represented by the high buildings that are present along the roadway. An example of such a situation is illustrated in Figure 6-28. On the left side of the figure, the GNSS position based on pseudoranges which is drifting due to multipath is plotted in red. The car reference position is illustrated with green. A deviation from the car reference trajectory occurs along the left building between the intersections. This might be the effect of signal reflections, due to the high building.

The car velocity is plotted together with the satellite availability on the right side of Figure 6-28. It is shown that the number of used satellites varies between 7 and 10. Because of the vehicle's vicinity to the high building on the left side, the satellites on the right side suffer strong reflections, therefore increased signal time-of-arrival. The multipath delay that is created by such a situation is short due to the proximity of the vehicle to the building. It was shown in section 5.2.2 that the NovAtel receiver is sensitive to short multipath delays. At the same time, the satellites on the left side suffer obscuration and cannot compensate for the multipath error. Consequently, the position drift to the opposite direction of the building occurs.

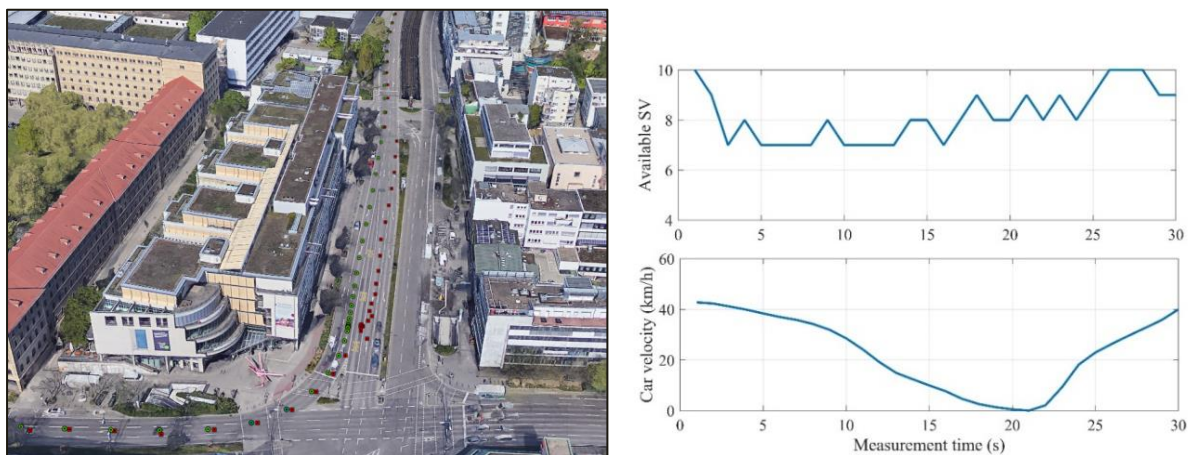


Figure 6-28: Position drift due to multipath reflections in urban highway, satellite availability and car velocity. Reference position (green) and multipath altered position (red) are shown over Google Earth®

Figure 6-29 shows the deviation in latitude, longitude, and height, as well as the RMS error for the investigated segment. Errors on latitude and longitude increase with approximately 4 meters when the car starts driving parallel to the building. The height is the most affected with a value around 10 meters. Overall, the RMS increases from 3.5 meters until a maximum of 16.9 meters.

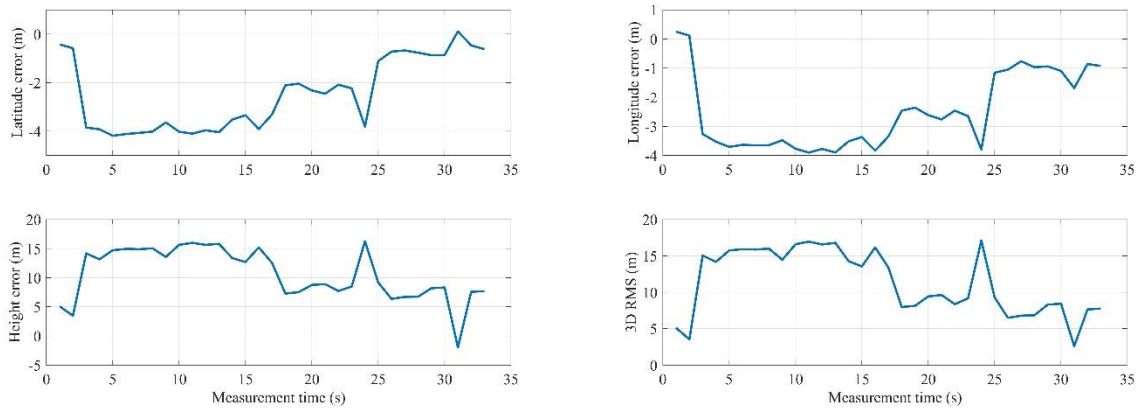


Figure 6-29: Deviation of 3D geographic coordinates and RMS error in the multipath environment determined by the high building

Traffic light

Sections 5.2.2.1 and 5.4.4 deal with simulations of static and kinematic users at different velocities. Further, section 6.2.4 shows experimental data for static and slow kinematic use cases. The results show that due to error characteristics and receiver architecture the errors due to multipath are larger for a static user. The analysis in the urban environment found experimental evidence that comes in agreement with the finding in the previous sections.

The left side of Figure 6-30 highlights a combined situation. The vehicle is driving along the street and then it stops due to traffic light. It is visible that the environment is similar, as the constructions on the left side represent multipath sources during both static and kinematic cases. Nevertheless, during the time the vehicle is stationary, the position is drifting, although the number of available satellites, therefore DOP value barely changes. The GNSS position computed based on pseudorange measurements is plotted with red and the reference coordinates of the vehicle are plotted with green.

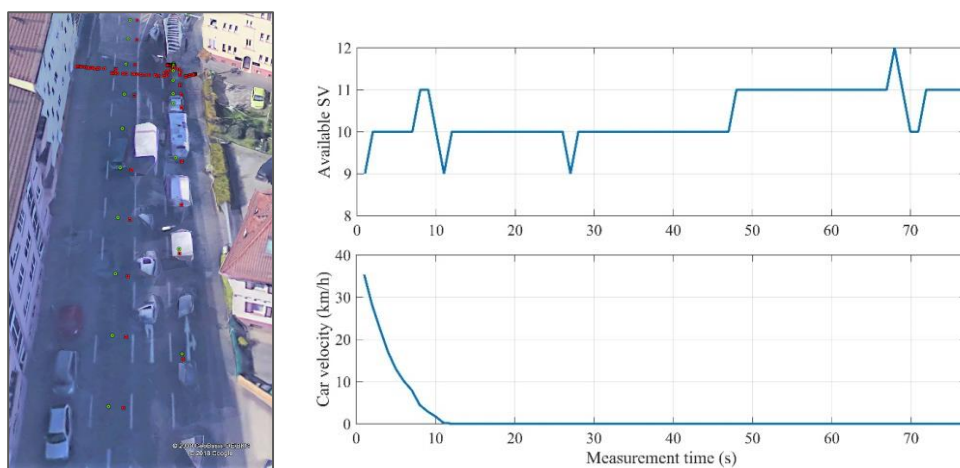


Figure 6-30: Google Earth[®] screenshot with the reference and multipath biased car coordinates. The plot on the right side shows the corresponding satellite availability and the car velocity

Figure 6-31 highlights the relationship between the positioning error caused by signal reflections and velocity. The position deviates from 0.4 to 1 meter during car kinematics and with 0.6 to 15.6 meters

in stationary conditions. Besides the car state, the RMS varies due to satellite geometry, building height, horizontal distance from GNSS antenna to the building, satellite position with respect to the car and receiver type. Hence, the values of RMS characterize the isolated situation that is described and cannot be generalized for the named velocities. However, the findings from simulations and experimental data confirm the different multipath behavior for static and kinematic users, as well as decreased errors for the latter case.

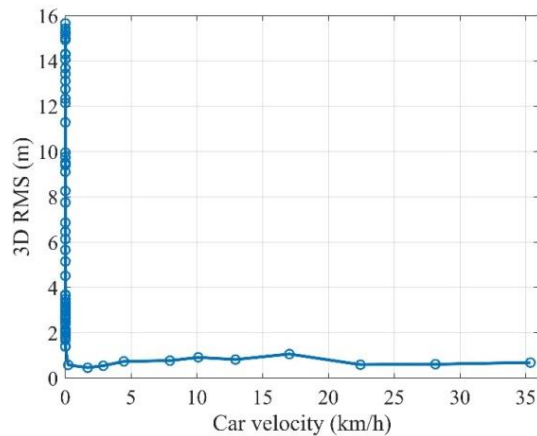


Figure 6-31: Experimental 3D root-mean-square position error with respect to car velocity in urban environment

Suburban area

To compare the inner city with the suburban multipath effect on position, an open sky test drive segment is further analyzed. The left side of Figure 6-32 illustrates the environment where the position is examined. It can be noticed that the number of available satellites increased from 8-12 in the inner city to 12-14 in the suburban area. This increase is present despite the fact that in this area buildings are present as well. Another similarity to the inner city situation is the road width, which determines the horizontal distance from the car to the reflections along the road.

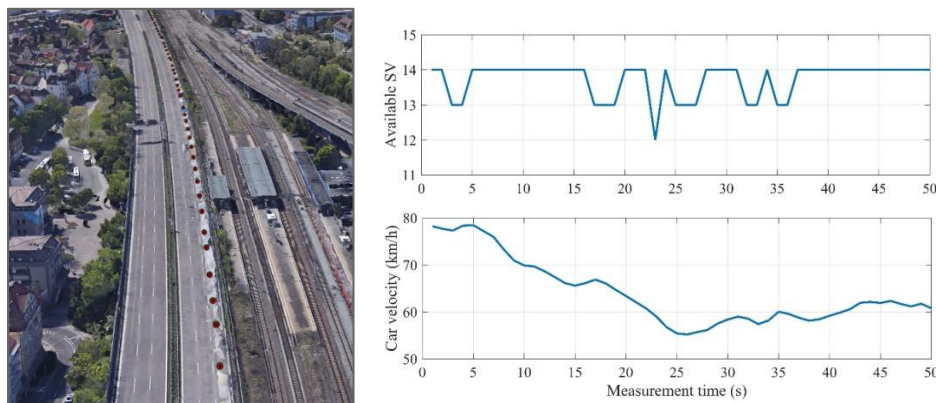


Figure 6-32: Google Earth® reference and multipath affected position in an open-sky suburban area. Information related to the car velocity and satellite availability is plotted on the right side

The position errors on the three-axis, as well as the RMS values of the GNSS only solution are plotted in Figure 6-33. The results show a smaller deviation for this environment, as expected. The error

magnitude is 0.6 and 0.9 meters for latitude and longitude, respectively. The largest error is found on the height component and measures 1.6 meters. This error growth on height can be explained by the fact that the GNSS signals are sent from angles above the horizon. The pseudorange errors that affect the height component cannot be compensated by GNSS signals arriving from the opposite direction i.e. north.

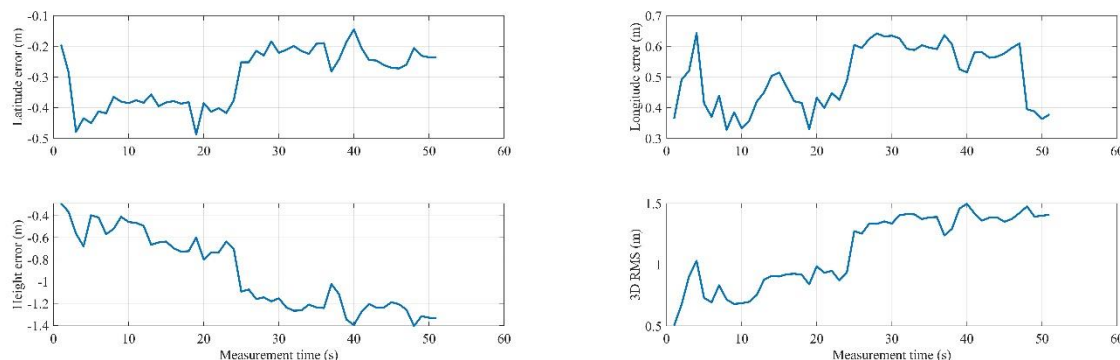


Figure 6-33: Deviation of 3D geographic coordinates in an open-sky suburban environment and RMS error during the analyzed segment

On the other hand, for an open-sky situation where signals arrive from both east and west directions, the errors compensate each other in the 2D plane. For this reason, the latitude and longitude error are comparable to each other and smaller than the deviation on height. By comparing the RMS error against the velocity plot over the time series, it is noticed that as the car is decelerating, the 3D position error increases. This is consistent with the multipath simulations and the previous experimental analysis, where the same inverse proportionality is found.

Overall error

An overall computation of the position deviation on each component, as well as the 3D RMS error is computed for the simulated and acquired data with the vehicle in an urban environment. Similar to the previous section, the reference position is given by the fused coordinates from iTraceRT 402-E, a GNSS/INS integrated system. For the simulated data, the reference consists of error-free simulations. The position which is affected by multipath is provided by NovAtel PwrPak7[®]. The observations are post-processed by means of code DGNSS. The average results are plotted in Figure 6-34.

These indicate that overall, the position is worse in reality than in the performed simulations. This finding is in agreement with the investigation results on the pseudorange error due to multipath. However, it should be taken into consideration that the positioning error in the urban environment is degraded also due to the limited satellite visibility. The position dilution of precision depends on the satellite geometry, which can be unfavorable and unstable, considering a kinematic vehicle in an urban environment. The resulted average 3D RMS error is 6.9 meters for the simulation and 8.8 meters for the measurement campaigns. Compared to the intercity highway, the average experimental 3D RMSE in the urban environment is approximately five times larger. This indicates the relevance of the multipath and environment on the positioning results for a kinematic user.

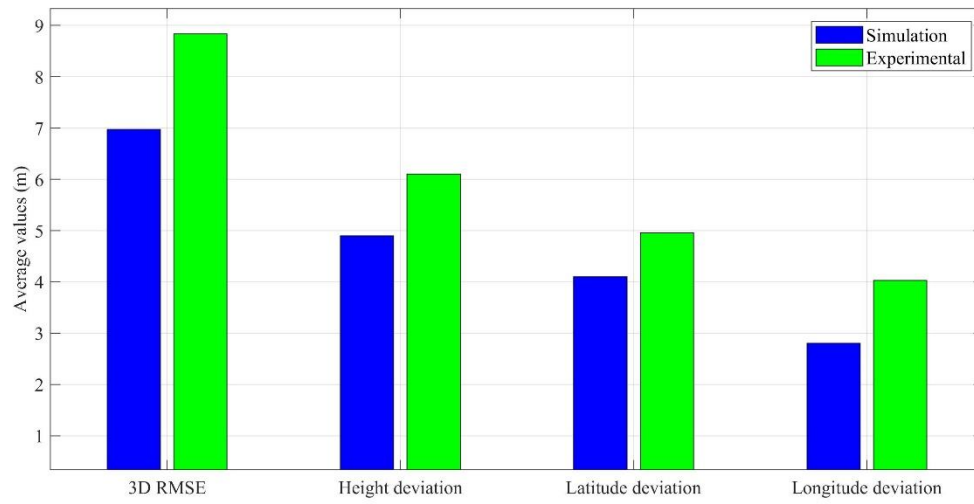


Figure 6-34: Absolute mean latitude, longitude, height, and RMS errors for simulated and acquired data in an urban environment

7 Conclusions and further work

7.1 Conclusions

The research within this work extends the existing literature regarding GNSS multipath effects, by modeling and simulation of the error for kinematic use cases. Considering the use of GNSS measurements for the autonomous driving purpose, analysis is required for kinematic use cases assuming a vehicle as GNSS antenna carrier. Within this dissertation, the complete chain is examined, from the multipath signal propagation to the impact of multipath on position. Besides the multipath related investigations, a Hardware-in-the-Loop (HiL) test bench for testing under multipath conditions for kinematic vehicles is implemented.

After the introduction, the following two chapters describe the theoretical background of this work. Within the first chapters, an overview related to GNSS and the multipath error is presented. Since multipath represents the core of this research, simulation models, as well as receiver sensitivity to this error are introduced. This represents the basis of the multipath simulations presented in chapter 5. The aim is to find the adequate model for multipath simulation, considering the GNSS setup for a kinematic vehicle. Chapter 4 introduces the implemented algorithms for multipath estimation. Based on these algorithms, multipath error models are computed for simulated and experimental data in chapter 6. The objective is to assess the errors due to multipath for various velocities and environments, typical for a vehicle. Additionally, this serves as an indicator of the multipath simulation's correlation to reality.

The implementation of multipath estimation algorithms in chapter 4 reveals advantages and disadvantages for kinematic measurements. Isolating the pseudorange multipath on experimental data is challenging due to data gaps and cycle slips. Advantages and limitations regarding kinematic multipath assessment are presented for each implemented method. Although the algorithms are known in literature, few details regarding the processing steps are offered. For this reason, within chapter 4, a detailed description of the implementation and intermediate results are presented. The two algorithms are verified by measured and simulated GNSS measurements in consecutive days. Cross-correlations between computed multipath series in consecutive days at 244 and 245 seconds indicate that both implementations are successful.

A HiL test bench is implemented for the simulations presented in chapter 5. Various simulations are carried out to assess the appropriate multipath simulation model for vehicles that carry a GNSS antenna. It is shown that the hybrid multipath model causes constant signal attenuation of 10 dB for all simulated velocities in the defined environment. The deterministic multipath model produces a signal attenuation from 13 to 19 dB and it is correlated with the vehicle velocities. Additionally, the latter multipath model induces pseudorange errors up to 1.1 meters. Due to the correlation of the multipath parameters with the velocity and increased errors on the GNSS measurements, the deterministic model is adopted for the HiL test bench. Since the architecture of GNSS receiver has an impact on the error's magnitude, the receiver sensitivity to multipath is tested as well within this chapter. Simulations unveil that due to the employed receiver properties, the multipath propagation in kinematic situations affects the receiver less than in static conditions.

The multipath propagation introduces an error on the pseudorange measurements, which has several dependencies. Chapter 6 focuses on two of them: velocity and environment. These two are investigated by means of measurement campaigns and HiL simulations. Further, measurement

campaigns with a static and kinematic vehicle in the same environment are carried out and evaluated. The multipath average errors in the static case vary from 5 centimeters to 42 centimeters. Within the same environment but with slow kinematics, the raw errors on pseudoranges are smaller than the average errors for the static vehicle. This agrees with the simulation results in chapter 5. Measurements on highway reveal pseudorange errors due to multipath in the interval from 10 centimeters to 62 centimeters.

Having the focus on environment, kinematic simulations with the implemented HiL setup and measurement campaigns are carried out on highway and in the city. Unlike static multipath simulations, a significantly large 3D model is required for kinematic applications. Deterministic i.e. ray-tracing algorithms require high computational power. Since the amount of computational power increases with the complexity and size of the 3D model, it is unfeasible to reproduce hundreds of kilometers that are driven in the measurement campaign. Therefore, a new approach is proposed and tested in this work. Synthetic 3D models, with the same environmental characteristics as the test drives are implemented. Multipath error models computed from simulations are compared against the ones computed from measurement campaigns, in the same environment. The results confirm that the HiL simulations for both investigated environments reproduce the multipath error distribution over satellite elevation. Additionally, the characteristics of the errors due to multipath are similar with respect to the investigated frequencies and satellite navigation systems. The magnitude of the errors due to multipath is reproduced within the same range as well. Pseudorange errors for the intercity highway are between 5 centimeters and 82 centimeters for experimental data and between 8 centimeters and 99 centimeters for simulated data. Compared to the previous environment, the multipath estimation for urban roadway reveals an increased error for both simulated and experimental data. These are between 28 centimeters and 260 centimeters for experimental data and between 32 centimeters and 230 centimeters for simulated data. Regarding the positioning errors, the average 3D RMSE is five times bigger in the urban environment, compared to the highway.

Within this dissertation, besides the multipath modeling and simulations for a vehicle setup, error models from experimental data are computed for GPS L1 C/A, L2C and Galileo E1 OS, E5b. The analysis and resulted multipath errors due to multipath are representative for a vehicle in the two investigated environments. This provides an assessment of the expected error levels for similar setups. The improved signal structure of Galileo over GPS is confirmed from simulated and experimental measurements, as the errors due to multipath are larger for GPS. Comparing the two frequencies, it is also shown that the second one is more susceptible to multipath for both navigation systems.

7.2 Further work

One of the limitations regarding multipath estimation for different velocities or environments is that it is dependent on the measurement system. This means, that the errors due to multipath vary for several antennas, receivers, and combinations between them. Within this dissertation, the presented multipath results are consistent with the presented measurement system. The same GNSS receiver is employed for both measurement campaigns and simulations. Nevertheless, further investigations can be employed with different equipment and especially various receivers, to check their capabilities in kinematic multipath conditions. The GNSS antenna can be placed in different places on the vehicle in order to find the location that yields the best results in terms of positioning.

Further work might extend the error models due multipath for a vehicle in additional environments. As outlined in chapter 6, even referring to a specific street sector as highway, the surroundings vary in different countries or continents. Besides the artificial reflectors i.e. buildings, natural reflectors as mountains can affect the errors due to multipath. Additionally, it was shown in the theoretical part that the reflection coefficients influence the multipath signal strength. Therefore, the weather impact should be considered as well, since water for example, changes the reflection properties of the environment.

Regarding the HiL simulations, these can be extended by employing several receivers. In order to perform simulations closer to reality, antenna phase and gain patterns for each frequency can be integrated in the test bench. Both RHCP (Right Hand Circularly Polarized) and LHCP (Left Hand Circularly Polarized) antenna patterns can be measured in an anechoic chamber. The measured patterns that represent the antenna model should be included in the HiL simulations. This would lead an improvement in the simulations, since the antenna influences the multipath signals that reach the receiver.

Further studies should also examine multipath signal filtering. Since the HiL is a hardware limited to a number of available channels to simulate multipath, investigations should aim to find the most adequate settings. Knowledge of which multipath reflections are typical for an environment and affect mostly a receiver can help to simulate corner case situations. Additionally, the hardware resources are used at their best capabilities.

The code minus carrier algorithm is better for assessing multipath in static conditions, compared to kinematic ones. This is the consequence of the cycle-slips, as the ambiguity changes. In this regard, a cycle-slip repair can be implemented. In this way, the data should not be split into continuous segments anymore. Regarding the linear combinations approach, the assessment is based on the assumption that the zenith satellites do not experience multipath. Nevertheless, in reality, all satellites in the sky plot experience the error, although in zenith directions less. An improvement can be made by removing the multipath bias for the zenith satellites before using its pseudorange for double differences.

Bibliography

- Aerts, W.; Bruyninx, C., Defraigne, P. (2010). Bandwidth and sample frequency effects in GPS receiver correlators. 5th ESA Workshop on Satellite Navigation Technologies and European Workshop on GNSS Signals and Signal Processing (NAVITEC), Noordwijk, pp. 1-7, DOI: 10.1109/NAVITEC.2010.5707983.
- Ahmed, E.-R. (2002). Introduction to GPS: The Global Positioning System. Boston, MA Artech House.
- Aloi, D. N., van Graas, F. (1999). Analysis of the Effects of Earth-Surface Based Multipath Reflections on GPS Code-Phase Measurements. Proceedings of the 55th Annual Meeting of The Institute of Navigation (1999), Cambridge, MA, June 1999, pp. 609-618.
- Ávila Rodríguez, J. Á. (2008). On Generalized Signal Waveforms for Satellite Navigation. DDC-Notation: 526.982, München, Dissertation: University of Munich.
- Avila-Rodriguez, J. Á; Hein, J.; Wallner, G.W.; Issler, S.; Ries, J. - L.; Lestarquit, L.; Latour, L.; Bastide, Godet J.; Pratt, F.; Owen, J. (2008). The MBOC Modulation: The Final Touch to the Galileo Frequency and Signal Plan. Journal of the Institute of Navigation, Volume 55, Number 1, pp. 14 – 28.
- Avram, A.; El Gemayel, N; Schwieger, V. (2018a). Assesment of the DLL error due to multipath models regarding a deterministic-tochastic channel and a GPS L1 receiver model for kinematic trajectories. Proceedings of the 31st International Technical Meeting of the Satellite Division of The Institute of Navigation (ION GNSS+ 2018) Florida, pp. 3552 – 3561.
- Avram, A.; Gonzales Rodriguez, E. (2018b). Multi-Sensor-System für Navigation, DVW – Gesellschaft für Geodäsie, Geoinformation und Landmanagement, Hamburg, Wißner-Verlag, pp. 191-203.
- Avram, A.; Schwieger, V.; El Gemayel, N. (2019). Experimental results of multipath behavior for GPS L1-L2 and Galileo E1-E5b in static and kinematic scenarios. Journal of Applied Geodesy, 13(4), pp. 279–289.
- Bao-Yen Tsui, J. (2005). GPS C/A Code Signal Structure. In: Fundamentals of Global Positioning System Receivers. A John Wiley & Sons, INC., New Jersey, pp. 68-70.
- Beitler, A.; Tollkuhn, A.; Giustiniano, D.; Plattner, B. (2015). CMCD: Multipath Detection for Mobile GNSS Receivers. Proceedings of the 2015 International Technical Meeting of The Institute of Navigation, Dana Point, California, January 2015, pp. 455-464.
- Bilich, A. L. (2006). Improving the Precision and Accuracy of Geodetic GPS: Applications to Multipath and Seismology. Dissertation: University of Colorado at Boulder, ISBN: 9780542942051.
- Bilich, A.; Larson, K. M. (2007). Mapping the GPS multipath environment using the signal-to-noise. Radio Science, Volume 42, Issue 6, DOI: 10.1029/2007RS003652
- Boeing1Commercial1Airplanes4(2005). Electromagnetic Modeling of Airframe and Ground Bounce Multipath, Boeing Comemrcial Airplanes, Document Number: D6-83447-2.
- Borre, K.; Akos, D.M.; Bertelsen, N.; Rinder, P.; Jensen, S.H (2007). A Software-Defined GPS and Galileo Receiver. Boston. Birkhäuser, ISBN 978-0-8176-4540-3.
- Braasch, M. S. (1992). On the characterization of multipath errors in satellite based precision approach and landing systems. Ohio, Dissertation: Ohio University.
- Park, B.; Lim, C.; Yun, Y.; Kim, E.; Kee, C. (2017). Optimal Divergence-Free Hatch Filter for GNSS Single-FrequencyhMeasurement.4Sensors Journal (Basel). doi: 10.3390/s17030448.
- Chang, C. L. (2011). Anti-Multipath Filter with Multiple Correlators in GNSS Receivers. In: Adaptive Filtering Applications, InTech Open, pp. 381-399. DOI: 10.5772/16696

- Chen, A.; Chabory, A.; Escher, A.C.; Macabiau, C. (2009). Comparisons of multipath modeling strategies for the estimation of GPS positioning error. 3rd European Conference on Antennas and Propagation, Berlin, 2009, pp. 2300-2304.
- Circiu, M-S.; Caizzone, S.; Felux, M.; Enneking, C.; Meurer, M. (2018). Improved airborne multipath modelling. Proceedings of the 31st International Technical Meeting of the Satellite Division of The Institute of Navigation (ION GNSS+ 2018), Miami, Florida, September 2018, pp. 2195-2209.
- Circiu, M-S.; Felux, M.; Belabbas, B.; Meurer, M.; Lee, J.; Kim, M.; Pullen, S. (2015). Evaluation of GPS L5, Galileo E1 and Galileo E5a performance in Flight Trials for Multi Frequency Multi Constellation GBAS. Proceedings of the 28th International Technical Meeting of The Satellite Division of the Institute of Navigation (ION GNSS+ 2015), pp. 897 - 906.
- Dafesh, P. A.; Parker, A.; Holmes, J. K; Sрни, H. (1998). Simulation of the Code Tracking Performance of Square-Wave Modulated Ranging Codes. Nashville, ION, pp. 633 - 641.
- Dai, Z.; Knedlik, S.; Loffeld, O. (2009). Instantaneous Triple-Frequency GPS Cycle-Slip Detection and Repair. International Journal of Navigation and Observation, Hindawi Publishing Corporation, DOI:10.1155/2009/407231.
- de Bakker, P.F.; van der Marel, H.; Tiberius, C.C.J.M. (2009). Geometry-free undifferenced, single and double differenced analysis of single frequency GPS, EGNOS and GIOVE-A/B measurements. GPS Solutions 13, pp. 305–314. DOI: 10.1007/s10291-009-0123-6.
- dos Santos Prol, F.; de Oliveira Camargo, P.; de Assis Honorato Muella, M. T. (2017). Comparative study of methods for calculating ionospheric points and describing the GNSS signal path. BCG: Bulletin of Geodetic Sciences, October 2017, pp. 669 – 683. ISSN 1982-2170.
- Eissfeller, B. (1997). Ein dynamisches Fehlermodell für GPS-Autokorrelationsempfänger. Dissertation, Studiengang Vermessungswesen, Universität der Bundeswehr München. Fak. für Bauingenieur- und Vermessungswesen, 1997.
- Farkas, H.; Kály-Kullai, K. (2007). The Fermat Principle and Chemical Waves. Science Direct, pp. 355-373. DOI: 10.1016/B978-008044488-8/50020-5.
- Fontan, F. P.; Abele, A.; Montenegro B.; Lacoste, F.; Fabbro, V.; Castanet, L.; Sanmartin, B.; Valtr, P. (2007). Modelling of the Land Mobile Satellite Channel using a virtual city approach. The Second European Conference on Antennas and Propagation, EuCAP, Edinburgh 2007, pp.1-7. DOI: 10.1049/ic.2007.1245.
- Fontan, F.P.; Vazquez-Castro, M.; Cabado, C. E.; Garcia J. P.; Kubista, E. Statistical modeling of the LMS channel. IEEE Transactions on Vehicular Technology, vol. 50, no. 6, pp. 1549-1567, Nov. 2001, DOI: 10.1109/25.966585.
- Fontán, P. F.; Espiñeira, M. P. (2008). Modeling the Wireless Propagation Channel. Spain, Wiley. DOI:10.1002/9780470751749
- Galileo System Status (2021). European GNSS Service Centre. Available at: <https://www.gsc-europa.eu/galileo/system> [Accessed 16 05 2021].
- Gallager, R. (2006). Principles of Digital Communications. Available at: <http://ocw.mit.edu/>, [Accessed 15 08 2018].
- Georgiadou, Y.; Kleusberg, A. (1988). On carrier signal multipath effects in relative GPS positioning. Manuscripta geodetica, 1988; Vol. 13, No. 3. pp. 172-179.
- Gianluca, F.; Pini, M.; Gianluca, M. (2017). Loose and Tight GNSS/INS Integrations: Comparison of Performance Assessed in Real Urban Scenarios. Sensors (Basel), Volume 17, p. 255. DOI: 10.3390/s17020255.
- Goldhirsh, J.; Vogel, W. (1998). Handbook of Propagation Effects for Vehicular and Personal Mobile Satellite Systems. Texas: The University of Texas at Austin.

- Guochang, X.; Yan, X. (2016). Theory, Algorithms and Applications, Springer. ISBN 978-3-662-50367-6.
- Hangerman, L. (1973). Effects on multipath of coherent and non coherent PRN ranging receiver, The Aerospace Corporation Rept. No. TOR-0073(3020-03)-3.
- Hannah, B.M.; Kubik, K.; Walker, R.A. (2003) Propagation Modelling of GPS Signals. Grafarend E.W., Krumm F.W., Schwarze V.S. Geodesy-The Challenge of the 3rd Millennium. Springer, Berlin, Heidelberg.
- Hannah, B. M. (2001). Modelling and Simulation of GPS Multipath Propagation, Queensland: Dissertation: Queensland University of Technology.
- Hegarty, C. (2013). GNSS Measurements and Error Sources, Bedford MA: International Centre for Theoretical Physics.
- Heiskanen, W. A.; Moritz, H. (1967). Physical Geodesy. San Francisco and London: W-H. Freeman and Company.
- Hobiger, T.; Jakowski, N. (2017). Atmospheric Signal Propagation. Handbook of Global Navigation Satellite Systems. Switzerland: Springer, pp. 170-171.
- Hofmann-Wellenhof, B.; Lichtenegger, H.; Wasle, E. (2007). GNSS - Global Navigation Satellite Systems. Wien: Springer.
- IGS (2020). International GNSS Service. Available at: <http://www.igs.org/about#citing> [Accessed 20 02 2020].
- Ikegami, F.; Takeuchi, T.; Yoshida, S. (1991). Theoretical prediction of mean field strength for urban mobile radio. IEEE Transactions on Antennas and Propagation, Volume: 39, Issue: 3, pp. 299 - 302.
- iMAR Navigation & Control (2018). iTraceRT-F402/7. Reihersbruch: iMAR Navigation Document Number.: DOC150709006.
- Irsigler, M. (2008). Multipath Propagation, Mitigation and Monitoring in the Light of Galileo and the Modernized GPS. München. Dissertation: Universität der Bundeswehr München.
- ITU (2015). Effects of building materials and structures on radiowave propagation above about 100fMHz.fGeneva:fInternationalhTelecomunication Union. Electronic Publication, ITU-R P.2040-1.
- ITU (2019). Propagation by diffraction. Geneva: International Telecommunications Union. Electronic Publication, P.526-15.
- Jacks W. C. (1974). Microwave Mobile Communications. New York: John Wiley & Sons Inc.
- Jenn, D. (2000). Radiowave Propagation. Monterey, California: Department of Electrical & Computer Engineering. Document Number EC3630.
- Jones, J.; Fenton, P.; Smith, B. (2004). Theory and Performance of the Pulse Aperture Correlator. NovAtel Inc., Calagary.
- Joseph, K. M.; Braasch, M. S. (2000). Validation of GPS Fading Multipath Effects through Modeling and Simulation. Anaheim, CA, ION, pp. 684-690.
- Kande, L. H.; Kamguia, J.; Yap, L.; Foyang, L. (2016). Reference Ellipsoid Parameters of Cameroon from GPS Data. International Journal of Geosciences, Vol 8, pp. 1049-1056.
- Kaplan,aD. E. (2018). Front End. Available at:https://gssc.esa.int/navipedia/index.php/Front_End [Accessed 27 04 2019].
- Kaplan, E. D.; Hegarty, C. J. (2006). Understanding GPS. Norwood MA, Artech House.
- Karaim M.; Elsheikh M.; Noureldin A. (2018). GNSS Error Sources, Multifunctional Operation and Application of GPS. IntechOpen, DOI: 10.5772/intechopen.75493.

- Keller, J. B. (1962). Geometrical Theory of Diffraction. *Journal of the Optical Society of America*, Vol. 52, Issue 2, pp. 116-130.
- Kerr, D. E. (1964). Propagation of short radio waves. New York: Dover Publications.
- Klobuchar, J. A. (1996). Ionospheric Effects on GPS. In: *Global Positioning System: Theory and Applications Volume I*. United States of America: American Institute of Aeronautics and Astronautics, pp. 485-501.
- Konno, H. (2007). Design of an aircraft landing system using dual-frequency GNSS. CA, USA, Dissertation: Stanford University.
- Lachapelle, G.; Falkenberg, W.; Neufeldt, D.; Kielland, P. (1989). Marine DGPS Using Code and Carrier in a Multipath Environment. *Proceedings of the 2nd International Technical Meeting of the Satellite Division of The Institute of Navigation (ION GPS 1989)*, Colorado Spring, CO, September 1989, pp. 343-347.
- Lau, K. Y. L. (2005). Phase Multipath Modelling and Mitigation in Multiple Frequency GPS and Galileo Positioning. London. Dissertation: Department of Geomatic Engineering University College London.
- Lehner, A. (2007). Multipath Channel Modelling for Satellite Navigation Systems. Dissertation: Technical University Erlangen-Nürnberg.
- Leick, A. (2004). GPS satellite surveying. 3rd Edition. Canada, Wiley.
- Li, H.; Liao, X.; Li, B.; Ling, Y. (2018). Modeling of the GPS satellite clock error and its performance evaluation in precise point positioning. *Science Direct*, Volume 62, Issue 4, pp. 845-854.
- Logan, S. (2013). Spoofing: Upping the Anti. *Inside GNSS*, July 2013, pp. 18-19.
- Logsdon, T. (1992). *The Navstar Global Positioning System*. New York: Van Nostrand Reinhold, 1992. ISBN: 0442010400.
- Lutz, E; Cygan, D.; Dippold, M.; Dolainsky, F.; Papke W. (1991). The Land Mobile Satellite Communication Channel-Recording, Statistics and Channel Model. *IEEE Transactions on vehicular technology*, vol. 40, no. 2, pp. 375-386. DOI: 10.1109/25.289418.
- Ma, C.; Gyu-In, J.; MacGougan, G.; Lachapelle, G. (2001). GPS Signal Degradation Modeling. Salt Lake City, *Proceedings of the 14th International Technical Meeting of the Satellite Division of The Institute of Navigation (ION GPS 2001)*, Salt Lake City, UT, September 2001, pp. 882-893.
- Mao, W.-L.; Tsao, H.-W.; Chang, F.-R. (2004). Intelligent GPS receiver for robust carrier phase tracking in kinematic environments, in *IEE Proceedings - Radar, Sonar and Navigation*, vol. 151, no. 3, pp. 171-180, 12 June 2004, DOI: 10.1049/ip-rsn:20040188.
- Mekik, C.; Can, O. (2010). Multipath Effects in RTK GPS and A Case Study. *Journal of Aeronautics, Astronautics and Aviation, Series A*. 42. 231-240.
- Mella, K. (2007). Theory, Simulation and Measurement of Wireless Multipath Fading Channels. Dissertation: Norwegian University of Science and Technology Department of Electronics and Telecommunications.
- Misra, P.; Enge, P. (2006). *Global Positioning System: Signals, Measurements and Performance*. Lincoln, MA: Ganga-Jamuna Press.
- Mohinder, G.; Angus, A.; Bartone, C. (2013). *Global Navigation Satellite Systems, Inertial Navigation and Integration*. New Jersey: Wiley.
- Mubarak, O. M.; Dempster, G. A. (2010). Exclusion of multipath-affected satellites using early late phase. *Journal of Global Positioning Systems*, 9(2), pp. 145-155.
- Murphy, T.; Geren, P. W; Pankaskie, T. K. (2005). Analysis of Airborne GPS Multipath Effects using High-Fidelity EM Models. *IEEE Transactions*, vol. 44, no. 2.

- Niemeier, W. (2008): *Ausgleichsrechnung: Statistische Auswertemethoden*. 2. Auflage. Walter de Gruyter, Berlin.
- NovAtel(2015). *Application Note APN-051*. Calgary: NovAtel Inc.
- Oestges, C.; Saunders, S. R.; Vanhoenacker-Janvier, D. (1999). Physical statistical modelling of the land mobile satellite channel based on ray tracing. *IEE Proceedings Microwaves, Antennas and Propagation*. Volume: 146 , Issue: 1, pp. 45 - 49.
- Oestges, C.; Vanhoenacker-Janvier, D. (2001). A Physical-Statistical Shadowing Correlation Model and its Application to Low-Earth-Orbit Systems. *IEEE Transactions on Vehicular Technology*, 5(2), pp. 416 - 421.
- Ondrej, D.; Nunzia, G. F.; Figueiredo e Silva, P. Nurmi, J. (2017). Understanding the GNSS Signal Model. In: *Multi-Technology Positioning*, Springer, pp. 14-17.
- Opaluwa, Y. D.; Okorochoa, C.; Abazu, I.; Odumosu, J.; Ajayi, O. (2015). The effect of the GPS satellite geometry on the precision of DGPS positioning in Minna, Nigeria. *Jurnal Teknologi*, 12 (ISSN 2180–3722), pp. 109-115.
- Panicciari, T.; Soliman, M. A.; Moura, G.(2017). Evaluation of a GNSS receiver performance in different multipath environments with a novel real-time multipath simulation system. *Proceedings of the 30th International Technical Meeting of the Satellite Division of The Institute of Navigation (ION GNSS+ 2017)*, Portland, Oregon, September 2017, pp. 427-435.
- Pany, T. (2010). *Navigation Signal Processing for GNSS Software Receivers*. Norwood: Artech House.
- Park, B.; Lim, C.; Yun, Y.; Kim, E.; Kee, C. (2017). Optimal Divergence-Free Hatch Filter for GNSS Single-Frequency Measurement. *Sensors (Basel)* 17(3), pp. 117-145.
- Parkinson, B.; Spilker, J.; Axelrad, P.; Enge, P. (1996). *Global Positioning System Theory and Applications Volume I*. California: American Institute of Aeronautics and Astronautics.
- Pathak, P. H.; Carluccio, G.; Albani, M. (2013). The Uniform Geometrical Theory of Diffraction and Some of Its Applications. *IEEE Antennas and Propagation Magazine*, Volume: 55, Issue: 4, pp. 41 - 69.
- Prieto-Cerdeira, R.; Perez-Fontan, F.; Burzigotti, P.; Bolea-Alamañac, A.; Sanchez-Lago, I. (2010). Versatile two - state land mobile satellite channel model with first application to DVB - SH analysis. *International Journal of satellite communications and networking*. Volume 28, Issue 5-6. DOI: 10.1002/sat.964.
- Principe, F.; Bacci, G.; Giannetti, F.; Luise, M. (2011). Software-Defined Radio Technologies for GNSS Receivers: A Tutorial Approach to a Simple Design and Implementation. *International Journal of Navigation and Observation*. DOI: 27. 10.1155/2011/979815.
- Proakis, J. (2001). *Digital Communications*. New York: McGraw-Hill.
- Rappaport, T. S. (2002). *Wireless Communications Principles and Practice Second Edition*. Massachusetts: Prentice Hall PTR.
- Ray, J. K. (2000). *Mitigation of GPS Code and Carrier Phase Multipath Effects Using a Multi-Antenna System*. Calgary. Dissertation: University of Calgary, Department of Geomatics Engineering.
- Rice, M.; Davis, A.; Bettweiser, C. (2004). Wideband channel model for aeronautical telemetry, *IEEE Transactions on aerospace and electronic systems*. Vol. 40, no. 1, pp. 57-69.
- Robert Bosch GmbH (2019). *Automated Driving Steps*, Abstatt. Internal document: unpublished.
- Rodgers, C. E., 1992. Multipath Simulation Software Developed for the Design of a Low Multipath DGPS Antenna for the U. S. Coast Guard. *Proceedings of the 5th International Technical Meeting of the Satellite Division of The Institute of Navigation (ION GPS 1992)*, Albuquerque, NM, September 1992, pp. 43-50.

- Rodríguez, J. A. (2014). Navipedia. Available: https://gssc.esa.int/navipedia/index.php/Galileo_Signal_Plan#Galileo_E5_Band [Accessed 31 01 2019].
- RTCA DO-253C (2008). Minimum operational performance standards for GPS local area augmentation system airborne equipment, December 2008, Washington.
- Saunders, S.; Aragon-Zavala, A. (1999). *Antennas and Propagation for Wireless*. New York: Wiley.
- Saunders, S. R.; Aragon-Zavala, A. (2007). *Antennas and Propagation for wireless communication systems*. Chichester: Wiley.
- Schaubach, K. R., Davis, N. & Rappaport, T. S., 1992. A ray tracing method for predicting path loss and delay spread in microcellular environments. 1992 Proceedings: Vehicular Technology Society 42nd VTS Conference - Frontiers of Technology, Denver, CO, USA, 1992, pp. 932-935 vol.2.
- Schmitz, A. (2012). *Ray Tracing for Light and Radio Wave Simulations*. Aachen: Dissertation: RWTH.
- Schmitz, A.; Rick, T.; Karolski, T.; Kobbelt, L.; Kuhlen, T. (2009). *Beam Tracing for Multipath Propagation in Urban Environments*. Berlin, Germany EuCAP 2009: 3rd European Conference on Antennas and Propagation, 23 - 27 March 2009, Berlin, Germany.
- Schneckenburger, N.; Jost, T.; Fiebig, U.-C.; Del Galdo, G.; Jamal, H.; Matolak, D.; Sun, R. (2017). Modeling the air-ground multipath channel. 2017 11th European Conference on Antennas and Propagation (EUCAP), Paris, pp. 1434-1438.
- Schnell, M.; Fiebig, U.-C. (2002). Report: Radiowave Propagation Modelling for SatCom Services at Ku-Band and Above, Noordwijk: ESA Publications Division.
- Schüler, T. (2000). *On Ground-Based GPS Tropospheric Delay Estimation*. München. Dissertation: Universität der Bundeswehr München.
- Seeber, G. (2003). *Satellite Geodesy*. Berlin: Walter de Gruyter GmbH & Co. KG.
- Sennott, W. J.; Pietraszewski, D. (1987). Experimental Measurement and Characterization of Ionospheric and Multipath Errors in Differential GPS. *Journal of the Institute of Navigation*. Volume 32, Issue 2, pp. 160-173.
- Seong-Cheol, K.; Guariano, B.J.; Willis, T.M.; Erceg, V.; Fortune, S.J.; Valenzuela, R.A.; Thomas, L.W.; Ling, J.; Moore, J.D. (1999). Radio propagation measurements and prediction using three-dimensional ray tracing in urban environments at 908 MHz and 1.9 GHz. *IEEE Transactions on Vehicular Technology*, vol. 48, no. 3, pp. 931-946.
- Simsky, A.; Mertens, D.; Sleewaegen, J.-M.; Willems, T. (2008). Multipath and Tracking Performance of Galileo Ranging Signals Transmitted by GIOVE-A, Proceedings of the 21st International Technical Meeting of the Satellite Division of The Institute of Navigation (ION GNSS 2008), Savannah, GA, September 2008, pp. 1525-1536.
- Sjöberg, L. E. (2018). On the geoid and orthometric height vs. quasigeoid and normal height. *Journal of Geodetic Science*, Volume 8, Issue 1, pp. 115-120.
- Sleewaegen, J.-M.; De Wilde, W. (2008). *Galileo AltBOC Receiver*. Available at: read.pudn.com/downloads192/doc/comm/902008/Galileo%20AltBOC%20Receiver.pdf [Accessed 26 03 2019].
- Smyrniotis, M.; Schön, S.; Marcos, N. L. (2018). Multipath Propagation, Characterization and Modeling in GNSS. In: *GNSS Error Sources*. London: IntechOpen, pp. 100-124.
- Spilker, J. J. (1980). GPS Signal Structure and Performance Characteristics. *Journal of Institute of Navigation*. Volume 24, Issue 2, pp. 29-54.
- Spirent Communications (2019). Document number: 1DGP01576AAA, 2Spirent1 Communications Plc.

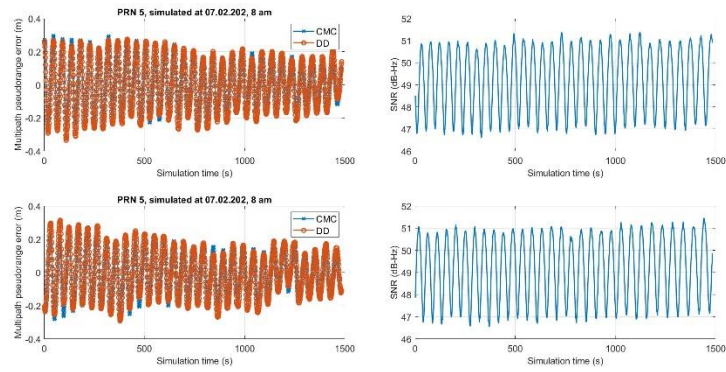
- Spirent Communications Plc (2017). Software for the Spirent Range of Satellite Navigation Simulation Products. England: Spirent Communications Plc.
- Spirent Communications (2017). Report: Sim3D Validation Results, Spirent Communications Plc, unpublished.
- Spirent Communications (2018). DGP00686AAA Issue: SimGen Software User Manual, Spirent Communications.
- Spirent (2018). Spirent PosApp Training: Multipath Models, unpublished.
- Srilatha, I. D. V. Dutt, I.; Sasi, G.; Rao, B.; Swapna, S.; Banu, S.-R.; Goswami, R.; Kumary, U. (2009). Investigation of GDOP for Precise user Position Computation with all Satellites in view and Optimum four Satellite Configurations. *The Journal of Indian Geophysical Union*, 13(3), p. 139148.
- Stutzman, W. (1993). *Polarization in Electromagnetic Systems*. Boston - London: Artech House.
- Subirana, J. S.; Zornoza, J. J.; Hernández-Pajares, M. (2011). *aPositioningaError.aAvailableaat: https://gssc.esa.int/navipedia/index.php/Positioning_Error*. [Accessed 15 02 2019]
- Subirana, J. S.; Zornoza, J. J.; Hernandez-Pajares, M. (2013). *GNSS Data Processing, Vol. I: Fundamentals and Algorithms*. ESA Communications.
- Teunissen, P. J.; Montenbruck, O. (2017). *Springer Handbook of Global Navigation Satellite Systems*, Springer. DOI 10.1007/978-3-319-42928-1.
- Todorova, M.; Donceva, R.; Bunevska, J. (2009). Role of functional classification of highways in road traffic safety. *DOAJ, Transport Problems: an International Scientific Journal* 4, Issue 3, Part 1.
- Torge, W. (2001). *Geodesy*. New York: Walter de Gruyter.
- Townsend, B. R.; van Nee, R. D.; Fenton, P. C.; van Dierendonck, K.-J. (1995). Performance Evaluation of the Multipath Estimating Delay Lock Loop. *Journal of the Institute of Navigation*, Volume 42, Number 3, pp. 503 – 514.
- Tran, M.; Hegarty, C. (2002). Receiver Algorithms for the New Civil GPS Signals. *Proceedings of the 2002 National Technical Meeting of The Institute of Navigation*, pp. 778-789.
- Tzaras, C.; Saunders, S. R.; Evans, B. G. (1998). Physical-statistical propagation model for diversity in mobile satellite PCN. *VTC '98. 48th IEEE Vehicular Technology Conference. Pathway to Global Wireless Revolution*, pp. 525-531.
- van Dierendonck, A.-J. (1992). Theory and Performance of Narrow Correlator Spacing in a GPS Receiver. *Journal of The Institute of Navigation*. Vol. 39, pp. 266-282.
- van Dierendonck, A. J. (1996). *GPS Receivers. In: Global Positioning System: Theory and Applications*. Vol. I. Washington DC: American Institute of Aeronautics and Astronautics, pp. 329-408.
- van Diggelen, F. (2009). *The Smartphone Revolution, GPS World*. Vol. 20, pp. 36-40.
- van Nee, R. D. (1992). Multipath Effects on GPS Code Phase Measurements, *Institute of Navigation*, Vol. 39, No. 2, pp. 915-924.
- Villacieros, M. (2011). *Two state model for Land Mobile Satellite Systems: Parameter extraction and time series synthesis*. Belgium. Dissertation: Universite catholique de Louvain.
- von Hünerbein, K.; Moura, G. (2014). A new tool for simulation of geospecific multipath and obscuration of GPS / GNSS signals with relation to realistic 3-D city models, 2014 - 34. *European Telemetry and Test Conference*, pp. 161-165.
- Wang, J., 2002. *Advanced Tracking Loop*. In: *Broadband Wireless Communications*. Boston: Springer, Boston, pp. 95-121.

- Ward, P. W.; Betz, W. J.; Hegarty, J. C. (2006). GPS Satellite Signal Characteristics. In: Understanding GPS Principles and Applications. Norwood: Artech House, pp. 113-124.
- NovAtel Inc. (2017). Waypoint Training Seminar, Spain, unpublished.
- Weiss, J. P. (2007). Modeling and Characterization of Multipath in Global Navigation Satellite System Ranging Signals, Colorado. Dissertation: University of Colorado.
- Whitted, T. (1980). An improved illumination model for shaded display. Magazine Communications of the ACM, vol. 23, Issue 6, pp. 343-349.
- Winkel, J. O. (2000). Modelling and Simulating GNSS Signal Structures and Receivers, München, Dissertation. Universität der Bundeswehr München.
- Wu, X.; Shuanggen, J.; Junming, X. (2017). A Forward GPS Multipath Simulator Based on the Vegetation Radiative Transfer Equation Model. Sensors (Basel). 17(6):1291. Published 2017 Jun 5. DOI:10.3390/s17061291.
- Xu, G. (2016). GPS Theory, Algorithms and Applications, Springer.
- Yedukondalu, K.; Sarma, A. D.; Kumar, A.; Satyanarayana, K. (2013). Spectral Analysis and Mitigation of GPS Multipath Error Using Digital Filtering for Static Applications. IETE Journal of Research, 59(2), pp. 156-166.
- Yedukondalu, K.; Sarma, A.; Satya Srinivas, V. (2011). Estimation and mitigation of GPS multipath interference using adaptive filtering. Progress in Electromagnetics Research, Vol. 31, pp. 133-148.
- Yedukondalu, K., Sarma, A. & Srinivas, S. V., 2009. Multipath Mitigation Using LMS adaptive filtering for GPS Applications. 2009 Applied Electromagnetics Conference (AEMC), Kolkata, pp. 1-4. DOI: 10.1109/AEMC.2009.5430568.
- Hu, Y.; Maozhong, S.; Meng, B.; Dang, X. (2013). An Efficient Method for GPS Multipath Mitigation Using the Teager-Kaiser-Operator-Based MEDLL. Radioengineering, 22(1210-2512), pp. 1202-1210.
- Zhang, L. (2016). Qualitätssteigerung von Low-Cost-GPSkZeitreihenofürppMonitoring Applikationen0000durch000zeitlich-räumliche Korrelationsanalyse.00DKG,000Reihe00C, Nr. 776, München 2016, ISBN 978-3-7696-5188-1.
- Zhang, X.; Huang, P. (2014). Optimal Hatch Filter with an Adaptive Smoothing Time Based on SBAS, 2nd International Conference on Soft Computing in Information Communication Technology, Atlantis Press. DOI: 10.2991/scict-14.2014.9
- Zimmermann, F.; Schmitz, B.; Klingbeil, L.; Kuhlmann, H. (2018). GPS Multipath Analysis Using Fresnel Zones. Sensors, 19, 25. DOI:10.3390/s19010025.
- Zuev, K. (2017). Statistical Inference. SSRN Electronic Journal. DOI:10.2139/ssrn.3125891.

Appendix

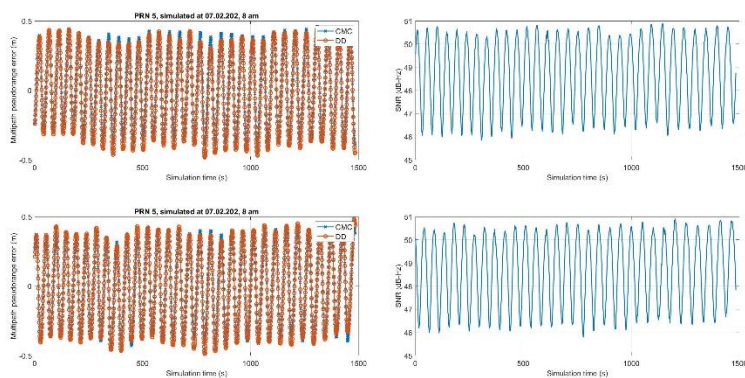
Appendix A

A.1 Multipath and SNR time series for simulated satellites in consecutive days



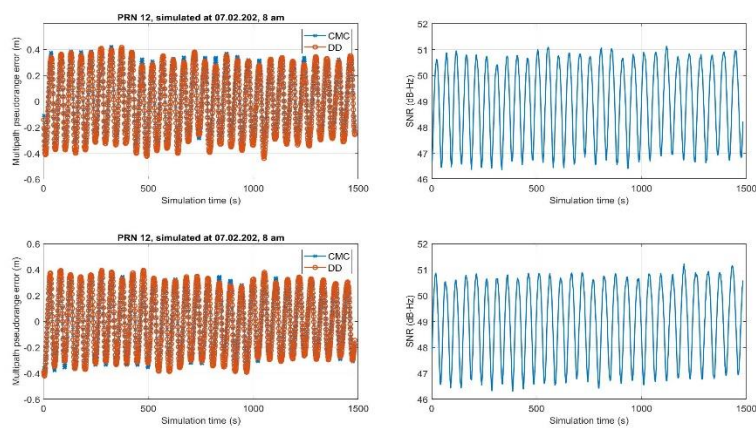
(a)

(b)



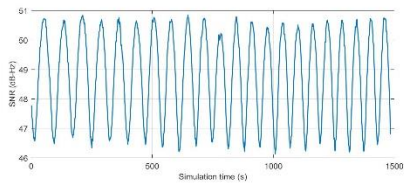
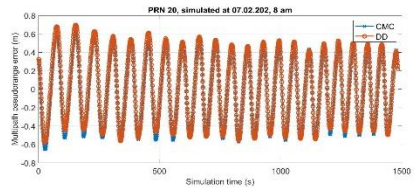
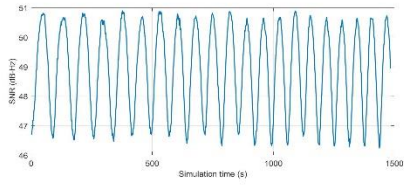
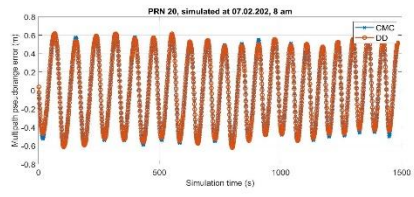
(a)

(b)



(a)

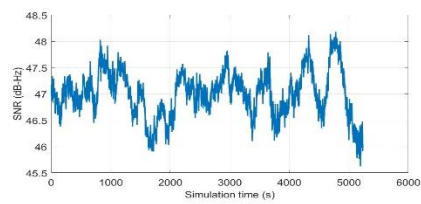
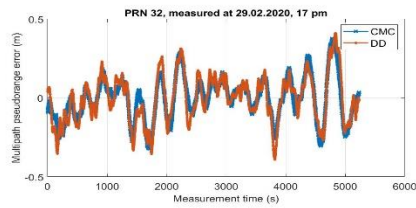
(b)



(a)

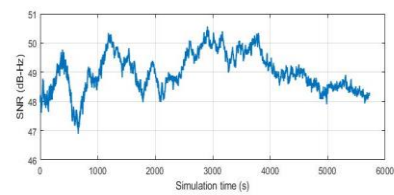
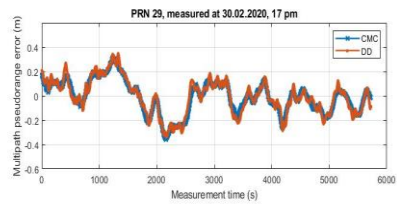
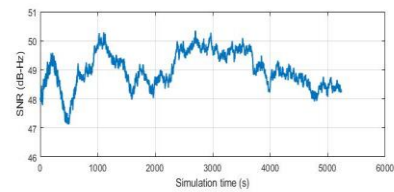
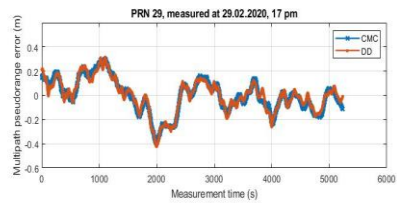
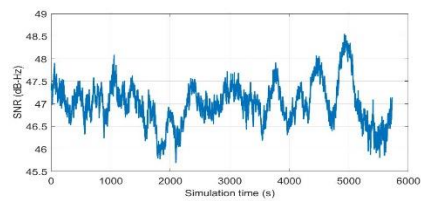
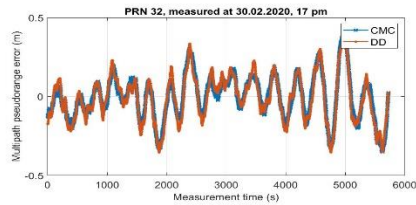
(b)

A.2 Multipath and SNR time series for measured satellites in consecutive days



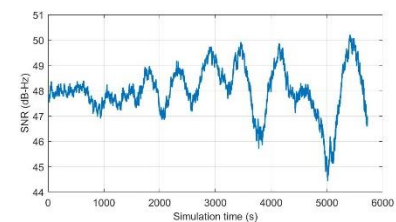
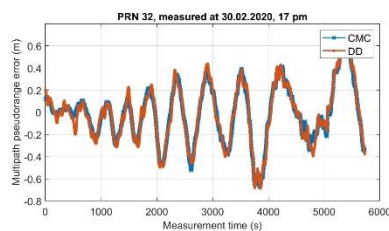
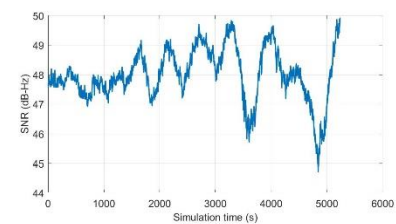
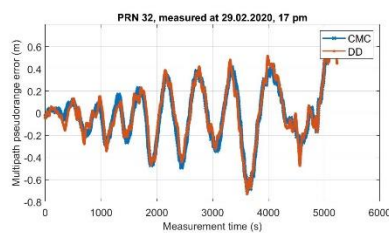
(a)

(b)



(a)

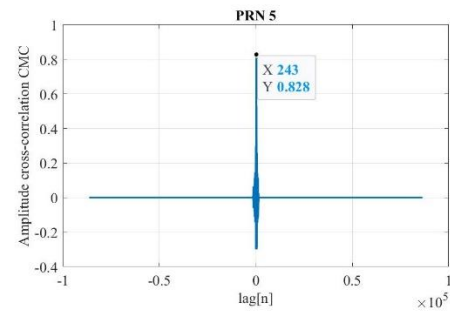
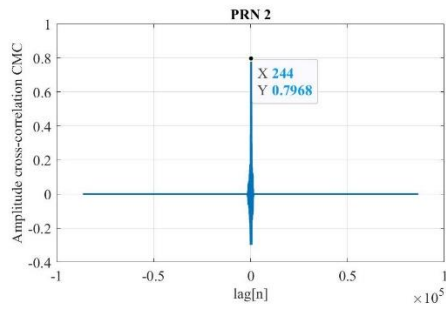
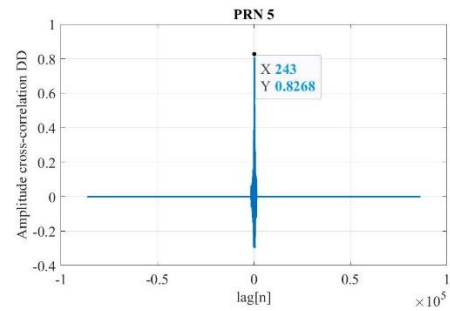
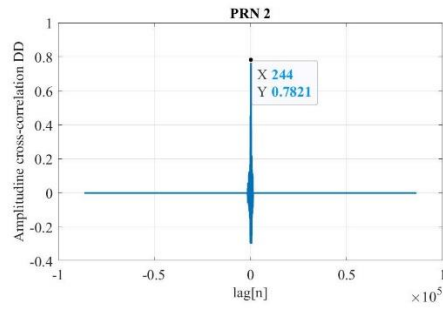
(b)



(a)

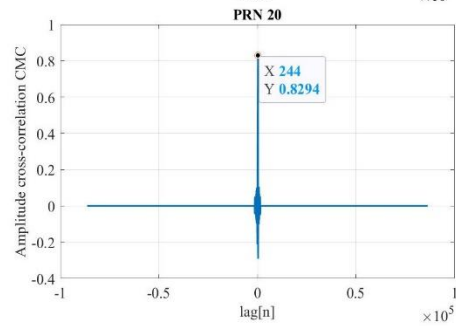
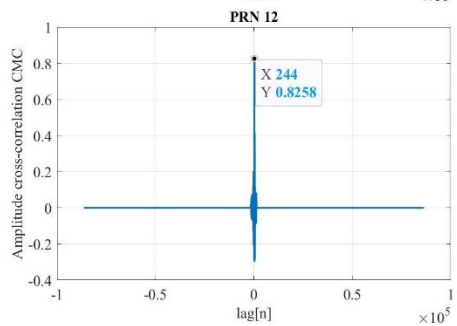
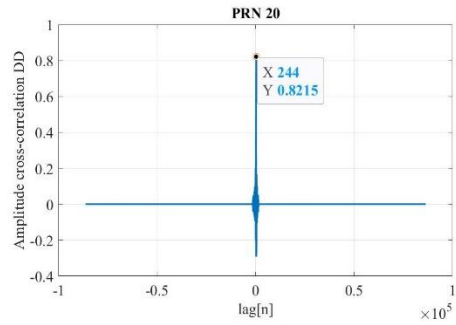
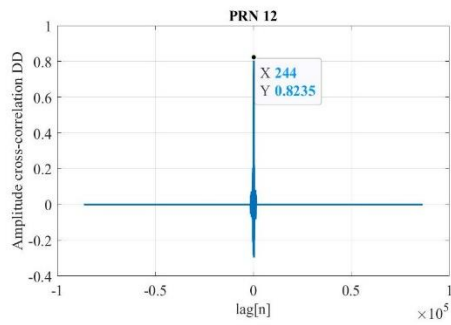
(b)

A.3 Cross-correlation between simulated multipath time series from consecutive days



(a)

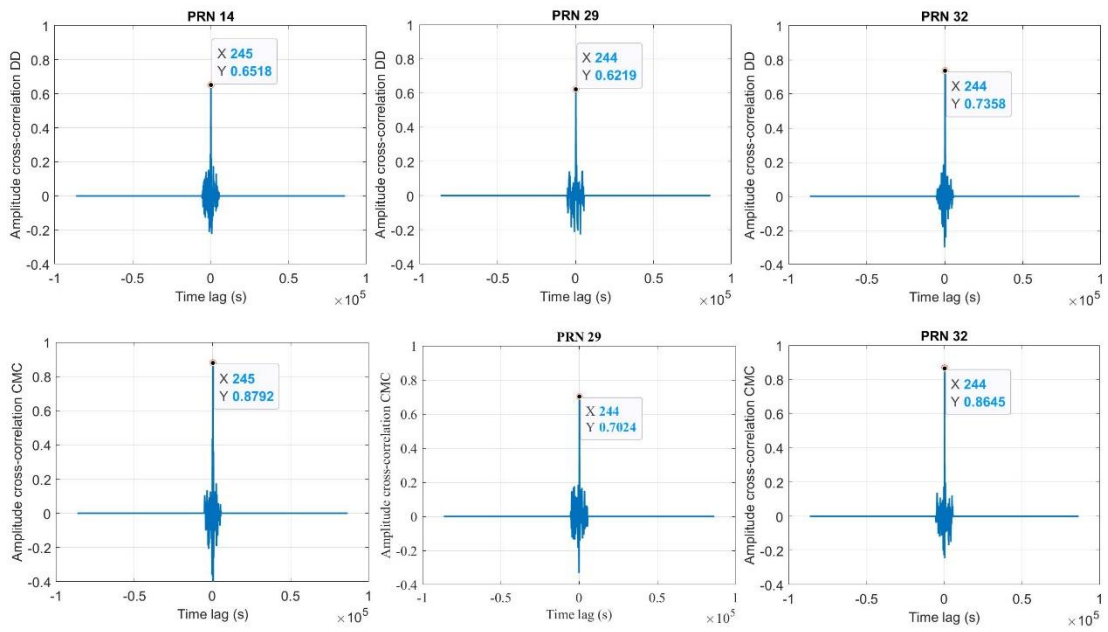
(b)



(a)

(b)

A.4 Cross-correlation between measured multipath time series from consecutive days



(a)

(b)

(c)

Appendix B

B.1 Signal generator settings

The software of the signal generator Spirent GSS7000, namely SimGEN, allows the parametrization of a simulation before generating the GNSS signals. The software SimGEN has the following capabilities:

- a. GNSS constellation definition through Keplerian elements or import of ephemerides;
- b. Atmospheric errors manipulation by applying different models;
- c. Definition of user static/kinematic position by WGS84 coordinates;
- d. Receiver antenna phase and gain patterns modeling;
- e. Modification of the satellite signal by adding multipath with the simulated characteristics;

GNSS constellation editor

SimGEN allows multiple constellation simulation that is Galileo, GPS, and GLONASS. To define the constellation, there are two possibilities:

- a. Definition of ideal orbits with Keplerian elements;
- b. Import of ephemeris data.

For the definition of an ideal orbit, the following parameters have to be set: time, date and simulation duration. This has the advantage of simulating with error-free orbits. This means that the pseudoranges of the simulated SV are not subject to biases due to ephemeris errors. On the other hand, for realistic simulations, the import of ephemeris files can be used to define a specific orbit. Orbital data can be imported in RINEX format. By doing this, the satellite parameters are automatically updated with real information sent from satellites. This use-case has the advantage of allowing the recreation of orbits from measurement campaigns.

Atmospheric errors manipulation

The atmosphere file consists of two error models: for ionosphere and troposphere. The available tropospheric models are STANG, BD2, RTCA96, and RTCA98. Additionally, the surface refractivity index can be enabled. There is the possibility either to choose from these models or to shut down the troposphere error completely. As for the ionosphere error, there are also various models to choose from. These can be applied constellation specific. For GPS and GLONASS, the Klobuchar model is available and for GALILEO the NeQuick model can be employed. The ionosphere has the possibility to be shut down as well. Thus, there is the possibility to simulate GNSS signals which are not affected by the atmospheric errors. Although not realistic, this option is helpful to carry out simulation where only multipath is affecting the GNSS observations. In the absence of other errors, its impact can be correctly assessed.

User position definition

The simulations are completed by assuming a static or dynamic user. For this, the position has to be defined for the simulation duration. A possibility to define the position is through batch files. These

define the user position with respect to the WGS84 ECEF frame (X, Y, Z). Table B-1 summarizes the command parameters that have to be defined for the batch file. It is to be considered that this file must have the same update rate as the multipath simulation. This allows that the biased GNSS observations are computed for each trajectory point.

Table B-1: User position command input

<timestamp>	From start of simulation (s)
<x>,<y>,<z>	Position on x-axis, y-axis and z-axis (m)
<vel_x>,<vel_y>,<vel_z>	Velocity on x-axis, y-axis and z-axis (m/s)
<acc_x>,<acc_y>,<acc_z>	Acceleration on x-axis, y-axis and z-axis (m/s ²)

Antenna modeling

The receiving antenna plays an important role in the multipath simulation. Antenna gain patterns define attenuation and gain for each frequency, according to the satellite elevation and azimuth. Prior research confirms that multipath has a higher probability to occur for the lower elevation satellites. This is the reason why the commercial antenna gains have a gain factor for the GNSS signals arriving from high elevation and an attenuation factor for the signals originating from low satellite elevation. The right side of Figure reveals a commercial antenna, where the gain is applied for the high angle of arrival signal. On the contrary, the ideal antenna illustrated on the left side has the same gain for all signals.

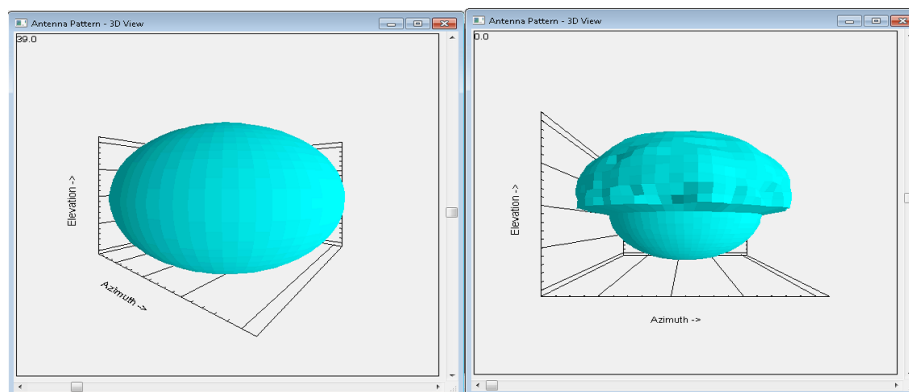


Figure B-1: Gain patterns for the ideal antenna (left) and measurement campaign antenna (right).

There is the possibility to take account for the antenna gain in the GNSS signal generator. An antenna gain file is a grid where each azimuth and elevation corresponds to attenuation or gain factor. This file can be imported in order to simulate with the same receiving antenna that is used for measurement campaigns, for example.

Another approach is to simulate with an isotropic antenna, which is a zero dB gain overall i.e. left side of Figure B-1. By making this, there is no influence due to the antenna during the simulations. Consequently, the multipath influence on the SNR can be directly analyzed because no modifications due to the antenna occur. However, for this approach, the use of a low noise amplifier (LNA) is recommended, as the GNSS signals must be amplified for the receiver to be able to process them.

Multipath data

SimGEN allows signal control commands through batch files of a defined format. This capability implies the state definition of signal for visible SVs, applies a specific number of multipath signals on the desired SV, defines for each time stamp the changes in power level, code, and carrier offset. Based on this facility, multiple multipath models can be implemented and simulated with an RF signal. Table B-2 shows the parameters that have to be given for each simulation timestamp in order to bias a GNSS signal with multipath.

Table B-2: Header format for multipath signal manipulation

<timestamp>	From the start of simulation (s)
MP_SWITCH	Command to add multipath
<signal_type>	GPS, GALILEO, GLONASS
<freq>	L1, L2, E1, E5
<svid>	Satellite number
<add_remove>	Add or remove multipath signals and keep or remove LOS signal
<number>	Number of multipath reflections
<sig_level>	Signal level (dB)
<carr_offset>	Carrier offset (m)
<code_offset>	Code offset (m)

When creating such batch files for multipath manipulation, the simulation-sampling rate has to be considered. This can be 1, 10, or 100 Hz. Moreover, each multipath signal occupies a so-called physical channel of the GSS7000. The timestamp to activate such a channel by activating multipath has to be considered. The latency, in this case, is found in Spirent Communications Plc (2017) to be 3 seconds. Therefore, multipath signals commands have to be sent 3 seconds before the desired action time.

B.2 Simulation settings

In Chapter 5, simulations are performed to assess which multipath model is adequate for kinematic multipath simulations. The settings of the GSS7000 signal generator remained identical during the simulations, besides the receiver velocity and multipath model. Table B-3 summarizes the settings that were applied.

Table B-3: Simulations settings

Date	02.04.2019
Time	00:00:00
Constellation	GPS (L1/L2), GALILEO (E1/E5b)
Ionosphere model	Klobuschar
Troposphere model	STANG
Antenna model	Isotropic
Multipath model	Physical Statistical / Sim3D

Receiver trajectory	Trajectory.umat
Velocity (km/h)	0, 30, 50, 70, 90, 110

Appendix C

C.1 Hardware receiver: NovAtel PwrPak7

The GNSS receiver that is used for measurement campaigns and simulations is NovAtel PwrPak7. An overview of the installation is shown in Figure C-1. Option 1 illustrates a GNSS antenna, which provides the signal to the hardware receiver. This setting was used for the measurements in the test vehicle. Option 2 is related to the simulations on the test bench. The GNSS signal is sent to the NovAtel PwrPak7 directly from the GNSS signal generator. For both measurements (i.e. vehicle and laboratory), the receiver must be connected to a power supply and a PC.

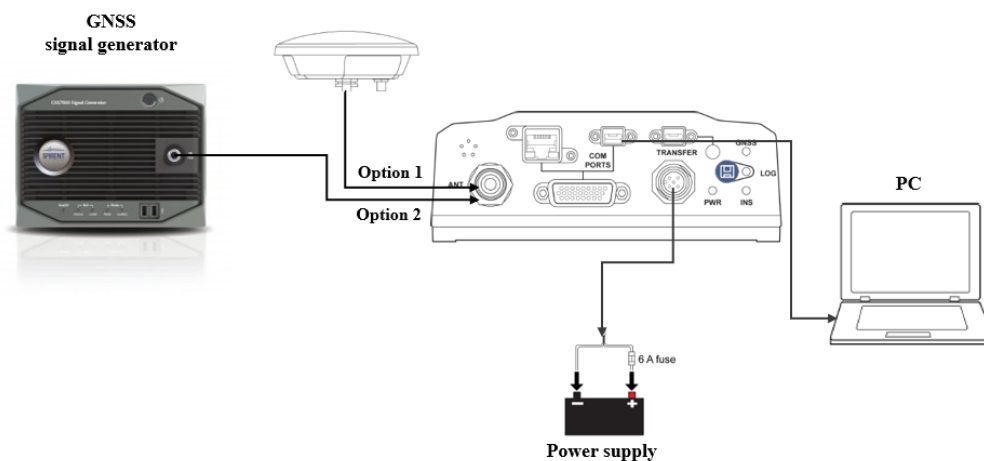


Figure C-1: NovAtel PwrPak7 installation overview as illustrated in NovAtel PwrPak 7 (2015)

To be able to setup the NovAtel PwrPak7 receiver and login the raw GNSS data, the software NovAtel Connect 2.2.1 is used. The open-source software with a window GUI is easy to handle and offers an overview of the real-time GNSS measurements that are saved.



Figure C-1: NovAtel Connect GUI window

In order to retrieve the GNSS data as RINEX format for the necessary post-processing, the data mentioned in Table C-1 needs to be saved for each measurement.

Table C-1: Raw data that needs to be logged in from NovAtel Connect

VERSION (ASCII/BINARY)
BESTPOS (ASCII/BINARY)
IONUTC (ASCII/BINARY)
RANGE (ASCII/BINARY)
RAWEPHEM (ASCII/BINARY)
GPSEPHM (ASCII/BINARY)
GALEPHEMERIS (ASCII/BINARY)

C.2 Vehicle reference system: iTraceRT-F402-E

The sensor iTraceRT-F402-E is activated during all measurement campaigns, to login data for computation of the ground truth trajectory. iTraceRT-F402 is a deeply coupled inertial navigation system that provides: acceleration, angular rate, attitude, true heading, velocity and position with an update rate up to 400 Hz. The technical specifications of the iTraceRT-F402-E are summarized in Table C-2. However, the mentioned accuracies are theoretical and unreachable in real test drives.

The on-the-fly position that is provided by the deeply coupled sensor is used for post-processing with virtual reference stations (VRS). The following measurements are post-processed with NovAtel Waypoint® Inertial Explorer®: VRS, RINEX observation files and iTraceRT-F402-E output files. The result consists of the PP (post-processed) file and represents the reference trajectory of the vehicle.

Table C-2: Technical Data of iTraceRT-F402-E (iMAR Navigation & Control, 2018). To be mentioned that the accuracy values are theoretical and unlikely to be reached in real measurements

	Roll/Pitch	Yaw	Remarks	
Accuracy	0.01°	0.025°	INS/RTK-GNSS	
Angles	0.01°	0.03°	after 10 sec RTK-GNSS outage	
	0.02°	0.04°	after 60 sec GNSS outage	
	Horizontal	Vertical		
Accuracy	±2 cm	5 cm+2 ppm	INS/RTK-GNSS	
	±10 cm	±12 cm	10 s GNSS outage	
	±90 cm	30 cm	60 s GNSS outage	
Position	±1.8 cm	±1.8 cm	pure GNSS	
	±2 cm	5 cm	post-proc, INS/RTK	
	Velocity			
Accuracy	0.01 m/s		NS/RTK-GNSS	
	0.02 m/s		10 s GNSS outage	
	0.04 m/s		30 s GNSS outage	

Acknowledgements

The work presented in this dissertation was possible thanks to a cooperation between the University of Stuttgart and Robert Bosch GmbH. I would like to gratefully acknowledge my doctoral supervisor Prof. Dr.-Ing. habil. Volker Schwieger for making the collaboration possible, for his support and guidance throughout my research. Furthermore, I would like to thank Univ.-Prof. Mag. Dr. habil. Thomas Pany for his helpful suggestions that further improved this work.

My sincere thanks to Dr. Noha El Gemayel for the valuable technical discussions and encouragement during the years of research. I would further like to thank my colleagues from the Institute of Engineering Geodesy (IIGS) and Robert Bosch GmbH for providing a pleasant environment and the resources necessary throughout the course of my research. Special thanks to my friend Dr. Simona Circiu who provided invaluable advice, support and help with programming topics.

Last but not least, I want to express my utmost gratitude to my family. To my parents who did every possible effort to support me. Thanks to their guidance towards knowledge, encouragement and love, I could achieve my goals. My appreciation and gratitude go also to my sister and husband, who supported me patiently during my research.

Curriculum Vitae

Personal Data

Name: Alexandra Avram
 Date of birth: 02.01.1991
 Nationality: Romanian

Education and training

10/2014 – 09/2016 International M.Sc. Program GEOENGINE
 University of Stuttgart
 10/2010 - 06/2014 B.Sc. Geodesy
 Technical University Bucharest
 06/2008 - 06/2010 High School Diploma
 Mathematics-Informatics High-School “Carol I”

Work experience

10/2019 – today Development Engineer for positioning sensor, Robert Bosch GmbH
 10/2016 – 10/2019 Research Engineer: A contribution to multipath modeling and simulation for kinematic trajectories
 University of Stuttgart - Robert Bosch GmbH
 04/2016 – 09/2016 Master Thesis: Optical Localization
 University of Stuttgart - Robert Bosch GmbH
 06/2015 – 08/2016 Working Student: GIS visualization and Mapping for “Digital Humanities”
 Institut für Amerikanistik, Universität Stuttgart
 03/2015 - 04/2015 Internship Intermetric – Integrated Field work
 CAD Department
 03/2014 - 06/2014 Bachelor Thesis: Airports 3D Model and GIS technology
 Technical University of Civil Engineering Bucharest
 07/2013 - 08/2013 Town planner - Land Management Projects
 Technical University of Civil Engineering Bucharest
 Faculty of Geodesy
 07/2013 - 08/2013 Cartographer
 Military Topographic Department Bucharest